

EXPERIMENTAL CHARACTERIZATION, DESIGN, ANALYSIS AND OPTIMIZATION
OF FLEXIBLE FLAPPING WINGS FOR MICRO AIR VEHICLES

By

PIN WU

A DISSERTATION PRESENTED TO THE GRADUATE SCHOOL
OF THE UNIVERSITY OF FLORIDA IN PARTIAL FULFILLMENT
OF THE REQUIREMENTS FOR THE DEGREE OF
DOCTOR OF PHILOSOPHY

UNIVERSITY OF FLORIDA

2010

© 2010 Pin Wu

To my mom 高卓敏 and dad 吴锦波, who have given me unlimited spiritual support
To all my families and relatives, without whose love I could not have progressed so far
To my true love 黄瑾, who has become my world and shared her beautiful heart with me
To my best friend Ivea 赵楠, who shares my hobbies and supports me in difficult times
To my best friend Meng 张萌, who's made me a better person by disagreeing with me
To my best friend Bret K. Stanford, who sets the example of hard work and dedication
To my advisor Prof. Peter G. Ifju, who has given me this exciting opportunity in research
To all my teachers, who always love their students
To many others who care for me and my work
And to myself 吴频

ACKNOWLEDGMENTS

I would like to first express my sincere thanks to my advisor Prof. Peter Ifju who gives me this awesome opportunity to work on the topic of flapping wings for micro air vehicles. I would also like to thank Prof. Laurence Ukeiley, Prof. Raphael Haftka, and Prof. David Bloomquist for being on my committee. I want to particularly thank Dr. Bret Stanford for his friendship, stimulation and input to myself and this work.

Along the research, there are many people who have contributed to this work and I would like to thank them all. I would like to thank Prof. Wei Shyy for leading the MURI project that allows students from different disciplines come together. I truly appreciate the opportunities working with Scott Bowman, Erik Sällström, Robert Love, Satish Chimakurthi, Hikaru Aono and Abhijit Gogulapati, who all are excellent friends and colleagues. I would also like to thank Prof. Roberto Albertani for his help with experiments and thank Prof. Rick Lind for his valuable input.

Interaction with other talented people in the lab is also very inspiring, therefore I would like to thank Kyuho Lee, Daniel Claxton, Frank Boria, Baron Johnson, Mike Sytsma, James Davis, Carlo Francis, Albert Lin, Yaakov Abudaram, Enoch Chen, Vijay Jagdale, Nancy Strickland, Lunxu Xie, Zachary Wilcox, and Mike Morton. Last but not least, I would like to thank all undergraduate and exchange students who spent both fun and productive time in my lab. They are Jeremiah Isaac, Alexis Schwartz, John Saxon, Brad LaCroix and Julien Bou. Finally, I want to thank Ron Brown and Michael Braddock for their help in the machine shop and thank Genevieve Blake for her time and information.

TABLE OF CONTENTS

	<u>page</u>
ACKNOWLEDGMENTS	4
LIST OF TABLES	9
LIST OF FIGURES	10
NOMENCLATURE	16
ABSTRACT	19
CHAPTER	
1 INTRODUCTION WITH LITERATURE REVIEW	20
1.1 Flapping Wing Micro Air Vehicles Overview	20
1.1.1 Definitions	20
1.1.2 Applications	22
1.2 Brief MAV History	24
1.2.1 Competitions, Prototypes and Toys	26
1.2.2 Flapping Wing Aircrafts	27
1.3 Flapping Flight Research Review	29
1.3.1 Aerodynamics	32
1.3.2 Wing Kinematics	39
1.3.3 Wing Structure	45
1.4 Research Goals and Methodology	48
1.4.1 Flapping Wing Characterization	48
1.4.2 Wing Design and Experimental Optimization Method	49
1.4.3 Computational Model Validation	49
1.4.4 Summary	50
Research goals	50
Methodologies	50
Major contributions	50
2 DEVELOPMENT OF DIGITAL IMAGE CORRELATION TECHNIQUE	52
2.1 Introduction	52
2.2 Experimental Setup	55
2.1.1 Test Subject	56
2.1.2 Test Environment	57
2.1.3 Cameras and Lenses	58
2.1.4 Image Acquisition	59
Camera and trigger setup	59
Light source configuration	61
2.1.5 Data Post Processing	62

	Image sequence reconstruction	62
	Correlation and transformation of data	63
2.3	Results	65
2.4	Conclusions	68
3	PASSIVE WING DEFORMATION	69
3.1	Mass Distribution	74
3.1.1	Elastic Membrane Wings	74
	Tested wings	74
	Full-field deformation measurements	76
	Data parameterization	81
	Effect of flapping frequency	84
	Effect of wing structure	87
3.1.2	Inelastic Membrane Wings	90
	Tested wings	91
	Deformation measurements	93
3.2	Structure Compliance	99
3.2.1	Stiff Wing	100
	Design and fabrication	100
	Deformation and thrust comparison	102
	Discussion	106
3.2.2	Compliant Wing Correlation Study	107
3.3	Discussion	111
4	STRUCTURAL DYNAMICS AND AERODYNAMICS MEASUREMENTS	113
4.1	Introduction	113
4.2	Materials and Methods	119
4.2.1	Tested Wings	119
4.2.2	Flapping Mechanism	121
4.2.3	Static Elastic Characterization	124
4.2.4	Dynamic Response Measurement with Laser Doppler Vibrometry	126
4.2.5	Wing Performance Evaluation	127
4.2.6	Full-Field Wing Kinematics and Deformation Measurement with DIC ...	131
	Hardware configuration	132
	Data post processing	133
4.2.7	Airflow Measurement with SDPIV	137
4.2.8	Experimental Procedure	139
	Multidisciplinary study procedure	139
	Correlation of aerodynamics and wing structure	140
4.3	Results	142
4.3.1	Static Elastic and LDV Measurement Result	142
4.3.2	Thrust Measurement Result	147
4.3.3	Wing Deformation	151
4.3.4	Fluid/Structure Interaction	159
4.4	Discussion	166

5	EFFECT OF KINEMATICS	170
5.1	Introduction	170
5.2	Flapping Frequency and Stroke Amplitude	173
5.2.1	Effect of Flapping Frequency	174
5.2.2	Effect of Stroke Amplitude	177
5.3	Wing Rotation	181
5.3.1	Overview	182
5.3.2	Experimental Setup	185
	Rotation mechanism	186
	Rotation kinematics verification.....	189
	Tested wings.....	193
	Control system	194
	Force measurement system.....	197
5.3.3	Results	201
	Effect of active synchronized rotation	203
	Effect of multiple rotation in one flapping stroke.....	206
	Effect of structural vibration.....	207
5.3.4	Conclusions	209
5.4	Discussion	210
6	EFFECT OF STRUCTURE	212
6.1	Overview	212
6.2	Topology Correlation Study	214
6.2.1	Introduction.....	214
6.2.2	Wings of Different Topologies	218
6.2.2	Experiment Configuration and Post Analysis.....	220
	Data acquisition and post processing	221
	Data analysis	223
	Measurement uncertainties.....	225
6.2.3	Results	226
	Effectiveness and efficiency.....	226
	Deformation of different wing structure	228
	Effect of aeroelastic coupling	230
	Thrust and deformation correlation	232
6.2.4	Conclusions	237
6.3	Experimental Optimization Methodology.....	239
6.3.1	Introduction.....	240
6.3.2	Flapping Wing Design Space	243
6.3.3	Aerodynamic Performance	245
6.3.4	Conclusions	250
	Experimental optimization steps	251
	Itemized topology study summary.....	251
6.4	Discussion	252

7	NUMERICAL MODEL VALIDATION.....	256
7.1	Review	256
7.2	Tested Wings and Experiment Configuration.....	259
7.2.1	Isotropic Tested Wings	259
7.2.2	High-Speed DIC System	260
7.2.3	PIV Configuration	261
7.3	Computational Model.....	263
7.4	Validation Results	266
7.4	Discussion	272
8	CONCLUSIONS AND FUTURE WORK	277
8.1	Conclusions	277
8.2	Future Work	284
8.2.1	More Complicated Kinematics	284
8.2.2	New Composite Wings	285
8.2.3	Forward Flight	286
	LIST OF REFERENCES	287
	BIOGRAPHICAL SKETCH.....	303

LIST OF TABLES

<u>Table</u>	<u>page</u>
1-1 Key events/research on MAV/FWMAV development	24
1-2 Selected successful flapping wing aircrafts	27
3-1 Summary of point mass loading relationship	73
3-2 Correlation coefficients of loads and deformation variables.	109
4-1 Frequency peaks of the average frequency response spectrum, Hz.....	146
5-1 Experimental data at different frequencies and stroke amplitudes	179
5-2 Experiments conducted in this work	201
6-1 The morphological, structural and kinematics parameters comparison	213
6-2 The number of carbon fiber layers used in each portion of the wings, as well as the final reinforcement weight.....	220
6-3 Measurement uncertainties	225
7-1 Geometric and mechanical properties of the Zimmerman aluminum flapping wing configuration.....	265
7-2 Flow properties associated with the Zimmerman aluminum flapping wing configuration.....	265
7-3 Dimensionless parameters associated with the Zimmerman aluminum flapping wing configuration.	265

LIST OF FIGURES

<u>Figure</u>	<u>page</u>
1-1 Ornithopter Microbat and Matthew Keennon	26
1-2 Tree map of FWMAV research literature review.....	31
2-1 Overall experimental setup.....	55
2-2 Flapping mechanism FL2D0.....	56
2-3 Tested wing with latex membrane.	57
2-4 Detail of DIC setup.	59
2-5 Trigger timing scheme.....	61
2-6 Image feature recognition.....	63
2-7 Construction of a fictional rigid wing through rotational transformations.....	64
2-8 Structural deformations (w/c) through the flapping stroke, in air.....	65
2-9 Structural deformations (w/c) through the flapping stroke, in vacuum.	66
2-10 Colored deformation comparison in air and in vacuum.....	67
3-1 Passive wing deformation in nature.....	69
3-2 Simplified scheme for loading analysis on a point mass.....	72
3-3 Test wing structures: speckle patterns (left), and topologies (right).....	75
3-4 Structural deformation of Wing 1 at 3.75 Hz, 5 Hz and 7.5 Hz in air.....	77
3-5 Structural deformation of Wing 1 at 3.75 Hz, 5 Hz and 7.5 Hz in vacuum.	80
3-6 Parameterization example of structural deformation into w_{tip} and θ	81
3-7 Deformation phase plot examples showing different bending pattern.	82
3-8 Deformation phase plot examples showing different twisting pattern.	84
3-9 Chord-normalized wing-tip deflection of Wing 1 BP.....	85
3-10 Passive wing twist at $2y/b = 0.75$, Wing 1BP.....	86
3-11 Chord-normalized wing-tip deflection of various structure, $f = 5$ Hz.....	87

3-12	Angle of twist θ and maximum camber w_{\max} at $2y/b = 0.75$, $f = 5$ Hz.....	89
3-13	Structural deformation of different topologies, downstroke, 5 Hz, in air.....	90
3-14	Batten parallel reinforced wing with speckled Capran® membrane.....	91
3-15	Tip deflection phase plot in air (left) and vacuum (right).....	94
3-16	Twist angle at $2y/b = 0.32$, in air (left) and vacuum (right).....	96
3-17	Twist angle at $2y/b = 0.8$, in air (left) and vacuum (right).....	96
3-18	Deformation at 25 Hz in air, downstroke (left) and upstroke (right).....	97
3-19	Deformation at 25 Hz in vacuum, downstroke (left) and upstroke (right).....	98
3-20	Manual fans for recreational thrust production.....	99
3-21	Stiff wing design.	100
3-22	Wing mold for the stiff wing fabrication.	101
3-23	The stiff wing (right) and the control wing (left).....	101
3-24	Structural deformation of the control (left) and the stiff wing (right) in air.....	102
3-25	Deformation phase plot comparison for the stiff and control wing.	103
3-26	Time-averaged thrust by the stiff and control wing.	104
3-27	Time-averaged thrust increment.....	105
3-28	Average thrust and maximum tip deflection versus flapping frequency.....	107
3-29	Average twisting and cambering versus flapping frequency.....	108
3-30	Regression of tip deflection and thrust using different functions.....	110
3-31	Regression of twist and thrust (left), and camber and thrust (right).	110
4-1	Flow chart of experiments.	119
4-2	Six flexible membrane wings of different reinforcement	121
4-3	FL2D3 wing flapping test bed, capable of 45 Hz, $\pm 60^\circ$	122
4-4	FL2D3 schematic drawings and kinematics analysis.....	123
4-5	Static test experimental setup CAD model by Brad Lacroix.	125

4-6	The LDV experimental setup and measurement by Robert Love.	126
4-7	The force and torque sensor installed under FL2D3.....	127
4-8	DIC system configured for large bending and twist deformation.	133
4-9	Deformation data post processing, code by Bret Stanford.	136
4-10	SDPIV experimental setup and laser location, by Erik Sällström.....	138
4-11	Experimental procedure of deformation and thrust measurements.	140
4-12	Wing stiffness (g/mm) compared at a) the leading edge, b) the mid-line and c) the trailing edge.	143
4-13	Asymmetry of wing flexibility measured at the trailing edge.	144
4-14	LDV measurement results.	145
4-15	Mode shapes at the first three available FRF peaks.....	147
4-16	Time averaged thrust as a function of flapping frequency.	150
4-17	Extreme thrust values (maximum and minimum in one cycle).....	150
4-18	Deformation contour plots of wing L3B1 are shown at 25 Hz.....	152
4-19	Deformation contour plots of wings L1B1 and L2B1 at 25 Hz in air.....	154
4-20	Deformation phase plots of L3B1, L2B1 and L1B1 at 25 Hz in air.....	156
4-21	Deformation comparison of L2B1 in vacuum and in air at 25 Hz.....	158
4-22	Flexible wing tip locations compared with a theoretical rigid case.	159
4-23	Flow structures developed around the deformed L1B1, L2B1 and L3B1 surfaces, as the wing passes through the mid-plane during the downstroke at 25 Hz.	164
4-24	Flow structures developed around the deformed L1B1, L2B1 and L3B1 at stroke reversal (beginning of the downstroke) at 25 Hz.....	165
5-1	Flexible membrane wings BP and LEO studied in 5.2.....	173
5-2	BP structural deformation at different frequencies: contour plots through the downstroke (upper plot), cyclic tip displacement (lower left), and cyclic wing twist (lower right).	175

5-3	LEO structural deformation at different frequencies: contour plots through the downstroke (upper plot), cyclic tip displacement (lower left), and cyclic wing twist (lower right).	177
5-4	Thrust and its coefficient at different flapping amplitudes and frequencies.....	178
5-5	Deformation contour and phase plot of BP under the effect of frequency and stroke amplitude. Note that case 40°@35 Hz has the same thrust coefficient as case 90°@15Hz.	180
5-6	General scheme of insect hovering, coordinate system and stroke plane shown on the left, and the three different stroke timings shown on the right, adopted from Shyy et al. ³	184
5-7	Rotation mechanism and the flexible membrane wing.	187
5-8	Actuation illustration for magnetic coil actuators.	188
5-9	Overall experimental configuration.	189
5-10	Full-field contour plot of downstroke and upstroke wing kinematics.	190
5-11	Wing kinematics of two cross sections.	191
5-12	Rotation angle and flapping angle relationship.	192
5-13	Tested wing skeleton layout.	194
5-14	MCA control signal and flapping motion phase difference in the three different hovering modes.	196
5-15	Force measurement system configuration layout.	199
5-16	Overall performance comparison in 11 experiment cases.	203
5-17	Time averaged thrust of 2-DOF kinematics, varying with motion phase difference at 10 Hz flapping frequency, flapping stroke angle $\pm 35^\circ$, rotation angle $\pm 45^\circ$	204
5-18	Time averaged thrust of 2-DOF kinematics, varying with motion phase difference at 15 Hz flapping frequency, flapping stroke angle $\pm 35^\circ$, rotation angle $\pm 45^\circ$	206
5-19	Effect of multiple rotation in one flapping stroke.	207
5-20	Thrust fluctuation range in different cases.	208
5-21	Thrust fluctuation range in different cases.	208

6-1	Reinforcement layout of the four tested wings.....	219
6-2	Loads measurement post processing and system noise (LEO at 37.5 Hz in air).	222
6-3	Structural deformation data analysis, defining enclosed area and phase.....	224
6-4	Average thrust (g) of the four differently reinforced membrane wings.	226
6-5	Net (left) and total (right) efficiency (g/W) of the four wings.....	227
6-6	Structural deformation for all four wings at 20 Hz: contour plots through the downstroke (upper plot), cyclic tip displacement (lower left), and cyclic wing twist (lower right).	229
6-7	BP at different frequencies in vacuum: contour plots through the downstroke (upper plot), cyclic tip displacement (lower left), and cyclic wing twist (lower right).	231
6-8	Correlation between average thrust and wing tip deformation.....	233
6-9	Correlation between average thrust and passive wing twist.	234
6-10	Correlation between efficiency and tip deflection.....	236
6-11	Planform and layup structure of tested wings.....	244
6-12	Performance and behavior summary for wing A0000.....	246
6-13	Thrust performance comparison of the 37 wing types normalized to A0000, at amplitude of 70°, and at five different frequencies.....	248
6-14	Overall thrust comparison in the range of 15 to 35 Hz, L2B2 as the overall optimal wing.....	250
6-15	Effect of bending stiffness and local optimum wings.	254
7-1	Isotropic wing with DIC speckles and Rhodamine coating.	260
7-2	Images of computational mesh for fluid dynamics.....	263
7-3	Structural mesh.	264
7-4	CFD grid sensitivity results for the Zimmerman aluminum flapping wing (lift coefficient)	265
7-5	Comparison of velocity magnitude and vorticity for a slice of the wing at the quarter chord going through the span for time instant $t/T = 0.3$	266

7-6	Comparison of velocity magnitude and vorticity for a slice of the wing at the quarter chord going through the span for time instant $t/T = 0.48$	267
7-7	Comparison of velocity magnitude between computation and experiment	269
7-8	Lift coefficient on the wing as a function of normalized time (time is normalized with respect to a period of flap rotation), DS- downstroke, US – upstroke.....	271
7-9	Iso-contours of vorticity magnitude on the aluminum wing and Z-vorticity contours.....	272
7-10	Aluminum wing response due to flapping excitation (normalized with respect to chord length at the root).	273
7-11	Mode shape comparison between experimental results and finite element model by Gogulapati et al. ^[192]	275
7-12	Time averaged thrust comparison by Gogulapati et al. ^[192]	276
8-1	Circle of Scientific Discovery.	278

NOMENCLATURE

<i>a</i>	acceleration in general in equations, m/s^2 ; in design drawing of FL2D3, <i>a</i> is the horizontal distance from the rocker base pin center to the reciprocator center, mm.
<i>b</i>	wing length or the semi-span at quarter chord, mm
<i>c</i>	wing root chord length, mm
<i>d</i>	distance in general. In design drawing, <i>d</i> is the length of rocking rod, mm; in magnetic force analysis, <i>d</i> is the distance from the end of the magnet to the rotation center, m.
<i>f</i>	frequency in general, Hz. In most cases <i>f</i> refers to the flapping frequency in this work.
<i>g</i>	SI unit, gram.
<i>h</i>	height in general.
<i>i</i>	vertical displacement of the reciprocator, mm.
<i>k</i>	reduced frequency, or wing camber, mm.
<i>l</i>	length in general. In design drawing, <i>l</i> is the length of the push rod in the crank-slider mechanism, 50 mm; in inertial force analysis, <i>l</i> is the distance between the point mass and the rotation center.
<i>m</i>	mass in general, kg.
<i>m, n</i>	integer in general.
<i>n</i>	number in general.
<i>r</i>	radius in general. In design drawing, <i>r</i> is the radius of the off-center pin in the crank module; in magnetic force analysis, <i>r</i> is the coil radius.
<i>s</i>	number of samples per cycle.
<i>t</i>	time in general, s. Occasionally <i>t</i> is also used for thickness.
<i>u, v, w</i>	respectively corresponding to the chord, span and transverse displacements in the local coordinate system of the flapping wing, mm.

v	velocity in general, m/s. In thrust coefficient calculation, v is the relative speed, which in hovering case is the average wing tip speed (0.636 of maximum speed).
W_{tip}	wing tip deflection, mm.
x, y, z	respectively corresponding to the chord, span and transverse directions in the local coordinate system of the flapping wing, mm.
x	unknown in general. In design drawings, x is the slider location measured to the center position.
AR	Aspect ratio.
B	magnetic field magnitude, Tesla.
C	covariance.
C_T	coefficient of thrust.
D	drag in general.
E	Young's modulus, GPa.
$E[]$	expected value operator
F	force in general.
F_D	drag force, N.
F_i	inertial force in general, N.
F_T	time averaged thrust, N.
F_x, F_y	thrust and lift component of the aerodynamic forces generated by wing flapping, N.
I	current in general, A.
L	cross section length, m.
N	number of complete cycles between each trigger
R	resistance in general, Ohm.
Re	Reynolds number.
R^2	coefficient of determination (Pearson's coefficient of regression)

S	single flapping wing area, mm^2 .
St	Strouhal number.
T	average thrust produced by the wings, g.
U	voltage in general, V. In dimension analysis, U is also the far field velocity.
X, Y	random variables
α	angle in general, deg or rad. In design drawings, α represents the flapping wing position.
α_{twist}	angle of twist at specific span location away from the root, deg
θ	angle in general, deg. In design drawings, θ is the motor rotation angle.
μ	mean value.
ν	kinematic viscosity.
ρ	air density, kg/m^3 . In correlation analysis, ρ is also the correlation coefficient.
σ	standard deviation.
ϕ	phase difference between the rotation input and the flapping motion, rad
ΔT	time interval between each trigger, s.
Φ	stroke amplitude, deg or rad.

Abstract of Dissertation Presented to the Graduate School
of the University of Florida in Partial Fulfillment of the
Requirements for the Degree of Doctor of Philosophy

EXPERIMENTAL CHARACTERIZATION, DESIGN, ANALYSIS, AND OPTIMIZATION
OF FLEXIBLE FLAPPING WINGS FOR MICRO AIR VEHICLES

By

Pin Wu

August 2010

Chair: Peter G. Ifju
Major: Mechanical Engineering

This work has advanced the understanding of flapping flight of flexible wings designed to be used in micro air vehicles. A complete new experimental setup that includes a wing actuation mechanism, a customized digital image correlation system, a control system, a load sensor and a vacuum chamber is realized for this study. The technique of digital image correlation has also been developed so that complicated wing kinematics and deformation can be measured. The flapping wing effectiveness and efficiency have been evaluated in different conditions. The results indicate that passive wing deformation can be utilized to enhance aerodynamic performance, under certain inertial loading mainly dictated by flapping frequency, amplitude, wing compliance and mass distribution. The wing deformation reflects the aeroelastic effect produced by the coupled aerodynamic loading as well as the inertial loading. Critical parameters extracted from the deformation data are used to characterize the structural properties of the wings and correlate with the aerodynamic performance. The correlation shows that for one-degree-of-freedom kinematics, wing deformation can be directly used to predict time averaged thrust. The intrinsic relationship between kinematics and inertial loading enables the design and optimization of wing structure based on the correlation results.

CHAPTER 1 INTRODUCTION WITH LITERATURE REVIEW

1.1 Flapping Wing Micro Air Vehicles Overview

In the time prior to any successful powered flight, flying by flapping wings had been the most intuitive form: being inspired by myriads of successful examples of natural flyers (birds, bats, and insects), people naturally associated flight with flapping wings. Early attempts for pilots to wear a “wing suit” to fly like a bird had been miserable failures because by then, the understanding for aerodynamics and powered flight was yet to be scientifically developed. Today, after over a century of glorious aeronautic history of engineering miracles, flight by flapping wing is brought back for discussion in the micro air vehicle realm; it has recently become one of the most focused topics in mechanical and aerospace research.

1.1.1 Definitions

Micro air vehicles (MAVs) are generally defined as an unmanned air/aerial vehicle (UAV) of maximum measurable dimension not exceeding 150 mm (or 6”), although many small UAVs (SUAVs) of wingspan less than 2000 mm (usually between 150mm ~ 914mm) are still often considered as MAVs. Recently, an updated definition of nano air vehicles (NAVs) is issued to emphasize a smaller size scale (under 75 mm or 3”) for indoor surveillance and reconnaissance missions.

In this particular size regime (wingspan ≤ 75 to 150 mm), facing the pronounced low Reynolds number condition ($10^3 \sim 10^5$), design under traditional aerodynamics guidelines will no longer be sufficient to produce an optimal aircraft: both fixed wing aircraft and rotary wing aircraft meet additional challenges after being scaled down. As for fixed wing MAVs, the smaller the vehicle, the less stable, the more skillful remote

control pilot required and the more challenging it is for autonomous flight. Therefore design and optimization work has been done by Abdulrahim^[1] and Stanford^[2] to increase the controllability and stability, respectively. As for rotary wing MAVs, the rotor efficiency drastically decreases as the size shrinks, because the rotational speed needs to increase to compensate for the smaller effective area, leading to a substantial increase of drag created at the tip of the rotor. Though maneuverability remains as an advantage, low power efficiency and significant noise signature limit the feasibility of an insect size reconnaissance/surveillance MAV.

For these reasons the research spot light is cast on the most natural and exciting form of flight: flapping. Flapping wing MAVs (FWMAVs) are defined as an aircraft capable of generating both lift and propulsion for sustained flight by a reciprocal wing motion. In other words, the FWMAV wings play two roles: to produce lift to overcome gravity and to counteract drag by generating thrust. Such aircraft has been successfully developed as ornithopters and entomopters by radio control (RC) hobbyists. Some aircraft that uses fixed wings for lift and flapping wings for thrust as designed by Jones et al.^[3] should be excluded from this category since it only employs the wing flapping as another type of propulsion.

Nature favors flapping wings because rotary motion cannot be performed with muscular and skeletal bio-systems¹, therefore contraction/extension mechanisms are applied. As observed in natural flyers, flight by flapping wings inherits certain advantages that are beneficial in many situations. Some advantages are briefly described as follows: 1) maneuverability – flapping flight allows an active system

¹ Except for the flagellar motor of bacteria. They can produce natural rotational motion, but they do not have musculoskeletal systems.

preventing/delaying stall, easy transition from forward flight to hover, short or vertical takeoff and landing and various flight speed with optimal efficiency; 2) power efficiency – flapping flight in MAV or NAV scale provides for potential/theoretical higher efficiency in both forward flight and hovering modes, as mentioned before, rotating propeller's mechanical efficiency drops as size decreases; 3) low noise signature – because of the nature of kinematics and wing structures, the noise produced by flexible flapping wings will be dissipated to a large range of frequencies, therefore it is much less noticeable comparing to rotary wing MAVs' high pitch sound at a certain frequency; 4) disguise – such bio-mimicry kinematics provides stealth. These features motivate scientific flapping wing research that will become the foundation for future practical applications.

1.1.2 Applications

One of the major applications for MAVs is remote sensing, visually, chemically, radioactively, biochemically, etc. MAVs are expected to be able to carry and/or deploy sensors in confined areas to gather information without risking human lives. They are supposed to accomplish the task efficiently and effectively because of the nature of their variable flight speeds and multi-unit coverage of large incommensurable spread, which is hard to reconnaissance with traditional UAVs. These locations could be building-concentrated urban areas or the space inside building structures. Presently, a two-foot wingspan military SUAV has been successfully deployed to take real-time videos on the battle field. It can be expected that it is only a matter of time for various MAVs to be developed for specialized missions.

The different features of fixed wing, rotary wing and flapping wing MAVs allow the best match between flight modes and flight conditions. Fixed wing MAVs generally have higher payload capacity and fly at higher speeds. Therefore they are suitable for

outdoor operation with higher tolerance against wind gust. Rotary wing MAVs do not require any forward speed. This allows them be operated in extremely confined space and carry out missions such as watching into a building through its windows. Ideally, flapping wing MAVs can combine the features of these two; even though the vehicle is expected to be much more complicated in both structure and control.

Man-made FWMAVs have several irreplaceable advantages. Imagine that if research in biomedical engineering or other disciplines could develop a device that directly controls birds or insects, then by just installing additional sensors the best bio-MAVs or bio-NAVs were generated. A related research has been initiated by Chung and Erickson^[4] who implanted controllers into beetles and uses low frequency pulse signals to control their flight. However, the control methods are in a very beginning stage and no superior performance is realized compared to artificial ornithopters. Moreover, biological creatures are limited by the materials that they can assimilate and the body parts that they can grow. These limitation constrains the duration and environment for operation. Modern industry has produced many materials that are lighter and stronger than anything that biological organisms can grow. Although current technologies in power density, mechanical efficiency, sensing, control and miniaturization are very deficient in creating a FWMAV that outperforms its natural counterpart, the possibility that it can be done in the near future is conceivable. Other applications such as emergency medicine delivery, indoor advertisement, and home entertainment are as well intriguing for FWMAVs development. One can anticipate once the technology is mature and reliable, people can depend on these robotic birds and insects to help them to solve many problems.

In all, FWMAVs have found a niche in the near future. At this time when fixed wing aircraft has been extremely well developed, studying and utilizing flapping wing flight is next.

1.2 Brief MAV History

MAV research was started in the mid 90s of the 20th century, although some would argue the birth of unmanned aerial vehicles (model airplanes) in the 19th century marks the beginning of micro air vehicles ^[5]. Several key events are listed in Table 1-1. The development in small parts provided in the RC hobby industry has opened up many opportunities for companies and universities to join the research. In the mean time research institutes also have started looking into low Reynolds number aerodynamics. Both theoretical and practical sides of this subject have attracted researchers' attention. Enthusiastic hobbyists who are from various disciplines have been the main input to practical MAV development. All fixed, rotary and flapping wing indoor flyers have debuted in the RC toy market. A pattern for MAV development is then emerged: prototypes developed in laboratories driven by scientific research and military applications; and commercialized products (toys) developed by RC companies driven by innovation and profits.

Table 1-1. Key events/research on MAV/FWMAV development

Time	Events
1993	1 st MAV feasible study by RAND Corporation
1995	DARPA workshop on MAV, research initiated
1996	DARPA funded the first MAV Small Business Innovation Research (SBIR)
1997	1 st Micro Air Vehicle Competition at University of Florida, the surveillance event winner had a wingspan of 610 mm
1998	AeroVironment was awarded Phase II SBIR contract, led to Black Widow development
	2 nd Micro Air Vehicle Competition at University of Florida, the winning MAV wingspan was reduced to 394 mm
	Microbat prototype flew for 9 seconds ^[6]
	Ionic polymer-metal composites IPMCs have been reviewed as biomimetic

- sensors actuators artificial muscles for FWMAVs^[7]
- 1999 3rd Micro Air Vehicle Competition at University of Florida, the winning surveillance MAV wingspan 305 mm (with flexible wings)
 - 2000 4th International Micro Air Vehicle Competition at Arizona State University, the winning surveillance MAV wingspan 254 mm (with flexible wings)
 - 2001 5th International Micro Air Vehicle Competition at University of Florida, the winning surveillance MAV wingspan 191 mm (with flexible wings)
 - 2002 6th International Micro Air Vehicle Competition at Brigham Young University, the winning surveillance MAV wingspan 140 mm (with flexible wings)
 - 2003 7th International Micro Air Vehicle Competition at University of Florida, the winning surveillance MAV wingspan 178 mm (with flexible wings)
 - 2004 8th International Micro Air Vehicle Competition at University of Arizona, the winning surveillance MAV wingspan 127 mm (with flexible wings)
 - 2005 9th International Micro Air Vehicle Competition at KonKuk University in Korea, the winning surveillance MAV wingspan 120 mm (with flexible wings)
 - 1st US-Euro Micro Air Vehicle Competition in Germany, emphasis on reliability and autopilot
 - 2006 10th International Micro Air Vehicle Competition at Brigham Young University, the surveillance winner wingspan 114 mm and the ornithopter winner wingspan 178 mm
 - 2nd US-Euro Micro Air Vehicle Competition in USA (FL)
 - 2007 3rd US-Euro Micro Air Vehicle Competition in France
 - 2008 1st Asia Micro Air Vehicle Competition in India
 - Harvard University published about the world's smallest mechanism that lifted itself by flapping wings^[8]
 - The smallest FWMAV of 60 mm wingspan was created and flown by [Yusuke Takahashi](#)
 - 2009 [Research group](#) at Cornell University installed electronics to beetles during their morphing stage and used pulses of different frequencies to control their flight, intending to transform insects directly in to MAVs.
 - 2010 Computational models coupling structural and fluid dynamics have made significant progress and the results were presented in AIAA conferences, however, experimental approach is still the most confident method to study flapping wings.
-

The first official FWMAV project was funded by DARPA. The project took five years and 1.5 million dollars to successfully create an ornithopter called Microbat^[6] that could have a flight duration of 15 minutes or more. Figure 1-1 shows the Microbat with one of its designers Matthew Keennon. Besides such mission oriented projects, the

development of MAVs was soon boosted by a series of competitions that has been pushing the form, size, and performance to the limit.



Figure 1-1. Ornithopter Microbat and Matthew Keennon

1.2.1 Competitions, Prototypes and Toys

In the last 15 years, the main history of MAV development was seen in competitions, as shown in Table 1-1. The first Micro Air Vehicle Competition was hosted at University of Florida in 1997. At that time the sizes of entries were on the order of 600 mm to 800 mm wingspan. Soon the competition became international, attracting teams from Asia and Europe. In 2006, the smallest mission-capable surveillance MAV had reached a maximum dimension less than 120 mm. It was able to obtain an image of a target 600 m away from launch point. In recent years the competition gave more emphasis on different forms of flight, flight performance and autopilot capabilities. The US-Euro competition started in 2005 has been focusing on MAV's mission performance and reliability instead of sizes. Indoor competitions were also held recently to allow flapping wing and rotary wing MAVs to compete. In all, the entries found in these competitions have represented the MAVs reaching extremity, either by size, control, form, or performance.

Competition MAVs are prototypes developed according to mission requirement. They are usually hard to control, complicated and expensive. Only some very successful models are commercialized to become toys. The Wowwee Dragonfly[®] (2007) and ifly Vamp[®] (2008) are two exceptionally successful flapping wing RC products. These two toys are worth mentioning because they represent the mature MAV design in forward flapping flight: small, maneuverable, long endurance, easy to control, resilient, affordable, able to take off from ground, well designed flapping mechanism, membranous wings, innovative control method, etc. As unsteady aerodynamics and flapping wing aeroelasticity are not yet fully understood, these are the manifestation on how trial-and-error experimentation leads computational simulation.

1.2.2 Flapping Wing Aircrafts

There have been many successful flapping wing aircraft designs that enable well controlled forward flight. Some of these designs can achieve very slow speeds that are comparable to hovering. Others that are beyond MAV-scale usually focus only on forward flight. They are called ornithopters because they mimic birds' flight, to which quasi-steady aerodynamics can apply. Entomopters, on the other hand, describe MAVs that mimic insects in size, form and aerodynamics. From large manned prototype to true MAV-scale sub-gram fliers, these are the pioneers that show the promising future of FWMAVs. Table 1-2 lists some of the most well-known models to date; both prototypes and commercialized models are included.

Table 1-2. Selected successful flapping wing aircrafts

Year	Photos	Model	Comments
2000		Microbat by Caltech and Aerovironment	Microbat has a wingspan of 229 mm, weighing about 11 grams. It has three-channel radio control (throttle, rudder and elevator). The later version has over 15 minute's duration.

Table 1-2. Continued

2000		EV8 Ornithopter Model by Horst Rabiger	This 2800 mm wingspan, 3.6 kg and 11.7 aspect ratio ornithopter model is the latest large scale robotic bird in its EV series. Utilizing Cardan gear mechanism to produce flapping motion and combining gliding with flapping, this model successfully mimics large birds' flight.
2002		Mentor by University of Toronto	Mentor claims to be the first hovering ornithopter with radio control. Simple radio batten structure with membranous X wings configuration is used. It is not designed for efficient forward flight.
2002		Cybird	One of the first popular flapping wing toys in the RC market, Cybird has very robust flapping mechanism that actuates wings of 978 mm wingspan. This toy has successfully educated general public about the feasibility and elegance of forward flapping flight.
2006		DeIFly II by Delft University of Technology	A successor of DeIFly I, DeIFly II is a 280 mm wingspan, 16 gram ornithopter that is able to transition between hovering and forward flight. It utilizes X wing (biplane) flapping and rudder and elevator for control. It carries a video camera as payload.
2006		Kolibri IMAVC Entry by University of Arizona	The ornithopter event winner of the 10 th International MAV Competition, this ornithopter has a wingspan of 127 mm and weighs 8.6 g. It flies for about 3 minutes. This ornithopter is designed and made by Bill Silin.
2007		Microrobotic Insect by Harvard University	A truly insect scale flapping mechanism and wings are realized. It has a 30 mm wingspan and the total body weight is 60 mg. Power supply, controls and other components are not equipped to the prototype.
2007		Dragonfly by Wowwee	Wowwee Dragonfly claims to be the first robotic insect mimicry toys available in the market (end of 2006). The mature X wing flapping configuration allows beginner-friendly radio control of this slow flapping wing flyer. Its enormous success leads to the company's further introduction of various toys from fairies to dragons.
2007		1 g Ornithopter by proxdynamics	Being awarded the world's smallest RC ornithopter in US-Euro MAV Competition in Toulouse, France, this 100 mm wingspan, 1.1 g flyer uses 8 mAh li-po battery that allows it to fly for less than 1 minute.

Table 1-2. Continued

2008		Vamp by ifly	<p>Vamp is another successful toy that has great impact to the public. Comparing to Wowwee Dragonfly, it is much smaller, more maneuverable and more efficient. Its wingspan is about 12 inches, weighing 12 grams and produces near 12 grams of thrust at full throttle. Its turning control is realized by introducing asymmetrical tension in the wing membrane. Clear tape battens are installed in the membrane wing to maintain airfoil shape and provide reinforcement.</p>
2008		60 mm Ornithopter by Takahashi	<p>This is the smallest FWMAV to date: wingspan 60 mm, total length 70 mm, vehicle weight 1.54 gram, and X-wing configuration. The membrane wings are reinforced with radial carbon fiber battens. Control by two channel infrared radio system (rudder and throttle). It is built by Takahashi in his dedicated ornithopter studio in Japan.</p>

1.3 Flapping Flight Research Review

Previous to MAV research, biologists have devoted tremendous effort to understand how animals fly by flapping wings. Insects, birds and bats represent three distinct groups of natural fliers. Insects are the most abundant in nature: there are more than one million different species estimated and over 9000 new species are discovered each year. Many of the insect species are capable of hovering flight: there are approximately 110,000 bee, wasp ant and sawfly (*Aprocrita*), 170,000 butterfly and moth (*Lepidoptera*), 360,000 beetle (*Coleoptera*), 5,000 dragonfly (*Anisoptera*), 2,000 praying mantis (*Mantidae*) species and more. Their flight performance has been proven by natural selection: their capabilities to escape from predators, to search and hunt for food, and to successfully reproduce. Their flight with complicated kinematics and thin membrane structure wings that accentuate on passive wing deformation, especially with *single* pair of wings (dipteral) and within extremely wide range of low Reynolds numbers

($10^1 \sim 10^4$), has fascinated scientists for a long time and a complete answer has not yet been found.

Birds, on the other hand, represent the evolved reptile descendents from dinosaurs. From albatross to hummingbirds, they also cover a large range of Reynolds numbers ($10^3 \sim 10^7$). Modern aerodynamics is capable of explaining birds' forward flight at high Reynolds numbers (over 10^6). For some low Reynolds number cases ($10^3 \sim 10^5$), quasi-steady aerodynamics is also sufficient. Hummingbirds are the only bird species capable of true hovering (by Ellington's definition ^[9]); its flight mechanics is the transition between birds' and insects' flight. The fact that most birds' muscular-skeletal system allows them to actively change their wing shape during flight has distinguished birds' flight from insects' (which mainly uses passive wing deformation). This has led to MAV research in wing morphing ^[1]. Bats are the only mammal species that can fly: their wing skeletal system and membrane properties serve particular interest to researchers. Bats' flight is complicated in all kinematics, aeroelasticity and aerodynamics.

Overall speaking, flapping flight in nature is accomplished by optimizing both wing structure and kinematics to create aerodynamic forces. Previous research has been heavily focused on flapping wing aerodynamics and kinematics, yet relatively little attention to wing structure; therefore flapping wing aeroelasticity is inadequately understood. Figure 1-2 shows the tree map of this literature review. In this figure, the asteroid symbol indicates a high percentage content of the literature surveyed/available from the specific topic or group of researchers. This dissertation is dedicated to the Artificial Wings branch under Wing Structure category, aiming at artificial wing design, manufacturing, structure characterization and validation of computation models.

designed to realize insect-like flapping motion. Aeroelasticity is a discipline involving both wing structural dynamics and aerodynamics. Although most of the references are for fixed flexible MAV wings, they serve good examples for wing optimization using computational models that integrate CFD and CSD codes; similar efforts for flapping wing study will be realized in near future. The detailed discussion on each individual discipline (aerodynamics, wing kinematics and wing structures) is presented in the following sections. Each section will first review work by topic and author as shown in Figure 1-2, and technical summary will be presented afterwards.

1.3.1 Aerodynamics

Understanding the aerodynamics of flapping flight in hover is the key to engineering robotic insects and hummingbirds. In 1984, Ellington^[9, 10, 11, 12, 13, 14] in his six-article-series of „*The Aerodynamics of Hovering Insect Flight*’ has elaborately explained and shown how quasi-steady aerodynamics has failed to fully explain insects’ hover flight. He has documented numerous morphological and kinematic data for various species in his paper II^[11] and III^[9] respectively, which supports his discussion about flapping flight mechanisms in paper IV^[12]. Unsteady aerodynamics theories including wake vorticity, the Wagner effect, virtual mass forces and gross circulation changes are discussed and mechanisms by wing rotation (pronation and supination) are presented. Paper V^[13] derives a generalized vortex theory that provides a method of estimating lift, power and velocity. A discussion encompassing all these topics is presented in Paper VI^[14], which analyzes the lift and power requirements for hovering flight. His systematic approach in trying to understand the nature of hovering insect flight has made this work remarkable in MAV scale flapping aerodynamics, not only has

he disproved previous attempts with quasi-steady method, but he has also reached some conclusions that help further research of unsteady aerodynamics.

At present, the flight of insects involving unsteady aerodynamics still cannot be fully explained; but there has been a tremendous effort to study the subject and several review articles have summarized. Wang^[15] in 2005 summarizes the aerodynamics of insect flight, trying to answer “What force does an insect wing generate?” She briefly and circumspectly reviews scaling methods, dragonfly wing motion observation, unsteady forces quantification, forward flight, and hovering. This work has compiled most basic aspects required to address unsteady aerodynamics in flapping flight. However, any solid conclusion is yet to be drawn. Similarly, Lehmann^[16] in 2004 has reviewed the lift enhancement mechanisms in insect flight. Ho et al.^[17] has also published a review paper on flapping wing flyers in 2003, summarizing findings in biological research and connecting that to MAV development requirements. In Ho’s paper, scaling and geometric similarity are presented (similar to Shyy’s^[18] paper in 1999). The section “Vortex dominated unsteady aerodynamics” has included many previous efforts in vortex theories in flapping flight. Aeroelastic coupling has been discussed as an individual section with various wing structure and experiments cited. Finally some control aspects of flapping flight are discussed. Ho’s paper is the latest one so far to have technically included, in detail, flapping wing aerodynamics, its application to MAVs and its potential control methods. Along a similar line, Sane^[19] has written another review article in 2003 focusing on insect aerodynamics. Dated back further to 2000, Templin^[20] has reviewed flapping flight and included larger scale animals. His work presents a wide spectrum data of flying animals, using statistical

techniques to indicate relationships between various parameters. All these works have been excellent in citing previous endeavor to understand animal flight; I should not try to review the review articles but to point out that these summaries are all stressing one point: too much unknown and more work required – as it always is in science.

Studying successful natural flyers is the first step in understanding unsteady aerodynamics. Ellington and his colleagues have accumulated a significant amount of data and analyses over various insects. Willmott et al. ^[21] in 1997 has analyzed the flow structure of the hawkmoth *Manduca Sexta*. The authors applied stereo photography with smoke seeding lit by four high power stroboscopes to capture the unsteady airflow over the tethered hawkmoth wings. From the images they were able to describe the vortices with diagrams and see into the behavior of the aerodynamics. In the same year, Van den Berg and Ellington ^[22] used a model hawkmoth, a flapping mechanism that performed the hovering kinematics of the wings, to study the vortex wake. Subsequently they analyzed the three dimensional leading edge vortices ^[23] and discussed the formation/growth of this circulation responsible for high lift production. Towards a different insect, dragonfly, Wakeling and Ellington ^[24] have studied the gliding flight and steady state aerodynamics using traditional analysis techniques, because dragonfly wings show exceptional steady-state aerodynamic properties in comparison to other insect wings. Later in 1999, Ellington ^[25] summarized his previous findings and describes the application towards FWMAVs. Sunada and Ellington ^[26, 27] subsequently published the approximate added-mass method for estimating induced power for flapping flight. This paper adds a new interpretation/explanation of the unsteady aerodynamics created by the flapping wings.

Wang and Dickinson represent the other two research groups that have published many papers about insect flight. While Wang's group focuses on simulation studies, Dickinson's group has done mainly experimental work. Wang^[28] has simulated insect hovering with a two dimensional model in 2000, and claimed that for the first time such a model can generate enough lift to support typical weight of an insect. By 2004, Wang^[29] analyzed the role of drag in inclined-plane hovering insects and revealed that drag force plays an important role in supporting weight and lift to drag ratio can no longer be used to estimate aerodynamic efficiency. In the same year, Wang, Birch and Dickinson^[30] collaborated and compared the two dimension computation model^[28] with experiments in several qualitatively different kinematic patterns. The computed drag compares well with all experiments while lift agrees in some particular kinematic cases.

Dickinson et al.^[31] have discussed the relationship between wing rotation and the resultant aerodynamics for insect flight in 1999. The authors' experimental approach and systematic analysis have rendered this article a remarkable work about insect flight. Birch and Dickinson^[32] have later in 2001 studied another aspect with a similar experimental setup: the spanwise flow and the attachment of the leading edge vortices. The authors have obtained reliable experimental results to reject the hypothesis that the leading edge vortex attachment observed in insect wings is analogous to the mechanism operating on delta-wing aircraft. This is an important finding in details about insect flight aerodynamics, leading to their next publication^[33] on the subject of wing-wake interactions, which are illustrated with particle image velocimetry data. Two effects of the wake of force production by the wing are identified: an early augmentation followed by a small attenuation. Focusing on the role of flapping frequency, Dickson and

Dickinson^[34] have studied the effect of advance ratio on revolving wing aerodynamics (2004). This study assumes the quasi-steady aerodynamics can be applied to hovering insect flight and intends to find if such assumption also applies to forward flight. Therefore the analyses are similar to steady aerodynamic work but on a robotic flapper. In the next year (2005), Fry et al.^[35] continue similar work on the study of fruit fly's hovering by filming the actual insect's flight and recreating the same kinematics with the flapper to estimate aerodynamic loads. Lehmann et al.^[36] use the same flapper and digital particle image velocimetry (DPIV) techniques to study force enhancement due to contra-lateral wing interactions during stroke reversal (the "clap and fling") for insect flight. The authors find it surprising that the effect of clap-and-fling is not restricted to the dorsal part of the stroke cycle but extends to the beginning of upstroke. Poelma et al.^[37] take the flow visualization work further to reconstruct the time-resolved full-velocity-field around the wings. Overall, Dickinson's research group has taken advantage of modern motor actuation, force measurement and flow visualization techniques to systematically investigate the low Reynolds number insect flight.

Other recent efforts on insect flight studies are in the similar way. Thomas et al.^[38], 2004, have studied the unsteady aerodynamic flow structure of dragonfly, revealing a diverse array of unsteady lift generating mechanisms. Bomphrey et al.^[39], 2005, used DPIV (comparing to Willmott and Ellington^[21], 1997) to observe the leading edge vortex of hawkmoth wings. The authors^[40] in 2006 expanded the study to include near wake measurements. Later in 2009, Bomphrey et al.^[41] captured the flight of bumblebees in wind tunnel and used smoke streams to reveal the airflow around the bee, revealing the complicated flow structure during flapping and suggesting that the bumblebee flight is

achieved with high thrust (brute force) with low aerodynamic efficiency. Sane ^[42] in the same year proposes a theoretical model for the induced airflow in insect flight and measured such for validation with Jacobson ^[43].

Besides investigation into insect flight aerodynamics, research is also done to understand birds' and bats' flight as well. Altshuler et al. ^[44], 2004, have experimentally studied hummingbird wings and wing models using traditional aerodynamic analysis. The authors focus on the forward flight cases in which coefficient of lift and drag of the wing are assessed. Warrick et al. ^[45], 2005, captured the flow structure of hummingbirds hovering with DPIV and measured the aerodynamic forces, finding that 75% of the weight is supported by downstroke flapping and 25% by upstroke. Bats' flight aerodynamics does not involve hovering; therefore the related literature is not reviewed here.

Animal flight study usually involves live animals and the experimental conditions are complicated. As aforementioned, Dickinson's research group has used robotic mechanisms to simplify the situation and obtain detail measurements. Many other researchers have also done experimental studies on unsteady aerodynamics. Mueller and Delaurier ^[46] have reviewed the general aerodynamics for MAVs in 2003, mentioning various prototypes and experimental methods. Rozhdestvensky and Ryzhov ^[47] have thoroughly summarized flapping motion for both hydrodynamic and aerodynamic propulsion, although their discussion cannot be directly used for understanding hovering unsteady aerodynamics. Heathcote et al. ^[48] on the other hand, studied flexible flapping/plunging airfoil propulsion at zero free-stream velocity in 2004. Maybury and Lehmann ^[49] put two flapping mechanisms in series and study the fluid

dynamics affected by the phase lag variation, emulating dragonfly's fore-hind wing interaction. Tarascio et al ^[50] realized flow visualization on a complex insect-hover-based flapping mechanism in 2005. But only qualitative results are presented. Later in 2006, Yu et al ^[51] investigated and confirmed dual leading edge vortices on flapping wings with DPIV, claiming the similarity with non-slender delta wings. The authors have covered a wide range of aspect ratios, angle of attack and low Reynolds numbers, making the results noteworthy.

Computational work also attracts researcher's attention and it plays an important role in helping understand flapping wing aerodynamics. In 1996, Vest and Katz ^[52] proposed an unsteady aerodynamic model that simulates the propulsion of a flapping wing, similar topic to Rozhdestvensky and Ryzhov's experimental work ^[47]. Smith et al. ^[53] used an unsteady panel method to model the aerodynamic forces on rigid flapping wings to accommodate large scale trailing vortices, more advantageous than quasi-steady models. Liu and Kawachi ^[54] later in 1998 created a model based on a time-accurate solution of the Navier-Stoke equations, unsteady, and viscous flow field structure around a flapping insect wing. The model is verified with experimental data, pointing out the importance of existence of a sophisticated lift-enhancement mechanism due to the spiral leading-edge vortex at insects' low Reynolds numbers. Liu ^[55], 2002, addressed a new paradigm of simulation-based biological fluid dynamics that can digitize and visualize swimming and flying by using computational mechanical modeling of the biological fluid dynamics through faithful reconstruction of morphology and realistic representation of kinematics of an individual object. Jones et al. ^[56] study the clapping wing propulsion in ground effect with both numerical modeling and

experimentation, expanding the simulation to wing-wing interaction (yet the paper is mainly an experimental study). Ramanurti and Sandberg ^[57] presented a three dimensional fruit fly wing simulation with a finite element flow solver, with results agreeing well to previous experiments. Wu and Sun ^[58], 2004, also studied the unsteady aerodynamic forces of a model fruit fly by solving the Navier-Stoke equations numerically. In the same year, Fritz and Long ^[59] used the unsteady vortex method to model the oscillating plunging, pitching, twisting, and flapping motion of a finite aspect ratio wing. In 2006, Ansari et al. ^[60] reviewed the main simulation approaches found in the literature, categorizing them into steady-state, quasi-steady, semi-empirical and fully unsteady methods. The unsteady aerodynamic model claims to be the most satisfactory to date and is discussed in detail in the paper. In summary, computational models created to simulate the unsteady aerodynamics of insect flight have been updated frequently, but an accurate model that can produce reliable results as in steady flight is yet to be found.

1.3.2 Wing Kinematics

Similar to “Aerodynamics” in Figure 1-2, studies on flapping wing kinematics also consists of three categories: kinematics of live animals, mechanisms and control theories. To some degree in flapping flight, kinematics is to aerodynamics as cause is to effect. The various wing kinematics observed in different insects and their different flight modes indicates that it is a key factor in generating aerodynamic forces. Both insects and hummingbirds wing motions have been carefully studied. Several aspects of kinematics are of major interest: wing motion (includes frequency, amplitude and flap/rotation), loading, power and efficiency.

Azuma et al. ^[61] have studied the flight mechanics of dragonfly systematically in 1985, showing a great example of documenting the kinematics of such complicated flyer. In 1997, Wakeling and Ellington ^[62, 63] reported more investigations about dragonflies: besides kinematics description, gliding velocities, accelerations and power requirements were measured. Using robust and modern techniques, Wang et al. ^[64] in 2003, measured the dragonfly in more details: wing kinematics in both forward flight and turning. Flight trajectories and body attitude are also measured for these two maneuvers. Although these dragonflies mentioned here are not of the exact same species, from a performance evaluation point of view, they are comparable. Similar studies have been done in other insects: locusts, bees, and moths, because these insects have flight features that attract particular interest. In 1992 Robertson and Reye ^[65] investigated desert locusts' wing kinematics that allows agile collision avoidance maneuverability. In the next year, Wortmann and Zarnack ^[66] also published on desert locust flight, associating wing kinematics with lift regulation. In 2003, Taylor and Thomas ^[67] approached the desert locust from a control point of view, seeking the dynamic stability in the flight. Both dragonflies and desert locusts interest researchers in their forward flight, while others are interested in the hovering flight of hawkmoths and bees.

In 1997, Willmott and Ellington ^[68] analyzed the flight mechanics of hawkmoth with high-speed videography that is used to capture the wing kinematics in both hovering and forward flight modes. The aerodynamic aspects are also investigated in the subsequent paper ^[69] to identify the causal effect of kinematic variation. Bumblebees' flight and hovering capability defies quasi-steady aerodynamic explanations, attracting attention from researchers. Dudley and Ellington ^[70] in 1990 investigated the kinematics

and part features of bumblebees in forward flight. The effort was limited by early technology but detailed kinematics data was still obtained. Recently in 2005, Sun and Xiong ^[71] by using current computational techniques, analyzed the flight kinematics and stability of bumblebees in hovering. On the experimental side, Altshuler et al. ^[72] used Dickinson's robotic flapper to study the kinematic parameters related to honeybee flight, because the honeybee uses a different kinematic strategy from other insects: low flapping amplitude and high frequency. The authors present the relation between kinematics and its aerodynamic consequences.

Hummingbirds are the next subject attracting researchers who are interested in their superior flight capability: dashing forward and perfect stationary hovering. Early studies focused on measuring key quantities of hummingbirds' flight: Gill's work ^[73] in 1985 plotted power requirements versus flight speeds (from hovering to fast forward flight). Wells ^[74] analyzed the muscle performance and kinematics of hovering hummingbirds. Chai et al. ^[75, 76] studied hummingbirds' performance from an energetics point of view under different conditions: body mass, sex, and payloads. Chai ^[77] also studied the wings' role in hummingbirds' flight performance by observing impaired/molting wings. Altshuler and Dudley ^[78] observed the altitude effect on hummingbirds' flight. Recently in 2007, Tobalske et al. ^[79] revealed the complete kinematics description of hummingbird flight. These papers represent a fraction of the research work done to understand hummingbird flight, showing how their kinematics has contributed to agile flight.

Other studies related to low Reynolds number avian flight also give insight to understand kinematics of flapping wings. Pennycuik ^[80, 81] observed the wingbeat frequency across various species and used statistical methods to predict the feasible

relationship between body kinematic parameters. His results are applicable in FWMAV development. Tobalske and Dial^[82] has published larger scale avian forward flight, trying to understand the correlation between morphological features and flight kinematics. Similarly, Rosen et al.^[83] studied the relationship between wingbeat kinematics and vortex wake. Although bats are kinematically different from birds, the work of Bullen and McKenzie^[84] also provides valuable insight into the relationship between flapping frequency and amplitude. Besides biological observations, theories are also developed to study flapping wing kinematics. Gustafson^[85] presented a mathematical model that includes thermal, structural and neural dynamical subsystems to explain hover flight. Such effort represents the integration of kinematics and aerodynamics.

To help design an FWMAV it is important to know both “what to mimic” and “how to mimic”. Studies on live animal kinematics have been reviewed so far. These observations offer partial explanation on flapping flight. Yet the accumulative optimization done by natural selection requires more work to be decoded. Therefore, artificial flapping mechanisms are designed to decompose such a complicated problem into more specific topics. As part of his publication series in 1985, Ellington^[86] estimated the power and efficiency of flight muscle of insects based on previous observations and literature records. He finds that the power output is inefficient to oscillate the wings unless there is elastic energy storage mechanism in the flight system. Such conclusion leads to the design of a flapping mechanism incorporated with tension springs to reduce sharp torque variation by Madangopal et al.^[87]. The application of springs to reduce power requirement is also seen in Issac and Agrawal^[88], who

conclude that springs are not useful at low flapping frequencies and only marginal improvement was observed at high frequencies, but the idea should not be abandoned prematurely. Another compliant design is suggested by Khatait et al. ^[89], who noticed the reduction in torque requirement. Madangopal et al. ^[90] also investigated the spring application from an insect mimicry energetics standpoint, finding that the design with springs can enhance some aspects of the mechanism performance.

As shown in Figure 1-2, three distinct research groups have done significant work in mechanism design. Agrawal's research group published many articles on various topics about mechanism design: encompassing force measurement ^[91], simulation ^[92], design optimization ^[93] and insect kinematics ^[94]. These designs and studies examined the possibility of insect-like wing kinematics and the related force generation for FWMAVs. Zbikowski's research group on the other hand, focuses more on the mechanical/kinematic side of the problem. In 2004, Zbikowski et al. ^[95] designed and analyzed a complicated mechanism that performs insect wing kinematics from aeromechanical considerations. Later in 2005, Zbikowski et al. ^[96] present a further study of such mechanisms. Galinski and Zbikowski ^[97, 98] subsequently present their mechanisms based on double spherical scotch yoke and a four-bar linkage. These mechanisms are complicated and face many practical challenges, but they do perform realistic insect kinematics and serve as a good test bed for lab studies. Fearing's research group realized micro robotic insects with high feasibility by investigating in these aspects: force generation ^[99, 100, 101], sensing and control ^[102, 103, 104], mechanism design ^[105, 106], and wing actuation ^[107, 108]. This group's work covers various disciplines and applies the latest sensing/control and manufacturing technology to realize an insect

size MAV prototype. These three groups are interested in the mechanism design part of flapping wing studies, although the scale and kinematic aspects are very different.

Besides these major groups, other researchers have also shown great interest in flapping mechanism designs. Valentine ^[109] proposed various design schemes for building flapping mechanisms that have variable amplitudes so as to induce kinematic asymmetry for ornithopter control. Khan ^[110] paid attention to the transverse bending of insect wings and designs such mechanism. Singh et al. ^[111] performed systematic experimental studies on insect hover kinematic flapping wings and Singh analyzed the dynamics and aeroelasticity in his dissertation ^[112]. Beyond mechanisms design, Deng et al. ^[113] took another approach that models the system as a whole. Unlike such “overall” perspective, detail studies on new materials, actuators and fabrication techniques are to be applied to the design problem. For example, Cox et al. ^[114] used piezoelectric actuators and carefully examine the feasibility for FWMAV applications.

One last branch in flapping wing kinematic study is the control theories, of which the literature is much less abundant for FWMAV comparing to the other two. Nevertheless, Taylor and Thomas ^[115] studied the longitudinal stability for animal flight, trying to understand the control method of natural flyers. Lehmann ^[116] compared the kinematics of real flies with the robotic counterpart to study kinematics control. Raney and Slominski ^[117] reviewed some mechanization and control concepts that summarize previous efforts in FWMAV development. Dickinson ^[118] used his experimental setup to study the maneuver initiation and control of fruit flies. These observation studies follow a similar pattern: to learn from natural flyers first, to understand and model the physics next and to engineer last.

1.3.3 Wing Structure

From insects' scaled or veined membranous wings to birds' feathered musculoskeletal wings, flapping wing structure is as complicated as, if not more complicated than, the kinematics that enables the natural flyers to maneuver for a living. This is because nature has to find the right material (food) to assimilate and grow the wing structure that is of the optimal strength and mass. If the wings are too weak, they cannot sustain aerodynamic loading for escaping from predators. If the wings are too strong, they may be too heavy and overbuilt, not ideal for maneuver and growth. From the literature one may notice that little is understood about the animal wing structure, because the structural properties change when the animal dies, but are very difficult to characterize when the animal is alive. Some artificial flapping wings have been designed and successfully taken flight in ornithopters. However, more systematic study is needed to develop effective and efficient structures for FWMAVs.

Flapping wing flight for micro air vehicles is an intricate multidisciplinary subject requiring understanding of aerodynamics, wing structure, kinematics, electronics, controls and examples from nature for design and development. Aeroelastic behavior of the wing is coupled of wing kinematics, structural dynamics and aerodynamics. In other words, the kinematics of the wing affects the inertial loading to the structure, causing deformation that is also affected by aerodynamic loading; while both the kinematics and wing deformation acts upon air to generate lift and thrust. As seen in nature, wing structural properties (flexibility and mass distribution) are crucial to flapping flight (aerodynamics).

In animal wing studies, as noted by Combes and Daniel ^[119], 2003, the insect venation patterns, and the roles of these patterns varies greatly among species:

dragonflies have a pleated leading edge for spanwise stiffening, flies have curved veins for chordwise bending, locust wings display a fan-like distribution of veins that promote bending/extension coupling, etc. The authors ^[120] later studied hawkmoth (*Manduca Sexta*) wings by comparing a fresh compliant wing with a dry one (the lost mass is made up from additional spray paint) and found that the more flexible one generates much more directed flow than the other (measured with particle image velocimetry). Of the same species, Combes and Daniel ^[121] have conducted similar experiments in helium to seek the deformation contributed by inertial loads in comparison to aerodynamic loads and found that the deformation is mainly caused by wing inertia. This result may be species specific and it means that the wing deformation may either be just a by-product of kinematics (acceleration) or another factor assisting kinematics in regulating airflow. Contradictory cases, however, are found by Sun and Tang ^[122], who conclude that passive wing deformation in insect fly is strongly coupled between both aerodynamic and inertial forces. The same results of artificial wings are reported by Wu et al. ^[123] in a series of studies that use passive wing deformation to produce aerodynamic forces.

Ennos ^[124], 1988, noticed the importance of the torsional compliance in insect wings and proposes a model to describe such property. In 1998, torsional deformation of dragonflies is observed by Suunada et al. ^[125] and detailed wing structure is studied. For deformation measurement, Zeng et al. ^[126], 2000, used a scanning projected line method to measure bumblebee's beating wings. Sudo et al. ^[127], 2002, experimentally examined various insect wings with modern techniques, proving the capability to quantify the wing shape, structural response and kinematics. More recently in 2006,

Tsuyuki et al. ^[128] investigated the relationship of insect morphology and aerodynamic performance. Other than insect wings, Hummingbirds' wing morphology is also studied and compared to flight kinematics by Stiles et al. ^[129] in 2005. Van den Berg and Rayner ^[130] have compiled the moment of inertia of flapping wings of birds and bats and found a strong correlation between the moment of inertia and the product of wing mass and length squared. The complexity of animal wings may seem too difficult to mimic, but these studies provide foundation for understanding what key characteristics should exist in an artificial wing. Pornsin-Siriak et al ^[131] discussed using titanium alloy MEMS technology to fabricate FWMAV wings, comparing spring constants of the artificial wings with real butterfly wings.

Lin et al. ^[132], 2006, measured the aerodynamic forces of artificial membrane flapping wings. The authors compared two different batten structures and measure the lift and thrust produced. Lee et al. ^[133], 2006, used computational models to design a flapping airfoil at low Reynolds numbers. Liani et al. ^[134], 2007, develop a numerical model to predict aerodynamic forces on a flapping airfoil, representing some of the research efforts in simulating flapping wing aeroelastic responses. Tsuzuki ^[135], 2007, also studied various insect wings' cross sections and found a design guide for rotary MAV wing airfoils. Wu et al. ^[136], 2008, compared three different batten-reinforced membrane wings and developed a full field technique ^[137] to measure the wing kinematics and deformation. Later in 2009, the authors ^[138] used a single-degree-of-freedom flapping mechanism to actuate flexible membrane wings to achieve a measurable time average thrust force comparable to a hovering hummingbird's. Then the authors ^[139] examined the performance of wings of various flexibilities and mass

distribution and later correlated the quantitatively measured structural deformation with time averaged thrust^[140], finding that intrinsic relationship exists. The recent effort by Wu and Ifju^[141] has been focused on exploring the design space of the reinforcement topology, as well as more complicated actuation kinematics^[142].

1.4 Research Goals and Methodology

In order to design an FWMAV, one has to understand the physics behind unsteady aerodynamics, be able to realize the flapping kinematics within power/weight requirements and have a sensing and control system. All these are still challenges to the current knowledge database. Wing structure is a particular area linking wing kinematics to aerodynamic performance. From the last section one can see it is a comparatively unexplored territory until recently. This dissertation intends to apply current measurement techniques to characterize MAV size flexible flapping wings, to establish a design guide for such wings by rigorous analyses, and to develop a methodology to optimize the wings for hovering flight.

1.4.1 Flapping Wing Characterization

Flexible flapping wings actuated under various kinematic parameters (frequency, amplitude, motion pattern) have not yet been thoroughly characterized. The complicated aeroelastic coupling (wings' elastic deformation causing and being caused by aerodynamic effects) makes the transfer function between kinematics and aerodynamics hard to identify. Therefore the first goal of research is to establish a property characterization routine to examine the flapping wings. A sophisticated experimental setup has been arranged to actuate wings in various flapping motion, to measure aerodynamic loads that evaluate the wing performance, and the wing deformation that describes the aeroelastic effect.

Several flapping mechanisms have been designed and built. Aerodynamic loads are measured with an industrial force and torque sensor. Wing deformation is obtained with a customized full-field out-of-plane digital image correlation system. A vacuum chamber is also built to isolate aerodynamic effect in the deformation, therefore the wing structure can be characterized. Although this only simplifies part of the coupling problem; because linearity cannot be assumed for superpositioning the inertial and aerodynamic effects. By using time averaged thrust to evaluate the wing performance and using structural deformation to characterize aeroelasticity, this procedure becomes a routine for examining a series of wings of different reinforcement.

1.4.2 Wing Design and Experimental Optimization Method

Once the characterization routine has been established, experimental optimization process can be used to seek the optimal design for flapping wings corresponding to specific kinematics. A design space is created to find a local optimum for a certain topology. The roles of bending stiffness and torsion stiffness in relation to lift and thrust generation is identified. Wings with complicated reinforcement structure are also compared for topological advantages. Power efficiency as well as aerodynamic forces are the main criteria for wing evaluation.

1.4.3 Computational Model Validation

This research is part of a Multidisciplinary Research Initiative (MURI) project studying the fundamental physics behind flapping flight for MAV applications. The project involves several teams from different disciplines. The research group at University of Michigan has been engaged in using a Computational Fluid Dynamics (CFD) and Computational Structural Dynamics (CSD) integration model to simulate hummingbird-like hovering flight. The experimental work carried out for this dissertation

will be used to validate the CFD/CSD numerical model, as well as other computational results. The experimental database also serves as valuable validation source for future computation works.

1.4.4 Summary

Research goals

1. Develop an experimental setup and evaluate its capability.
2. Establish a routine for characterizing flexible flapping wings.
3. Investigate the design guideline for flapping wing structure.
4. Experimentally optimize flapping wings within a design space.
5. Validate the CFD/CSD model for the MURI teammates.

Methodologies

1. Design and build flapping mechanisms to actuate wings with different kinematics.
2. Use digital image correlation techniques to measure wing kinematics and deformation.
3. Measure aerodynamic loads with a transducer.
4. Study inertial effect in vacuum chamber to characterize wing structure.
5. Fabricate wings in design space with composite lay-up and other manufacturing techniques.
6. Develop software with LabVIEW and MATLAB to simplify experimental process and automate post processing.

Major contributions

1. Identify the anisotropic properties of flexible flapping wings and their effect in lift and thrust production.

2. Generate a design guideline for MAV flapping wings.
3. Develop and explore the application of digital image correlation techniques in FWMAV research.
4. Develop an experimental setup for flapping wing characterization and experimental optimization.
5. Validate computation models.

CHAPTER 2 DEVELOPMENT OF DIGITAL IMAGE CORRELATION TECHNIQUE

2.1 Introduction

Biologically-inspired wing designs call for extremely flexible structures, where a combination of inertial and aerodynamic forces bend and twist the rapidly-actuated wing into a shape favorable to lift and thrust production. One of the challenges of small scale flapping wing research is to separate the rigid body kinematic motion and the concomitant structural deformation of the wings. Therefore further development of digital image correlation (DIC) technique is required to assess the following outstanding issues: capturing and digitizing the rapid motion of a test subject, recording large out of focal plane displacement, reconstructing the flapping motion, and accurately describing wing deformation.

Two configurations can be used to capture the motion of the flapping: high-speed cameras, or synchronization of low speed cameras with a stroboscopic system to captures a similar sequence of images. The former would require very high continuous light to enable appropriate exposure for a shutter speed of $1/125000$ to be comparable to the latter that has a natural stroboscopic duration of 8 micro seconds; therefore it is usually restricted to lower flapping frequency tests with over 200 to 500 micro second exposure time ($1/2000$ to $1/5000$ shutter speed or equivalent frame rate), and the cost of the high-speed cameras is prohibitive. They also present a bigger challenge if the system needs to be placed in a constrained environment such as a wind tunnel or a vacuum chamber, due to their large volume (as in 2010). The latter is advantageous in all three aspects: the amount of light available from the strobe's short burst is much more than the continuous sources used by the high-speed cameras, the low-speed

cameras are relatively affordable, and the size of these cameras can be extremely small. Utilizing two sets of cameras, four in total, the experimental setup can record the motion of one flexible wing flapping within an 180° sweep. Techniques are described to record the complicated motion of the flapping wing, and decouple the rigid body wing kinematics from the elastic wing deformations.

Initial DIC concepts are given by Sutton et al.^[143] for displacement measurements over a flexible structure, and the technique has been improved over many times since. DIC uses stereo triangulation to digitize a random speckling pattern placed over an object, and thus compute its three-dimensional features. This is followed by a temporal matching process, where the system tracks a subset of the speckling pattern, and minimizes a cross correlation function to compute the un-deformed location of this subset, and thus the displacements. Lu and Cary^[144] implement a second-order displacement gradient to achieve more accurate strain and deformation measurements, while Cheng et al.^[145] use B-spline deformation functions to obtain a full-field correlation. Tay et al.^[146] develop a method to measure full-field out-of-plane displacements with a single camera, bypassing the stereo-setup.

Researchers have also characterized system errors caused by image quality and lens distortion to improve the correlation results. Schreier et al.^[147] calculate the systematic errors caused by intensity interpolation, which is a common way to increase an image's contrast by adjusting the level value (similar to increasing the image sensor sensitivity or gain value). Their analysis is very important to general DIC users, since light conditions vary in different environments and post processing the images to increase their quality is often favorable. They also conclude that high-order interpolation

methods with smaller phase errors are preferable. Yoneyama and Kikuta^[148] provide a lens distortion correction for DIC by measuring rigid body displacements. This further improves DIC's capacity since its theory presumes that the captured images are distortion-free. Siebert et al.^[149] use a detailed DIC analysis to show the influence of the different camera parameters (and thus error sources) on the attainable accuracy.

The use of digital image correlation systems for aeroelastic wing measurements has thus far been confined to the area of micro air vehicles: both fixed wings^[150] (in a wind tunnel) and flapping wings^[151] have been tested. Similar types of structurally anisotropic wings are studied in this work, with a combination of thin membrane skin (latex, silicone, Mylar, Teflon, etc) and a stiffer reinforcement (carbon fiber laminates, for example): an artificial analogy to the biological venation patterns of insect wings. The topological distribution of these two materials throughout a wing determines its response to the flapping kinematics and/or the oncoming flow, in terms of the lift and thrust generated during a flapping cycle. The overall relationships between these disparate variables is not well understood, but the aforementioned venation patterns seen in insect wings, coupled with the spectacular agility and maneuverability routinely demonstrated by these flyers, would certainly indicate the crucial role of wing flexibility.

Several challenges are addressed: the wing membrane may be reflective, translucent, or transparent, leading to glare, dark zone, or other problems in the image correlation. Capturing the motion of rapidly actuated systems leads to a challenging light configuration problem: a dark image is undesirable, as error is introduced when intensity is interpolated^[152]. Recording large out of focal plane displacement requires strict control of several lens parameters. For the low-speed cameras used here,

reconstructing the flapping motion requires additional post-processing to account for minor variations in the flapping frequency (drift, for example). Additional analysis is also required to separate the rigid body kinematics from the structural deformation.

2.2 Experimental Setup

The overall experimental setup is shown in Figure 2-1. The system includes a flapping mechanism, a vacuum chamber, a customized digital image correlation system, a synchronization and trigger system and a force and torque sensor. One of the most outstanding capabilities of the experimental setup is being able to measure the full-field out-of-plane structural deformation of flexible membrane wings in both static air and vacuum. When the experiments are conducted in air, the bell jar is lifted up 0.6 m (24") above the aluminum base plate.

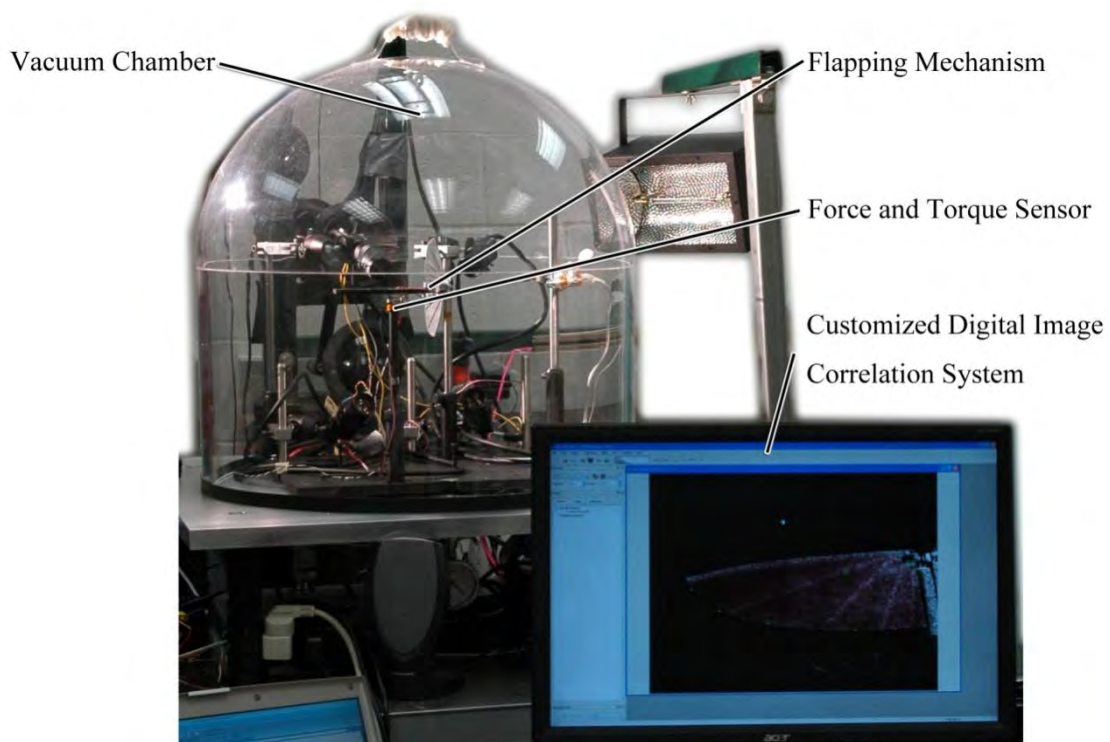


Figure 2-1. Overall experimental setup.

2.1.1 Test Subject

The flapping mechanism FL2D0 is given in Figure 2-2. This transmission-based design has a single degree of freedom motion; wings move up and down in the plane perpendicular to the motor axis. The horizontal distance between the motor axis (the symmetry plane of the mechanism) and the pivot of each wing is 0.9 mm, while the distance between the pivot and the wing mount is 3 mm. Each push rod is 40 mm long, and the radius of the crank is 3 mm. A Mabuchi M20-HV-1.5 motor is used to power the mechanism to run at flapping frequencies between 0~10 Hz, with a flapping amplitude of 90°. The tested wing is shown in Figure 2-3, with a Zimmerman wing planform. The aspect ratio of this wing is 7.65 (80 mm wingspan and 26 mm chord), formed by two ellipses which intersect at the quarter-chord point.

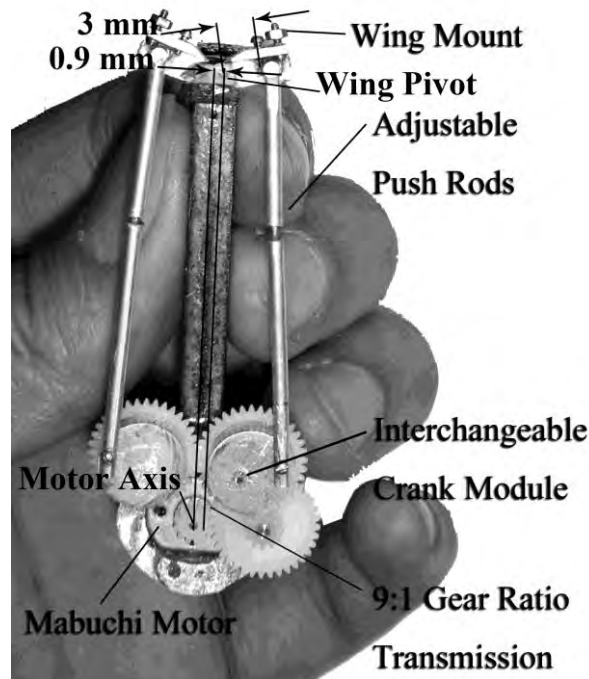


Figure 2-2. Flapping mechanism FL2D0.

The structure of this wing is similar to a hummingbird's feather quill layout, with a flexible trailing edge capable of passive deformation due to the aerodynamic loads.

Five batten structures emanate from the leading edge of the root. One serves as a stiff leading edge (three layers of unidirectional carbon fiber), and the remainder attach to the trailing edge (two layers of carbon fiber). To the top of this carbon fiber skeleton is affixed a thin latex rubber membrane, with no pre-stretch. The density of the membrane skin is 990 kg/m^3 , while that of the carbon fiber is 1600 kg/m^3 , resulting in a 0.3 g wing. A random speckling pattern can also be seen in the wing of Figure 2-3, applied with flat black spray paint. Despite the fact that the battens can be clearly seen through the membrane, the DIC system is still able to achieve a satisfactory correlation in these areas.

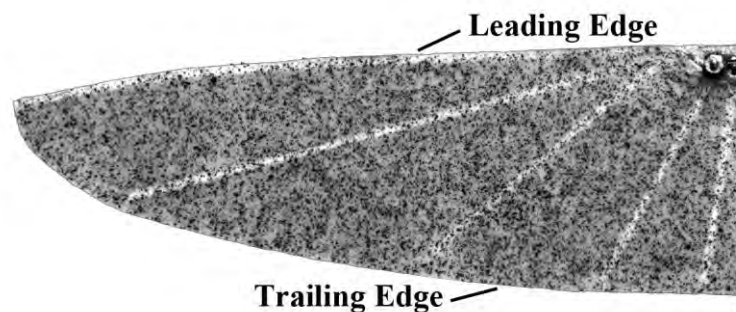


Figure 2-3. Tested wing with latex membrane.

2.1.2 Test Environment

In order to distinguish between the aerodynamic and the inertial effects within each wing beat cycle (as well as the structural deformations caused by each) separate measurements in static air and vacuum need to be performed. To meet these needs, a vacuum chamber is constructed. A square aluminum base plate (30" x 30" x 1", approx. $0.76 \text{ m} \times 0.76 \text{ m} \times 0.03 \text{ m}$) is used as the platform for all instrumentation. A half-inch thick (12.7 mm) clear acrylic bell-jar, with 24" (610 mm) inner diameter and 24" (610

mm) inner height, is placed on the base plate and encloses all equipment: four digital image correlation cameras, the mechanism/wings, and other instruments.

2.1.3 Cameras and Lenses

The correlation system consists of four Point Grey Research Flea2 cameras divided into two pairs. Such a setup should be able to capture the rigid displacements (wing kinematics) and structural deformations of a single wing up to 180° flapping amplitude. Each pair of Flea2s can capture stereo pictures of a wing moving through a 90° sweep angle after fine-tuning the depth of field. These Flea2 cameras have 1/1.8" progressive scan CCDs with 1624 x 1224 pixel resolution: as such, a very fine speckle pattern can be applied to the surface for a better image correlation. At such resolution, the cameras can operate at 15 frames per second. The large relative size of the CCD (compared to the usual 1/3" or 1/2") also enables a high sensitivity. Furthermore, their 29 x 29 x 30 mm³ dimension allows them to fit within the aforementioned bell jar. The Flea2s support data transfer rates up to 800 Mb/s, and multiple cameras networked on the same IEEE-1394 bus are automatically synchronized to within a maximum deviation of 125 μs.

Computar's 12-36 mm F2.8 C-mount lenses are chosen for the Flea2 cameras. This combination gives the cameras a field of view between 61° and 22°. Careful selection of each parameter is a crucial step towards obtaining a large enough depth of field (DOF) for clear images of the large wing actuations. For example, a theoretical value of 95.2 mm DOF is the result of a 0.25 m object distance and a 20 mm focal length, shot at F/16 aperture with a circle of confusion defined as 20 microns for the speckle recognition. These zoom lenses provide flexibility in positioning the cameras, and their continuous iris aperture helps adjust for the desired DOF. The cameras are

positioned symmetrically about the plane of flapping motion. They are tilted towards the same wing and zoomed in so that the wing fills the picture frame. The upper pair captures the stroke above the flapping mid-plane; the lower pair captures the stroke below the mid-plane. The complete setup is shown in Figure 2-4.

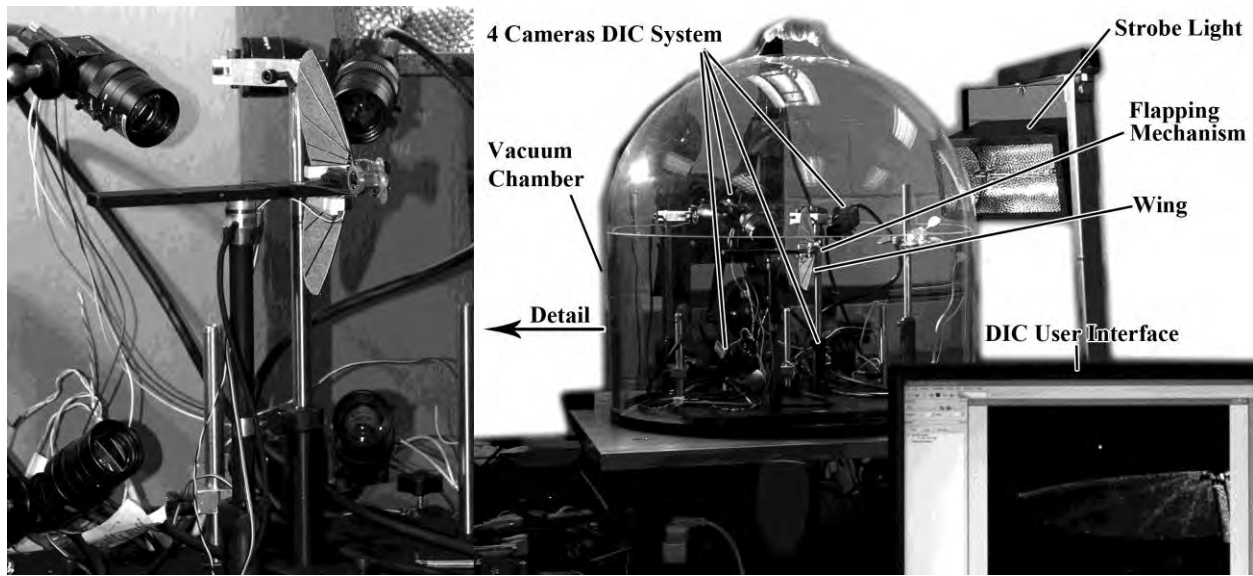


Figure 2-4. Detail of DIC setup.

2.1.4 Image Acquisition

Recording images for correlation analysis consists of setting up a camera trigger, configuring the light source, and providing a well-speckled specimen. For successful correlation, each image needs to be within the depth of field, free from motion blur, correctly exposed, speckles well contrasted, and captured with the correct synchronization. The following steps explain the process in achieving such objectives.

Camera and trigger setup

By using the nine-pin 1394b interface to control all attributes of the camera system, registry values that control exposure, triggering modes and strobe signal output are easily modified. The cameras are set to high gain values according to the aperture

value that gives a reasonable depth of field. This high gain setting drastically enhances the picture contrast, while also allowing a large amount of noise which will not affect the correlation analysis. Without this step, images require post level adjustment to have a recognizable contrasted speckle pattern, which is achievable in software such as Adobe Photoshop. But this would induce error that is more difficult to quantify.

After the cameras are set with correct gain values, adequate lighting is available, and the lenses are set to a reasonable aperture for clear pictures, the timing of the trigger firing becomes the main issue. Reproducing a sequence of images that simulates what could be captured with high-speed videography requires that the cameras trigger at a frequency which allows several complete cycles to pass by. The time interval between each trigger is determined by the following relationship:

$$\Delta T = \frac{N + 1/s}{m}$$

where ΔT is the trigger time interval, s is the number of samples per cycle, m is the flapping frequency at steady state, and N is the number of complete cycles between sequential triggers. Therefore, the stroboscope flash frequency is:

$$f = \frac{1}{\Delta T} = \frac{ms}{Ns + 1}$$

Controlling ΔT in milliseconds can then control the sampling rate, and allows the low-speed cameras to capture sequential images. However, this method requires very steady flapping frequency of the mechanism (0.1 Hz command resolution). If the wings are heavily loaded due to high speed flapping (aerodynamic loads) or heavy wing structure (inertia loads), a frequency fluctuation is expected, and sampling rate will not be constant. In this case, different offset ΔT 's will be used to encompass the situation

and a post-processing technique will reconstruct the images into the correct sequence, as discussed below. Figure 2-5 illustrates the trigger timing scheme.

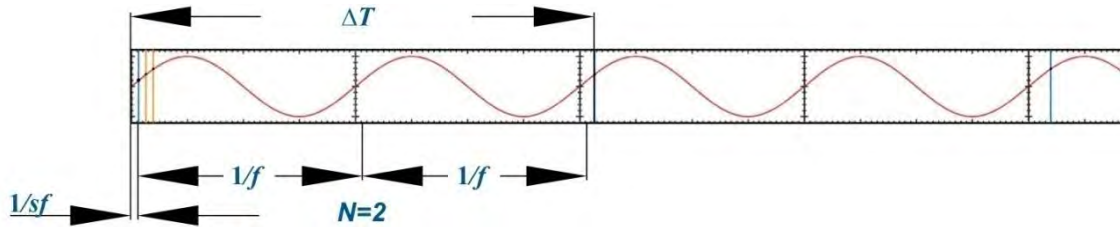


Figure 2-5. Trigger timing scheme.

Light source configuration

The light source determines the exposure time, which directly renders the motion blur that can cause a failure in correlation. Motion blur is related to wing size, flapping rate, amplitude, and the duration of exposure. For constant light sources, such as black light or incandescent light, exposure duration is the time of shutter release, down to tens of microseconds for required clarity. A small wing undergoing low frequency, low amplitude flapping motions can realize a clear picture with a relatively longer exposure time. For an intermittent light source such as a stroboscope (current case), exposure depends on the duration of each burst. A linear stroboscope (Checkline LS-10-6000), triggered by the shutter of the cameras, bursts an 8 to 10 μs duration pulse of light over the flapping system. The energy burst is 0.72 joules with 1960 Lux illumination. This short burst duration powerfully freezes the flapping motion with a dark background. Mirrors and sheets of reflective material are used to direct the emitted light onto the wings, in order to gain higher contrast.

2.1.5 Data Post Processing

Image sequence reconstruction

As mentioned previously, if the flapping mechanism's performance is not affected by loading conditions, the flapping frequency will not vary with time, and images taken with the progressive scanning trigger will already be in the correct sequence within the flapping stroke. However, aerodynamic and inertia loads play such significant roles that the actual frequency may fluctuate up to ten percent about the commanded frequency. This causes the images taken with the previous method to be out of sequence. An automated post-processing technique is therefore developed to reorganize the images into the correct sequence, in order to reconstruct one cycle of flapping motion. This technique consists of two parts: sequence recognition and file reorganization.

To find the correct order of the images, an image feature that corresponds to each unique flapping position is located. For the current mechanism, reflective paint is applied to a screw head that rotates with the push rods. This portion of the mechanism is located by digitizing the image (originally taken with the DIC system), and removing all portions of the image that do not contain the reflective paint. The intensity map is converted to a binary variable, hopefully locating the coordinates of the reflective point, as seen in Figure 2-6. This process is repeated for all the images, eventually forming an elliptical trace. By using the geometric center of the trace of these points, and the relative angle and distance from the points to the center, correct image order can be determined. Given a desired number of samples per cycle, a list of equally spaced images is generated. These pictures are then renamed and relocated to a target folder. This is feasible because the image files produced by each set of cameras share the same sequence number in their names.

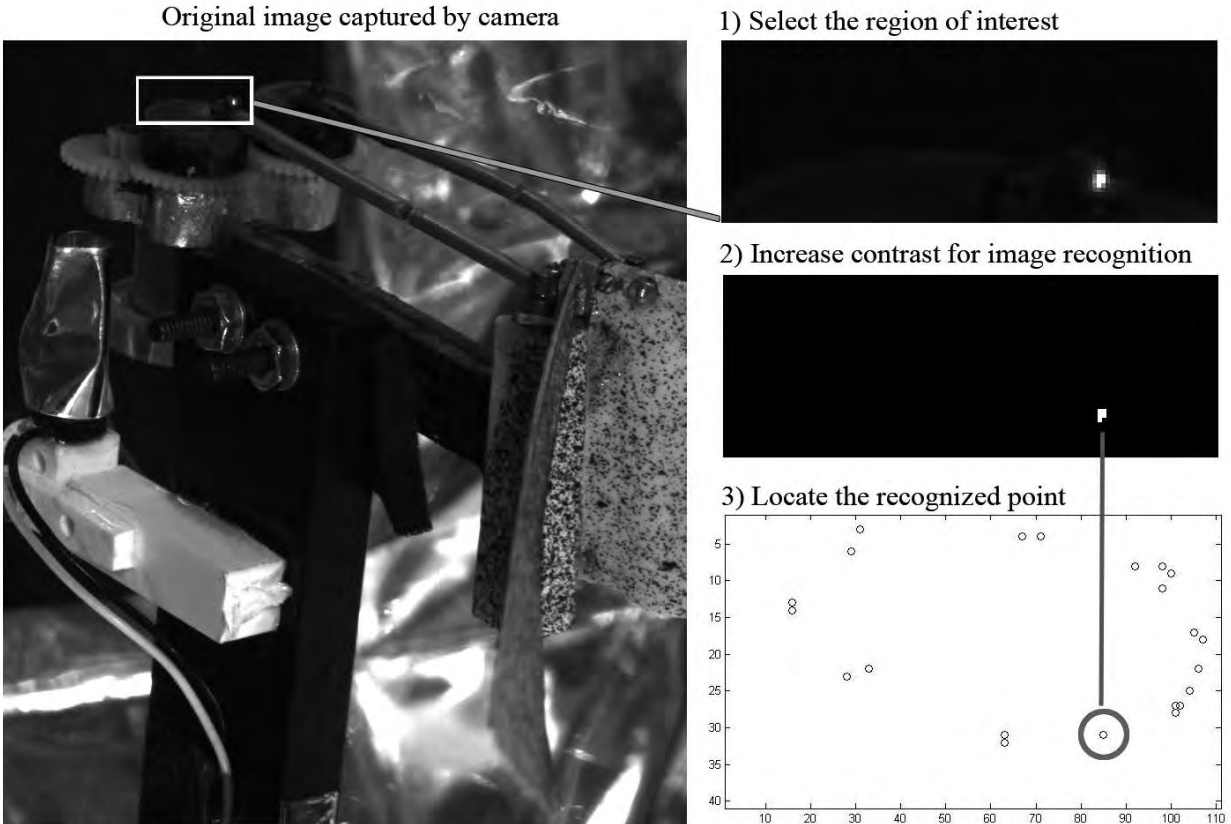


Figure 2-6. Image feature recognition.

Correlation and transformation of data

The commercial software VIC3D correlates the images and output the coordinates of data points along the wing surface into text files. These coordinates are referred to a reference frame correlated from a designated reference image. For this work, it is convenient to use the mid-plane of the flapping cycle, well captured by both sets of cameras, as the reference. The program thus provides the initial un-deformed coordinates (which are nothing more than the static wing at the mid-plane), as well as the displacements, which are composed of both rigid body motions (kinematics) and structural deformations. It is desired to separate the two: the latter is much smaller than the former, but is expected to be the sole source of lift and thrust. For the mechanism described above, single degree of freedom flapping of a rigid wing won't produce time-

averaged loads, but a flexible wing that deforms in both spanwise and chordwise direction will.

These motions are separated by creating a fictional rigid wing surface with the same flapping angle as the flexible wing. First, three data points are selected very close to one another, and very close to the leading edge of the wing root. As these points are located close to the wing joint, it is assumed that their motion follows the rigid body kinematics, with no elastic deformation. The displacement data for each flapping image can then be used to find the new coordinates of these three data points throughout the stroke. For each flapping image, local coordinate systems are computed for the two pairs of triplets (one set which remains stationary at the mid-plane, and one which travels with the wing), and the rotational transformation matrix is subsequently computed. The static wing at mid-plane is then appropriately rotated, and then translated so that the two triplets coincide. This technique is graphically depicted in Figure 2-7. The difference between the fictional rigid surface and the elastic wing provides the sought-after structural deformations, indicated by w in the figure.

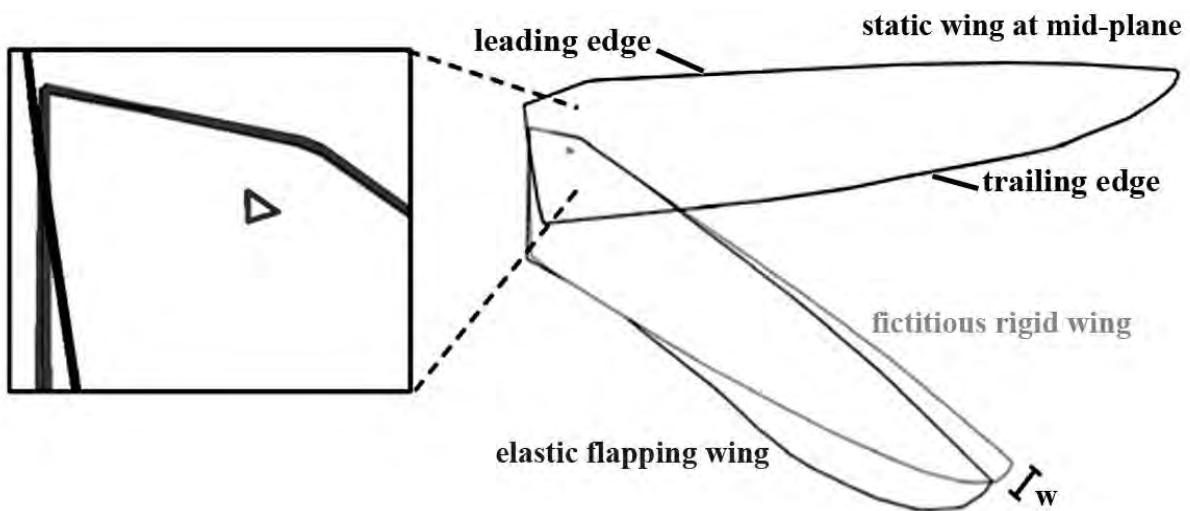


Figure 2-7. Construction of a fictional rigid wing through rotational transformations.

2.3 Results

The results of this study are obtained for a flapping frequency of 5 Hz and a flapping amplitude of 90° . Normalized out-of-plane elastic displacements (w/c , where c is the root chord of the wing) are contoured along the wing at various positions within the flapping stroke, for both the downstroke and the upstroke. Data is given for flapping in air (Figure 2-8) and in a vacuum (Figure 2-9). Solid lines not filled by contour lines indicate the fictional rigid wing surface.

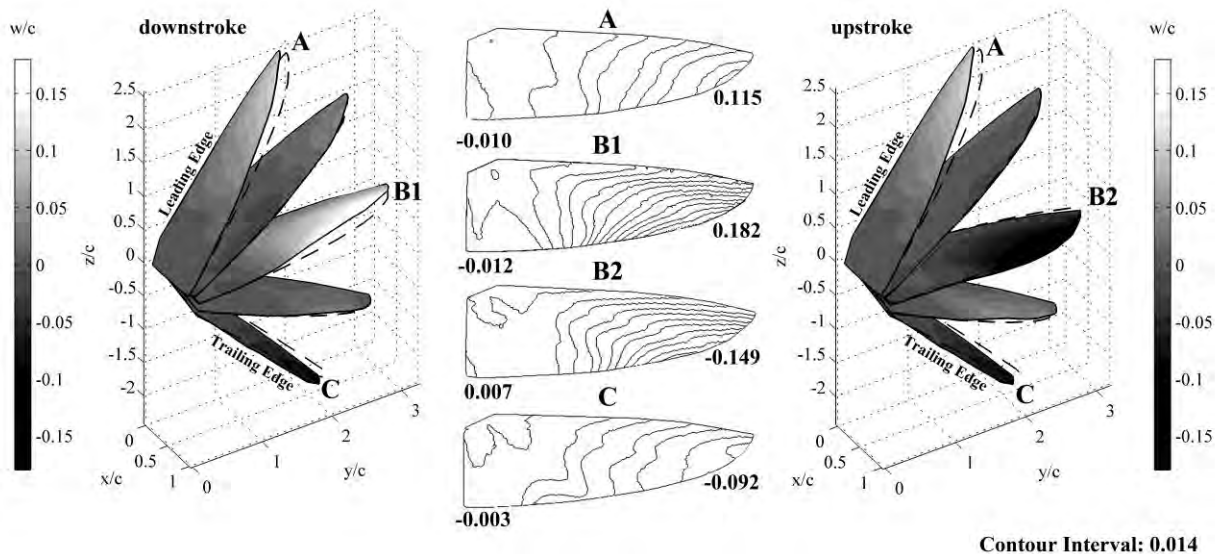


Figure 2-8. Structural deformations (w/c) through the flapping stroke, in air.

It should first be noted that the elastic deformation, for all cases, is relatively large: 18% of the root chord in some locations within the flapping stroke. This is despite the relatively low flapping frequency (5 Hz). Higher flapping rates will exacerbate this effect, placing more of a strain on the DIC camera system to record such exaggerated motions. For flapping in air (Figure 2-8), the elastic surface typically trails the fictional rigid wing, due to the prohibitive effect of the air loads. The top and bottom of each stroke see substantial spanwise bending of the wing, increasing the maximum and minimum

locations traveled by the wing tip. At the mid-plane, the elastic wing sees a substantial deformation at the trailing edge: washout on the downstroke, and washin though the upstroke. Washout means that the trailing edge of the wing deforms away from the unloaded position, decreasing the angle of attack of the local washout section; washin vice versa, increasing the angle of attack. The induced angle of attack is indicative of the thrust-generating capabilities of the membrane wing. At the stroke locations midway between the mid-plane and the peak (or minimum) flapping angle, structural deformation is negligible.

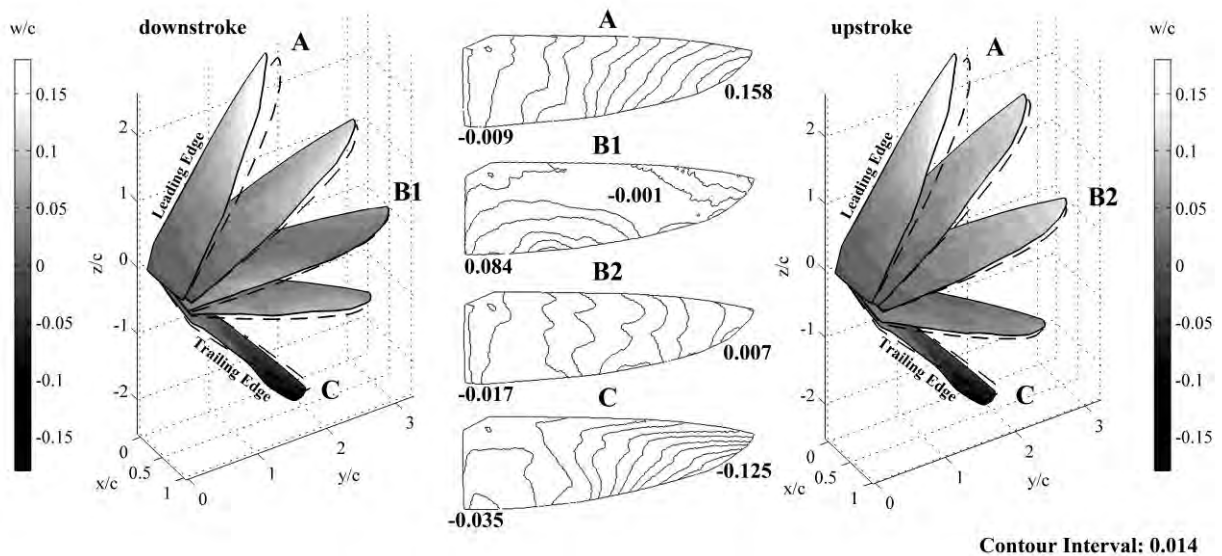


Figure 2-9. Structural deformations (w/c) through the flapping stroke, in vacuum.

The results for flapping in a vacuum (Figure 2-9) are different. Though the spanwise bending at the top and bottom of the stroke plane is very similar to that seen in air (as the forces at work here are primarily inertial in nature), there is very little structural deformation at the mid-plane. This contrasting comparison explains and confirms the aerodynamic effect occurred at B1 and B2 in Figure 2-8. As discussed above, flexibility (for these kinematic motions, at least) is probably necessary to

generate thrust: at the point of peak velocity, the induced angle of attack is nearly zero. As above, the flexible surface lags the fictional rigid wing on the downstroke, but it leads on the upstroke. This seemingly counter-intuitive idea may be the result of high-frequency vibration throughout the flapping wing, not adequately captured with the strobe-trigger system described above. Figure 2-10 compares both cases with a colored interpretation.

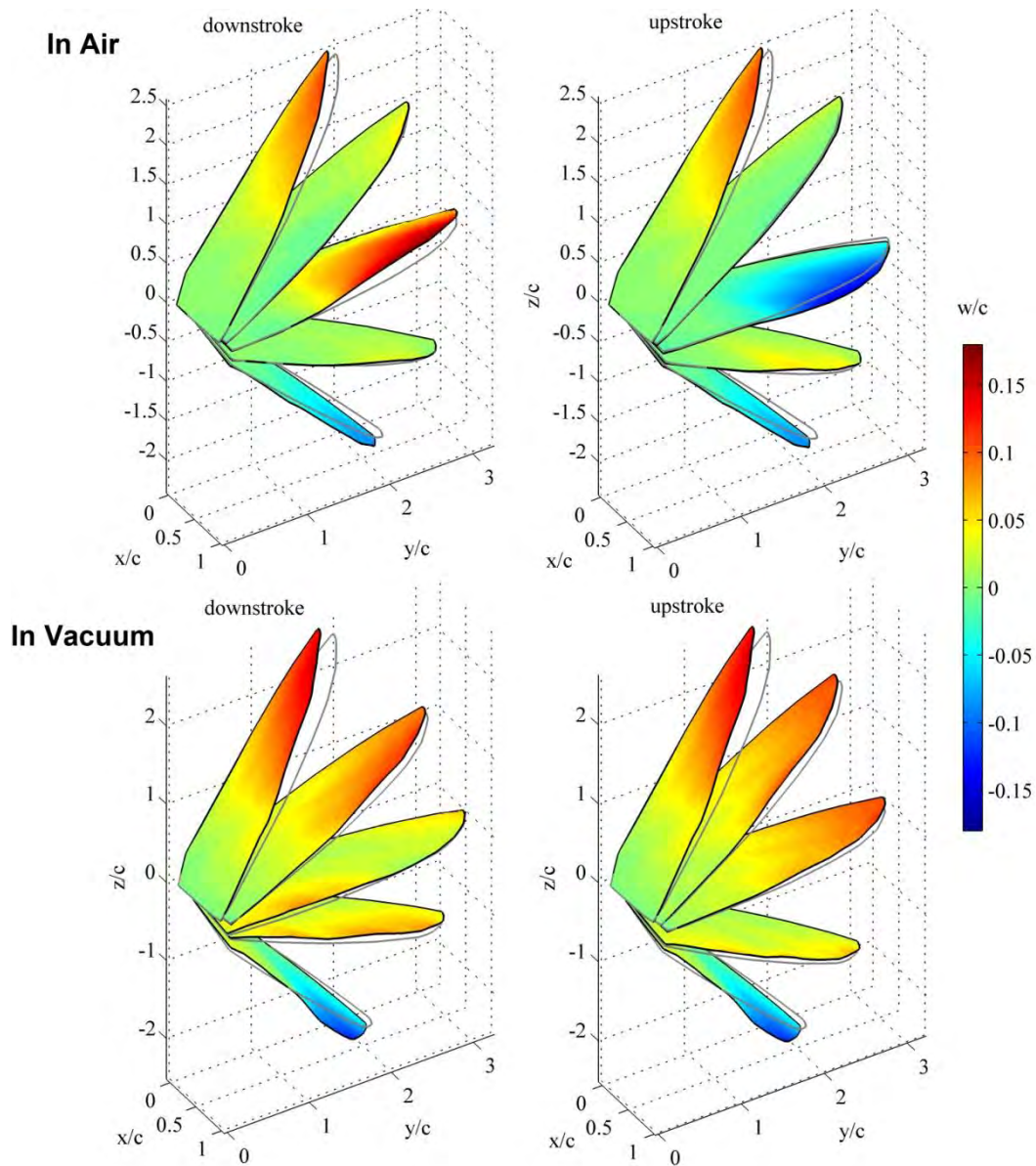


Figure 2-10. Colored deformation comparison in air and in vacuum.

2.4 Conclusions

The development of DIC techniques has successfully captured the motion of a rapidly actuated flapping membrane wing with a pair of low-speed stereo cameras and a triggered strobe light. The techniques are further detailed for separating the rigid body kinematic motions from the structural deformation. This is expected to be a necessary step, as a rigid wing (or a flexible wing in vacuum) is not expected to generate sufficient lift and thrust loads. Indeed, inspection of deformation results from flapping in both air and vacuum reveals the passive trailing edge feathering for thrust generation only in the former case.

In the following chapters, the experimental configuration is adjusted accordingly (such as camera parameters, positions and orientations), but the key concepts are the same as what is presented here. The capability to perform tests in both static air and vacuum (as well as in wind tunnels in future) enables a quantitative measurement of the aeroelastic behavior, essential to both structure characterization as well as identification for aerodynamic mechanisms. One of the most important results to be presented is that the deformation pattern is the only cause for propulsion under a simplified single-degree-of-freedom kinematics. Therefore tailoring the structural deformation is the key for flapping wing optimization.

CHAPTER 3 PASSIVE WING DEFORMATION

Insects and hummingbirds can only actuate their wings near the wing joint with limited authority over the wing structures: insects may regulate internal pressure to change the wing stiffness; and hummingbirds can control the spread angle between feathers to change the wing planform. During flight, significant passive aeroelastic deformation occurs. For example, ladybugs have an extremely compliant and foldable wing structure that can be deployed by increasing pressure and stiffness of the leading edge; and then the wing compliance allows a beneficial cambered airfoil profile to be formed during flapping, as well as the implementation of the clap-and-fling mechanism to enhance lift production. On the other hand, hummingbirds have compliant feathers that deforms adaptively in both upstroke and downstroke, enabling them to be more stable under wind gust, have a low noise profile and produce more aerodynamic forces. Reference images are shown in Figure 3-1.



Figure 3-1. Passive wing deformation in nature².

² Examples are taken from Google Image search. The author would like to thank the anonymous photographers for their contributions of the ladybug (left) and hawkmoth (right) images. Photo courtesy of the hummingbird (middle) by Greg Scott at <http://www.gregscott.com>.

For artificial MAV systems, similar principles can be applied to simplify the actuation kinematics, therefore reducing parts and overall weight, increasing mechanical efficiency and allowing for controls to be incorporated. As cited in references in Chapter 1, flapping mechanisms that are able to perform an insect-inspired kinematics are very heavy and not suitable for aircraft use. The current successful ornithopters employ a simple one degree-of-freedom motion created with a motor-gear mechanism, in combination with flexible membrane wings to generate sufficient lift and thrust. If a multi-degree-of-freedom mechanism is used, the large number of parts will have tremendous inertia and friction, lowering the overall mechanical power efficiency. Therefore, the use of passive wing deformation should be exploited for simplified kinematics to generate desired aerodynamic forces. If the structural property of the wing can be changed during flapping (insect wings do so by regulating internal pressure), then different control methods can also be realized without changing the kinematics.

There are three factors dictating the passive wing deformation: 1) aerodynamic loads (action and reaction), 2) inertial loads (kinematic acceleration), and 3) elasticity (structure compliance/stiffness). The aerodynamic loads are coupled with the deformation; therefore it cannot be determined until the other two factors are known. The inertial loads are determined by kinematics and mass distribution across the wing, equivalent to mass timing acceleration. From a design point of view, both kinematics and wing mass can be well defined: the former realized with a robust actuation mechanism and the latter by parameterized fabrication. Once this loading condition is known, inertial passive deformation can be calculated in finite element analysis (FEA)

environment if the structure elasticity (i.e. elastic modulus) is known. From a manufacturing point of view, to control the wing elasticity is to control the materials (therefore their properties) and the structure (composition, topology, cross section, geometry, etc.).

Aerodynamic loads, coupled with passive wing deformation, are rather a pursued result than a controlled factor. At present, computational tools are still in development stage, attempting to compute coupled structural and fluid dynamic simulations. However, current experimental techniques are mature enough to fully characterize the phenomenon: high sensitivity sensors can be used to measure aerodynamic forces; digital particle image velocimetry (DPIV) can be used to measure airflow around the wing; and digital image correlation can be used to depict the full-field structural deformation. Combining these techniques, examination of the effect of passive wing deformation on aerodynamics can be performed. This is presented in detail in the next Chapter.

Inertial loads are studied experimentally with tests performed in vacuum, but a simplified conceptual case is presented here to qualitatively describe the relationship of kinematic parameters and wing loading. For each designed experiment, kinematics is designed along with each flapping mechanism; while mass distribution is resulted from wing design and fabrication. The following derivation includes both aerodynamic and inertial loading relationships with flapping frequency (f) and stroke amplitude (ϕ), two of the most basic kinematic parameters. The derivation is under these assumptions: 1) any point on the flapping wing surface can be treated as a point of mass of no volume, l is the distance to the flapping wing joint; 2) the points can be integrated by area to

represent the wing; 3) the kinematics of each point is defined as a simple sinusoid motion: $\alpha(t) = 0.5\Phi\sin(2\pi ft)$, as shown in Figure 3-2.

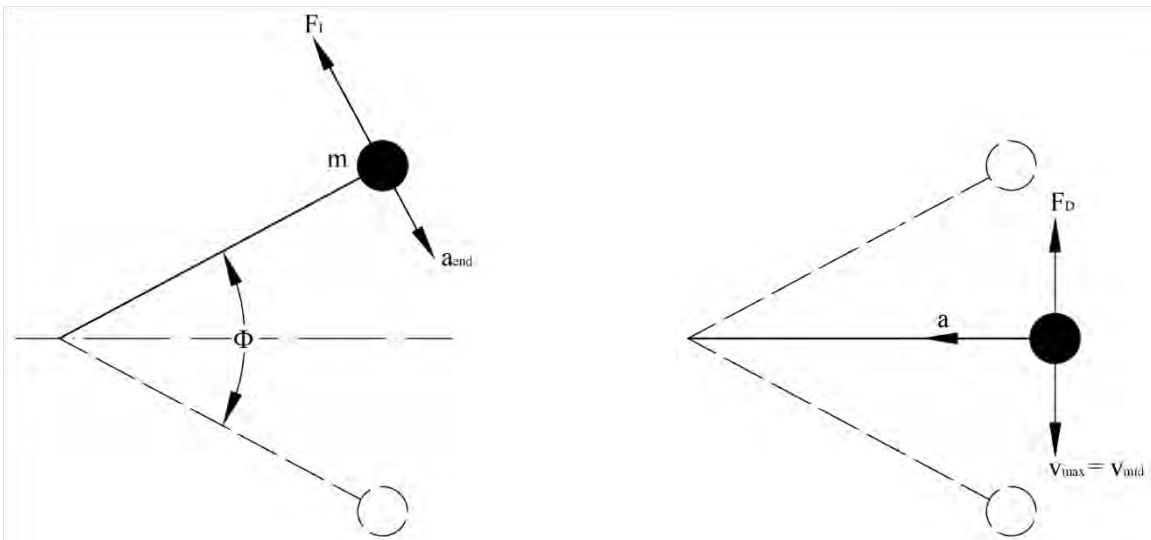


Figure 3-2. Simplified scheme for loading analysis on a point mass

The velocity can be expressed in the following equation. The maximum velocity occurs at mid-plane when $t=0.5n\pi$, (n is an integer greater than 0).

$$v = l\dot{\alpha} = \pi f\Phi l \cos(2\pi ft)$$

$$v_{max} = v_{mid} = l\dot{\alpha}(t = 0.5n\pi) = \pi f\Phi l$$

Aerodynamic forces (such as drag: F_D) may be proportional to v^2 at some instances (for example, the initial stroke in static air), therefore being proportional to Φ^2 and f^2 , from $(\pi\Phi fl \cos(2\pi ft))^2$. However, the unsteady aerodynamics in flapping wing of this scale has different mechanisms to produce forces (mainly because of the wake and vortices around the wing in steady state), rendering this relationship invalid. The time-averaged thrust is then usually not in a quadratic trend of flapping frequency, and occasionally observed to have a linear relationship to frequencies. This is presented in detail in the Chapters 4 to 6.

Only maximum out-of-wing-plane inertial loading, which occurs at wing reversal, is considered here. The acceleration at wing reversal when $t=(0.5n-0.25)\pi$, (n is an integer greater than 0), can be expressed as:

$$a_{end} = l\ddot{\alpha}(t = (0.5n - 0.25)\pi) = 2\pi^2 f^2 \Phi l$$

Therefore the maximum inertial force in the direction that would cause out-of-plane deformation would be ma_{end} , therefore the force is proportional to l , Φ and f^2 . These relationships, although simplified to a point mass, can be observed in later experiments.

The discussed relationships are summarized in Table 3-1.

Table 3-1. Summary of point mass loading relationship

	Linear proportional parameters		
Steady aerodynamic loading	l^2	Φ^2	f^2
Out-of-plane inertial loading	l	Φ	f^2

The structure elasticity can be very complicated for a wing with a varying cambered profile and a sophisticated topology. FEA is an ideal (and probably the only) tool in the design stage; because any complicated geometry, topology or materials can be modeled, and the details of wing structure can be examined before fabrication^[153]. However, the computation model would require experimental validation, which cannot measure elasticity directly. Traditional methods would measure strain locally under known loading condition to determine elastic properties. In the flapping wing study, the loading condition is too complicated and cannot be fully controlled yet. The elastic properties can only be examined as part of a global measurement: different deformation as a result of different compliance.

The following sections will present such passive wing deformation measurement that reflects inertial and aerodynamic loading, as well as structure elasticity. Several

wing types are examined. First, the wing membrane is studied using an elastic and heavy material in comparison with an inelastic and light material. This gives an insight of how mass quantity and distribution would cause different passive deformation as well as the effect of elastic membranes. Then, the structural compliance is studied with a nominal rigid wing, a semi-rigid wing and flexible wings to observe their deformation and effect on aerodynamics, which are corresponding to the qualitative analysis in this section.

3.1 Mass Distribution

3.1.1 Elastic Membrane Wings

University of Florida's Michael Morton Micro Air Vehicle Laboratory has an extremely successful history using flexible membrane fixed wing structure to improve the flight performance: gust alleviation with batten reinforced wings and improving longitudinal stability with parameter reinforced wings. Latex membrane has been selected for those vehicles because of its hyperelastic properties: forming adaptive washout and increased camber profiles during flight. For flapping wing studies, such hyperelastic material would also present some interesting behaviors such as billowing and adaptive deformation. Therefore in this section, three differently reinforced wings are laminated with the elastic membrane to examine the passive wing deformation.

Tested wings

Each wing has a length of 80 mm and a root chord of 26 mm. A Zimmerman shape, formed by two ellipses which intersect at the quarter-chord point, is selected as the wing planform. Three different wing structures (topologies) are tested, as shown in Figure 3-3. A triangular structure, made of two layers of bidirectional carbon fiber plain weave, is built at the cross-section of the leading edge and wing root. Its high stiffness

allows it to serve as a reference for later deformation measurements, and to connect to the FL2D0 flapping mechanism.

The leading edge of each wing is a thin strip of unidirectional carbon fiber made of three layers. Wings 1 and 2 have batten structures that travel from the leading to the trailing edge for reinforcement; wing 3 does not. Wing 1 has straight battens parallel to the root chord, therefore named BP for battens parallel. Wing 2 is named Hum for having diagonal battens similar to hummingbird's quill structure. Wing 3 is named LEO for leading edge only because there is no other batten reinforcement. These three wing types are studied intensively through this dissertation using different membrane materials, kinematics and structure.

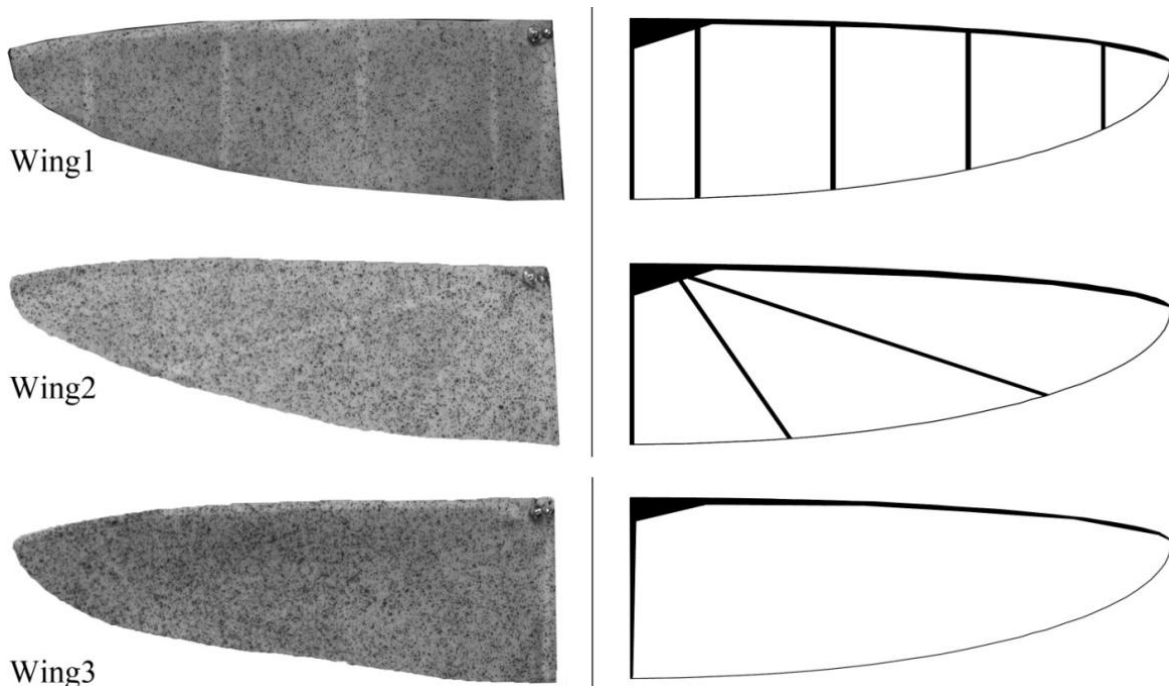


Figure 3-3. Test wing structures: speckle patterns (left), and topologies (right).

BP is similar to the design used in a toy ornithopter: “VampTM”, by Interactive Toy. This design places an emphasis upon controlling the chordwise stiffness through transparent tape battens that also maintains the airfoil profile, while the leading edge

alone determines the spanwise rigidity. Significant bending and torsion coupling can be expected from this wing. Hum is commonly seen in ornithopters with only one diagonal batten (Wowwee's "DragonflyTM"). This topology has been proven to be very successful in forward flight. Its diagonally-placed batten structure reinforces both wing bending and torsion. LEO reinforces the leading edge only; ornithopter kits using such a design can achieve near hovering in indoor flight. This design is expected to produce thrust by adaptive billowing of the wing membrane.

The wing fabrication process is briefly described as follows. Carbon fiber elements are first cut into strips and pieces to lay up on a flat plate that has the topology printed in the back of a piece of release material (Teflon). Then the skeletons are laid up, vacuum-bagged and put into an oven for a curing cycle. Once the carbon fiber laminate skeletons have cured, they are painted a mid-tone color so that the contrast between the batten and membrane is reduced. A speckled latex rubber membrane is glued to the painted surface. The average weight of the resulting wings is 300 milligrams. Most of the wing mass is on the membrane (over 200 milligrams).

Full-field deformation measurements

The structural deformation of Wing 1 BP in air is presented in Figure 3-4, at three different flapping frequencies. A grey line is used to indicate the rigid body motion: if the wing did not deform, the wing contour would have been at the same profile. The color contour shows the out-of-plane deformation normalized to the root chord (26 mm) from a range of -0.75 to 0.75. Instantaneous frames in one flapping cycle are selected to represent the dynamic movement; they are also numbered for discussion. At 3.75 Hz, the deformation scale is from -0.12 to 0.12. The frames 1 and 7 shows the tip snap deformation caused by inertial loading at wing reversal. Such deformation stores part of

the kinetic energy into elastic energy. Therefore when the inertial loading reduces, a rebound motion is observed in frames 2 and 8. As the wing velocity increases, the aerodynamic loading increases. Therefore at mid-plane 4 and 10, significant washout (4) and washin (10) can be observed. The maximum aerodynamic effect occurred at the mid-plane is probably due to the low frequency, which allows the steady aerodynamic principles to remain valid. This effect can further be examined by comparing with the vacuum case shown in Figure 3-5.

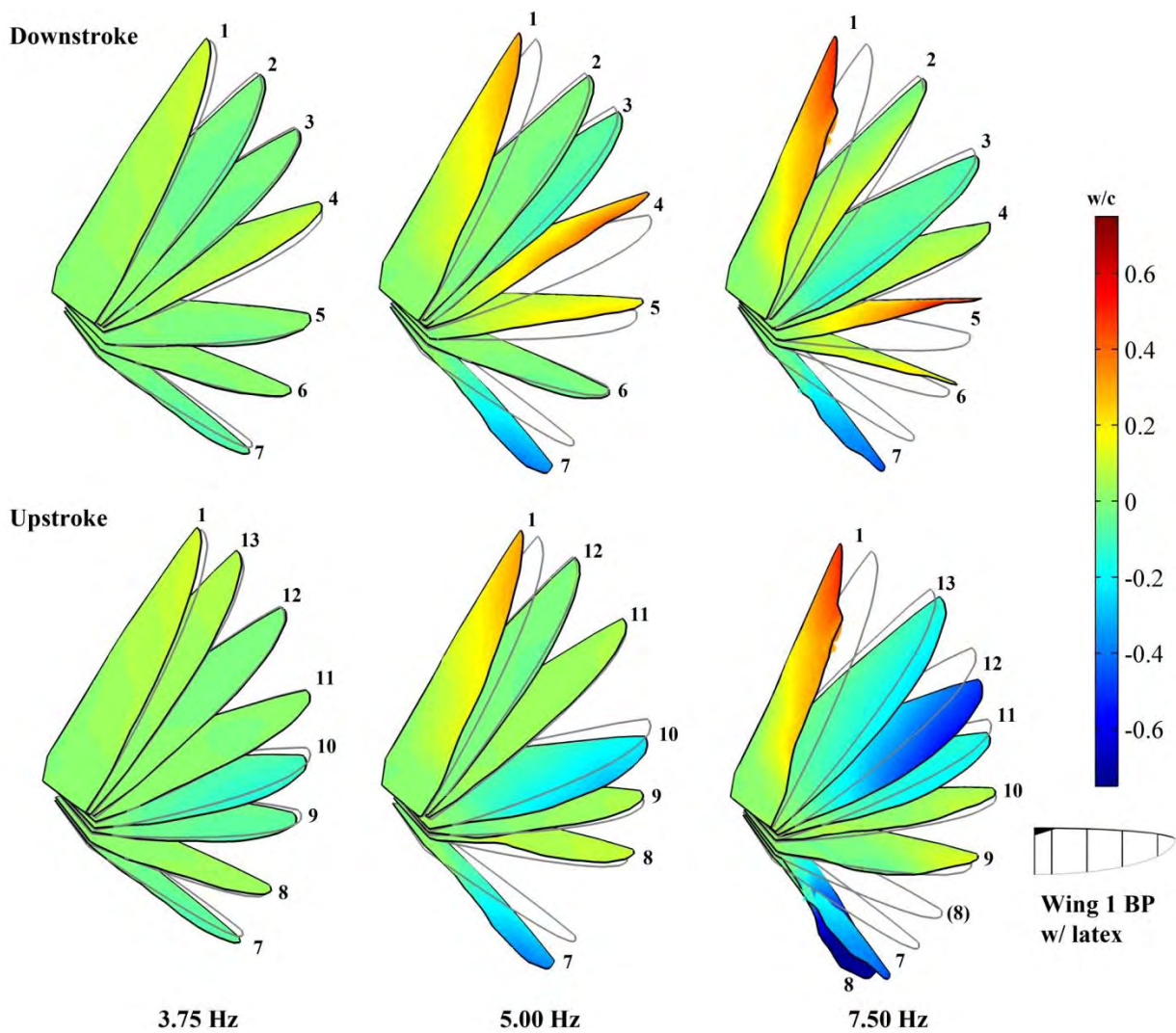


Figure 3-4. Structural deformation of Wing 1 at 3.75 Hz, 5 Hz and 7.5 Hz in air.

At 5 Hz, similar deformation pattern can be observed: tip snaps at the end of each stroke (frames 1 and 7) and aerodynamic washout and washin at frames 4 and 10. But the deformation scale has increased from ± 0.12 to ± 0.35 . Another significant change is that the elastic recovering process after the mid-plane can be observed with frame 5: as the velocity reduces, the deformation reduces. A symmetrical frame during upstroke lies between frames 10 and 11 but is not captured due to limited measurement resolution. Frames 6 and 11 shows the wing shape is restored to the undeformed condition, indicating the minimum loading condition during transition.

At 7.5 Hz, the deformation pattern becomes very interesting: much higher inertial loading (proportional to f^2) causing larger tip snap and the delayed washin and washout. Frames 1 and 7 again depict the inertial tip snap due to wing reversal. However, a delayed deformation enlargement occurs at frame 8 (the other (8) shows the rigid body motion position). The wing bends the most near the root and twists away from the plane. The delayed deformation can be explained with the compliant leading edge: inertia overwhelms the controlled kinematics. The symmetrical frame is not shown during downstroke. Then the wing is recovered at frames 2, 3, 9 and 10, showing the aerodynamic damping effect (otherwise the wing deformation would overshoot to the other direction as later seen in the vacuum case), as well as the conversion between potential energy and kinetic energy, which causes the delay of the observable washout (frames 5 and 6) and washin (frames 11, 12 and 13) deformation.

In vacuum, the structural deformation of Wing 1 BP is shown in Figure 3-5. The normalized deformation range is ± 0.2 at 3.75 Hz, ± 0.38 at 5 Hz and ± 0.8 at 7.5 Hz. At 3.75 Hz, the tip snaps at frames 1 and 7 are apparently larger than those in the air case

in Figure 3-4, revealing the damping effect in air. The washout and washin no longer exist at frames 4 and 10 due to the absence of air. At 5 Hz, the deformation pattern is again similar to the 3.75 Hz case, except that noticeable structure vibration is captured at frames 5, 8 and 10. The vibration is initiated at the end of each stroke when kinetic energy is transformed into elastic potential energy. Then the energy is released in the rest of the cycle, damped only by the membrane structure. This phenomenon is accentuated as the frequency increases. At 7.5 Hz, significant passive wing rotation and tip snap occur at the end of each stroke, at frames 1 and 7. This energy is later released through the stroke: frame 2 shows the deformation starts to overshoot, then frame 3 shows extended deformation. This reciprocation repeats itself at frames 4, 5 and 6. Until the wing reaches the end at frame 7, the vibration resets for the next half flapping cycle. Frames 2, 6, 9, and 14 are captured when this high frequency vibration reaches a neutral position.

The deformation in vacuum illustrates the basics of inertial loading on the wings. As mentioned in Table 3-1, out of plane inertial loading is proportional to frequency squared. The maximum tip deflection ratios are 1.9 (5 Hz case over 3.75 Hz case: $0.38/0.2$) and 2.1 (7.5 Hz case over 5 Hz case: $0.8/0.38$), which are very close to $(5/3.75)^2=1.78$ and $(7.5/5)^2=2.25$. The quotient relationship matches very well with the simplified conceptual model, even though the actual wing elasticity is not simple/linear, meaning the ratio between tip deflections are not necessarily the same as that of the inertial loads.

The deformation measurements presented in Figure 3-4 and 3-5 not only reveal the details of the surface response, but also illustrate both the aerodynamic effect

(washout and damping) and inertial effect (tip snap and vibration). However, expressing the structural deformation with full-field color contours is limited by the instantaneous frames. In order to see the history of a complete cycle, different description methods needs to be adopted.

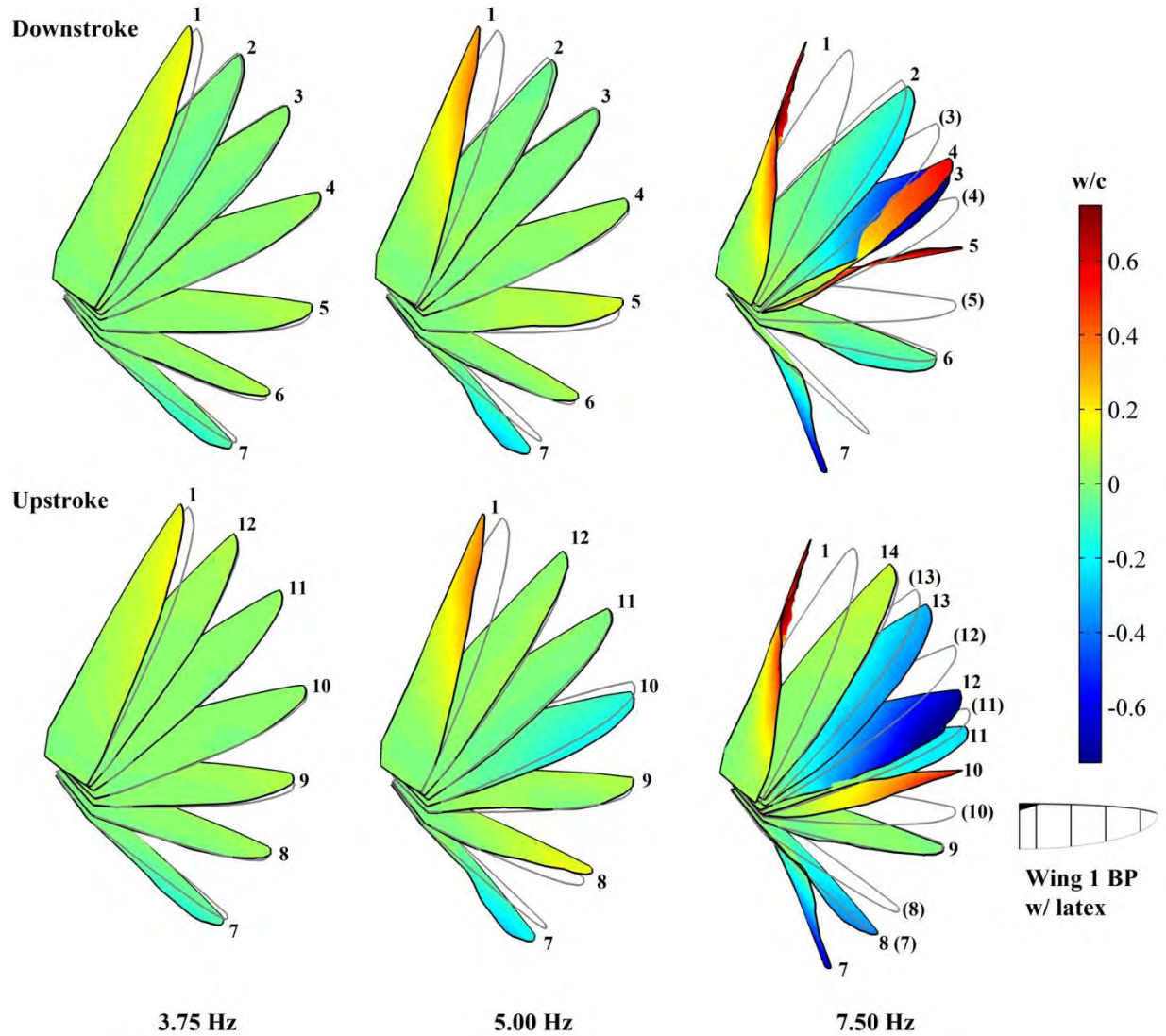


Figure 3-5. Structural deformation of Wing 1 at 3.75 Hz, 5 Hz and 7.5 Hz in vacuum.

Data parameterization

The data set is further distilled into three elastic metrics to indicate bending, twisting, and inflation of the membrane wings. The wing tip deflection (w_{tip}) is measured from the actual tip position to that of the undeformed reference plane. Geometric twist (angle of attack) and aerodynamic twist (maximum camber) are both measured at 75% of the semi-span. This is illustrated in Figure 3-6, where the tip deflection w_{tip} and the angle of twist θ are shown. These values can simplify the full-field deformation into numbers: w_{tip} reflects the magnitude of wing bending, θ represent the amount of passive wing twist and the maximum camber indicates the aerodynamic pressure on an elastic membrane. If these values are plotted against the wing position (flap angle), then a cyclic history can be represented.

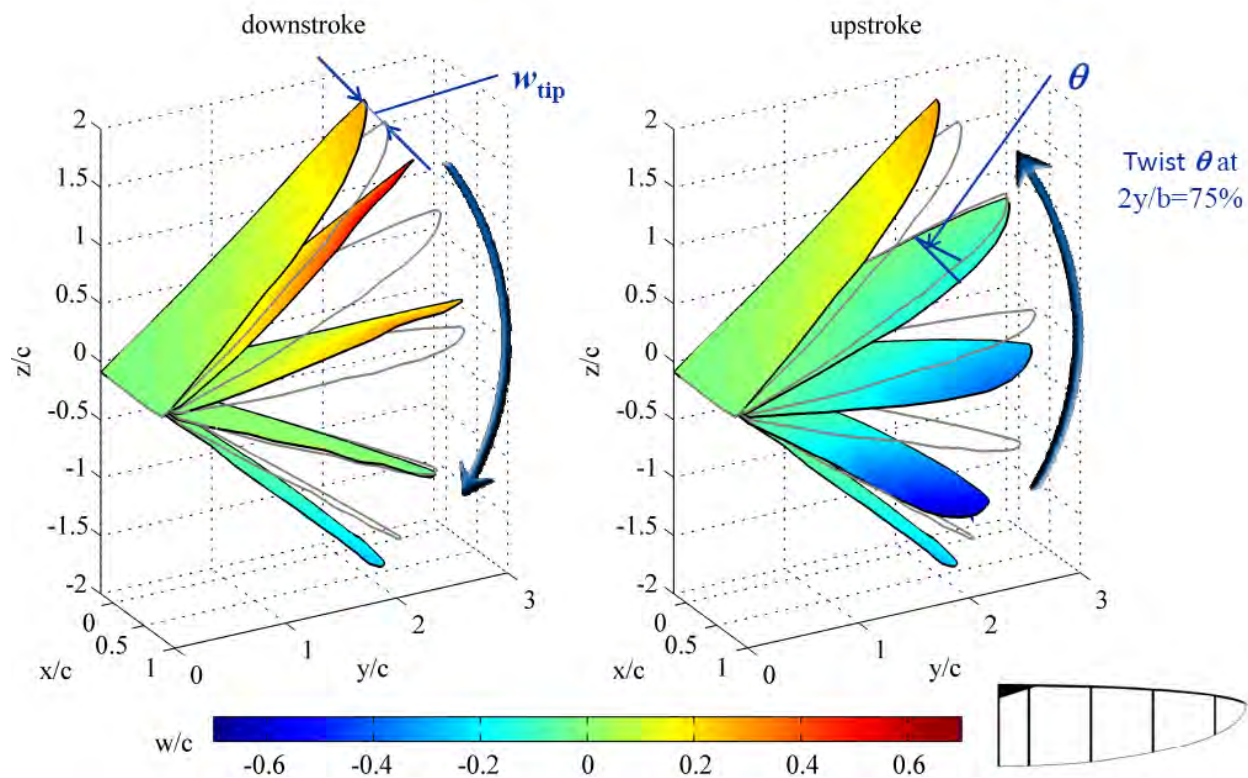


Figure 3-6. Parameterization example of structural deformation into w_{tip} and θ .

Figure 3-7 and 3-8 show a few examples of the figures with deformation versus flap angle. The former shows the wing bending history measured with the normalized tip deflection. The latter shows the wing twist history measured with angle of twist. These figures are called deformation phase plot. If a wing is absolutely rigid, then the plot would look like (a), a straight line at $y=0$. Wing compliance is then reflected in the shape of the phase loops: different wing structure would have their unique loop shape in both air and vacuum. These phase loops explain the aeroelastic interaction, as well as serving as a signature for structural characterization.

In both figures, the deformation histories of a heavy flexible wing and a light one are compared. These wings are actuated under similar single degree-of-freedom flapping motion, with different stroke amplitude. The heavy wing is actually the Wing 1 BP presented above, at 7.5 Hz. The light one, which is selected from the following chapter 4, has a similar skeleton but uses a different membrane material. It is actuated at a much higher frequency, 25 Hz. However, the passive deformation phase loops, although caused by kinematics, does not require kinematic information. If wings of different wing structures are actuated with exactly the same motion, then each of their deformation pattern can be used to identify and explain their behavior.

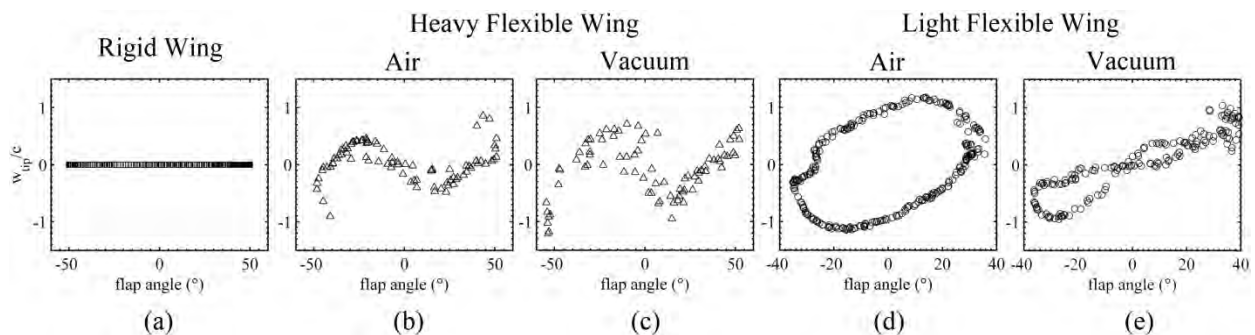


Figure 3-7. Deformation phase plot examples showing different bending pattern.

For example, here (b) and (c) have similar maximum deformation magnitude, but located at different wing position. In air (b), the maximum tip deflection occurs at the end of each stroke, due to maximum out-of-plane inertial loading. In vacuum (c), the maximum tip deflection in vacuum occurs at two locations where the structure is bent by energy conversion. Combining the two, it can be seen that the aerodynamic effect is overwhelmed by the structure elastic vibration: the aerodynamics can only damp the structure deformation pattern, reducing high frequency vibration; but the passive deformation pattern is mainly dictated by the structure inertia and elasticity. A completely different case is presented in (d) and (e). As the membrane to structure weight ratio changes, the wing can be driven to higher frequency, changing the weight between aerodynamic and inertial effects. In vacuum (e), the wing has a different elastic recovering pattern because the membrane weight has been reduced. The maximum tip deflection in vacuum is also smaller than that in air (d). This is because the deformation in (d) has a beneficial combinative effect of both aerodynamic and inertial loading. The area created in the phase loop, comparing (d) to (e), shows how significant the aerodynamic loading is.

The passive wing twist can be used to perform complicated insect-inspired kinematics while using simple actuation kinematics at the wing joint. Figure 3-8 shows the wing twist pattern of the same cases described above. In the heavy flexible wing (Wing 1 BP) case, the high frequency vibration is now more visible in (c) where the heavy membrane vibrates without air damping. The global trend, however, is still maintained. In air (b), the wing twist caused by aerodynamic effect is accentuated in the flapping angle range of (-40, -20) and (25, 30). Again, the structural elasticity dictates

the deformation pattern due to insignificant aerodynamic loads. In the light flexible wing case, similar to the tip deflection, the passive wing twist in air (d) shows enormous aerodynamic effect, reaching a passive twist angle near 40 degrees. Such large passive wing twist also sustains through more than half of the stroke: during downstroke (top left of d) from -35° to 0° (the mid-plane) and during upstroke (bottom right of d) from 35° to 0° . In the vacuum (e), the pattern can also be explained with energy conversion. But the most important point would be at the mid-plane, the wing twist is 0 in the absence of air.

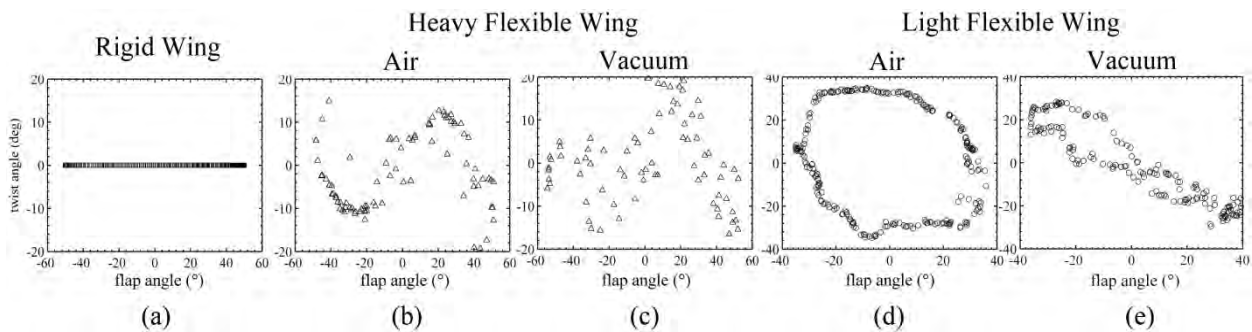


Figure 3-8. Deformation phase plot examples showing different twisting pattern.

The discussion above shows how the use of parameterization enables examination of the complete history of passive deformation. Further exploration using this method is presented in the following sections. All data in the following two sections are analyzed by assuming that the flapping angle ϕ is a sinusoidal function of time within each cycle. This allows for a more intuitive understanding of the cyclic structural response.

Effect of flapping frequency

The wing tip deflection of wing 1, normalized by the root chord, is given in Figure 3-9, for four different flapping frequencies (3.75 to 7.5 Hz, in 1.25 Hz intervals). Data is given for flapping in air, and in vacuum. Similar data is given in Figure 3-, for the angle of twist of the flexible wing section at $2y/b = 0.75$. It should first be noted that the wing-

tip deformations are very large and nonlinear, the same order of magnitude as the chord of the wing.

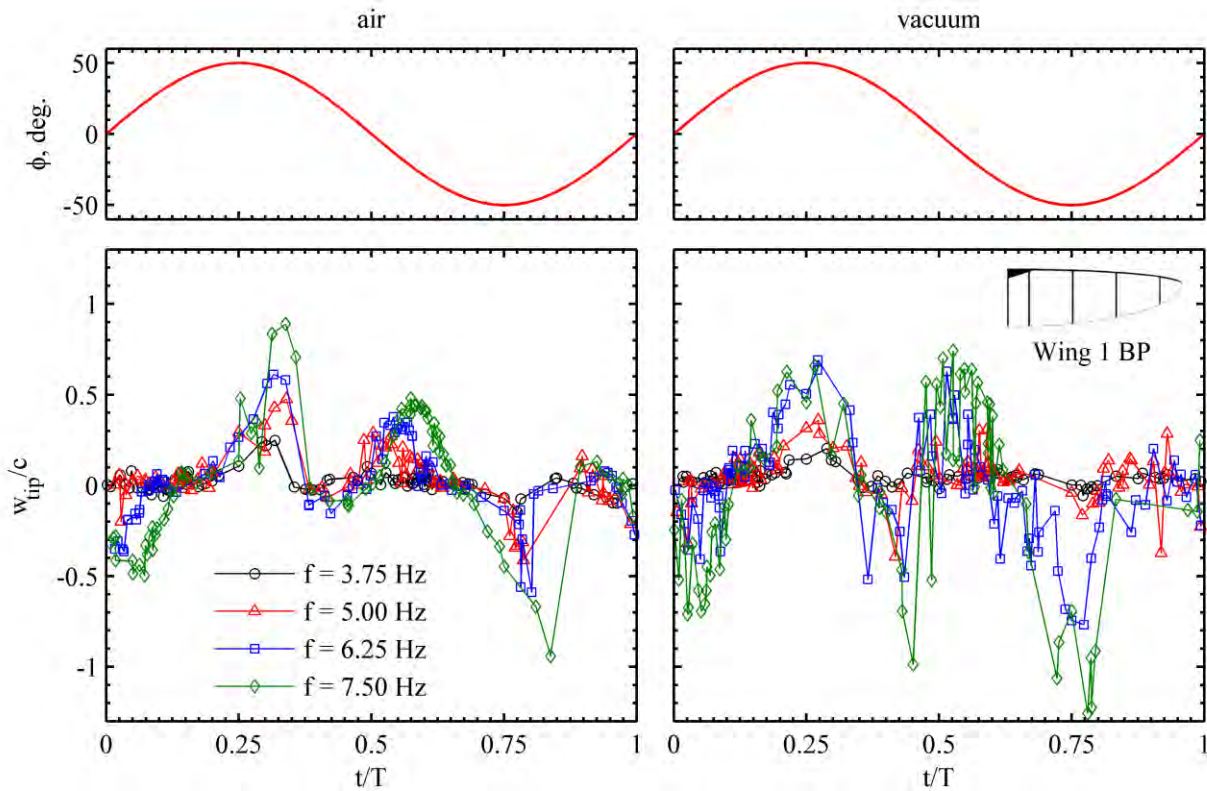


Figure 3-9. Chord-normalized wing-tip deflection of Wing 1 BP.

For the data in air, the tip deflection generally peaks slightly aft of the top and bottom of the flapping stroke ($t/T = 0.25, 0.75$). As the base of the wing reverses direction, the tip of the wing snaps to a peak displacement. Such a deformation should be increased when testing in vacuum, but such behavior is only seen on the downstroke. The data garnered from the vacuum tests are substantially noisier than seen in air, an indicative of a high frequency content, as shown in Figure 3-5. However, details cannot be obtained with the current facilities, unless high speed cameras are available. The asymmetries in the vacuum profile may result from wing/mechanism manufacturing errors, exacerbated without the damping effect of the air. Referring again to the data

from flapping in air, a second peak in tip deflection is seen slightly aft of the mid-plane, as the wing velocity is highest at this point. As expected, increased flapping frequencies generally increase the deformation, but the overall behavior throughout the flapping stroke is unchanged.

Similar behavior can be seen for the angle of twist data (Figure 3-10) which are, as before, very large: 30° to 40° . Four peaks can be seen in the data set: as the wing crosses the mid-plane during the downstroke, the flexible trailing edge washes out to decrease the angle of attack. The opposite is true during the upstroke.

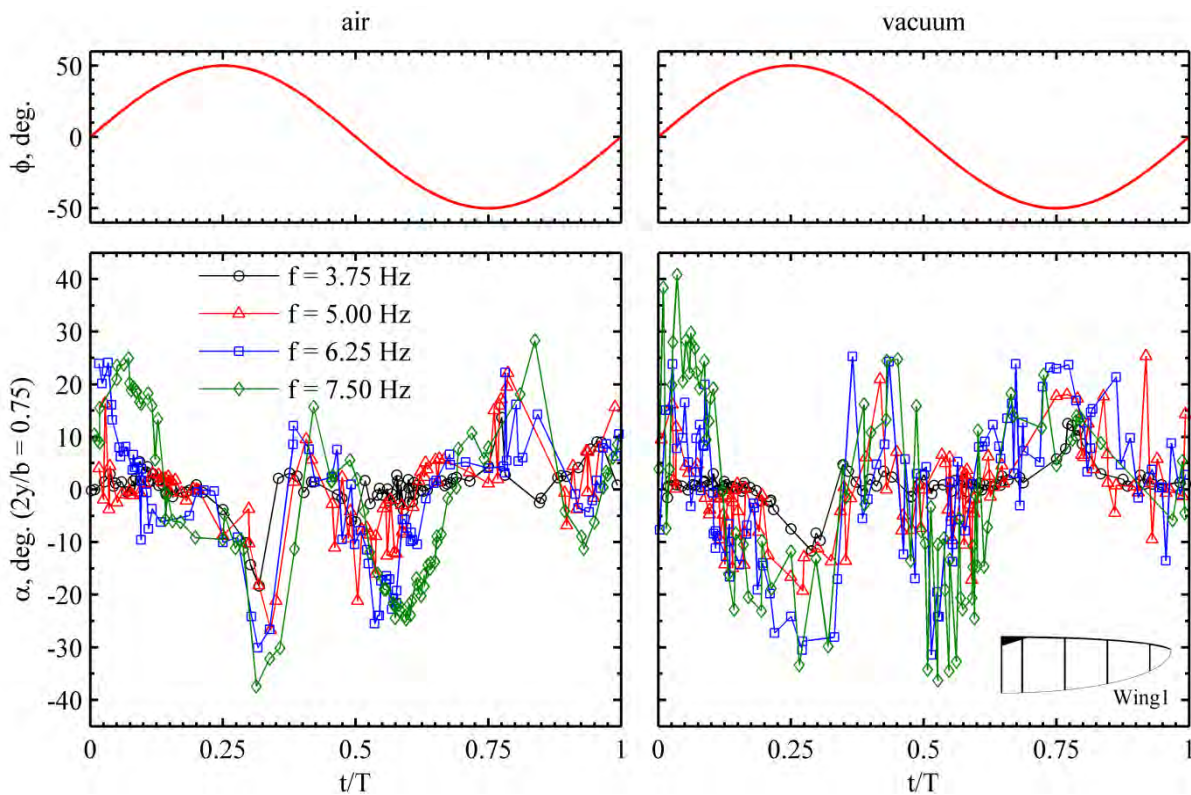


Figure 3-10. Passive wing twist at $2y/b = 0.75$, Wing 1BP.

Both of these behaviors are thought to contribute to time-averaged thrust. This figure also indicates that the large tip-deformations aft of the top and bottom of the flapping stroke in Figure 3-9 are accompanied by a very large dynamic wing twisting as

well: this bend-twist coupling will further increase the thrust. As before, the results from the vacuum tests are very noisy and asymmetric, but do follow similar trends to the data from air, with larger magnitudes.

Effect of wing structure

The wing tip deflection of all wings 1 (BP), 2 (Hum), and 3 (LEO), normalized by the root chord, are given in Figure 3-11, for a single flapping frequency (5 Hz). As before, data is given for flapping in air, and in vacuum.

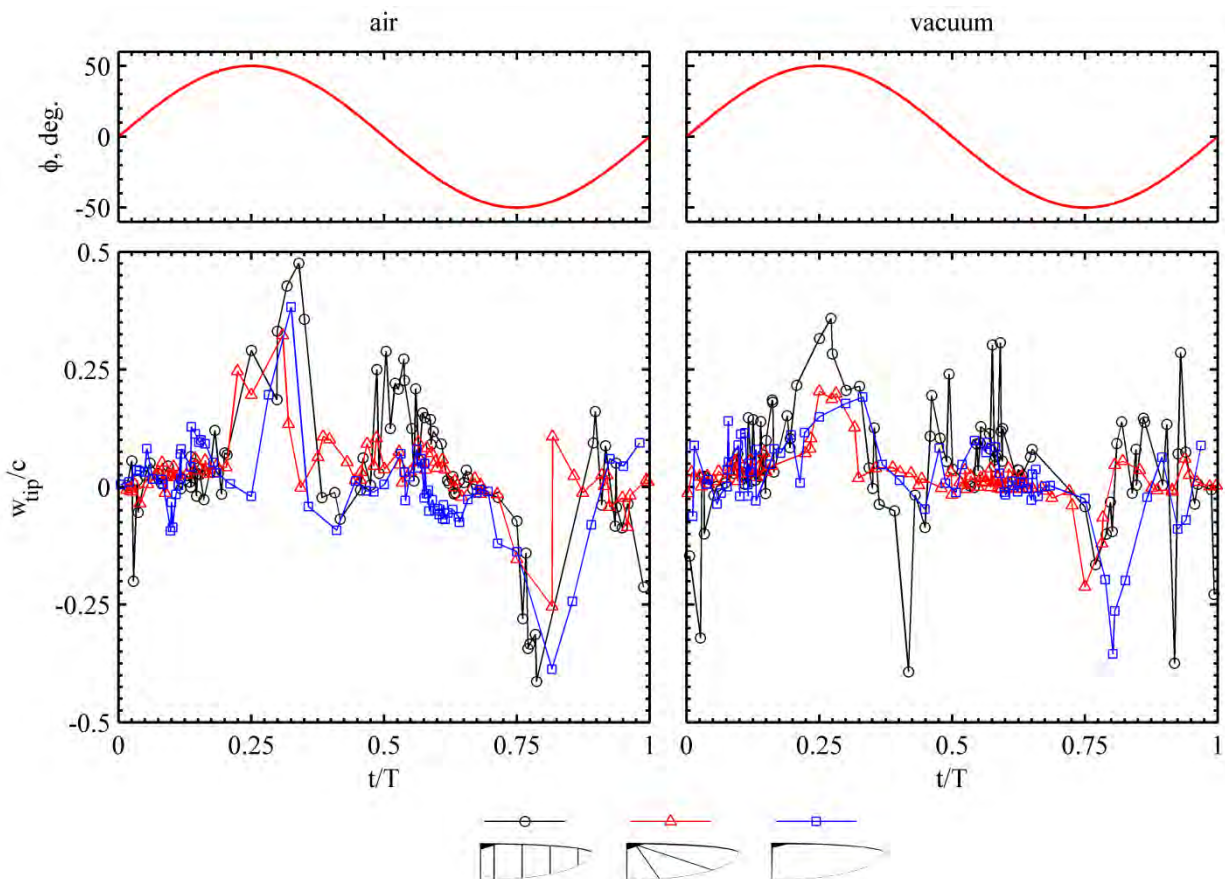


Figure 3-11. Chord-normalized wing-tip deflection of various structure, $f = 5$ Hz.

In air, all three wing structures show a peak tip deflection at the top and bottom of the flapping strokes, but only wing 1 shows appreciable tip deflection as the wing crosses the mid-plane during the downstroke. This is probably due to both mass and

stiffness factors: the chordwise battens provide little spanwise stiffness (compared to the diagonal batten of wing 2), but do increase the mass towards the wing tip (compared to the batten-less design of wing 3). These effects also provide wing 1 with the highest tip deflections at the top and bottom of the flapping stroke, though the difference is not as large.

Similar data is given in Figure 3-12 for the angle of attack and maximum camber (chord-normalized) at 75% of the semi-span. In air, the increased chordwise stiffness of wing 1 generally decreases the feathering of the trailing edge, compared to wings 2 and 3 (upper left). This is particularly evident just after the wing crosses the mid-plane of the upstroke ($t/T = 0.1$, where the latter wings washout by 20° , but wing 1 is largely untwisted), and as the wing begins the upstroke ($t/T = 0.8$). As before, the data from the vacuum tests has too large of a frequency content for proper explanation, an effect which seems to particularly afflict wing 3, which has a large amount of unconstrained membrane skin, prone to trailing edge flutter.

Of the three wing structures, only wing 3 shows an appreciable cambering of the membrane skin (lower part), a deformation which is generally prohibited by the batten structures. This cambering is substantial ($\sim 6\%$ to 8% in some portions of the flapping stroke), and is equally prone to both negative and positive inflations. As mentioned above, the vibrations in this wing are very high-frequency, and not easily explained within the experimental procedures used here. This section concludes with out-of-plane deformation data for the three wing structures in Figure 3-13, similar to that seen in the full-field deformation section. The results from the three wings are very similar: the inertial behavior of the membrane dominates the deformation; but they are also

essentially different: wing 2 over-constrains the deformation and the lack of batten reinforcement is very evident at the top of the downstroke for wing 3.

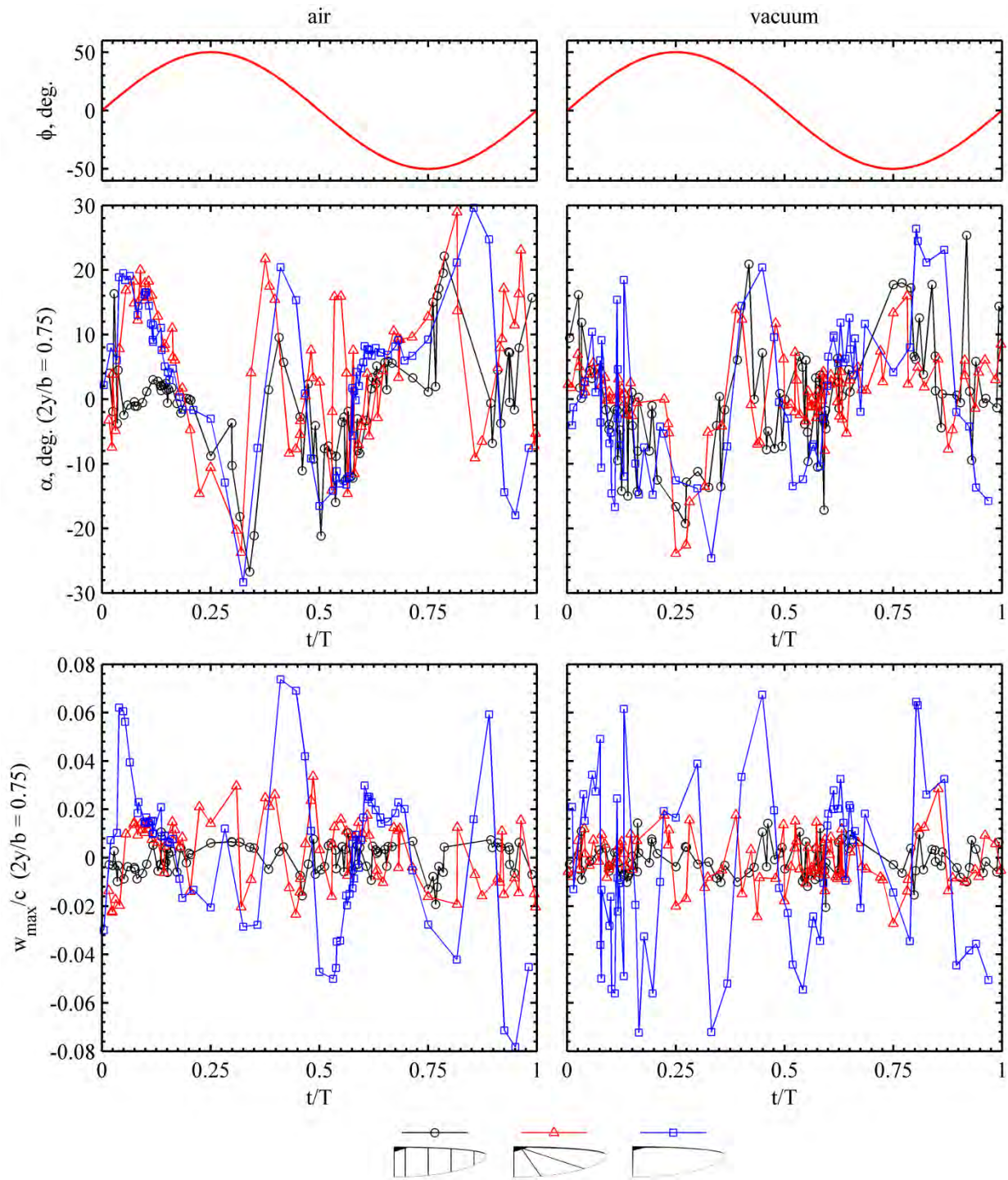


Figure 3-12. Angle of twist θ and maximum camber w_{\max} at $2y/b = 0.75$, $f = 5$ Hz.

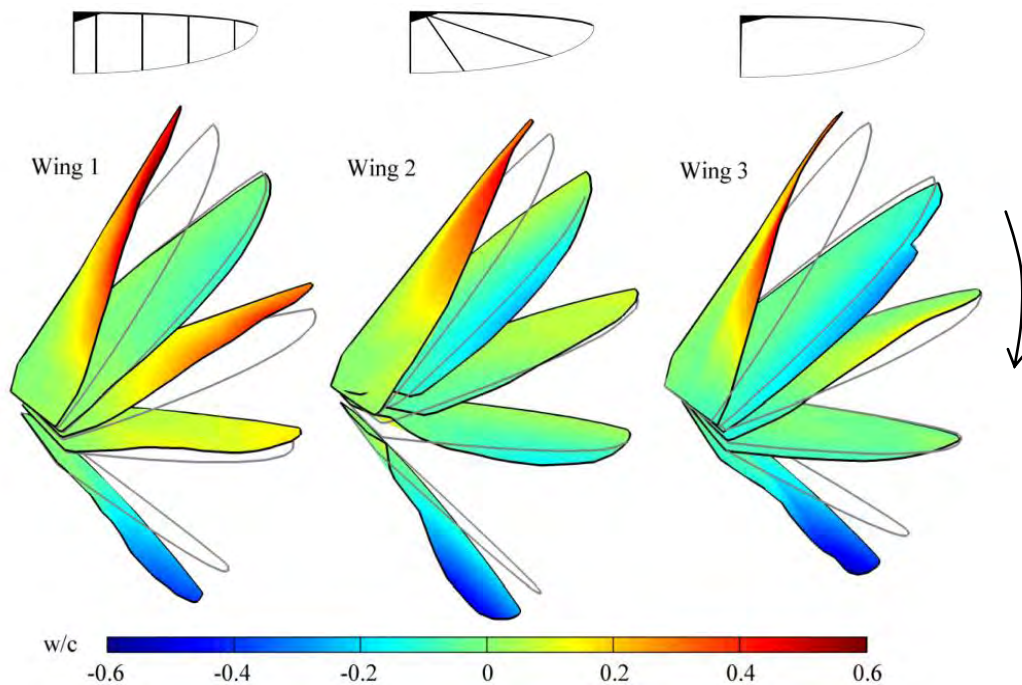


Figure 3-13. Structural deformation of different topologies, downstroke, 5 Hz, in air.

3.1.2 Inelastic Membrane Wings

The flexible membrane wings made of latex rubber has a disproportional weight ratio between the membrane material and the composite structure (2 to 1). Seen from the results presented above, the wing inertia leads to excessive deformation at frequencies above 5 Hz. This is very useful reference from a structure study point of view, but is not practical for aerodynamic studies. Because the Reynolds number at such low flapping frequency is too small comparing to that of natural flyers. A hummingbird this size (6 inch wingspan) would have flapping frequency between 20 to 40 Hz, while a smaller one (3 inch wingspan) between 30 to 80 Hz, to achieve hover. Therefore a much lighter wing of a membrane that is thinner and less density is preferred. This would allow reasonable deformation at a higher frequency range. The main problem with latex rubber is its thickness, which is required for its hyperelastic behavior. This means if a new material is used, of a much smaller thickness, an

inelastic property would be expected and preferred. The new material also needs to be able to allow DIC measurements, to which the original latex rubber is extremely user-friendly due to its diffusivity and translucence. Given the three requirements: thickness, density and diffusivity, a nylon film originally used for packaging is found. It is called Capran from Honeywell, Inc.

Tested wings

As shown in Figure 3-14, instead of 80 mm, the length of the wing is chosen to be 75 mm, so that the wingspan can be 150 mm, within the definition of the maximum dimension for MAVs. Because the focus of this research is on the structural properties, the wing is flat (no camber): the skeleton should be symmetric about the x-y plane before laminating with the membrane material. Therefore the wings are cured on a flat plate. As explained above, the wing structure is called BP. The distance between each batten is 18.75 mm, with the wing root reinforced as well.

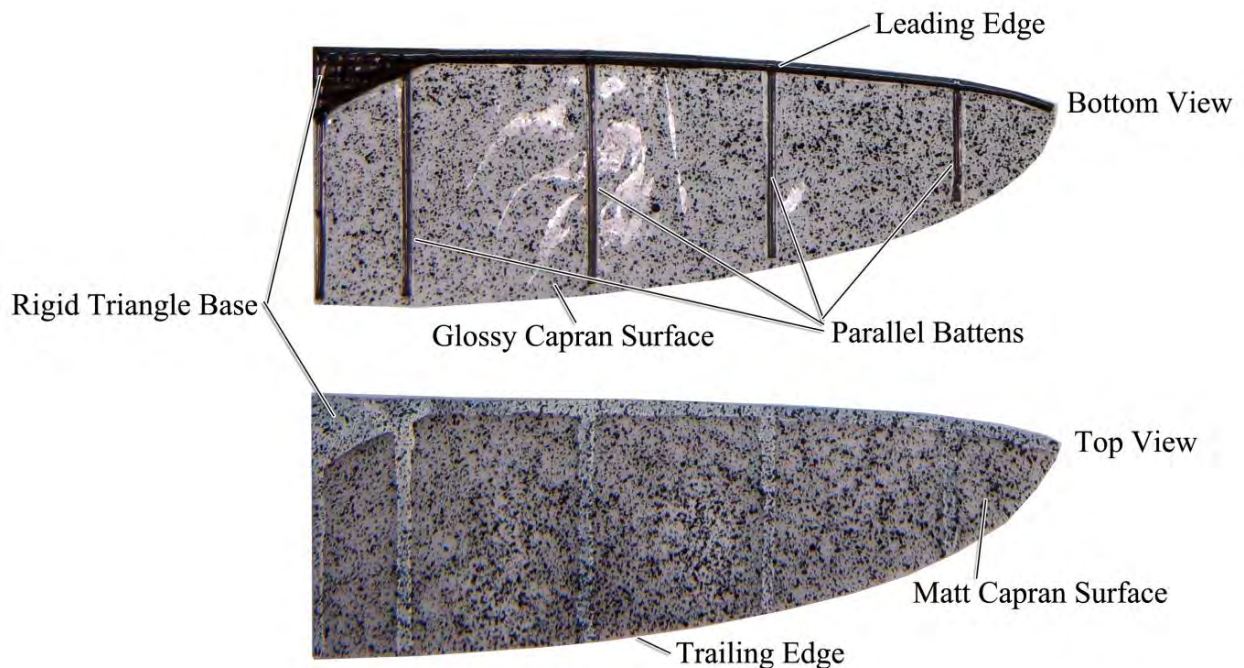


Figure 3-14. Batten parallel reinforced wing with speckled Capran® membrane.

The BP wings are made of three materials: pre-impregnated unidirectional carbon fiber, pre-impregnated 12k bidirectional carbon fiber and 12 μm thick matt Capran[®] membrane. The bidirectional carbon fiber is used to form the nominally rigid triangle at the base, where the leading edge and the root chord intersect. Three layers of 12 by 6 (weave units) triangle pieces of the carbon fiber are applied, sandwiching the unidirectional carbon fiber that forms the leading edge and the root. Cured, the triangle base is orders of magnitude stiffer than any other part of the wing. Therefore, it will serve as the reference in defining the profile of the undeformed surface in post processing; it is also the contact place mounted on FL2D3.

The leading edge, the parallel battens and the root are made of unidirectional carbon fiber. The leading edge is made of two layers of full length strips with one layer of half length strip to achieve a varying bending stiffness along the structure. Close to the root, the width of the leading edge strip is 1.2 mm, and gradually reduces to 0.8 mm at the wing tip. The gradual variation is realized by allowing the stacked fibers to flatten during the cure cycle. This gives the wing more stiffness at the root, enabling more lift in forward flight; and more flexibility at the tip, providing more thrust during flapping. The parallel battens are all one layer of 0.8 mm carbon fiber, carefully placed and sandwiched by the leading edge layers. The root is made of one layer of full length 0.8 mm strip and another half length strip.

After the carbon fiber skeleton is cured, the piece is applied with spray glue and laminated to a membrane material called Capran[®] (Honeywell's Capran Matt 1200), a biaxially oriented nylon film used in food packaging. Unlike the low elastic modulus and deteriorative latex rubber, Capran[®] is as light as Mylar[®] (density: 1.16 g/cm^3), as tough

as Tyvek[®] (tensile strength at break: 193~276 MPa) and as consistent as Kapton[®] (thermal shrinkage coefficient: 1% ~ 2% at 160° C). This thin film is available in matt surface finish, making it amenable to digital image correlation. It also has an extremely low heat shrink coefficient (<2% at 160° C), making it possible to cure the film with carbon fiber without building up excessive thermal stresses. Its high elastic modulus and tear resistant properties eliminate concerns on reinforcing the trailing edge. These characteristics make it a better choice over Mylar[®] or latex.

Random patterns of flat black speckles are painted onto the matt side of the wings for digital image correlation. As seen in Figure 3-8, the difference of matt and glossy surfaces under strobe light is significant. Since Capran[®] is translucent, flat white paint is applied to the carbon fiber structure. Given a proper background, the cameras see the surface as generally white; the slight difference in color between the battens and the membrane does not affect correlation. The final weight of each wing is 0.125 grams: the wings are overbuilt at the base triangle, or the weight could be 0.025 grams less. Comparing to the previous Wing 1 BP made with latex membrane, the Capran saves about 180 milligrams of mass. At the base triangle, the wings are adhesively fixed to the wing mount on FL2D3, with a 4 x 4 mm square overlap between the two surfaces.

Deformation measurements

The wing deformation history in one flapping cycle is well expressed by plotting wing deformation as a function of flapping angle. Figure 3-15 shows the normalized tip deflection versus flapping angle in air and in vacuum at 5 Hz, 15 Hz and 25 Hz. All values of tip deflection are normalized to the chord length: $c = 25$ mm. In the figure on the left, the data of tip deflection at 5 Hz flapping frequency is nearly coincident with the $w_{tip}/c=0$ axis; the same is observed on the right. This indicates that at such low

frequency the tip deflection is minimal. The data for 25 Hz, on the other hand, depict a substantial hysteresis loop in both air and vacuum. The arrow indicates the loop direction in the flapping cycle as the wing flaps in a sinusoidal manner. The data for 15 Hz lies in the middle of these two cases. The data points at the center of both figures are the data taken before actuation begins: they indicate the reference wing position.

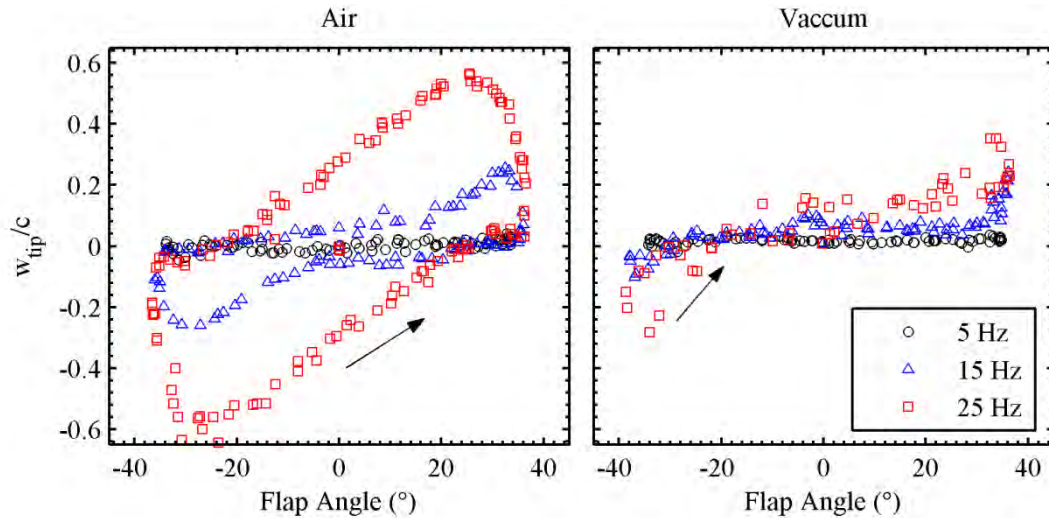


Figure 3-15. Tip deflection phase plot in air (left) and vacuum (right).

It can be seen that the maximum tip deflection at 25 Hz data in air occurs at a position after the wing moves through the end of each stroke. There is almost no deflection at the end of each stroke when the velocity direction of the wing is changing. Surprisingly, the BP wing has a nearly linear bending deformation versus flapping angle between the four extreme values: maximum/minimum tip deflection and maximum/minimum flapping angle. This rectangular shape may be a combinative result of the wing's structural properties and kinematics. Concerning the data in vacuum, an asymmetry is clearly observed. This may be the result of the aforementioned structural asymmetry caused by membrane lamination. However, the non-zero tip deflection at the mid-plane is unexpected. At this position the wing should be experiencing a maximum

velocity and minimum acceleration, indicating minimum inertial loads. With the absence of air, there should not be any deformation. However, if the wing structure is not exactly symmetrical to the x-y plane, a deformation bias may exist due to release of elastic energy after inertial tip snap. As the frequency increases, high frequency content vibration would pollute the tidiness of the data, as seen at 25 Hz in vacuum.

Similarly, the plots of twist angle at $2y/b=0.32$ and 0.8 versus flapping angle are plotted in Figure 3-16 and Figure 3-17, respectively. The data is plotted for the same three frequencies as above. The arrows indicate the cycle direction of the loops. Since both of these figures are of the angle of twist measured at different locations of the wing, it is interesting to make a side by side comparison. In Figure 3-16 the magnitude of twist angle is expectedly much smaller than that much closer to the tip (Figure 3-17). This may be because the structure is stiffer in this location ($2y/b = 0.32$) and the aerodynamic loads are also smaller (due to a lower velocity).

The loop pattern in air for both locations is very similar. When the wing is passing the mid-plane where the flap angle is zero and the velocity is maximal, the twist angle in air is significant while the data in vacuum is near zero. In air, the twist angle at $2y/b = 0.32$ demonstrates a more linear relationship with flap angle than the data at $2y/b = 0.8$. The extreme values are at very similar locations. At $2y/b = 0.8$, the twist angle also has registered significant motion at low frequency 5 Hz. The maximum twist angle occurs at a point that lags where maximum acceleration is anticipated (the end of each stroke). In vacuum, the extreme values are found at the same places as in both $2y/b = 0.32$ and 0.8 cases. Those extreme values are close to, but still not at the end of each stroke. However, the lag is much smaller due to the lack of aerodynamic effect.

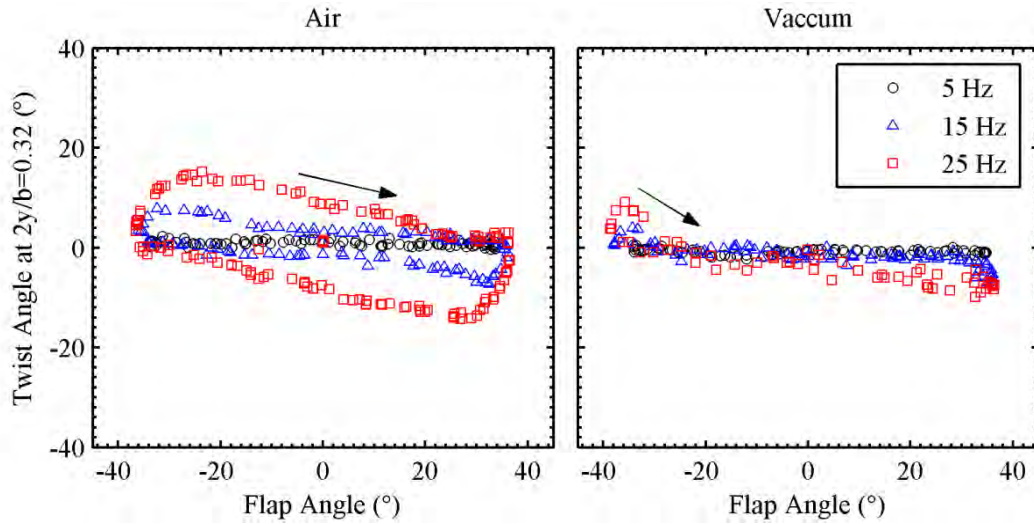


Figure 3-16. Twist angle at $2y/b = 0.32$, in air (left) and vacuum (right).

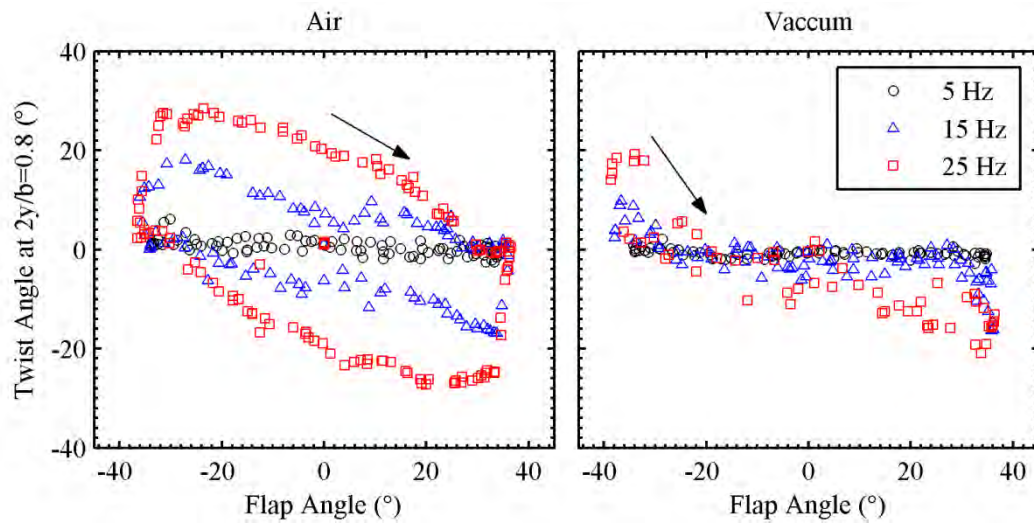


Figure 3-17. Twist angle at $2y/b = 0.8$, in air (left) and vacuum (right).

The wing deformation at 25 Hz in both air and vacuum is plotted in Figure 3-18 and Figure 3-19, respectively. Figure 3-18 has been used above to illustrate the parameterization location. As mentioned above, the DIC system is able to capture full-field information over the wing surface. Unlike the previous figures that only plot a certain variable at a certain location; these two plots describe wing deformation in a more global manner. However, only five frames are selected in each case here. A solid grey line is drawn to indicate the rigid body motion. The color contour shows the chord-

normalized out-of-plane deformation measured from the reference undeformed wing. The color bar is ranged from -0.7 to 0.7.

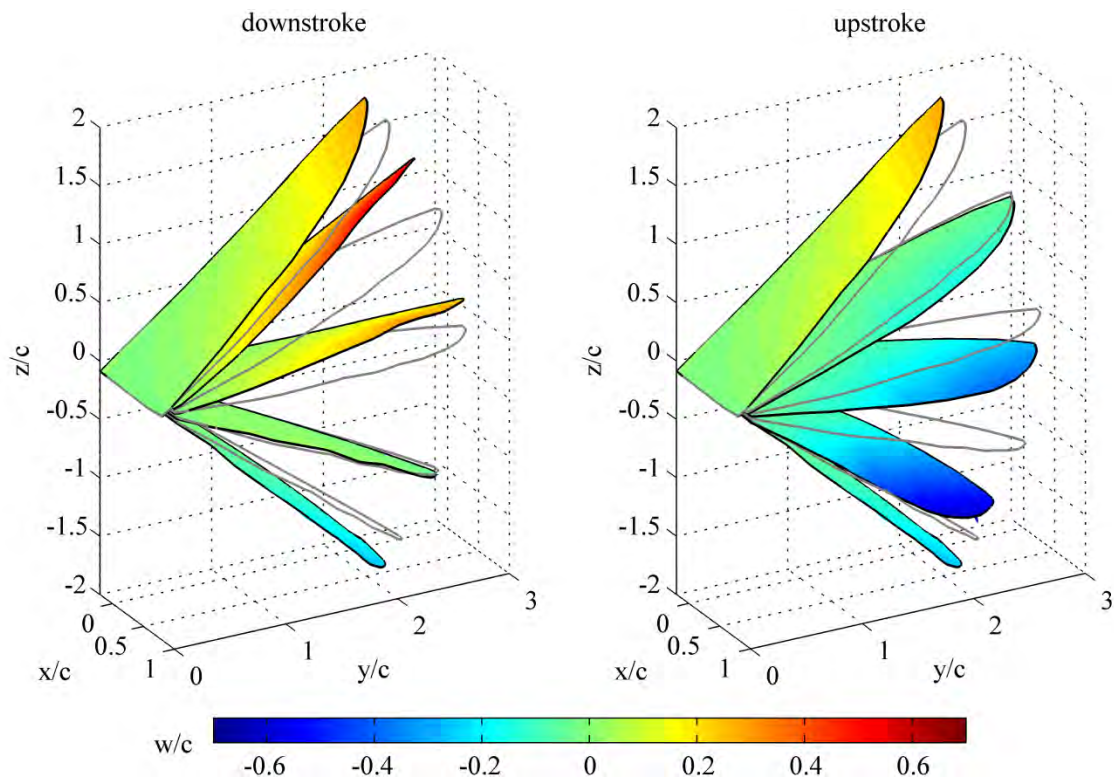


Figure 3-18. Deformation at 25 Hz in air, downstroke (left) and upstroke (right).

Both air and vacuum cases share the same deformation range in these two figures. The unified scale then enables direct deformation magnitude comparison. In both downstroke and upstroke, the same frames are selected for the two ends. In Figure 3-18, significant passive bending and twisting motion are observed in air. The wing snap at the end of each stroke is mainly due to inertial effects. The wing washout in the downstroke and washin in the upstroke can be clearly observed; this is caused by aerodynamic loads. Comparing this figure to the above figures, the tip deflection and wing twist angle correspond very well. Maximum tip deflection and twist occur at the flapping angle after the end of each stroke. Counting from top to bottom, it is the second frame in the downstroke and the fourth in the upstroke.

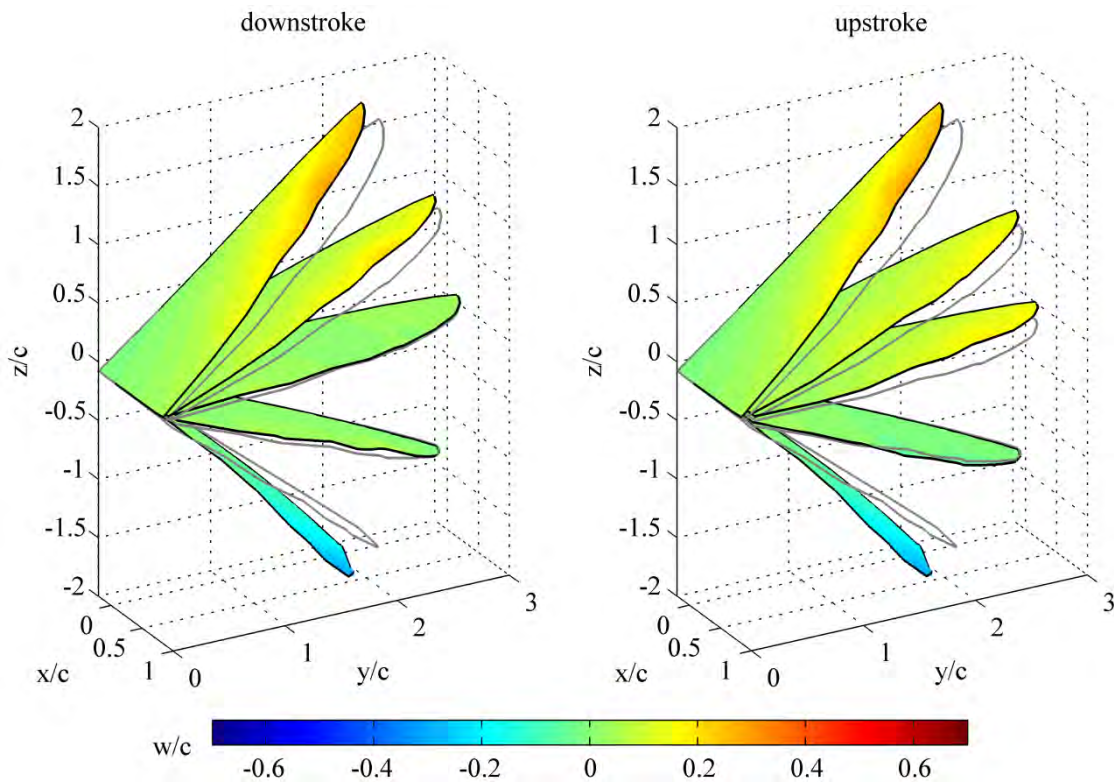


Figure 3-19. Deformation at 25 Hz in vacuum, downstroke (left) and upstroke (right).

In Figure 3-19, the absence of aerodynamic forces has taken away most of the deformation observed in the air case. In the mid-plane of both upstroke and downstroke, no washout or washin is observed. However, some high frequency content has caused the wing to show some tip deflection and twist angle, as observed in the upstroke. The snapping of wing tip due to inertia is clearly captured. Similar results have been captured in earlier sections. However, the results presented here have a better connection to each other and certain variables (such as tip deflection and angle of twist) are plotted against wing position. In the next section, the thrust measurement will also be plotted against wing position so that further investigation into the relationship between wing deformation and aerodynamic performance can be studied.

3.2 Structure Compliance

Under simple flapping actuation, a rigid wing would produce thrust in the direction perpendicular to the maximum (mid-plane) tangential velocity and in the plane of the flapping motion, such as using a manual fan in the summer (Figure 3-20). This idea has been used to produce MAVs using clapping wing motion for propulsion^[3]. To achieve performance inspired by insects or birds, the flapping wings must be able to produce thrust in the direction rotated 90 degrees from the above mentioned one, out of the plane of the flapping motion and against aerodynamic drag. This can be realized either with a sophisticated kinematics as seen in large birds, or by tailoring the wing compliance as observed in insect wings. Only the latter is considered here.



Figure 3-20. Manual fans for recreational thrust production.

In order to emphasize on thrust production using passive wing deformation, the next section examines the deformation and thrust production of a stiff wing. A control data reference is created with a similar compliant wing. The two wings are built of the same structure and similar overall weight. The objective is to prove that passive wing deformation can be used to create a kinematics beneficial to thrust production. The section after the next, then, examines the data correlation between deformation parameters and thrust production of the flexible wing shown in Figure 3-14.

3.2.1 Stiff Wing

Design and fabrication

The design and fabrication of a stiff membrane wing is a collaboration process between research groups of Prof. Peter Ifju and Prof. Tony Schmitz. Prof. Ifju chose the new topology shown in Figure 3-21. The new design uses three quarter elliptical battens to provide membrane support. Wing stiffness (both bending and torsion) is then controlled with the batten cross section, which varies linear from the wing root to the trailing edge (from 0.45 mm to 0.2 mm). A rectangular cross-section is selected for machining precision and convenience. Such shape also provides a reasonably large bending moment of inertia.

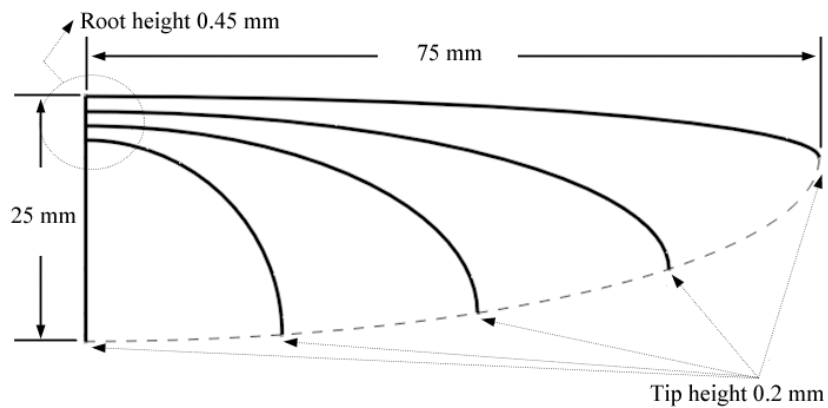


Figure 3-21. Stiff wing design.

A wing mold is then manufactured with high precision computer numerical controlled (CNC) milling machine Mikron UCP 600 Vario, using a 0.5 mm diameter two-flute square end mill, as shown in Figure 3-22. The wing skeleton will then be fabricated with a composite lay-up process similar to that of previous wings. A release coat is first applied to the mold (similar to using Teflon but allowing minimum coating thickness). Then an excessive amount of pre-impregnated unidirectional carbon fiber strips is filled into the grooves. After a vacuum-pressured and high temperature cycle, the carbon

fiber cures. The excessive amount of material protruding the wing mold is then sanded away on a flat surface. After the skeleton is taken out from the mold, it is painted and glued on the Capran membrane. For more detail pertaining the manufacturing process please refer to Xie et al.^[154].

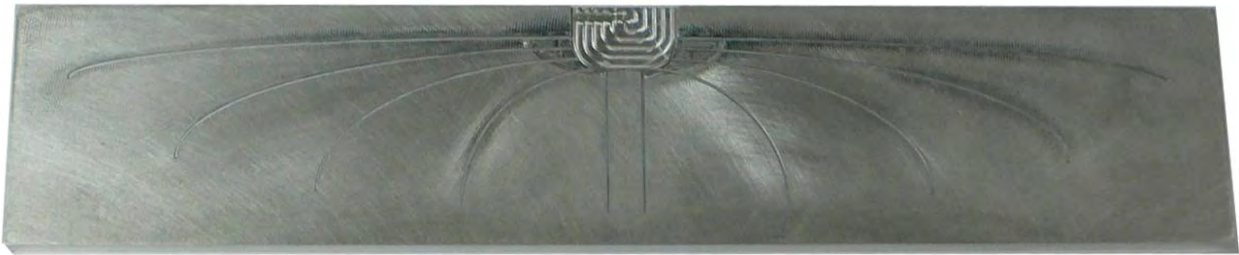


Figure 3-22. Wing mold for the stiff wing fabrication.

Another control wing is fabricated using the exact same dimension, topology and amount of materials. The manufacturing method is the same as that described in 3.1.2. These two wings are shown in Figure 3-23; they are fabricated by Lunxu Xie.



Figure 3-23. The stiff wing (right) and the control wing (left)

These two skeletons almost use the same amount of material in volume. Both the leading edge and the wing root of the control wing are reinforced with two layers of unidirectional carbon fiber strip with 0.8 mm width, all other battens are built with one layer. A single layer of unidirectional carbon fiber strip is 0.15 mm thick, so the leading edge batten of original wing can be treated as a beam which has uniform $0.8 \times 0.3 \text{ mm}^2$ rectangular cross section, and other battens have $0.8 \times 0.15 \text{ mm}^2$ uniform cross section. Therefore, the volume of all structural members of the control wing is 38.4 mm^3 . The

stiff wing has rectangular cross sections changing linearly from $0.5 \times 0.45 \text{ mm}^2$ to $0.15 \times 0.2 \text{ mm}^2$, resulting in a total volume of 39.7 mm^3 . The Capran membranes on both wings are identical. Therefore the only variable is the structure compliance.

Deformation and thrust comparison

In this section, all results are measured at flapping amplitude $\pm 35^\circ$ and at flapping frequency 20 Hz. In Figure 3-24, the structural deformation color contours during downstroke for both the control wing and the stiff wing are shown. All x, y and z dimensions are normalized to the chord length 25 mm. The grey line shows the undeformed reference rotated to the same flapping position, representing the rigid body kinematics. It can be seen that indeed the stiff wing has a much stiffer structure and experience much less wing deformation, especially if the comparison is made in the mid-plane where large washout (0.8 of 25 mm deflection) exists in the control wing. The control wing exhibit similar deformation pattern as mentioned in 3.1.2: inertial tip snaps at the end of each stroke and washout due to aerodynamic loading.

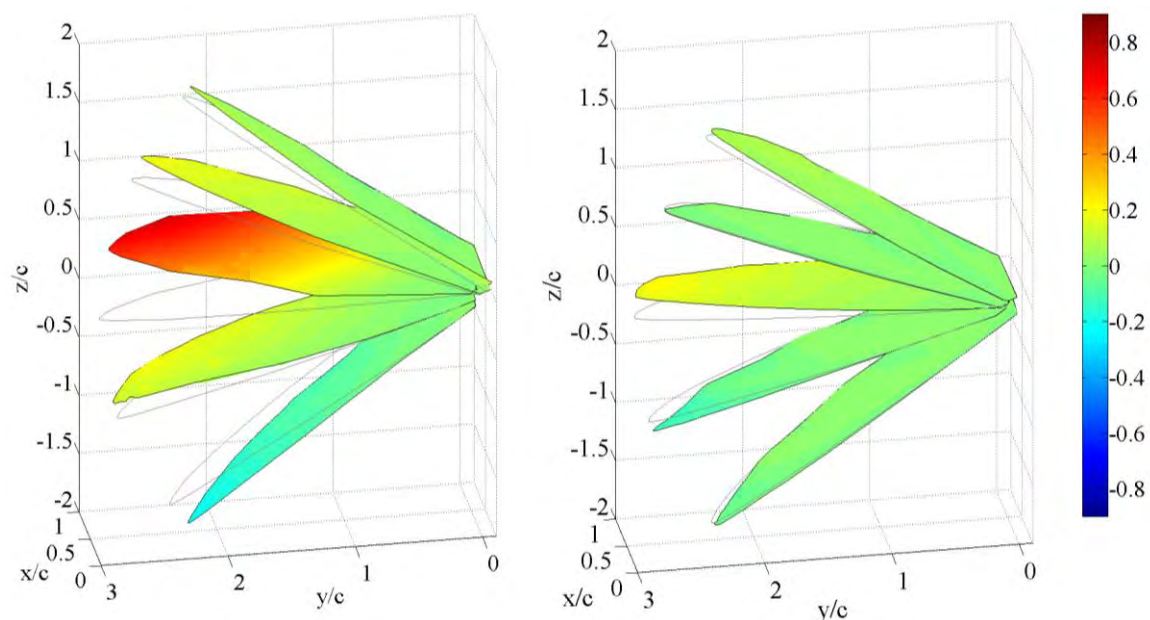


Figure 3-24. Structural deformation of the control (left) and the stiff wing (right) in air.

If parameterized data are shown, a clearer comparison can be made through out the complete cycle. Figure 3-25 shows the deformation history in one flapping cycle: normalized tip deflection on the left and wing twist rotation angle on the right. The control wing behaves similar to the previous flexible wing (Figure 3-14). The counterclockwise tip deflection loop shows that maximum wing bending occurs at $\pm 20^\circ$. The large value is resulted from the combinative effect of inertial tip snap and aerodynamic loading. Similar behavior is observed for wing bending: a clockwise loop showing inertial effect at the end of each stroke and sustained passive rotation throughout the stroke. However, the extreme values are at the mid-plane where the velocity is highest. This makes sharp contrast with the results of the stiff wing. The wing tip deflection pattern of the stiff wing is unclear. The randomness is not due to lack of aerodynamic damping, but the lose pin joints of the actuation mechanism. The wing is undergoing similar inertial loadings at the end of each stroke, but the wing stiffness suppresses the amount of deformation. Random data points show the high frequency content vibration after the input of the inertial loads.

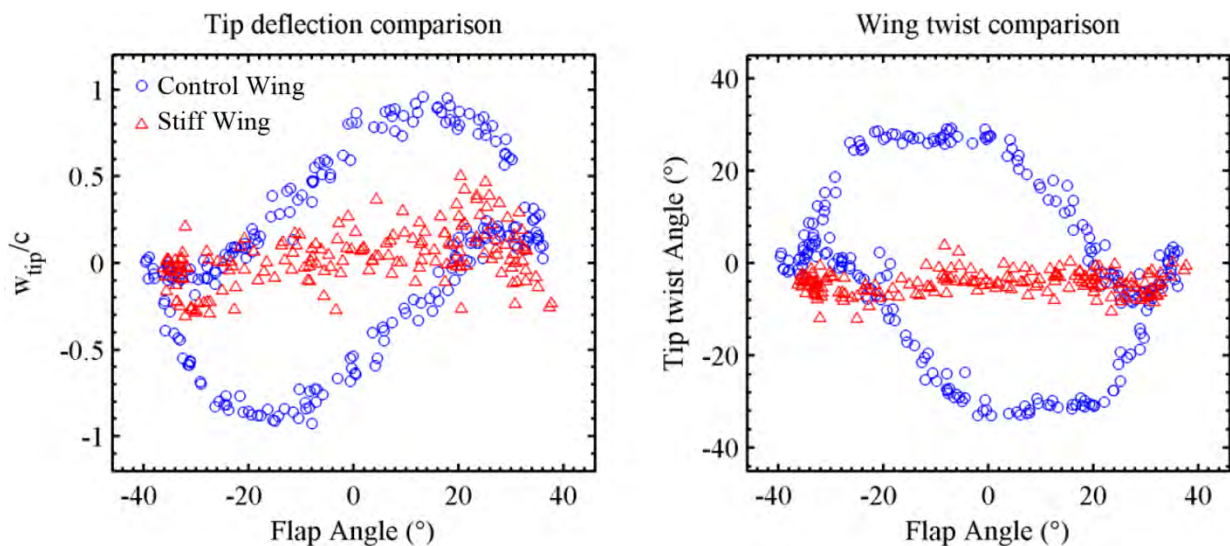


Figure 3-25. Deformation phase plot comparison for the stiff and control wing.

The passive wing twist of the stiff wing is negligible, as shown on the right of Figure 3-25. The random pattern indicates that the measurable twist deformation is merely vibrating at high frequency within $\pm 10^\circ$. Therefore it proves that the structure has enough stiffness to hold its shape profile under reasonable loading conditions. Since the data only shows the results at 20 Hz, as the frequency increases, the inertial loads would increase quadratically, significantly deforming the stiff wing.

The time-averaged thrust³ as a function of flapping frequency is now examined to understand the aerodynamic effect of passive deformation, as shown in Figure 3-26. The thrust magnitude of the control wing is apparently superior to that of the stiff wing. For the more compliant control wing, thrust increases nearly linearly from 15 Hz to 35 Hz; while the thrust produced by the stiff wing shows a quadratic trend.

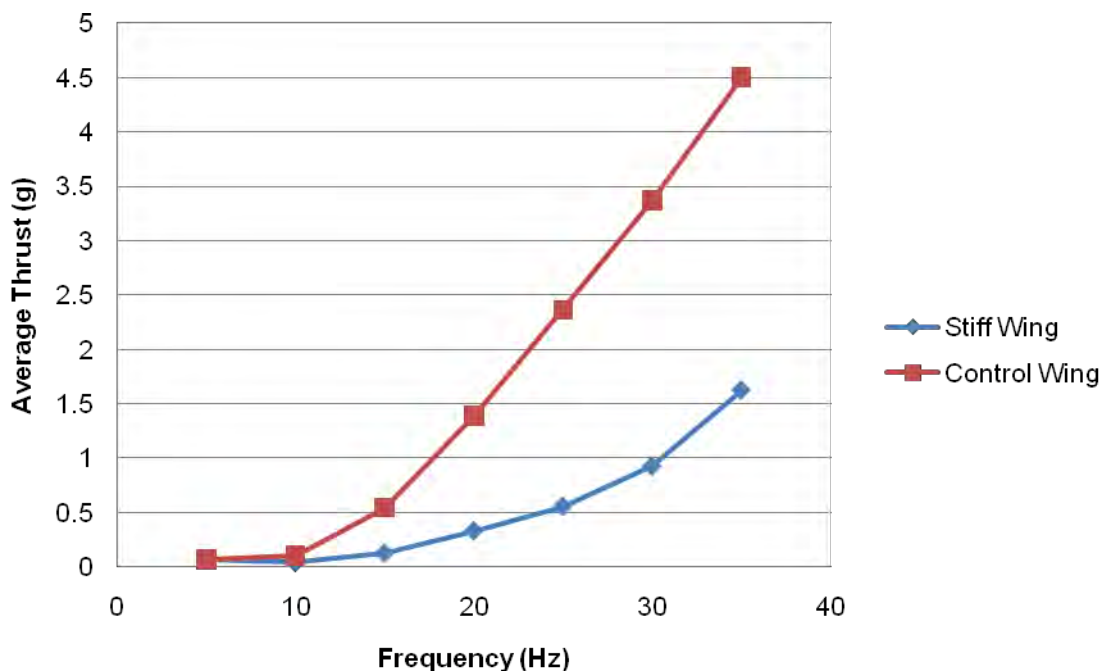


Figure 3-26. Time-averaged thrust by the stiff and control wing.

³ Detail experimental setup is explained in the next chapter.

As mentioned at the beginning of this chapter, the aerodynamic mechanism for aeroelastic coupled flapping wings must include complicated wake and vortex information, therefore the relationship between thrust and velocity is not simply quadratic. This is confirmed here with the compliant control wing. However, for the stiff wing that has no adaptive deformation (the deformation pattern is random but measurable), the aerodynamic forces produced follows agreeably with the simplified conceptual model (proportional to f^2).

Figure 3-27 shows the incremental thrust produced by these two wings. The compliant control wing allows large deformation at low frequency range (10 Hz to 20 Hz), in which the thrust increases drastically. As the membrane lamination constrains the maximum amount of deformation, the thrust increment reaches a plateau. This can be explained with a simple momentum theory: if the wing structure is constrained at a certain deformation that propels a certain amount of air, then the amount of thrust should be proportional to the total amount of air propelled, therefore to the frequency.

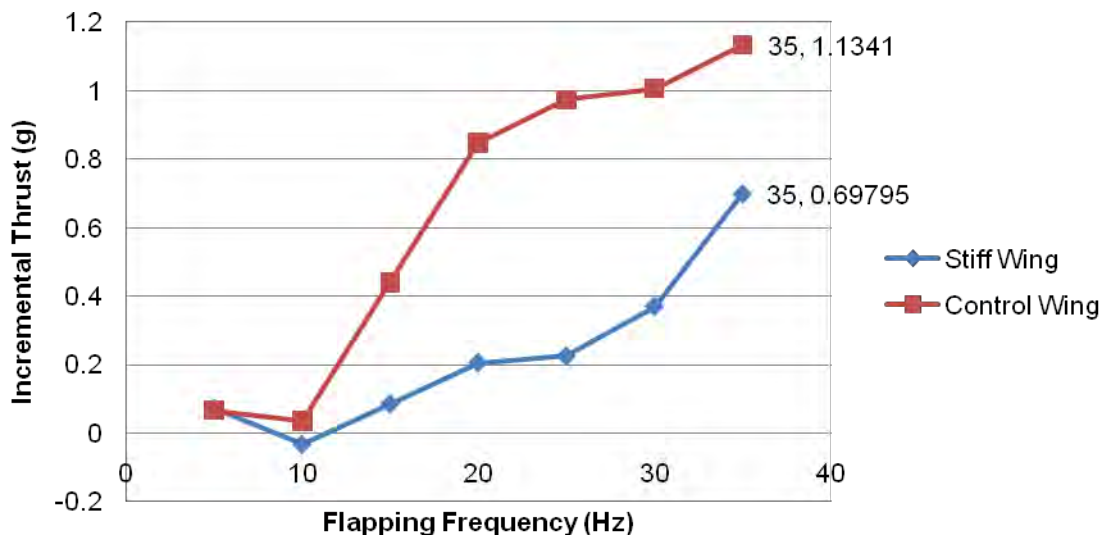


Figure 3-27. Time-averaged thrust increment

The assumption of this theory is never true, because the elastic deformation is constantly changing with kinematics and aerodynamic loading. However, there can be a range where the applicability of the air momentum theory is insensitive to the change. Moreover, the lamination of the inelastic Capran membrane does constrain the deformation (such as passive twist) to certain limit - this is further explored in Chapter 6.

The stiff wing has no significant deformation at frequencies lower than 20 Hz as explained in Figure 3-25, therefore the thrust produced is negligible. The inertial loading increases quadratically with a linear increase of the flapping frequency, therefore significant deformation occurs at high frequencies (30 Hz and above). This creates more meaningful thrust and the rate of increase of the thrust increment becomes much higher than that of the control wing.

Discussion

In this section the causal relationship between passive wing deformation and thrust is examined with a stiff wing made of a sophisticated fabrication process and a control wing similar to the previous Capran BP wing. Deformation measurements quantifies the structural properties of the wings with both color contour and phase plots. Then the time-averaged thrust is measured for comparison. The compliant control wing has superior performance to the stiff wing, because its low bending stiffness battens as well as the batten mass distributed outwards near the trailing edge induce larger passive deformation. The stiff wing may be more suitable for complicated kinematics because of its low inertia; but if a simple flapping kinematics is used, the optimal wing would require a tailored structure (compliance and mass distribution) to achieve high aerodynamic performance utilizing passive wing deformation.

3.2.2 Compliant Wing Correlation Study

Section 3.1.2 has examined the deformation of the inelastic wing (Figure 3-14). In this section, the time-averaged thrust will be measured and correlated with the deformation parameters. Figure 3-28 shows the average thrust T and the maximum tip deflection w_{tip} measured at different frequencies, in both air and vacuum. On the left, the thrust measurement in vacuum is within the noise floor of the measurement system. This is thought to be due to the fact that in the F_x direction, the structural vibration does not result in a net force register. The measurement in air starts to register at 15 Hz and grows parabolically, reaching about 5 grams of thrust at 30 Hz. This result shows that the passive wing feathering indeed generates thrust. This also indicates the range of frequency is not large enough to completely identify the wings. It is expected that a certain frequency corresponding to maximum thrust production can be found and further increase beyond that frequency would decrease thrust production as phase cancellation or wing self-destruction may occur.

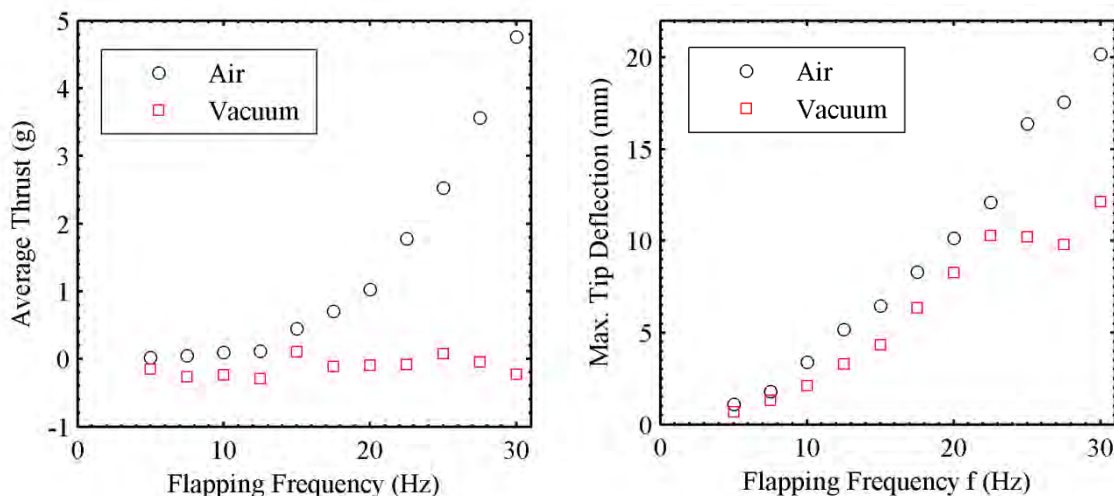


Figure 3-28. Average thrust and maximum tip deflection versus flapping frequency.

On the right, maximum tip deflection processed from DIC data is plotted against flapping frequency. In air, it shows a near linear relationship with the flapping

frequency, with none-zero origin. If the origin (static, no deflection) is considered, a parabolic relationship may also be expected. A similar trend can be observed in the vacuum case at frequencies below 22.5 Hz. It can be seen that in the absence of air, viscous damping is no longer available, providing structural vibration that might cancel out the tip deflection, potentially explaining why the maximum tip deflection drops at higher flapping frequencies. It is also possible that the deformation in vacuum at high frequencies has exceeded the measurement capability. Also, the difference between the two does not directly indicate the wing deformation caused by aerodynamic loads.

In Figure 3-29, maximum twist angle (left) and camber (right) are plotted versus flapping frequency. In air, the angle of twist at $2y/b=0.8$ displays a very linear trend versus flapping frequency. A similar trend is seen in vacuum, although two abnormal points occur at 20 and 22.5 Hz. The wing twist angles are significantly lower in vacuum than they are in air, which is expected since the twist angle in air contains contribution from both aerodynamic loads and inertial loads while in vacuum, this is only caused by inertial loads. Further details can be seen in the deformation analysis below.

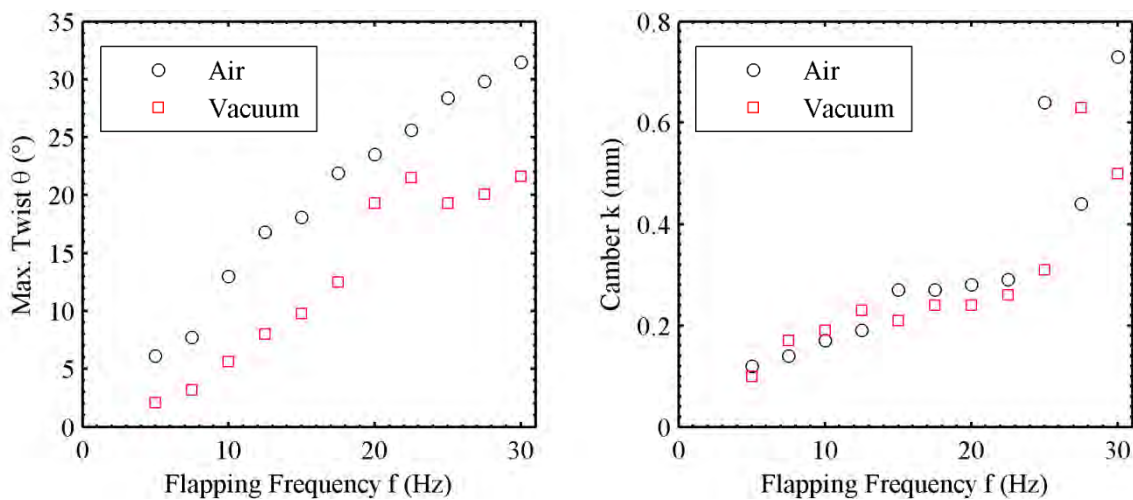


Figure 3-29. Average twisting and cambering versus flapping frequency.

The plot on the right of 3-29 shows the maximum camber plotted against flapping frequency. The camber data does not have a consistent trend across flapping frequencies. In air, the maximum camber recorded increases with flapping frequency until 25 Hz. The last three data points jump irregularly, indicating that the structure might experience some phase cancellation at 27.5 Hz or vibration resonance at 25 Hz and 30 Hz. In vacuum, a similar trend is observed at frequencies below 25 Hz. There is no apparent significant difference between the cambers measured in air and those measured in vacuum. This may be because Capran® has a very high elastic modulus (2.4 ~ 3.5 GPa), preventing appreciable elastic membrane inflation for camber formation, as documented in 3.1.1.

Table 3-2 lists three linear correlation coefficients between thrust and deformation descriptors, along with the Pearson's regression coefficients, which include two extra parabolic cases between thrust, tip deflection and twist.

Table 3-2. Correlation coefficients of loads and deformation variables.

Correlation Method	Thrust	Deformation Descriptors	ρ	R^2
Linear	T	W_{tip}	0.96	0.914
Parabolic	T	W_{tip}	N/A	0.989
Linear	T	θ	0.82	0.675
4 th order	T	θ	N/A	0.996
Linear	T	k	0.92	0.842

A better visual interpretation of the relationships between these variables is plotted in Figure 3-30. On the right, the correlation between thrust and maximum tip deflection is indeed parabolic, with $R^2 = 0.989$. However, a linear regression can also be used, as seen on the left. This is quite an interesting result because these trends correspond to each variable's behavior relative to flapping frequency as presented above.

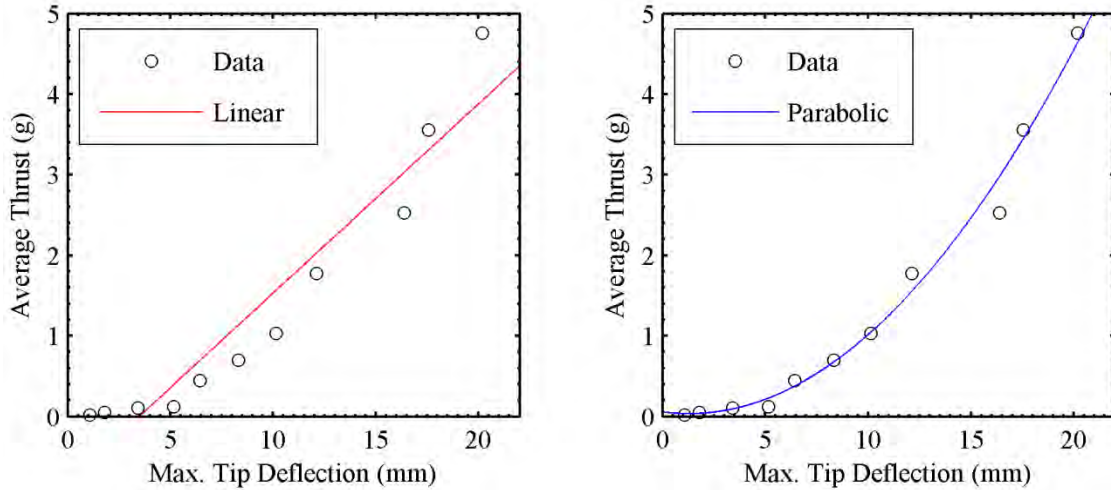


Figure 3-30. Regression of tip deflection and thrust using different functions.

Figure 3-31 shows a 4th order polynomial regression between thrust and twist. From the coefficients in Table the data has a much higher Pearson's coefficient of regression in the 4th order polynomial ($R^2 = 0.996$) than in the linear case ($R^2 = 0.675$).

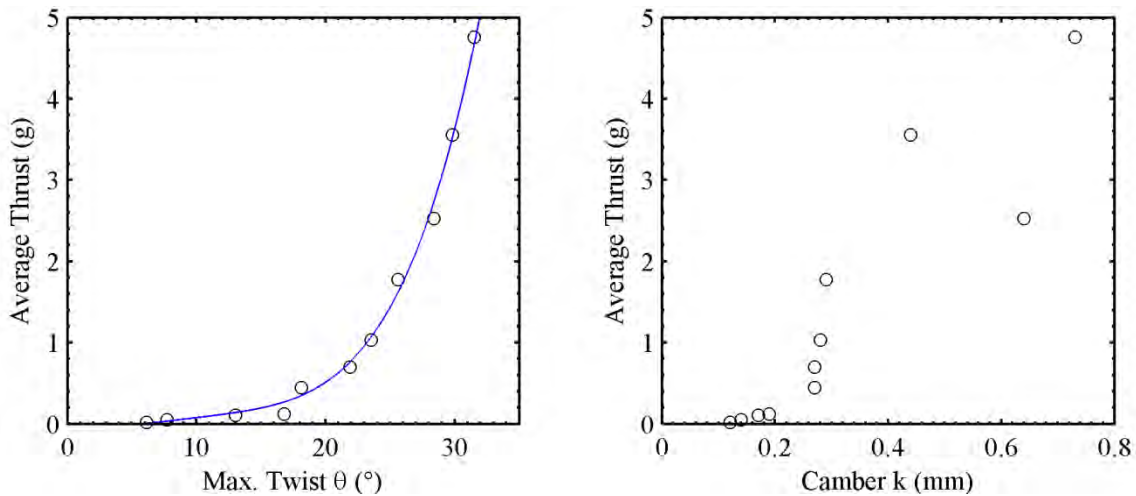


Figure 3-31. Regression of twist and thrust (left), and camber and thrust (right).

However, these relationships are only from a statistical point of view, the causal relationship cannot be assumed and must involve kinematics. However, the correlation result represents how the aerodynamic and structural dynamic effects are linked to each other. As mentioned earlier, since the Capran membrane has a very high elastic

modulus, there is no clear trend of how the wing camber behaves as a function of frequency. Though the linear correlation coefficient is high ($\rho = 0.92$), the unclear trend prevents the determination of a convincing relationship between the camber and thrust.

3.3 Discussion

This chapter is dedicated to examining the passive wing deformation and showing how it can be used to create complicated wing kinematics (output) with simple single degree-of-freedom actuation kinematics (input). It is important to separate the concepts of the two: the actuation kinematics refers only to the motion at the wing joint, where the flapping mechanism can input force and energy through; while the wing kinematics is the result of the actuation kinematics and aeroelastic interaction. The simpler the actuation kinematics, the lighter, more efficient and more reliable the flapping mechanism can be. This is the main incentive to understand the aeroelastic interaction so that better wing structures can be designed.

Flexible wings of different membrane elasticity are first compared. The hyperelastic latex membrane is too thick and heavy for flapping actuation in a reasonable frequency range. But their deformation pattern gives a good insight into inertial effect: the tip snaps at the end of each stroke are due to out-of-plane inertial loading, and the high frequency content of vibration is clearly observed in vacuum. The inelastic wing, presents similar deformation at much high frequencies. A parameterization method is used to extract the full-field deformation information into a few descriptors to represent wing bending (tip deflection w_{tip}), twisting (angle of twist at a certain span location) and billowing (maximum camber). These descriptors enable deformation phase plot to show the cyclic history of the structural response. Data

acquisition in vacuum also provides quantitative identification of inertial and aerodynamic effects.

A stiff wing is manufactured for studying aerodynamics of wing compliance. By measuring time averaged thrust and comparing the results with that of the compliant control wings, the effectiveness of the passive wing deformation in generating thrust is shown. The study concludes that 1) without passive deformation, a flapping wing of single degree-of-freedom produces little thrust; 2) the passive wing deformation can be controlled by tailoring the wing stiffness and mass distribution; and 3) the passive wing deformation can be predicted or simulated with known kinematics and structural properties. Finally a correlation study is performed over the inelastic flexible wing to find the intrinsic relationship between structural deformation and thrust. Both wing bending, represented by tip deflection, and wing twisting, represented by angle of twist at 80% span position, show statistical trends with thrust. This will be examined further in Chapter 6.

In summary, the passive wing deformation is the key to understand aeroelastic interaction, to characterize the wing structure, and to improve the flapping aerodynamic performance.

CHAPTER 4 STRUCTURAL DYNAMICS AND AERODYNAMICS MEASUREMENTS

4.1 Introduction

Flapping wing flight as seen in insects and hummingbirds poses an interesting multidisciplinary problem: coupling of wing kinematics, structural dynamics and aerodynamics. There have been numerous studies on kinematics and aerodynamics of rigid wings in both experimental and computational cases. Yet observation in nature affirms that passive wing deformation is crucial for aerodynamic performance. This chapter presents a comprehensive multidisciplinary experimental endeavor in correlating flapping micro air vehicle (MAV) wing's aeroelasticity and thrust production, by quantifying and comparing elasticity, dynamic response, deformation, and airflow of six pairs of membranous hummingbird-shaped wings of different properties. The results show that for a certain spatial distribution of flexibility, there is an effective frequency range in thrust production. Wing deformation corresponding to those frequencies indicates the importance of flexibility: both bending and twisting motion can interact with aerodynamic loads to enhance wing performance under certain conditions. The effort in this chapter overcomes many challenging aspects: measuring small magnitudes of aerodynamic and inertial forces, describing wing aeroelasticity through different techniques, obtaining rapid motion measurements from flexible membrane wing materials and post-processing the data for correlation. Major experimental techniques include: digital image correlation, particle image velocimetry and laser Doppler vibrometry. The result is the first of its kind: full-field flapping wing deformation and airflow data combined together; this not only explains the needed structural properties for a thrust effective flapping wing, but has also demonstrated how the current

experimental techniques can be used in flapping wing studies and suggest a guideline for future flapping MAV wing design.

The structural properties of insect wings have long been studied by biologists [124, 125, and 128] to understand the roles of flexibility in producing unsteady aerodynamic forces that enable flapping flight. Indeed, since insects can only actuate the wings at the wing joint, the anisotropic flexibility of the wings may be the key to the fantastic agility, efficiency, and stability routinely demonstrated by these flyers. Hummingbirds, because of their specialized wing skeleton, fly in a manner similar to insects', which has no muscular control for active shape morphing of their wings [127], rather than larger birds'. Recent research interest in micro air vehicles (MAVs) has focused on MAV development utilizing flapping flight. The advantage of a flapping wing MAV lies in its maneuverability – smooth transition from hovering to forward flight and low noise flight signature, as compared to the same scale fixed or rotary wing aircrafts.

One of the main issues in designing a flapping wing MAV is defining the wing's aeroelastic properties, which in combination with the prescribed actuated kinematics determine the lift and thrust production that eventually dictate flight performance. Aeroelasticity is an interdisciplinary study of aerodynamics, dynamics and elasticity. Therefore the term includes a wing's structural properties (elasticity and dynamic responses), dynamics (kinematics and flight mechanics) and aerodynamics around the wing. In most fixed wing aircraft, investigations of wing aeroelasticity tends to avoid or reduce unstable vibration/flutter, or improve flight performance via structural tailoring. Experimental characterization and computational optimization have been done for flexible membranous wings for fixed wing MAVs^[2]; the study has provided a design

direction for MAV wings with more stability and controllable mission-based lift and drag coefficients. Similarly, in flapping wing aircraft, the ideal situation is to tailor a wing's aeroelastic properties to enhance lift and thrust production. However, present computational models on this topic are still in a formative stage, requiring intensive experimental validation. Numerical optimization may be performed in the near future once the computational platform is well developed. Prior to this, the relationship between the aeroelastic properties of flapping wings and aerodynamic force production needs to be experimentally identified.

In natural wing structure studies, the wing flexibility in insects (Combes and Daniel, 2003^[119]) is found to follow a particular trend: the spanwise flexural stiffness is 1~2 orders of magnitude higher than the chordwise flexural stiffness. A substantial amount of passive wing deformation has been observed in insect flight, where the wing flexibility is thought to yield mean advective flows with substantially greater magnitudes and orientations more beneficial to lift than those of stiff wings (Mountcastle and Daniel, 2009^[155]). These observations provide a natural impetus for the design of artificial aircraft with flexible flapping wings via benevolent aeroelasticity. In artificial wing structure research, flapping membrane wing structures with and without batten reinforcement at the trailing edge of the wing tip have also been studied as a function of advance ratio (Ho et al., 2003^[17]). For large values of this metric, the lift capabilities of the two wings are identical, but as the unsteady features of the flow are enhanced (low advance ratio), the wing without this reinforcement is inferior. The authors stated that the excessive feathering of the wing disrupts the leading edge vortex, and the concomitant lift. Thrust, however, relies heavily upon wing flexibility for its development,

and so an adequate compromise must be found. This concept for a membrane wing with an unconstrained trailing edge, whose feathering motion develops significantly more thrust force than one reinforced all along its perimeter, has been experimentally demonstrated (Singh and Chopra, 2008^[155]).

Aeroelasticity is an interdisciplinary study of aerodynamics, dynamics and elasticity (Bisplinghoff et al. 1955^[156]): including a wing's structural properties (elasticity and dynamic responses), dynamics (kinematics and flight mechanics) and aerodynamics around the wing. It has been observed in both nature and experiments that flapping wing elasticity/flexibility is crucial to flapping flight. Fresh hawkmoth (*Manduca sexta*) wings have been compared^[157] with dry wings (laminated with spray paint to recover the weight loss) and found that the more compliant fresh wing has much superior aerodynamic performance with airflow visualized via particle image velocimetry (PIV). Dynamic response is another important aspect: it is a direct benchmark for both the wing inertia (mass) and stiffness (inverted flexibility). This aspect has been studied by measuring the wing deformation caused by inertial loading and aerodynamic loading (Combes and Daniel, 2003^[121]); the results show that a hawkmoth's wing deformation at 26 Hz is mainly caused by inertial loads, as the experiments conducted in air and in helium (approx. 15% air density) produce similar deformation pattern, suggesting aerodynamic forces have minimal effect. This may indicate that the passive deformation caused by inertia is utilized to affect aerodynamics. However, as pointed out by the authors, the result may be species specific and many contradictory conclusions have been reported (Sun and Tang, 2002^[122]; Wakeling and

Ellington, 1997^[24]). Nevertheless, the physics behind flapping flight is a coupled problem: kinematics, structural dynamics and aerodynamics all strongly interact with each other.

Knowing the key factors in flapping wing aeroelasticity, modern methods can be applied to measure the kinematics and structural dynamics (deformation). Preliminary research details the use of high speed film videography to capture the wing kinematics of different insects (Ellington, 1984^[9]). After digital imaging becomes common, similar method is still used to measure static compliance (Mountcastle and Daniel, 2009^[157]) and kinematics (Combes and Daniel, 2003^[121]), with improved post processing capabilities for data extraction. Additional studies based upon point-wise techniques include the kinematics measurements of Raney and Slominski^[117], who place small light-emitting diode devices at the wing tip, and capture the entire wingtip trail in a single image. For deformation measurements, Tian et al.^[158] utilize similar multiple reflective markers over a bat wing, and stereo high-speed cameras to quantify the motion.

A more full-field strategy involves the use of a fringe shadow method to measure the flapping and torsional angle of a dragonfly wing (Zeng et al. 1996^[159]). Similar fringe-based methods have also been used along with sign points placed on the wing, to measure deformation of a free-flight dragonfly (Wang et al. 2002^[160]). Cheng et al.^[161] extend this technique with a windowed Fourier transform to process the fringe patterns and extract phase. Recently, digital image correlation has been applied to the flapping wings to obtain full-field and high resolution measurements of a complete flapping stroke, capturing both kinematics and deformation (Wu et al. 2008^[137]). Due to its full-field nature, high temporal and spatial resolution, and ease of use, digital image correlation has been identified as a superior deformation measurement method in a

wide variety of engineering disciplines (Orteu, 2009^[162]); these advantages are thought to translate to flapping wing research as well.

Similarly, a large amount of work has been conducted on the flow visualization of flapping wing flyers (Ho et al. 2003^[17]; Tarascio et al. 2005^[163]; de Clercq et al. 2009^[164]; Fuchiwaki, 2009^[165]; among many others). However, a great deal of this literature results from scaled models in oil or water chambers: flow visualizing over an insect-sized flapping wing is not commonplace, and cases where the elastic characteristics of the flapping wings produce substantial structural deformations (and, implicitly, benevolent aerodynamics) throughout the actuation stroke are very rare.

In this chapter, six pairs of carbon fiber battened wings laminated with a thin membrane (Capran®) are used. A flapping mechanism, designed to perform simple kinematics, actuates these wings at various frequencies. To experimentally identify the aeroelastic properties of the tested wings, several techniques are employed. Stereo digital particle image velocimetry (SDPIV) is used to visualize the averaged airflow structure around the flapping wings. A customized digital image correlation (DIC) system is used to record the kinematics and full-field local deformation of the flapping wings. DIC experiments are carried out in both static air and a vacuum chamber, which can help to separate the inertial and aerodynamic contributions to the wing deformation, both of which will depict the coupled phenomena of wing aeroelasticity. Laser Doppler vibrometry (LDV) is applied to measure the dynamic responses (mode shapes) of the wings. Two pairs of the wings are purposely constructed with low natural frequencies; flapping tests reveals the wings performance at different bending and twisting modes: this is captured with SDPIV and DIC as well. Furthermore, the thrust is monitored and

recorded with a force and torque sensor mounted to the flapping mechanism. Data of all these experiments are correlated to examine the effect of structural properties on wing performance and behavior. Figure 4-1 shows the experiment flow chart of this study.

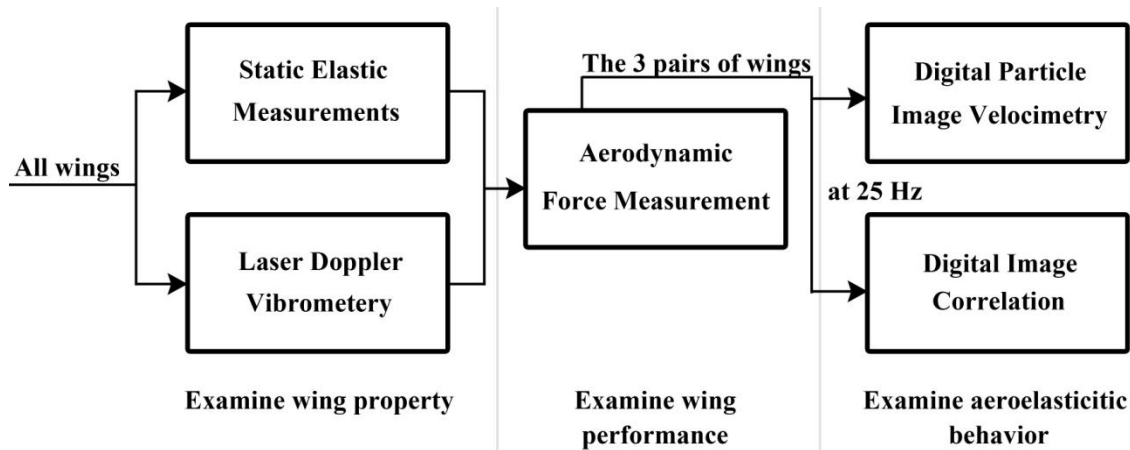


Figure 4-1. Flow chart of experiments.

4.2 Materials and Methods

4.2.1 Tested Wings

The wings tested are again of a Zimmerman planform, formed by two ellipses which intersect at the quarter-chord point. The wings are constructed to have comparable features with real hummingbird wings (Altshuler et al., 2004^[44]), with an aspect ratio of 7.65, a 75 mm wing length and a 25 mm root chord, as shown in Figure 4-2 a). For this work, the wing design is two dimensional: no camber or airfoil profile is applied. Wings are constructed with unidirectional carbon fiber to form the skeleton and Capran® as the membrane. All six pairs of the tested wings are made of exactly the same topological layout: reinforced leading edge, wing root and battens that are parallel to the x-axis. There is no trailing edge reinforcement. At the intersection between the leading edge and wing root, there is a triangle base made of three layers of bidirectional carbon fiber that serves as a stiff reference for wing mounting and deformation

calculation. The layup scheme is presented in Figure 4-2 b): the lines represent the number of layers for layup – leading edge varies from 3 to 1 layers of unidirectional carbon fiber and battens vary from 1 to 2 layers. The wing root is always reinforced with 2 layers. Therefore the wings are named L(#)B(#) with L standing for “Leading edge”, B for “Batten” and # for the number of reinforcement layers. Therefore the wings L3B1, L2B1 and L1B1 have different bending stiffness because of the different reinforcement layers. So do L3B2, L2B2 and L1B2; but the latter three wings also have higher torsional stiffness due to the additional reinforcement in the battens. The weight of each wing is listed in the left column.

The wing manufacturing process includes four major steps: wing mold preparation, composite material layup, pre-skinning preparation and membrane lamination. The wing mold in this stage is a stiff flat plate with a skeleton pattern printed on, covered with Teflon film for easy release. This is followed by placing the pre-impregnated carbon fiber material on top. At first the aforementioned triangle base (1 layer, 12K bidirectional weave) is placed at the crossing of the leading edge and the root. Then unidirectional carbon fiber strips of 0.8 mm width are placed to form the leading edge, the root and the battens. This forms an order of placing: the triangle, the leading edge, the root and the battens. Each time only one layer of material is placed, resulting in a sandwiched structure. For example: L3B2 would have leading edges and battens in between each other and L3B1 would have the battens in between the first two layers of leading edge strips. This prevents delamination in loaded conditions. After layup, another Teflon film is placed to cover the plate, and a sealed bag is made to apply vacuum pressure (< -

762 mm Hg). The temperature is then elevated to complete the curing cycle (127 °C, 3 hours).

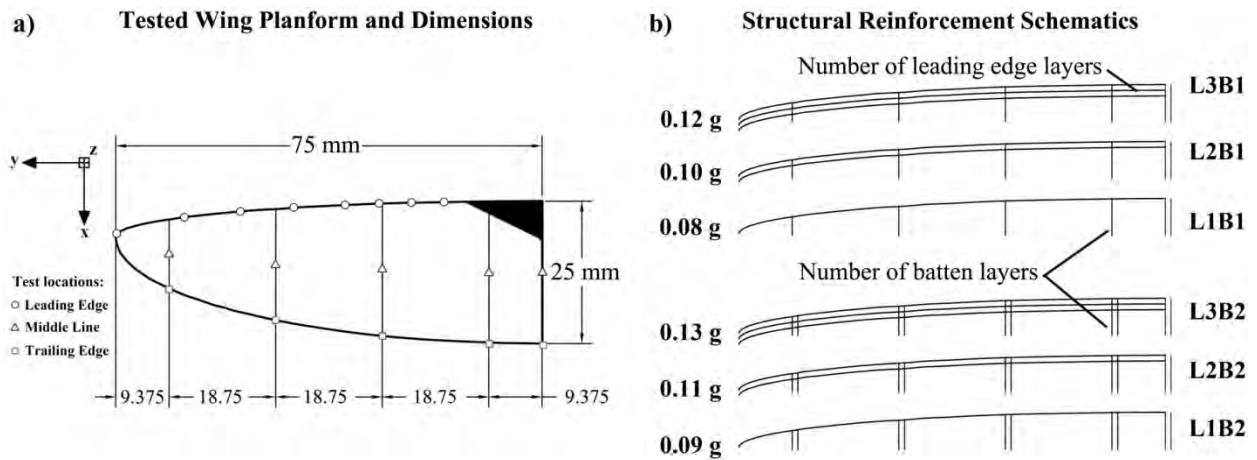


Figure 4-2. Six flexible membrane wings of different reinforcement

Pre-skinning preparation includes removing excess cured resin in the skeleton and applying base paint and adhesive. The base paint is important for reducing color contrast between the battens and the wing membrane in later deformation measurements with digital image correlation. Either grey, white or khaki can be used as the base paint, depending on the lighting conditions. The selected membrane material Capran® 1200 Matte (Honeywell International Inc. New Jersey, USA), which is also used in industry for packaging, is thin (12~14 microns) and tough (elastic modulus 2.5~3.4 GPa, tensile strength 234~276 MPa). The membrane is bonded to the carbon fiber skeleton with spray adhesive. Finally, the wings are cut out by tracing the edge of the planform.

4.2.2 Flapping Mechanism

Another single-degree-of-freedom flapping mechanism FL2D3 is designed and built, as shown in Figure 4-3 with major components labeled. The design is created around a Maxon motor system (<http://www.maxonmotorusa.com>) that includes a 15 W

brushless DC motor EC16, a 57/13 reduction ratio planetary gear head, a 256 counts-per-turn encoder and an EPOS 24 controller. This system provides precise control of the motor system: the sensor provides position and velocity feedback to the controller that actively regulates the motor. Utilizing the high precision pre-assembled planetary gear head rather than constructing a custom gear transmission is also advantageous. The final output range of the motor shaft is: speed 0 to 45 revolutions per second (RPS) and nominal torque 0 to 21 N•mm. In this work, data are taken with flapping frequencies varying from 5 to 40 Hz, corresponding to 5 to 40 RPS.

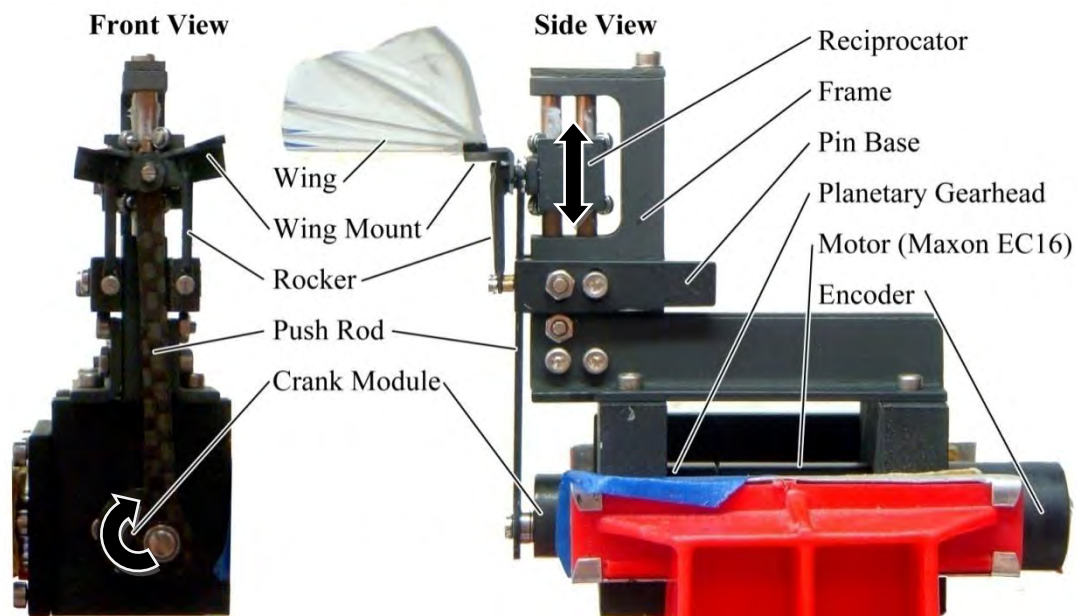
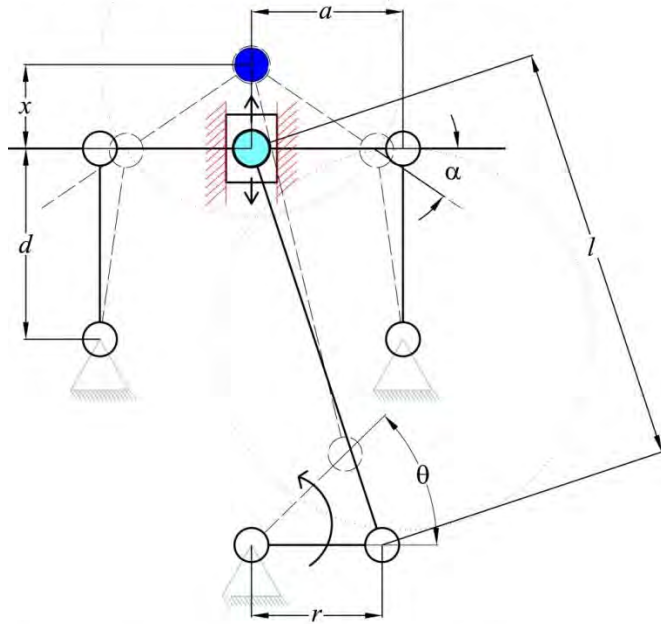


Figure 4-3. FL2D3 wing flapping test bed, capable of 45 Hz, $\pm 60^\circ$.

The rotation output from the motor is first transformed into a reciprocating motion with a crank-slider mechanism; then a bar linkage mechanism realizes the flapping motion at the wing mount. A detailed schematic description of the flapping kinematics is presented in Figure 4-4 a).

a) Schematic drawing of the flapping mechanism



b) Flapping kinematics compared to a sinusoid

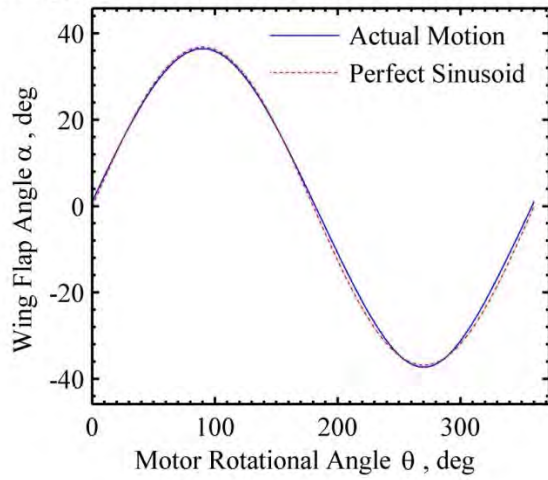


Figure 4-4. FL2D3 schematic drawings and kinematics analysis.

The geometric relationship between motor rotation (angle θ) and flap angle α is expressed in these equations:

The crank-slider mechanism:
$$x = r \sin \theta + \sqrt{l^2 - r^2} - \sqrt{l^2 - r^2 \cos^2 \theta}$$

The bar linkage mechanism:
$$x = a \sin \alpha + d \left(1 - \sqrt{1 - \frac{(1 - \cos \alpha)^2 a^2}{d^2}} \right)$$

where α is the flap angle; θ is the motor rotational angle; x is the vertical displacement from the center point when the wings are horizontally positioned;

$a = 5$ mm, the horizontal distance from the rocker base pin center to the reciprocator center;

$d = 16$ mm, the length of the rocker bar;

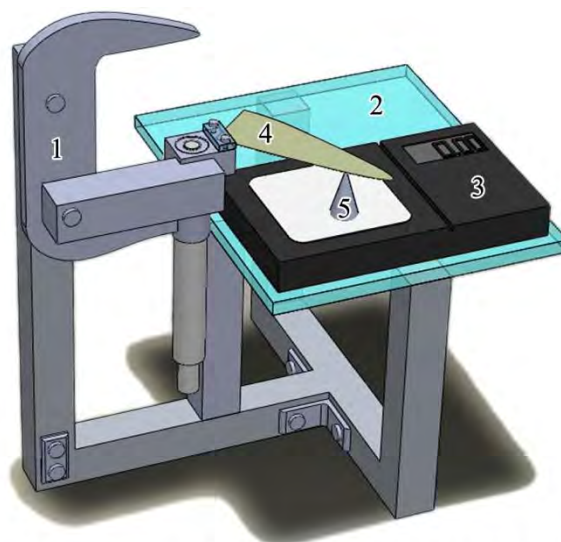
$l = 50$ mm, the length of the push rod in the crank-slider mechanism;

$r = 3$ mm, the offset distance in the crank module, adjustable to change the flapping amplitude. These dimensions define the final flapping amplitude: a nominal $\pm 35^\circ$ with a near-sinusoidal kinematic profile, as seen in Figure 4-4 b).

4.2.3 Static Elastic Characterization

The purpose of this step is to compare the stiffness amongst the various wings. The experimental setup is similar to that used by Combes and Daniel^[119]: translating the wing in the vertical direction while measuring a point force as a result of wing bending, as shown in Figure 4-5. The design model shows the static elastic test experimental setup, where the wing (4) is clamped at the micrometer (1) mounted on the test stand (2). Data are taken with a given displacement at the micrometer that creates a force through the point contact (5) to the digital scale (3). However, since the goal is not to examine the flexural stiffness but to seek the variation trend of these six pairs of wings, the metric selected for comparison is the elastic coefficient: g/mm (instead of using $EI = FL^3/3\delta$, which is only applicable to uniform cross section wings and often misused in characterizing the complicated insect wings). This is a simplified model treating the

whole wing as a spring system: given displacement input to measure force output. The wings are fixed at the stiff triangle base on a measurement table that travels up and down in the z-axis. It should be noted that this method of mounting the wings mimics the way in which they are attached to flapper in order to keep the same boundary condition. A digital scale (resolution 0.01 g) is placed to measure the spring force perpendicular to the wing at several locations as shown in Figure 4-2 a). Eight data locations are taken in the leading edge, of which the bending stiffness varies with the number of carbon fiber layers. Five data locations are taken in both the middle line and the trailing edge, where the torsional and bending stiffness extended from the leading edge is measured. Therefore by observing the change of the spring constant at different locations along the wing, the static stiffness of the wings can be quantified and compared. It is noteworthy that since the force measured is always vertical and the point contact cannot move during each measurement, the assumption that this spring system is linear is only valid for very small displacements at the wing base.



1) Micrometer; 2) Test stand; 3) 0.01g digital scale;
4) Wing; 5) Point contact

Figure 4-5. Static test experimental setup CAD model by Brad Lacroix.

4.2.4 Dynamic Response Measurement with Laser Doppler Vibrometry

This experiment examines the different dynamic structural properties (mode shapes and natural frequencies) of the wings. A Polytec PSV-400 scanning laser Doppler vibrometer (<http://www.polytec.com/usa/default.asp>) is used for the analysis of wings under a simple shaker excitation (Ling Dynamic Systems V201/3-PA 25E electrodynamic shaker; a burst chirp is used as shaker input with excitation frequencies from 0 to 1000 Hz over 1 second.) The experimental setup is shown in Figure 4-6.



Figure 4-6. The LDV experimental setup and measurement by Robert Love.

The LDV scanning head emits a laser beam onto the structure and measures the light reflected back, of which the phase shift (the Doppler effect) is proportional to the change of the structure's velocity and the beam wavelength. Therefore LDV can be used to calculate the frequency response function (FRF) of the structure, which is done with the Polytec system by comparing the input signal sent to the shaker and the output

of the structure. Polytec software is used to conduct the experiments and post process the data.

4.2.5 Wing Performance Evaluation

Time-averaged aerodynamic forces produced by the flapping wings are measured with a force and torque sensor (ATI Industrial Automation's Nano17, <http://www.atia.com/>), which is mounted underneath the flapping mechanism, as shown in Figure 4-7. The sensor has 0.319 g of force resolution, which is adequate for the current application.

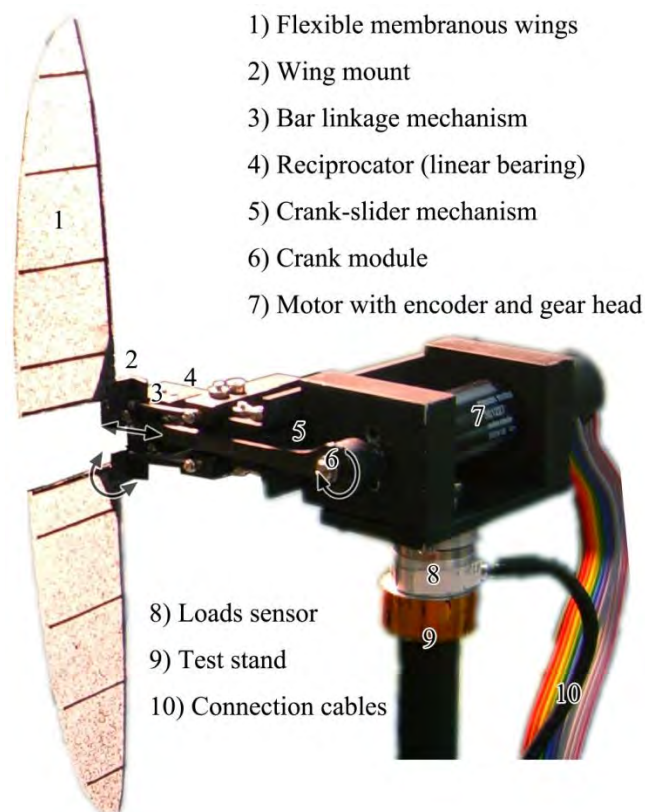


Figure 4-7. The force and torque sensor installed under FL2D3.

The forces in the x and y directions correspond to the thrust and lift directions; both have the stated measurement resolution. Both the flapping mechanism and the sensor are controlled with a LabVIEW virtual instrument program, which allows users to define sampling parameters and duration. The sampling rate is set to change along with

the flapping frequency so that a constant sampling resolution of 500 samples per flapping cycle can be achieved (i.e. at 10 Hz, 5000 samples per second and at 30 Hz, 15000 samples per second). The data structure contains a number of rows of 500 data points, saved in a text file. Each row represents the force history of one flapping cycle. Usually 40 to 150 rows of data are taken for averaging. Due to random delays occurring at the hardware interface (for example, time delay at reading from computer memory buffer), each cycle recording is slightly shifted (phase delay). This is corrected by identifying a known value (such as zero) in the loading history and calculating the average time difference between each measurements.

In this particular one degree-of-freedom case, however, if both the kinematics and structural properties are symmetrical to the wing's leading edge, the average lift measurement should be zero. This leaves only the time averaged thrust as the metric to evaluate aerodynamic performance. There are three points that needs to be made clear in this force measurement step: 1) why the inertial forces of the wing and the mechanism would not affect the averaged measurement in both lift and thrust directions; 2) why the aerodynamic lift generated with a symmetrical one degree-of-freedom motion should be zero and why with a non-deforming wing such kinematics would not produce significant thrust (as demonstrated in 3.2.1); and 3) why the average thrust value can be used as a metric to evaluate flexible flapping wing performance.

Inertial force in the measurement

Because of the nature of flapping, both the wings and the actuation mechanism are in reciprocal motion. Therefore inertial loading of parts during acceleration and deceleration will be significant and measured with the sensor. The flapping mechanism

is a complicated mechanical system that consists of many parts (gears, bearings, bars, etc.), making it inevitable that vibration signals are also recorded. However, both the inertial loads and vibration would only affect the instantaneous readings on the sensor, not the time-averaged measurement. This is because the system on top of the sensor is conservative for momentum and the initial system momentum equals to zero, the same as the final one. If there is no external force applied to the wing or the mechanism, the time-averaged measurement will be zero, no matter how large the inertial or vibration force is. This is also validated with measurements in vacuum. Indeed, in the absence of air, both average lift and thrust measurements are negligible within the sensor resolution (± 0.32 g). Therefore, measuring the time-averaged forces exempts the problem from complicated dynamic loads and allows for an effective evaluation of the wing performance.

Average aerodynamic forces of one degree-of-freedom flapping wings in hovering

The symmetry in wing kinematics and structure makes the net lift (cycle-averaged lift) force zero; because the same structural fluid interaction occurs in two opposite directions that let the results cancel with each other. If the wing planform is symmetrical to any line parallel to the spanwise direction (such as a rectangle), and if the wing does not deform, then the flapping motion around the root chord will not generate any net thrust in the chordwise direction due to symmetry (net thrust is the cycle-averaged thrust). The one degree-of-freedom flapping motion in this case, can only generate airflow in the spanwise direction. If the wing planform is not symmetrical, without any deformation the chordwise net thrust will still be negligible. As discussed in Chapter 3,

Xie et al.^[154] has designed a high stiffness wing of light structure and confirmed this statement.

Thrust and thrust coefficient as an evaluation metric

As the result of the previous two reasons, time-averaged thrust F_T and the thrust coefficient c_t^4 can be used to evaluate the aerodynamic performance. The wing deformation (which is the result of the air/structure interaction) is the sole source for generating aerodynamic thrust. As shown in the last chapter 3.2.1, wings under the same aerodynamic and kinematic conditions perform differently due to difference in structure. Although the airflow can be directed to different directions during one cycle, the symmetry of the kinematics and deformation makes the chordwise direction the only one that allows for net force. In the case of asymmetrical deformation pattern caused by the asymmetrical wing structure, airflow may be deviated and result in some lift. In this case thrust would be the resultant force of both lift and thrust.

The dynamic measurement error and resolution can be very different from the static one if there is a high level carrying signal. If the measurement resolution of the sensor is defined as x , then each measurement will be $n(i) \times x \pm x$, $i = 1, 2, 3, \dots m$. m is the number of data points available (1000 samples per second for 5 seconds would result in $m = 5000$). Therefore the time averaged data can be expressed as:

$$\sum_1^m n(i) \times x / m \pm x = \left(\sum_1^m n(i) / m \pm 1 \right) \times x$$

This means that the error would depend on the magnitude of each measurement. If the average force magnitude is 60 grams (common in this study), the average of $n(i)$

$c_T = \frac{F_T}{\rho v^2 S}$ where ρ is air density, v is average wing tip speed, and S is single wing area.

would then be $60/0.32 = 187$, and the error range would be within 0.6%. The lower the sampling rate and baseline magnitude, the larger the error.

4.2.6 Full-Field Wing Kinematics and Deformation Measurement with DIC

The kinematics and deformation of the flapping wings are measured with a four-camera DIC system, as shown in Figure 4-8. DIC is a well-developed non-contact measurement technique used to capture full-field displacement and deformation of surfaces via stereo-triangulation. A random speckle pattern is applied to the flapping wing, which is then digitized into wing surface coordinates with stereo triangulation. The full-field displacements of the wing during the flapping motion are computed with temporal matching, by minimizing a cross correlation function between discrete regions of speckle patterns on a deformed wing surface and an un-deformed. The DIC system (Correlated Solutions Inc., South Carolina, USA) has two systems using four Point Grey Research Flea2 cameras (<http://www.ptgrey.com/index2.asp>). Such a setup can capture the rigid displacements (wing kinematics) and concomitant structural deformations of a single wing up to a $\pm 90^\circ$ flapping amplitude. The upper pair camera system monitors the upper half stroke and the lower pair the lower half stroke. The cameras are positioned and configured so that there is enough depth of field to obtain clear images during the whole flapping cycle. The four cameras are synchronized internally with an output to trigger a stroboscope for the lighting. The whole system can be enclosed in a vacuum chamber so that the aerodynamic effects can be excluded from the experiments. Since the camera and stroboscope comprise a low speed system, the kinematics and deformation sequences are generated by triggering at a progressing moment in the repeating cycle.

Hardware configuration

The camera configuration is mainly concerned with enclosing the large motion of the wing and obtaining a large depth of field. The order for adjusting the camera parameters is: focal length, focus, gain and aperture. After positioning the cameras, the aperture is maximized and the focal length is adjusted so that the wing fills the field of view when the wing area appears to be maximal. Then the wing is moved to flap angle $\pm 17.5^\circ$ and the foci of both pairs of cameras are adjusted. Once the focal plane is defined, the aperture is minimized (closed). Then all camera gain values are adjusted to the mid-point of the available range (in this case, 9.96 dB). The stroboscope is activated after this step. Then the aperture of each camera is opened so that the image has reasonable contrast between the base paint and the black speckles. The aperture is kept as small as possible to obtain the sufficient depth of field. Cameras are then calibrated. A calibration grid is placed to imitate four wing locations for each camera pair: mid-plane without rotation, mid-plane with maximum rotation, the end of each stroke without rotation, and the end of each stroke with rotation. This step also double checks all previous parameters.

The reference image is taken when the still wing is at the mid-plane (Figure 4-8, part 4). This reference image is taken for both camera pairs and is used to unify the data in post process. The mechanism is actuated at the commanded frequency and the corresponding trigger signal is sent to both cameras and stroboscope so that an progressing cine of 40 frames per cycle is taken. During the experiment, the ambient light is turned off and reflective materials are placed around the setup so that the strobe light can be bounced onto the wing, otherwise when the wing is undergoing large

motion shadow will appear. Images are saved in .tiff format for later analysis. More detail pertaining the image capture trigger has been described in 2.1.4.

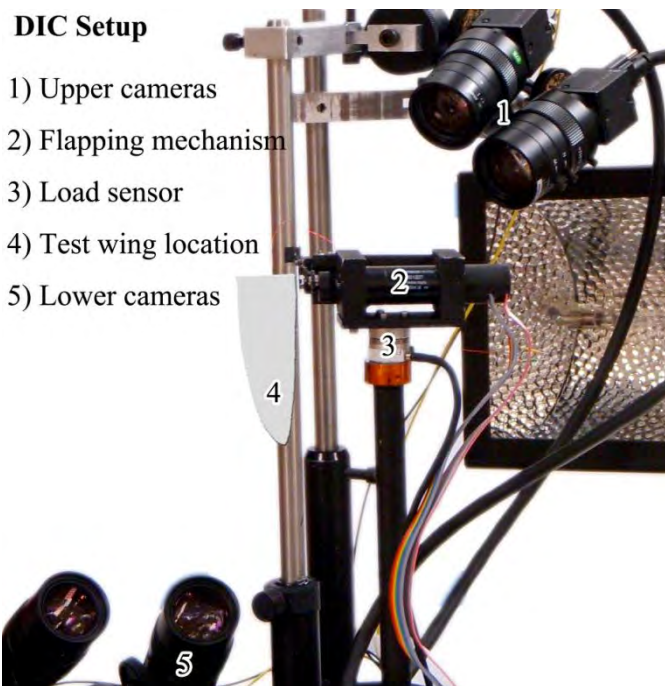


Figure 4-8. DIC system configured for large bending and twist deformation.

Data post processing

The TIFF files are processed with commercial software VIC3D provided by Correlated Solution Inc. The program correlates each pair of images and outputs the coordinates of data points on the wing surface into text files. These coordinates are computed relative to a reference image, which is given by the mid-plane of the flapping stroke at time zero. For this work, data post processing includes combining the upper DIC system data with the lower (stitching in time), separating structural deformation from rigid body dynamics, and combining deformation data with airflow data. This process is illustrated in Figure 4-9. As discussed above, this reference image, taken of the static wing at mid-plane, is captured by both pairs of cameras. Based upon the position/orientation of each camera, various calibration parameters, and the orientation

of the static wing with respect to each camera, the reference coordinate system established by each pair of cameras cannot be expected to coincide. Care must be taken then to stitch the two systems together, so that the flapping profile remains smooth as the data transitions from one camera system to the other, as shown on the left. This is done by rotating both sets of reference data such that the static wing lies parallel to the x-y plane, and the leading edge is tangential to the y axis at the root. A separate transformation matrix is then available for each camera system. Next, each pair of wings is translated such that the wing root coincides with the x axis and the leading edge with the y axis. A separate displacement vector is then available for each camera system. Each image of the dynamic flapping wing captured with the upper pair of cameras is then rotated with the transformation matrix, and translated with the displacement vector corresponding to the upper pair of cameras. A similar process is undertaken with the lower pair of cameras. Figure 4-9 part a. also shows the undeformed wing at upstroke and downstroke ends. Having stitched the two systems together, the DIC data can be used to compute the kinematic parameters.

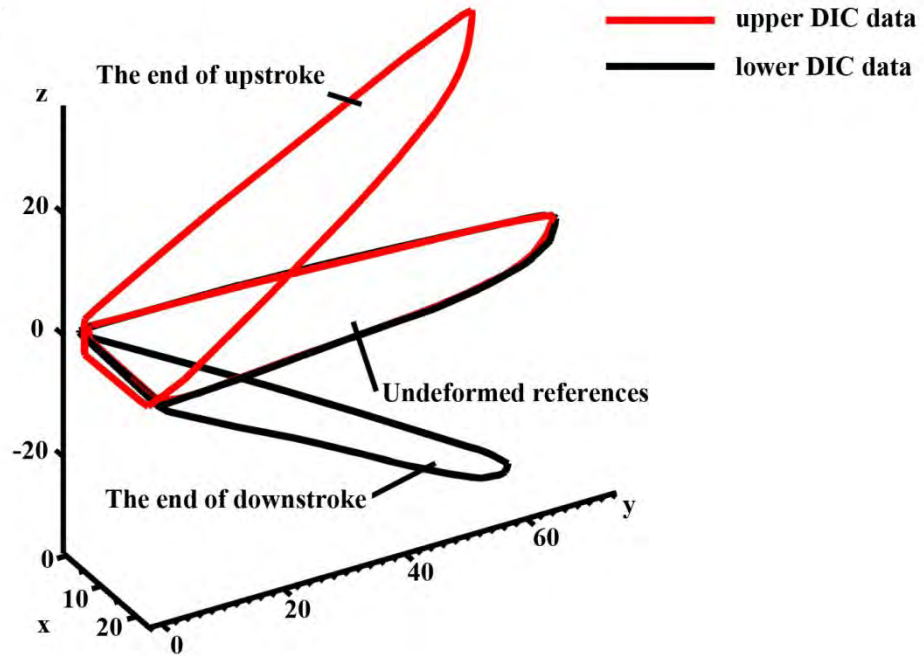
VIC3D then generates the displacements of the wings at other positions during flapping. The displacements are composed of both rigid body motions (kinematics) and structural deformations. It is desired to separate the two: the latter is much smaller than the former, but is expected to be the sole source of lift and thrust. For the test bed mechanism in this study, the single DOF flapping of a rigid wing does not produce time-averaged loads, but adaptive feathering of the trailing edge will. As such, the flexible wings designed and built in this work are very compliant to provide a large amount of bending and twisting. The rigid body motions and local surface deformations are

separated by creating a fictitious undeformed wing surface at the same flapping angle as the deformed wing measured during flapping. Transformation of the reference wing profile is performed to match with the deformed profile at the rigid triangle base (Figure 4-9, part b). First, three data points are selected on the rigid triangle base. They are very close to one another, and very close to the leading edge of the wing root. As these points are located close to the wing joint, where the rigid triangular structure locates and is assumed that their motion follows the rigid body kinematics without elastic deformation.

The displacement data for each flapping image can then be used to find the new coordinates of these three data points throughout the stroke. For each flapping image, local coordinate systems are computed for the two pairs of triplets (one set which remains stationary at the mid-plane, and one which travels with the wing), and the rotational transformation matrix is subsequently computed. The static wing at mid-plane is then appropriately rotated, and then translated so that the two triplets coincide. The difference between the fictitious rigid surface and the elastic wing provides the sought-after structural deformations, indicated by ω in the figure. Three parameters describing the wing deformation are extracted from the data: the tip deflection ω_{tip} , and the angle of twist α_{twist} . The tip deflection is the value of the aforementioned ω at the wing tip, in mm. This value indicates how much the wings bend during flapping. The angle of twist α_{twist} is measured at $2y/b = 83\%$ of the wing. This is the angle between the cross section of the deformed profile and the undeformed profile. This value indicates the amount of wing twist (feathering) during flapping, in degrees. The wing camber is measured at the

same span station as the twist angle. It is the highest point of inflation of the membrane during flapping (adaptive cambering), measured in mm.

a. Joining DIC data



b. Structural Deformation Separation

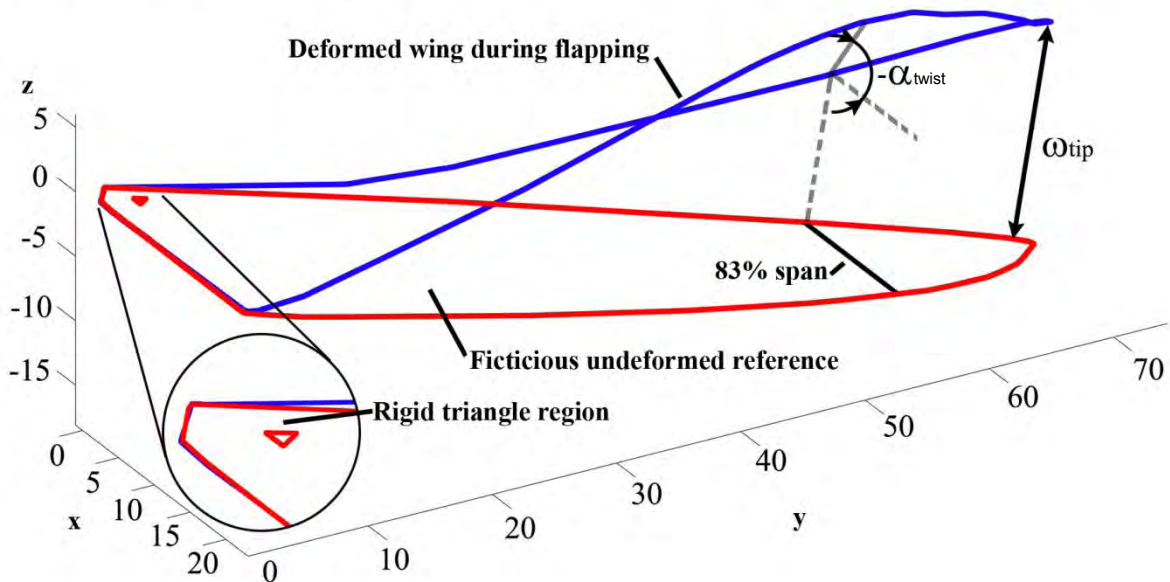


Figure 4-9. Deformation data post processing, code by Bret Stanford.

4.2.7 Airflow Measurement with SDPIV

SDPIV, a mature technique used to measure the velocity of particles (assumed to follow the airflow) in the flow of interest (Raffel et al., 2007; Wang et al., 2003; and Warrick et al., 2005), is applied to examine the airflow that develops around a flapping wing. The flow field measurement area is defined by the confluence of the position and dimension of a laser sheet, along with the cameras' field of view. Images are captured at each laser flash so that the particle spatial displacement can be extracted by correlating two images taken within a small time interval. By using an additional camera in a stereoscopic configuration, the out of plane velocity can also be extracted. Therefore SDPIV can capture three components of velocity in the two-dimensional plane illuminated by the laser sheet. Two IDT MotionPro X3 cameras (Integrated Design Tools, Inc. www.idtvision.com) capable of capturing image pairs at a resolution 1280x1024 down to a 100 ns integration time each at more than 500 Hz are used. The cameras are mounted at approximately 45 degree angles to the imaging plane to produce snapshots for stereoscopic PIV, as shown in Figure 4-10. A laser sheet is generated from a Series 800-PIV/40G Nd:YAG (approx. 14 mJ per pulse) laser system (Lee Laser, Inc. www.leelaser.com) and was directed at the target from below. The air is seeded by Expancel™ 461 DE 20 d70 microspheres (<http://www.expancel.com>), with an average radius of approximately 20 microns and an average density of 70 kg/m³. These particles were specifically chosen for the large size and low density in order to minimize the effects of gravity in simulated hover environment. The particles are dispensed using a small fan and a tube to disperse the seeding particles into the test section. Dantec Dynamics PIV system and Flow Manager Software (Dantec Dynamics, Denmark, <http://www.dantecdynamics.com>) are used to control the PIV system and

process the data. The measurements are made in the test section of a sealed open jet wind tunnel which is a cube with 8 foot sides to ensure that the flapping does not induce a significant global circulation pattern. Snapshots of the velocity field are acquired at 7 different y-locations, shown on the lower right in Figure 4-10. Snapshots are acquired in series of 815 snapshots at 102 hz. Three series are taken at each location. The first and second exposure of each snapshot is separated by 160 μ s.

a) SDPIV experimental setup



b) Schematics of laser location and cameras' field of view

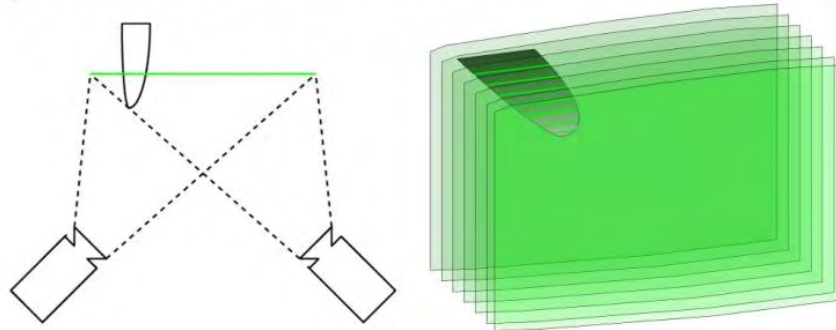


Figure 4-10. SDPIV experimental setup and laser location, by Erik Sällström.

The nominal image diameter of a particle, d_e , is defined as $d_e = (M^2 d_p^2 + d_s^2)^{1/2}$ where $d_s = 2.44(M + 1)f\#\lambda$ is the point response function diameter of a diffraction-limited lens. (Adrian and Yao, 1985) M is the magnification of the camera (~ 0.12), d_p the particle diameter (20 μ m), $f\#$ the f-number (2.8), and λ the wavelength of the laser (532 nm). With these figures, $d_e \approx 6 \mu$ m, compared to the pixel center to center distance of

the pixels of the camera, which is 12 μm . This gives a value for the ratio between the imaged particle size and that of the cameras pixel below the recommended value which is on the order of 2 (Westerweel, 1998). However, the PIV measurements are taken at such a high angle that only the horizontal center of the images can be completely in focus. Since the rest of the images is slightly out of focus, pixel locking should only be an issue in a region around the horizontal center.

4.2.8 Experimental Procedure

Multidisciplinary study procedure

As shown in Figure 4-1, five experiments are performed to fully characterize the wing properties and behavior: the first step is to examine the wing properties with static and dynamic tests, the second is to evaluate the wing performance by measuring aerodynamic loads, and the third is to measure the wing deformation and the surrounding airflow. The first two steps have generated some interesting results: 1) the static test has confirmed the different bending and twisting flexibility amongst the 6 wings; 2) the LDV dynamic test has obtained the mode shapes (vibration curvature) of each wing; and 3) the thrust produced by each wing is measured as a function of flapping frequencies (5~40 Hz). At 25 Hz, the L1B1 is being actuated near its first natural frequency while L2B1 outperforms both L1B1 and L3B1. Because these three wings are under exactly the same conditions except for their structural properties, structure/fluid interaction must be the cause for different aerodynamic performance. The objective of this chapter is to capture such phenomenon and understand why certain flexibility leads to superior aerodynamics.

Correlation of aerodynamics and wing structure

A flow chart is shown in Figure 4-11 to illustrate the experimental procedure that includes: control/input, operation, data acquisition and data analysis. The experiment requires three control inputs: flapping frequency (5 to 35 Hz), the number of samples per flapping cycle (500 in this study) in load measurements and time interval between triggers (300 to 450 ms) for the DIC cameras and stroboscope. The first two inputs are given to a virtual instrument (VI) program created for this experiment. The ΔT input is given to commercial software called VIC-Snap, which generates calibration correlation files and sends out trigger signals to the cameras.

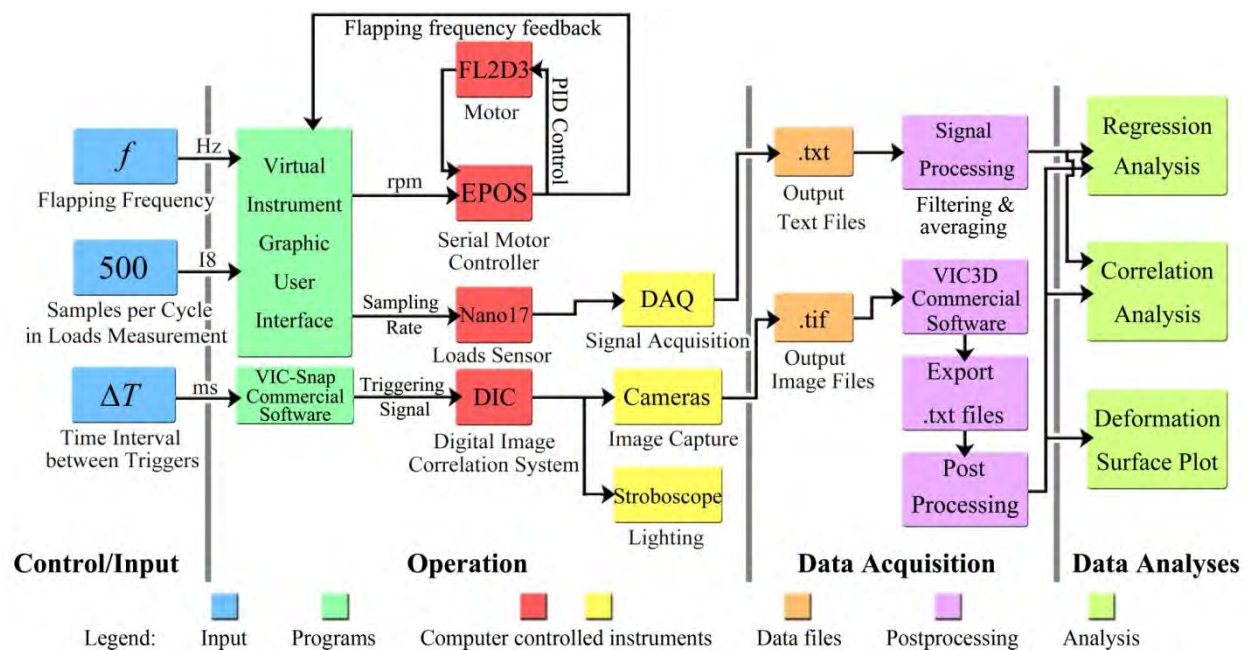


Figure 4-11. Experimental procedure of deformation and thrust measurements.

The VI graphic user interface consists of two modules: one that communicates to the EPOS serial controller of the flapping mechanism and the other that communicates to the data acquisition (DAQ) box of the Nano17. In the first module, the program establishes communication parameters and has the motor controller standing by. One

can command position, velocity, and acceleration to the motor. At this stage, PID gains have already been tuned for operation. The information is stored in the EPOS controller and is called out by the VI. The PID control is performed by the EPOS controller and does not require resources from the VI. The VI controls input values to the EPOS controller and synchronizes with the other module. This module also records the electric current consumed by the motor, which is later converted to average power. In the second module, the VI specifies sampling rate and number of samples per measurement to the Nano17 DAQ box. A constant number of samples per flapping cycle is first specified by the user (500 in this case), then the sampling frequency is calculated as the product of the flapping frequency and samples per cycle. Both of the modules allow users store the motor feedback data and loads measurements into text files. Only two components of the forces are recorded, corresponding to the thrust and lift.

In this study, the wings are actuated from 5 Hz to 35 Hz (the highest frequency for each of the four wings varies because of different structure). In all cases the wings start at the same initial position. The operation sequence is as follows. After the user has defined a flapping frequency, sample number and time interval, the VI control loop starts and establishes communication with the EPOS controller and Nano17. DIC cameras are then initiated, taking pictures at the calculated frequency. The cameras control the stroboscope by a pulse signal generated with camera shutter actuation. Immediately, a trigger button is pressed in the VI to activate the flapping mechanism and loads sensor. From the initial position, the wings accelerate at 2000 rpm/s to reach the command flapping frequency. The mechanism then stays at that frequency until the measurement

is completed. About 40~100 cycles of load measurement data are taken in each run and three separate runs of data are taken for calculating system errors. Three cycles of deformation measurements are recorded and there are about 50 frames of pictures in each cycle. This is done for each frequency and in both air and vacuum. This procedure outputs the text files for loads measurements and TIFF files for DIC measurements.

4.3 Results

4.3.1 Static Elastic and LDV Measurement Result

The stiffness comparison of the six pairs of wings is shown in Figure 4-12. In a), the leading edge bending stiffness is demonstrated to be dictated by the number of carbon fiber layers: the stiffness increases as the reinforcement layers increase. Both L1B1 and L1B2 behave in the most flexible manner and their data overlap consistently. Similarly, L2B1 and L2B2 lie in the middle between the three-layer wings and the single-layer wings. L3B1 and L3B2 are the stiffest.

As expected for all cases, the wing stiffness monotonically decreases as the test location moves away from the clamped root (due to a larger moment arm). The batten reinforcement does not affect the leading edge stiffness: the variation between data points of the same number of leading edge layers is probably due to slight manufacturing errors and measurement precision (0.025 g/mm). Part b) and c) show the torsional stiffness comparison at the mid-line and the trailing edge (the data point location is shown in Figure 4-2 a).) The torsional stiffness of the wing is dictated by the twist of the leading edge and the bending of the battens. The wings with 2 layers of batten reinforcement are consistently stiffer than the wings with only 1 layer, as seen in L2B1, L2B2, L3B1 and L3B2. However, for L1B1 and L1B2, the leading edge torsional

stiffness is a dominant factor: only minor differences are observed between the two wings.

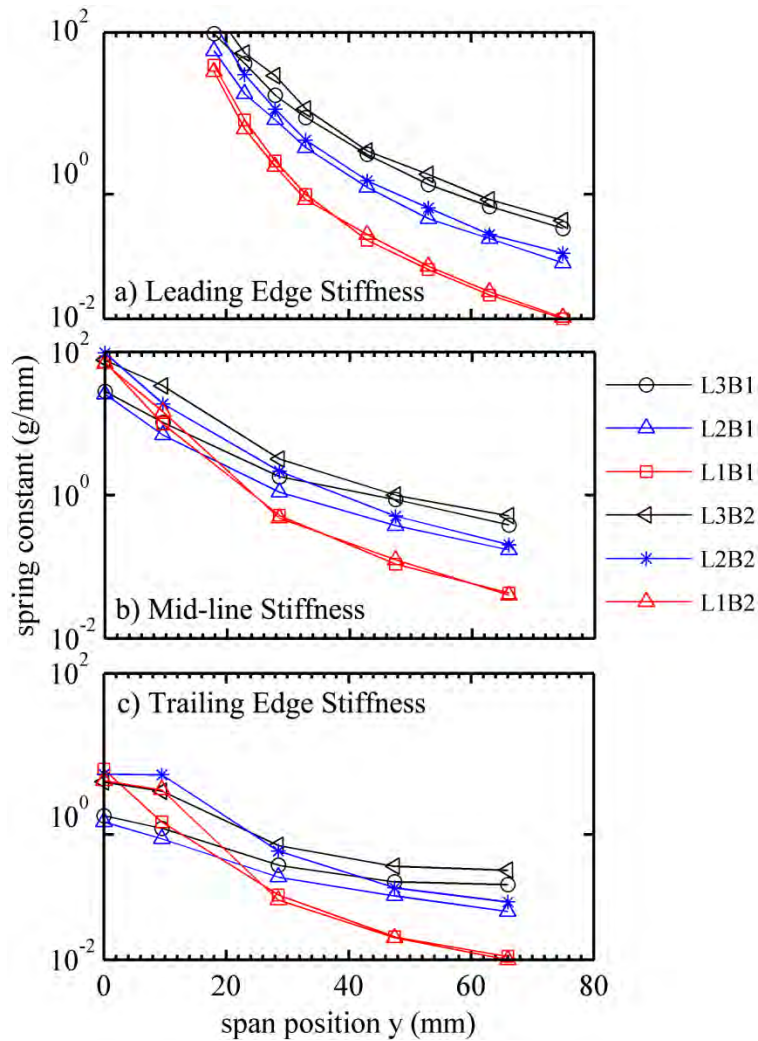


Figure 4-12. Wing stiffness (g/mm) compared at a) the leading edge, b) the mid-line and c) the trailing edge.

Because the membrane is only laminated on one side of the skeleton and they have different properties, small asymmetry of structural properties is expected. Figure 4-13 shows the results on the trailing edge with loading in both directions. The “up” stiffness is corresponding to deformation in the positive z direction (Figure 4-2) and “down” in the negative z direction. Therefore when the wing is traveling through the

downstroke, the wash-out deformation is related to the “up” flexibility and when the wing is traveling through the upstroke, the wash-in deformation is related to the “down” flexibility. It can be seen in Figure 4-13 that all six wings have higher “down” flexibility (or lower “down” stiffness). Although the differences between “up” and “down” stiffness may seem small, at high frequencies the structural asymmetry will result in different thrust peaks: with more flexibility generating higher thrust (as discussed below).

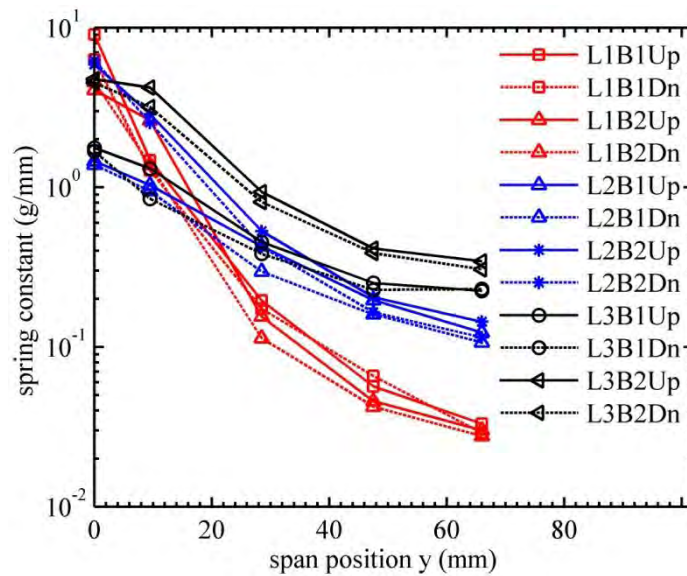


Figure 4-13. Asymmetry of wing flexibility measured at the trailing edge.

LDV results are output as FRFs and the mode shapes of the wings at specified resonant frequencies, such as Figure 4-14. In a), an example of the FRF output from the L1B1 and L1B2 wings is shown. The results are obtained from the average response of the structure at each point during shaker excitations sweeping from 0 to 1000 Hz over 1 second. Only 0 to 250 Hz is shown here, as these are expected to play the greatest role during the flapping stroke. Vertical lines are provided over the FRFs in order to indicate the high-energy-peaks of particular interests. The peaks are selected by inspecting the corresponding mode shape at that frequency. In b), the mode shapes

of L1B1 (left column) and L1B2 (right column) are shown at the first three FRF peak frequencies (from bottom to top: 1st peak to 3rd peak).

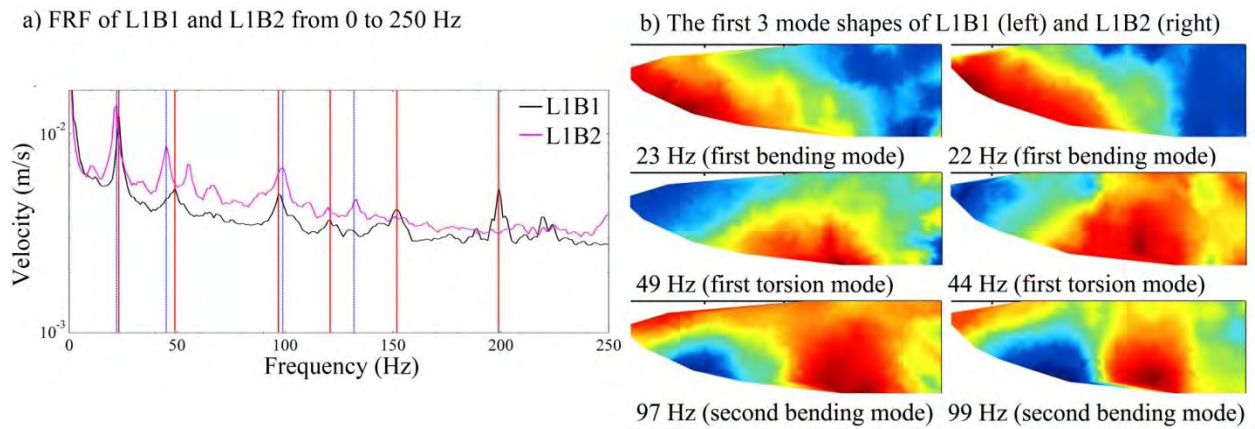


Figure 4-14. LDV measurement results.

Table 4-1 shows the corresponding frequencies of each of the mode shapes by identifying the peaks of the FRF. The first column of frequencies indicate the first bending mode resonant frequencies; but the fact that the wings are different from a simple beam renders the use of the term “first bending mode” less accurate. The comparison of relative stiffness of the wings is indicated by these frequencies, where a higher frequency (for the same mode shape) is indicative of a stiffer wing (though mass distribution also plays an important role). In the first column, adding successive leading edge layers causes a nearly linear increase in the first bending resonant frequency of L1B1, L2B1 and L3B1. Stiffer battens raise the frequency of membrane shapes as seen by comparing the higher frequencies (the last two columns) of L1B1 to L1B2; however, little change is seen in the frequency of the bending shapes (the first and second column). The not available (N/A) cases are due to no identifiable mode shape in that frequency range (no significant FRF peaks).

The mode shapes of L1B1 and L1B2 are first presented in Figure 4-14 b) (only their spectrum peaks are within the flapping frequency test range 0 ~ 40 Hz, as in Table 4-1). The contours are indicative of the vibration energy/amplitude throughout the wing. At the first peaks of both wings, 23 Hz for L1B1 and 22 Hz for L1B2, the wing tip and the outer half of the trailing edge show significant vibration energy, bearing some resemblance to a first-mode bending shape. Therefore, a large amount of tip deflection is expected at these frequencies, which will be examined with deformation measurements. At the second peak (49 and 44 Hz, respectively), the excited vibration location moves to the mid-rear of the wings, analogous to a torsional mode: such behavior is potentially beneficial for thrust production (Ho et al., 2003; Ennos, 1988). The actual wing deformation at the frequency range of interest (20 ~ 40 Hz) should be a combination of all of the mode shapes, but the first two will dominate. The third peak (97 and 99 Hz, respectively) shows the mode shapes of the wings that are similar to the second bending mode of a beam. In general, L1B1 and L1B2 are built such that their flexibility can be observed in the subsequent experiments: structural excitation at resonant frequencies to enhance aerodynamic performance.

Table 4-1. Frequency peaks of the average frequency response spectrum, Hz

Wing Type	1 st peak	2 nd peak	3 rd peak	4 th peak	5 th peak	6 th peak
L1B1	23	49	97	123	152	198
L1B2	22	44	99	132	250	364
L2B1	42	84	126	233	248	N/A
L2B2	41	84	133	167	261	366
L3B1	59	104	138	256	303	675
L3B2	67	N/A	135	515	N/A	N/A

The mode shapes of the remaining four wings are presented in Figure 4-15. It can be seen that, though at different frequencies due to different structure flexibility, the first

resonant mode shapes across all six wings are very similar. So are the second modes, except for L3B2, whose FRF results do not contain clear peaks to generate a clear mode shape. The high energy response concentrates in the membrane behind the leading edge and outwards from the second straight batten. This, as will be seen below, improves thrust production yet may not be the best configuration because the portion between the root and the second batten may be under-utilized.

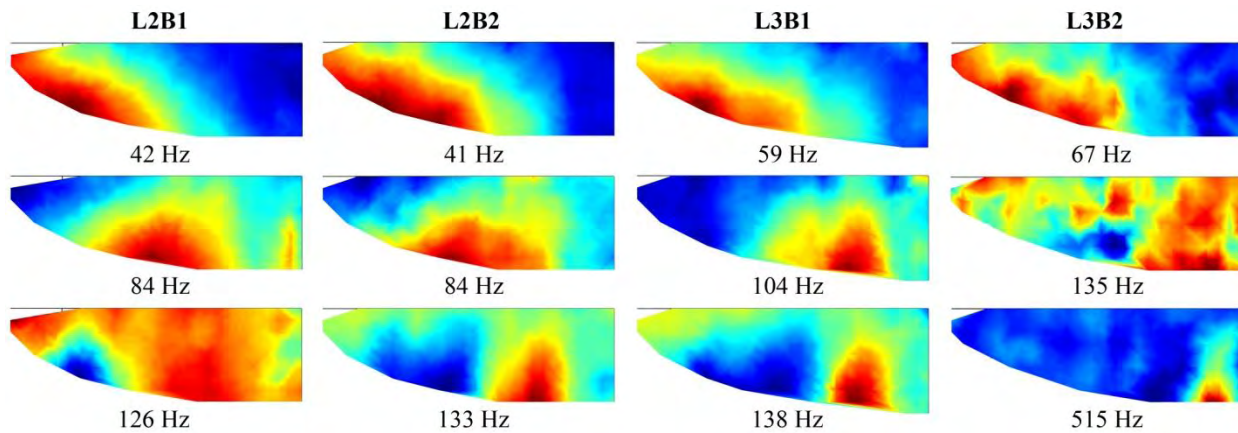


Figure 4-15. Mode shapes at the first three available FRF peaks.

4.3.2 Thrust Measurement Result

The cycle-averaged thrust produced by all six wings is shown in Figure 4-16 (for hovering with a horizontal stroke-plane, such as seen in many insects and hummingbirds, the use of “thrust” and “lift” is interchangeable). One tare case is taken with no wing attached to the flapping mechanism to show the noise level of the system (within its sensitivity 0.32 g). In general, the average thrust increases as the flapping frequency increases, though the thrust of different wings increases at different rates, and occasionally decreases.

The effect of wing bending stiffness in thrust production is clearly illustrated at three critical frequencies: 15 Hz, 25 Hz and 40 Hz. At the low frequency of 15 Hz (also

at 10 Hz), the most flexible L1B1 and L1B2 outperform other stiffer wings and the lowest thrust is produced by the stiffest wings. As the flapping frequency increases, the average thrust increases at different rates: from 20 to 30 Hz, the two-layer leading edge L2B1 and L2B2 generate more thrust than the other four wings, with the difference maximized at 25 Hz. After this frequency range, the stiffest wings L3B1 and L3B2 climb fastest and outperform the rest of the wings after 35 Hz, reaching more than 9 grams at 40 Hz while L1B2 reaches a thrust plateau and L1B1's thrust decreases. These trends show that at a certain flapping frequency, specific wing flexibility in bending can improve aerodynamic performance; and for certain flexibility, there is an effective operation frequency range. The stiffer the structure, the more thrust can be produced at higher frequencies, while the opposite is true at lower frequencies.

On the other hand, the stiffer batten structure can also improve wing performance via torsional phenomena. Seen with L1B1 and L1B2, the thrust produced by L1B2 that has larger mass on the battens and a greater tendency to twist is much more than that produced by L1B1. L1B1 reaches its thrust peak at 25 Hz while L1B2 keeps climbing until 30 Hz. Such behavior matches very well with the dynamic response data, which shows that the first and second bending resonant frequencies of these wings are between 22 Hz and 50 Hz (Figure 4-14 and Table 4-1). This suggests that between 20 and 25 Hz L1B1 reaches its resonant frequency and effectively produces peak thrust due to enhanced deformation; once the wing goes past that frequency, the actuation starts canceling with the deformation, causing the thrust to drop. Similarly, the wing L1B2 has a higher resonant frequency, and the thrust peaks at a higher actuation frequency.

The effect of the stiffer batten structure can also be seen in the other four wings. For L3B1 and L3B2, the stiffer batten structure is inferior to the more flexible one prior to 30 Hz, producing less thrust; but at higher frequency range, L3B2 outperforms L3B1. Therefore the beneficial effect is seen only in the frequency range where effective thrust is produced. A similar case can be observed in L2B1 and L2B2 from 5 to 25 Hz. However, the trend for these two wings changes at higher frequencies. Referencing Table 4-1, both L2B1 and L2B2 have the first peak of their FRFs near 40 Hz. From the change of thrust climb rate of L2B2, a thrust peak would be expected between 41 and 52 Hz (as indicated by the first two peaks of its FRF). While a higher frequency for thrust peak is expected for L2B1 as its first two FRF peaks are 42 and 84 Hz; this corresponds to the smaller change in gradient for this wing. Further study is needed to confirm a more generalized hypothesis: flexible wings would have a certain actuation frequency (between the first two FRF peaks) for peak thrust production and the performance would degrade once that frequency is passed. Further discussion concerning the relationship between structural resonance and optimal thrust production for flapping wings is given by Frampton et al. (2001). Maximum and minimum thrust (peaks and valleys of averaged and filtered cycle history) in each flapping cycle of all six wings versus frequencies are shown in Figure 4-17. The tare case shows the vibration of the flapping mechanism in the y-axis (thrust measurement direction).

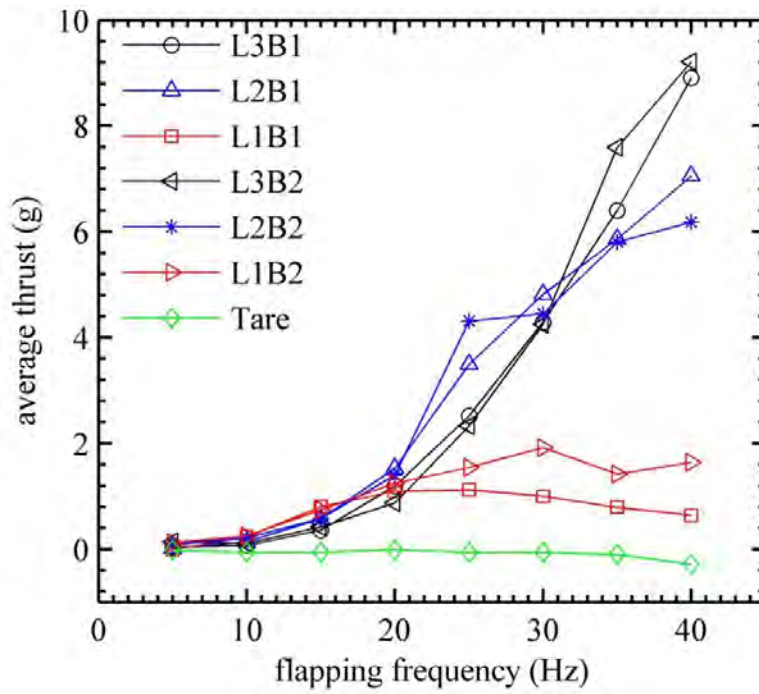


Figure 4-16. Time averaged thrust as a function of flapping frequency.

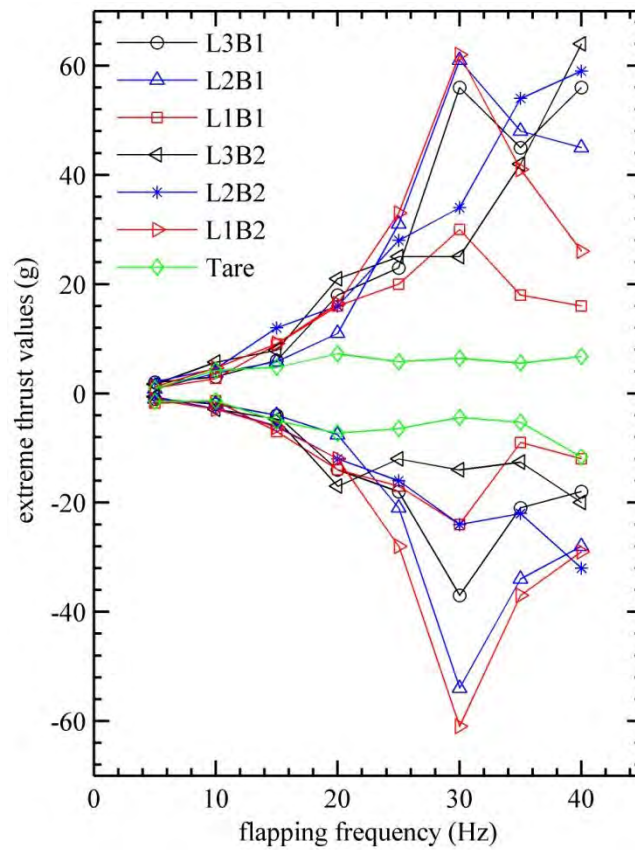


Figure 4-17. Extreme thrust values (maximum and minimum in one cycle)

It is noteworthy that the extreme values measured in a cycle can be orders of magnitude higher than the integrated/averaged value: in some cases over ± 60 grams of thrust are recorded in one cycle. L3B2 shows significant data asymmetry: higher values at peaks (more than 60 g) and lower values at valleys (less than 25 g), which is presumably due to the asymmetric trends noted in Figure 4-13. L2B2 behaves similarly while other wings are much more symmetrical in peak thrust and drag. The effect of wing bending stiffness is less clear in Figure 4-17 than in Figure 4-16. Particularly for L1B2, the wing surprisingly produces peak thrust and drag at higher values than all other wings at 30 Hz. The current study is not able to identify the cause for the instant force peak of this wing, but since all other parameters are identical except for structural properties, one would consider such phenomenon a result of aeroelastic behavior. In summary, except for L1B1 and L1B2, the stiffer battens cause wings to have more asymmetric thrust peaks and valleys therefore higher average thrust value can be achieved.

4.3.3 Wing Deformation

Wing deformation of L3B1, L2B1 and L1B1 are measured at 25 Hz. Figure 4-18 shows the deformation of L3B1 in both air and vacuum: each case contains five frames through the downstroke and the upstroke. The deformation is depicted with the color contour and a reference grey line shows the undeformed case. The color bar shows the transverse wing deformation normalized by the root chord (25 mm). Although minor asymmetry of wing flexibility in the positive and negative z direction exists, the deformation history of upstroke can be seen as mostly mirroring that of downstroke by the mid-plane. There are three important features in Figure 4-18: wing deformation during reversal (the end of each stroke), the deformation at mid-plane and the maximum

deformation's phase and magnitude. At wing reversal the maximum acceleration occurs due to inertia; therefore tip-snaps can be seen in both the air and vacuum cases. However, the tip-snap magnitude is seen higher in vacuum, where the aerodynamic damping effect is eliminated. When the wing is passing through the mid-plane in air, significant deformation (wash-out during downstroke and wash-in during upstroke) due to aerodynamic loading is observed. This is confirmed with little deformation at the mid-plane in the vacuum case: because at this flap angle (zero), the acceleration is zero but velocity is the highest: no deformation is caused by inertial loads but the high speed movements result in substantial aerodynamic loads. In air, the maximum structural deformation happens after each wing reversal due to both inertial and aerodynamic loads; in vacuum, the maximum structural deformation occurs at each wing reversal due to only inertial loads. Therefore thrust peaks are expected in between where the maximum deformation occurs and the mid-plane.

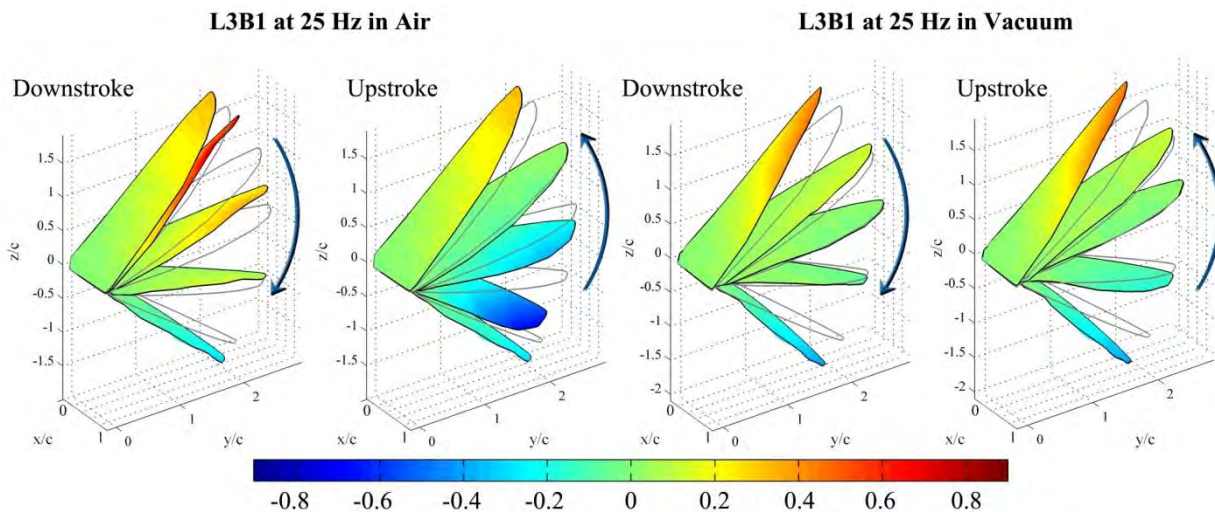


Figure 4-18. Deformation contour plots of wing L3B1 are shown at 25 Hz

Figure 4-19 shows the deformation contour plots of wings L2B1 and L1B1 in a less intuitive manner compared to Figure 4-18, because the deformation is significantly

higher and frame interference would occur if plotted in the same way. Therefore the eight frames of one flapping cycle are decomposed onto a circle. The solid grey line represents the still mid-plane reference; the translucent grey wing represents the fictitious undeformed wing at each flap angle; and the color contours represent both deformed L1B1 and L2B1 at the same flap angle. The color bar again shows the transverse wing deformation normalized by the root chord, but much higher (-1.5~1.5) comparing to that of Figure 4-18 (-0.8~0.8). This deformation is measured in a floating frame which rotates with the flapping wing, and thus does not include the large rigid body motions of the flapping. Flap angles for each location are marked on the right: 0° , $\pm 17^\circ$ and $\pm 35^\circ$.

The insert on the bottom right of the figure shows the definition of deformation descriptors: the tip deflection indicates how much bending has occurred at the wing tip and the twist angle reflects the elastic wing rotation (positive twist corresponds to a depression of the trailing edge). With these descriptors defined, it is useful and important to examine the contour plots along with deformation history presented in Figure 4-20, which depicts the deformation at different flap angle in a complete cycle. The three phase loops describe the structural dynamic deformation of the wings: on the left, tip deflection versus flap angle loops counter-clockwise; and on the right, the twist angle at $y = 62$ versus flap angle loops clockwise. This means that if the 0° flap angle during upstroke is defined as the start of each cycle, the tip deflection loops start at the bottom while the twist angle loops start at the top.

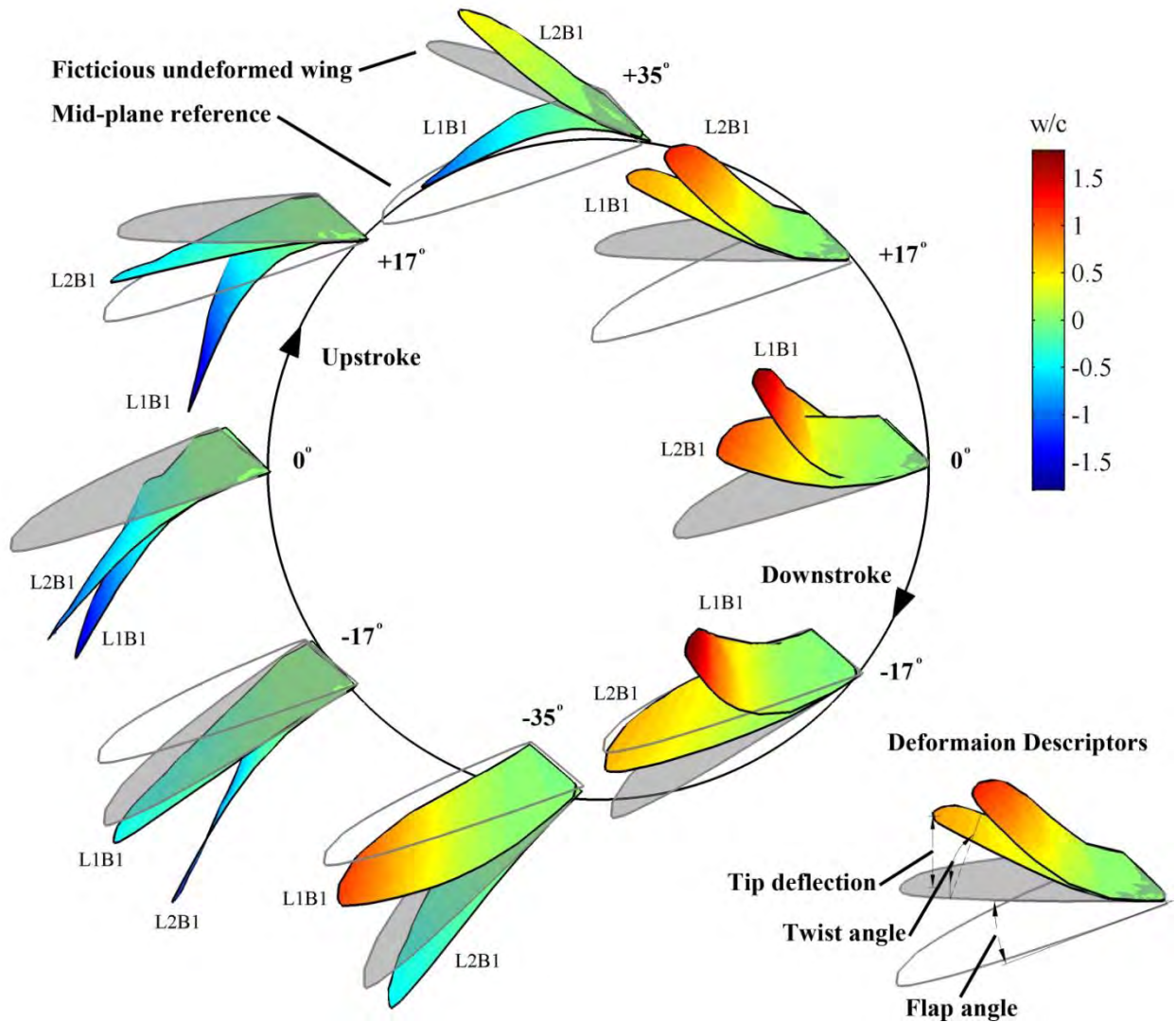


Figure 4-19. Deformation contour plots of wings L1B1 and L2B1 at 25 Hz in air

At 25 Hz, L2B1 represents a flexible wing that effectively produces thrust; while L1B1 represents a wing that has reached its maximum available thrust and experience excitations above its first resonance; and L3B1 represents a fairly stiff wing undergoing minor deformation. The following discussion will first analyze L2B1 and L1B1, and then L3B1. During the upstroke at 0° flap angle, both L1B1 and L2B1 experience a large amount of wing bending and twisting: Figure 4-19 shows the contour and Figure 4-20 shows the exact deformation value, which indicates that while L1B1 has a larger tip

deflection its twist angle is much smaller than L2B1's. As the flap angle increases to 17°, the tip deflection of L2B1 decreases while L1B1's increases (contour seen in Figure 4-19 upstroke 17°). This is potentially due to the fact that L2B1 is experiencing maximum velocity and thus maximum aerodynamic loads at mid-plane (causing it to have large deformation), and as the velocity decreases towards the end of upstroke, the aerodynamic loads decrease and deformation decreases. L1B1 on the other hand, has a much weaker structure and aerodynamic loads dominate its deformation, preventing the wing from following the prescribed motion: a significant phase lag develops between the two motions. Furthermore, L1B1 is being actuated at a frequency above its resonance (Figure 4-20) and its bending vibration may cancel with the wing kinematics. Therefore L1B1's deformation experiences a large phase lag behind the flapping actuation (Figure 4-20). As the wings reach the end of upstroke (flap angle 35°), the L2B1 first lines up with its undeformed position (wing reversal), then overshoots due to wing inertia, bending in the other direction (called tip snap) as seen in the contour of Figure 4-19. As before, L1B1 is struggling with the aerodynamic loads, falling behind its commanded kinematics, though its tip deflection is decreasing while its twist angle reaches the peak. This phase lag inherent within the deformation of L1B1 may be the cause of the low thrust values measured at 25 Hz. A very similar phenomenon is noted in the work Heathcote et al.^[166]: extremely flexible plunging wings see a large phase lag between the commanded root motion and the tip deformation, along with a substantial drop in thrust. For stiffer structures, however, the lag is much less and thrust is augmented over the rigid case.

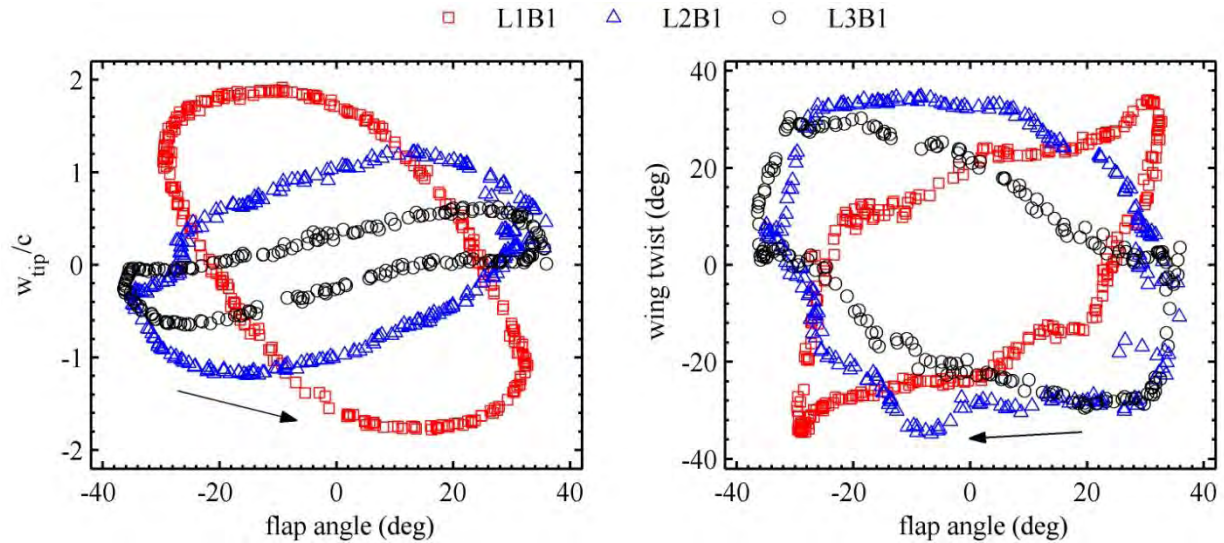


Figure 4-20. Deformation phase plots of L3B1, L2B1 and L1B1 at 25 Hz in air

As the wings begin to flap through the downstroke (flap angle 35°) L2B1 should experience a maximum angular acceleration (as defined by the nearly sinusoidal actuation kinematics). This combination of inertial and aerodynamic loads causes L2B1 to quickly reach its near-maximum (negative) wing twist (Figure 4-20). At the same time, the twist angle of L1B1 starts to decrease sharply. The maximum wing bending does not occur to L2B1 until the flap angle is near 17° in the down stroke. At this moment, L2B1 has larger deformation than L1B1 (seen in Figure 4-19). Also seen in Figure 4-20, both tip deflection and wing twist of L2B1 are larger (absolute value) than those of L1B1. As the wings pass through the mid-plane of the downstroke, the deformation contour symmetrically occurs as the last half cycle in Figure 4-19 (symmetric to the origin in Figure 4-20). However, some surprising behaviors of L2B1 are observed: there is a dip in the tip deflection loop near the end of the downstroke and there is a bump (absolute value) of twist angle from 0° to 17° during downstroke. The reason for such unsymmetric behavior is currently unknown, but may be due to the wing's interaction with vortices shed at an earlier location in the flapping stroke. The full-field deformation of

L1B1 (Figure 4-19) is comparable to the 23 Hz mode shape presented in Figure 4-21. This is as expected: the operating deflected shape of the elastic wing should be a combination of all the mode shapes, though obviously the first mode will dominate (both because it contains the most energy of all the modes, but also because the operating frequency of Figure 4-19 is very close to the first resonance).

In Figure 4-20, the phase loop patterns of tip deflection and wing twist of L3B1 is very similar to L2B1's. The phase loop for the tip deflection has a near linear portion in the middle of both upstroke and downstroke. The maximum and minimum tip deflection locations are much closer to the end of each stroke. Similar trend exists for the wing twist loop, which forms a rectangular shape (the full-field deformation of L3B1 is combined with the airflow structures captured with DPIV presented below.) The tip deflection loops on the left in Figure 4-20 show that the enclosed areas increase as the wing flexibility increase, though this does not necessarily equate to an increase in thrust as well. The larger area enclosed by L2B1 (than that by L3B1) correlates to higher thrust production. Although L1B1's loop encloses much larger area, the phase lag of the loop has shifted significantly, and the thrust drops. On the right in Figure 4-20, the twist angle phase loops show similarity: larger enclosed area by L2B1 than L3B1 in the same diagonal direction, yet smaller enclosed area by L1B1 in an opposite diagonal direction. However, because of the constraint by the membrane, maximum twist angles of these three wings are similar.

Figure 4-21 shows the deformation of L2B1 at 25 Hz under a vacuum in comparison with the data in air (reproduced from Figure 4-20). As would be expected, the results are starkly different: the former includes deformation only due to inertial

loads, while the latter includes effects from both aerodynamic and inertial loads. At the stroke-reversal portions of the loop, the deformations of the wing under a vacuum are larger than the air counterpart, as angular acceleration (and thus inertial loads) should be highest in this location.

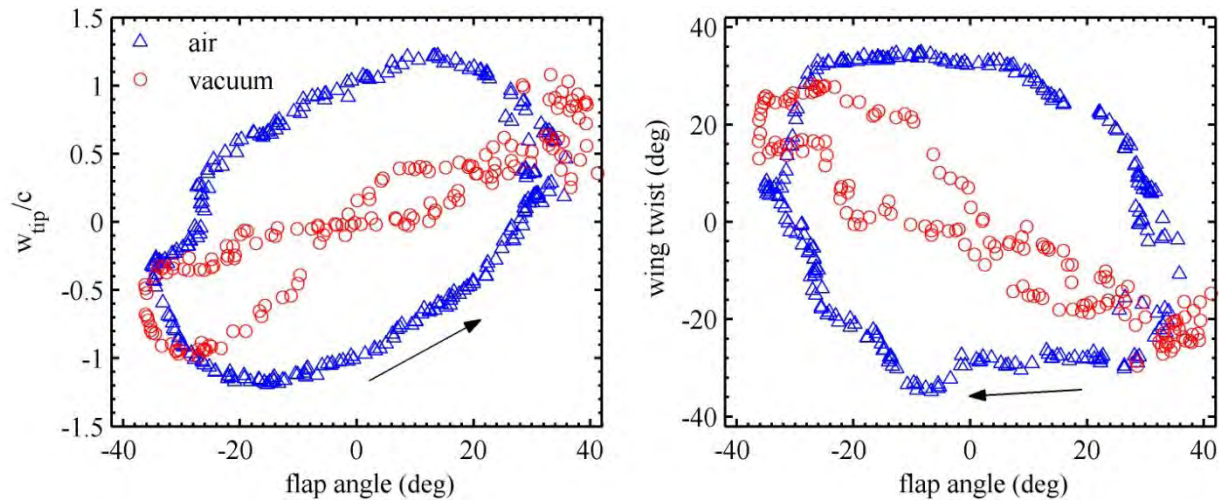


Figure 4-21. Deformation comparison of L2B1 in vacuum and in air at 25 Hz

The wing flapping in air is subjected to these same inertial loads, but the response is smaller, which may be due to an aerodynamic damping effect, or an added-mass effect. Through the middle of the flapping stroke (either up or down) the inertial loads (along with the angular acceleration) become very small, and hence the deformation of the wing under vacuum does as well, forming a hysteresis loop that intertwines twice, with three small loops. Contrastingly, aerodynamic loads scale with flapping velocity (squared), and the wing flapping in air has very large deformations in this location of the phase plot. It can also be seen that the data measured from a vacuum is generally noisier (particularly near the end of the upstroke). This may be due to the lack of an aeroelastic feedback mechanism known to damp out high-frequency vibration associated with the natural frequencies of the flapping structure (Stanford and Beran, 2009), or a mild deterioration of the mechanism's ability to provide smooth kinematic

motions. Obviously, the strobe-synchronization method used in this work will struggle to accurately capture such high-frequency content.

In order to compare the effect of wing flexibility upon the wing tip trajectory, the wing tip location (displacement) is plotted versus flap angle in Figure 4-22. Unlike the previous deformation metrics, this displacement is measured in a fixed inertial frame, and so includes both structural deformation and rigid body flapping motions. As such, a solid black line is drawn as a reference of the tip trajectory of a theoretically rigid wing. As the wing leading edge stiffness decreases from L3B1 to L2B1 to L1B1, the tip path deviates further and further from the reference. The pattern of L1B1 shows that the wing is no longer performing the commanded kinematics of the flapping mechanism: a similar phenomenon is noted in the work of Heathcote et al. (2008).

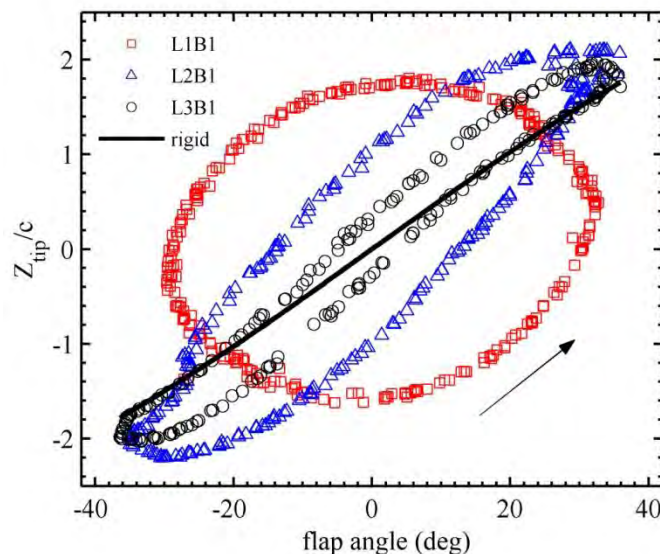


Figure 4-22. Flexible wing tip locations compared with a theoretical rigid case.

4.3.4 Fluid/Structure Interaction

By combining the DIC and SDPIV measurements, the fluid/structure interaction of flapping wings can be further elucidated. Figure 4-23 and 4-24 show the velocity and vorticity fields around the three wings flapping at 25 Hz at two instances: passing

through the mid-plane during downstroke and experiencing wing reversal at the beginning of downstroke, respectively. The actual SDPIV data contains 2445 frames and is averaged into 50 phases spread out evenly in time over one flapping cycle. Therefore the results are under the assumption that the airflow is periodic based on a single flapping cycle; this appears to be reasonable from the clean deformation data of Figure 4-20 (which is not measured consecutively but distributed over several flapping cycles). Moreover, the fluid/structure interaction is better viewed in an image sequence (video); but the current format is limited to static figures shown at two wing positions. Nevertheless, the result has proven a successful combination of experimental techniques and revealed part of the aeroelastic phenomena of flapping wings.

In Figure 4-23, the cross comparison of wing deformation can be related to Figure 4-20 around $x = 0$: phase lag of L1B1 causes large wing bending (over $1.5 w_{tip}/c$) and twisting (below -20°); L2B1 shows moderate bending (near $1 w_{tip}/c$) and the largest twisting (below -30°); and L3B1 has less observable deformation. As described in Figure 4-19, L1B1's structure is too flexible to follow the commanded kinematics; inertial load causes the outer part of the wing to lag to the root motion significantly. The fluidic forces around the wing damp the structural deformation but no substantial airflow is generated, as seen in a). The magnitude of the airflow parallel to the chord of the wing (from leading to trailing edge, along the x axis) must be thought of as a strong indication of the amount of thrust produced by the flapping motion. As discussed in Figure 4-15 and 4-17, the thrust produced by L1B1 at 25 Hz is relatively small, which correlates strongly to the weak flow structures of Figure 4-15, as do the other results in this section.

The vortical structures shed into the wake for L1B1 can be seen in d) at $y = 50, 60$ and 70 mm: opposite sign vorticity is shed from the trailing edge and travel outward along the y direction. L2B1 on the other hand, possesses beneficial structural properties at this frequency, producing the most thrust (3.5 grams on average). In b) the airflow around L2B1 reaches near 6.8 m/s at $y = 50$ mm behind the trailing edge. The planes $y = 30, 40, 50,$ and 60 mm show airflow directed along the x direction, corresponding to the wing washout. In e), the 3D vortex structure is clear: an area of low pressure develops at the leading edge as the wing flaps downwards, creating negative vorticity in a clockwise direction near the wing surface (seen at $y = 20, 30, 40, 50,$ and 60 mm). These vertical structures grow larger spanwise from $y = 20$ to 60 mm, corresponding to the increase in the flapping wing velocity. This low pressure also interacts with the wing structure, causing the substantial wash-out noted above (compared to the vortices at the same relative location in f)-L3B1).

Concurrently, positive vorticity (counterclockwise) is being shed away from the trailing edge, growing from $y = 20$ mm to 60 mm. This is caused by the velocity difference when air is “pushed” away from the flapping wing. At $y = 40$ and 50 mm, the net effect of the vorticity pairs direct the flow direction along the x axis; the pressure gradient forms the airflow around the wing seen in b). Similar flow structure can be seen in L3B1 c) and f), producing 2.5 grams of average thrust. In comparison with L2B1, the relative positions in both high speed airflow and vortices pairs are much closer to the leading edge. In c), maximum flow speed is present at $y = 50$ mm, focused in front of the leading edge. This may be a result of the leading edge vortex pair seen in f) at $y = 50$ mm. The 3D vortex structure extending from the root towards the tip can also be

clearly seen (the leading edge vortex pairs are more visible, as less masking is required). But the positive vorticity which is shed from the trailing edge is much weaker compared to e), due to the stiffer structure. Comparing b) and c), it may seem that L3B1 should be more thrust productive at this instant because of higher speed airflow around the wing; but the flow direction and sustainability are the keys to average thrust: L2B1's flexibility achieves a higher average value. Vorticity generated at the leading edge appears to be captured in Figure 4-23 f), but the necessary masking cut out some portion needed for further identification. Further discussion pertaining to the relationship between leading and trailing edge shedding for flapping wing thrust production is given by Issac et al. (2008).

In Figure 4-24, similar deformation correlation can be made with Figure 4-19 and Figure 4-20. Here the fluid/structure interaction is compared after the end of the upstroke when the wing direction is reversed and starts traveling down (at flap angle about 24° , seen in Figure 4-20). Wing deformation of L1B1 and L2B1 are related to Figure 4-19: L1B1's flexibility is causing the wing to lag so much that the wing appears to be near the mid-plane; and L2B1 has significant tip snap bending and twisting, traveling much further than L3B1 (though the allowable flap angle at the wing root is the same for all cases). For L1B1, no significant airflow is expected, as seen in both a) and c). For L2B1, the wing reversal kinematics should cause vortices to be shed into the wake: as seen in e) at $y = 70$ and 77 mm. Two vortex pairs are clear at $y = 70$ mm, shed away from the wing tip and propagating into the z and y direction (disappearing at $y = 77$). Vorticity shedding can also be seen at $y = 40, 50$ and 60 mm; however, the glare caused by the wing membrane has to be masked away so only part of the vorticity can

be seen. Some airflow is seen in b) at $y = 50$ and 60 mm where the masked-out vorticity pairs are expected in e). For L3B1, less apparent but similar vorticity shedding is observed in f) at $y = 70$ and 77 mm. From planes $y = 30$ to 60 , vorticity are shed in the z and x direction. In comparison to L2B1 e), the vorticity pairs are weaker and much closer to the wing, corresponding to lower speed airflow in c) at $y = 50$ and 60 mm. The flow velocity along the thrusting direction of L3B1 is less than seen with L2B1, though the relationship is reversed in Figure 4-23. As noted above, L3B1 presumably has superior instant thrust as the wing travels through the mid-plane, but less at the stroke reversal, and as such, the time-averaged force is lower.

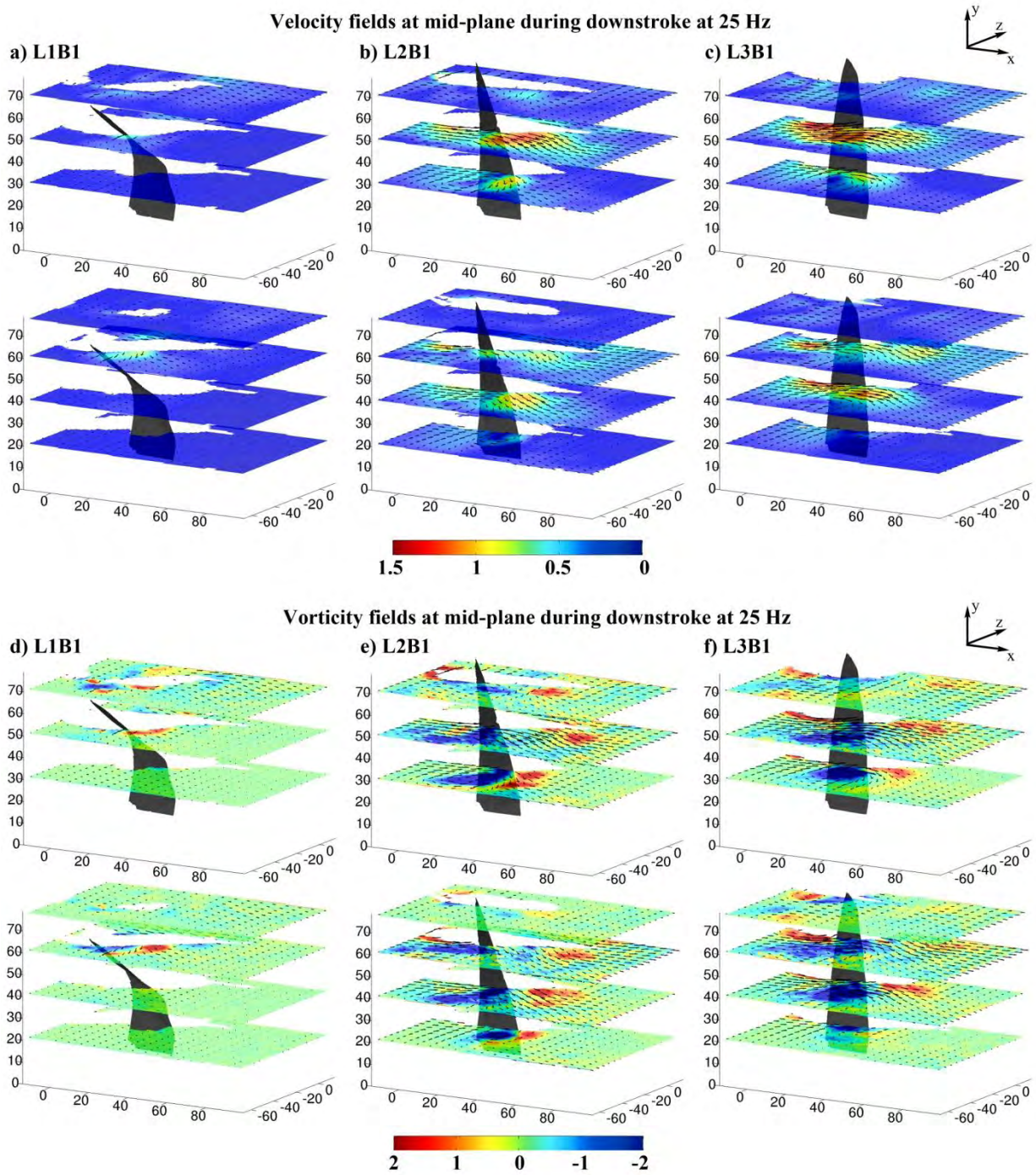


Figure 4-23. Flow structures developed around the deformed L1B1, L2B1 and L3B1 surfaces, as the wing passes through the mid-plane during the downstroke at 25 Hz.

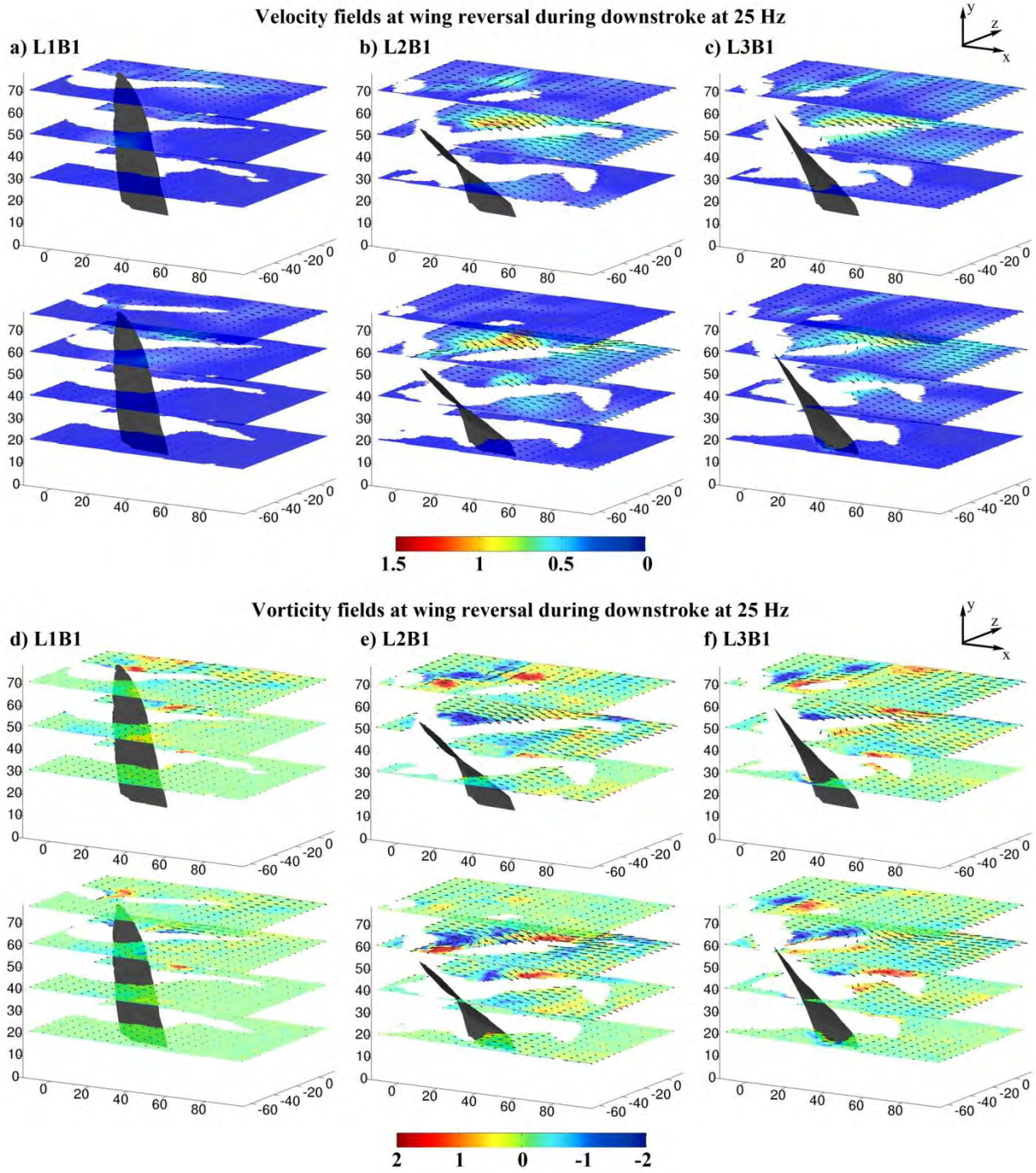


Figure 4-24. Flow structures developed around the deformed L1B1, L2B1 and L3B1 at stroke reversal (beginning of the downstroke) at 25 Hz

4.4 Discussion

Wing flexibility has been proven to be a crucial part in flapping flight in this study. Six pairs of wings, created to be comparable in both appearance and structural properties, are tested for their properties and aerodynamic performance in hovering flight that is realized with a reliable mechanism in the frequency range matching with the natural flyers'. Experiments are performed to both statically and dynamically identify their properties and to evaluate their aerodynamic performance by measuring thrust.

Results indicate that certain wing flexibility leads to an effective thrust production frequency range: more flexible wings are more thrust effective at lower frequencies and stiffer wings become superior at higher frequencies when passive deformation is induced. Furthermore, at those thrust effective frequencies, higher torsional stiffness or inertia would cause higher thrust. The reinforcement topology adopted in this study tends to decouple bending and torsional members by using leading edge and parallel battens. Leading edge reinforcement is the only factor affecting wing bending; and the wing twisting is contributed by the torsional stiffness of the leading edge, the bending stiffness of the battens and the membrane lamination constraints. As first confirmed with static elastic measurement, the variation in bending and torsional stiffness shows the anticipated trend. Slight structural asymmetry due to membrane lamination is also observed and is thought to cause different magnitudes of thrust peaks: the more flexible side achieves higher thrust.

A correlation between the first natural resonant frequency and the maximal available thrust is observed: for a particular wing, a thrust maximum can be realized near the first natural frequency. The excited deformation is expected to be a combination of mainly the first and the second mode shapes. As the flapping frequency

continues to increase over the first natural frequency, thrust does not increase and tend to decrease. Measurements on L1B1 and L1B2 have proved this idea but further study is required to confirm this observation. Because of the symmetric actuation, aerodynamic performance is only evaluated with thrust production, which is summarized as average values, maximum and minimum values, and time histories. The cycle history reveals the thrust pattern, peaks, phase and area asymmetry of each wing at different frequencies. A wing capable of generating effective thrust would have high thrust peaks and a very asymmetric pattern: producing propulsive force during both the upstroke and downstroke and avoiding negative thrust at wing reversal (such as L3B2 at 40 Hz). However, the details in creating such favored flexibility require further study to correlate structural deformation with thrust and the design capability to realize such passive deformation.

The aeroelasticity analyses are focused on three wings L1B1, L2B1 and L3B1 of identical geometries with varying stiffness through the application of DIC and SDPIV measurements. DIC results show that wing tip deflection and twist are large at both stroke reversal (where inertial forces are large) and through the mid-plane (where flapping velocity is highest, and hence the aerodynamic forces are strong), whereas a wing flapping in a vacuum has little deformation through the mid plane. For L1B1, deformation at 25 Hz shows a significant phase lag behind the actuation: aerodynamic and inertial forces are thought to outweigh the actuation bending moment at the leading edge. The path traced out by this wing is very different from the commanded actuation at higher frequencies, and the thrust is not competitive with the stiffer wings. However, for L1B1's own performance, flapping with such deformation reaches its thrust peak.

Wing deformation is superimposed with the airflow fields in order to detail aerodynamic behavior at 7 different span locations, allowing close observation of fluid/structure interaction. Only two wing positions are presented in this section: wings passing the mid-plane during downstroke and wings at reversal at the start of downstroke. The differences in both structure deformation and airflow are apparent: velocity and vorticity magnitude, location and variation of the shedding are determinant factors in generating thrust.

Interestingly, the deformation measurement results do not agree with similar tests with hawkmoth wings (Combes and Daniel, 2003^[121]): the aeroelastic behavior in air is substantially different from that in vacuum, meaning that the structure/fluid interaction is significant and the deformation consists of both aerodynamic and inertial effects. The effect of aerodynamic loads is predominant at the mid-plane and it dictates the maximum wing deflection magnitude and location. Such is true for all L1B1, L2B1 and L3B1 wings, although the complete cycle deformation is only presented with L2B1 (Figure 4-21) and only several intuitive frames of L3B1 are shown (Figure 4-18). Vacuum data for L1B1 is not available because the wings clap and crash into each other when there is no damping effect provided by the air. Therefore the structure/fluid interaction cannot be neglected for flapping wing studies.

Significant differences in aeroelastic behavior are seen across the spectrum of the tested wings: stiffer wings generally show superior thrust characteristics (through passive feathering of the elastic trailing edge) at higher flapping frequencies, though more compliant wings are preferred at lower frequencies. Furthermore, the more compliant wings tend to show peaks in thrust at actuation frequencies corresponding to

the first vibration mode, as measured with LDV. Therefore L1B1, whose first bending resonant frequency is at 23 Hz, is tested at 25 Hz in both air and vacuum. At the same frequency L2B1 and L3B1 are found to have similar deformation pattern; and the larger deformation is corresponding to higher thrust production, given that no significant phase lag is observed. In summary, this multidisciplinary experimental study has systematically examined wings of different structural properties, successfully captured their aeroelastic behaviors and identified the necessary structure properties for an effective flapping wing: flexibility and mass distribution should be tailored to a particular flapping frequency to enable passive deformation that is beneficial in generating forces. The understanding of these effects is crucial as engineers begin to introduce more complex bio-inspired features into robotic systems.

CHAPTER 5 EFFECT OF KINEMATICS

5.1 Introduction

The effect of kinematics can be categorized into two: the inertial effect caused by actuation kinematics and the aerodynamic effect caused by wing kinematics, which results from the actuation kinematics and the structural deformation. The actuation kinematics can be described with two main parameters: flapping frequency and stroke amplitude. However, the actual kinematics can be very complicated such as summarized by Azuma^[167]: three degree-of-freedom wing movement consists of the flapping, rotation and yawing motions that are functions of time. The only reason that the one degree-of-freedom case is studied here is to explore the feasibility to achieve complicated wing kinematics by passive deformation, which simplifies the actuation mechanism and therefore is beneficial in many aspects. The actuation kinematics is what caused the wing to accelerate and interact with air; its effect therefore is best examined with structural deformation contours and phase plots. The wing kinematics is what needs to be tailored for improved aerodynamic performance. For example, the outboard of the wing has much higher flexibility and velocity, the deformation should be enlarged to enhance thrust force in hovering flight; while the inboard of the wing is structurally better reinforced and slower, the deformation should be limited so that an airfoil profile can be maintained to generate lift for forward flight. Aerodynamics therefore is partially dictated by kinematics.

Natural fliers tend to maximize flapping frequency and stroke amplitude in extreme conditions such as takeoff, predation, escape and courtship. It is intuitive that these two variables are trade-offs to each other: for the same energy input, the larger the stroke

amplitude, the slower the flapping frequency, vice versa. As explained in Chapter 3, in the point mass case the out-of-plane inertial loads have quadratic relationship with the frequency but only linear relationship with the amplitude. This means the passive wing deformation is more sensitive to the flapping frequency; changing the frequency of the actuation mechanism is also much easier to realize than changing the amplitude.

Therefore it should be used as the main variable in controlling passive deformation. A higher velocity can be obtained if the stroke amplitude increases with a fixed frequency. This would have more significant aerodynamic effect than the inertial effect.

Some metrics that characterize the aerodynamics of flapping flight are summarized in the following. In hovering flight, if the chord length of wing root and mean wing tip velocity use the values of the reference length and velocity respectively, then the Reynolds number can be defined as:

$$Re = \frac{U_{ref} L_{ref}}{\nu} = \frac{2b\Phi f c}{\nu}$$

and the reduced frequency can be defined as:

$$k = \frac{\pi f L_{ref}}{U_{ref}} = \frac{\pi f c}{2b\Phi f} = \frac{1}{\Phi} \frac{c}{2b} \pi,$$

where b is the wing length, f is the flapping frequency, Φ is the flapping amplitude, ν is kinematic viscosity of fluid, and c is the chord length of wing root, respectively. In forward flight, if the forward velocity is defined as the velocity and the reference length definition is unchanged (c as above), the Reynolds number, reduced frequency and Strouhal number can then be respectively expressed as:

$$Re = \frac{U_{ref} L_{ref}}{\nu} = \frac{U_{forward} c}{\nu}$$

$$k = \frac{\pi f L_{ref}}{U_{ref}} = \frac{\pi f c}{U_{forward}}$$

$$St = \frac{f L_{ref}}{U_{ref}} = \frac{f c}{U_{forward}}$$

where $U_{forward}$ is the speed of forward flight. These metrics are used to put different flapping flight cases into comparable conditions. For example, two individuals of different wing sizes can still have the same Reynolds number if the larger one has a lower flapping frequency. This is the case for hummingbirds: a hummingbird with wing length under 70 mm may usually flap at 60 Hz to 80 Hz while a larger one with wing length 200 mm may flap at around 10 Hz to 20 Hz. In the experimental cases conducted in this chapter, both the Reynolds number and the reduced frequency are within a common range of large insects (body length over 40 mm) and hummingbirds. The wing length is set at 75 mm, the flapping frequency from 5 Hz to 45 Hz and the stroke amplitude from 40° to 90°. This means the stroke amplitude in this study is much smaller than a natural counterpart (160° or higher by hummingbirds), but the frequency is also higher for the same wing length.

The rest of this chapter will first examine the flapping frequency and stroke amplitude, presenting experimental results showing the deformation and aerodynamics variation of certain wing structures. The tradeoff between the frequency and amplitude is consequently demonstrated with a through case study. Then the effect of the second degree-of-freedom: active wing rotation, is examined with a new setup of flapping mechanism. The results show that active supination and pronation motion can indeed enhance thrust production. High frequency rotation vibration is also examined to confirm the insignificant effect of membrane structure vibration on aerodynamics.

5.2 Flapping Frequency and Stroke Amplitude

In 3.1.2 and 3.2.2, a preliminary study of the Capran wing BP (Figure 3-14) has been presented to show the structural deformation as a function of flapping frequency, which in air, demonstrate linear correlations in both wing bending (Figure 3-28) and passive twist (Figure 3-29). In this section, the investigation continues with flexible membrane wings made with Capran; but two structure topologies are selected as shown in Figure 5-1. The topology drawing is shown on the left and the actual wing photos are shown on the right. It is noteworthy that the photos have certain perspective distortion. In addition, the LEO wing has a wrinkle band resulted from membrane deformation, which is captured in the measurements and discussed later. BP is the same wing as the one used in Chapter 3: the leading edge has two layers of carbon fiber strips and an additional layer from the root to the second batten counted from the tip. LEO has only two layers of reinforcement on the leading edge, therefore more flexible in bending. There is also no battens to support or constrain the membrane deformation in LEO.

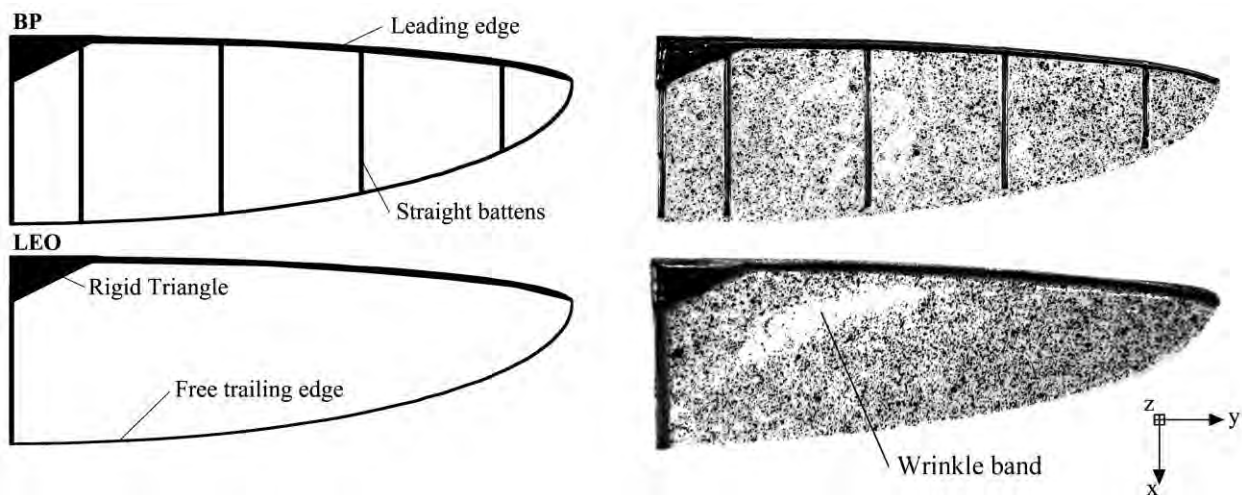


Figure 5-1. Flexible membrane wings BP and LEO studied in 5.2.

The experimental setup from Chapter 4 is used, with minimal changes including different flapping frequency range and interval resolution. The Nano17 sensor control program is upgraded so that a large number of measurements can be taken automatically. More details are presented in 5.3.2.

5.2.1 Effect of Flapping Frequency

Higher flapping frequency corresponds to stronger inertial and aerodynamic loads imparted on the flapping wings, resulting in larger passive wing deformation. Figure 5-2 shows BP's structural deformation under actuation frequencies from 5 to 35 Hz. The upper portion of the figure shows five selected frames during the downstroke for each frequency. The color contour represents the out-of-plane deformation normalized to the root chord length, which ranges from -1 to 1. The fictitious reference plane is plotted with solid grey lines to indicate the rigid body kinematics. It can be seen that the full-field DIC technique has captured all the relevant details of the structural deformation: inertial forces cause the tip of the wing to snap at stroke reversal (where the acceleration of the commanded kinematics are highest), and significant washout (wing twist) caused by aerodynamic loading near the mid-plane (where the wing velocity is highest). The complete cyclic deformation history is depicted with ω_{tip}/c and α_{twist} in the lower portion. It can be seen that at 5 Hz, the wing experience no significant deformation (also shown in the contour plots). As the flapping frequency increases, the area enclosed by the loops as well as the phase angles increases. The small structural asymmetry (i.e., slightly different behavior through the upstroke as compared to the downstroke) is due to the one-sided membrane lamination, and can be seen in the deformation phase loops, especially in the bending case shown in ω_{tip}/c .

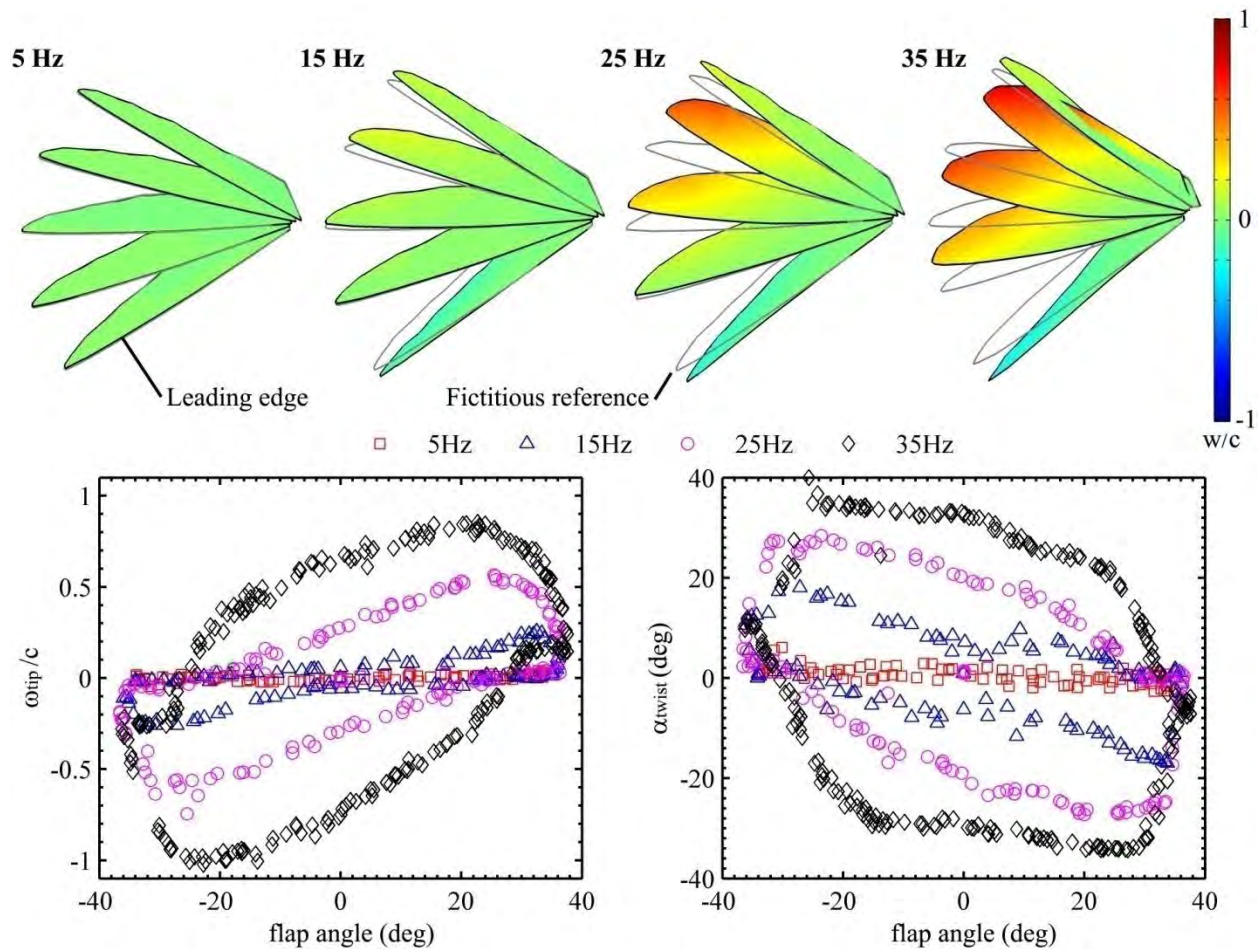


Figure 5-2. BP structural deformation at different frequencies: contour plots through the downstroke (upper plot), cyclic tip displacement (lower left), and cyclic wing twist (lower right).

Figure 5-3 shows LEO's structural deformation under frequencies from 15 to 22.5 Hz. Only downstroke of the deformation contour is shown. The color contour scale in the upper portion of the figure now ranges from -1.5 to 1.5: larger deformation is observed compared to BP, even in a lower frequency range. This is because BP has a higher bending stiffness due to an extra layer of leading edge reinforcement (Table 6-2). Furthermore, LEO's lack of batten reinforcement also allows for excessive membrane deformation. In the lower portion, the relationship between tip deflection and flap angle is similar to the data plotted above for BP, with a gradual increase in the area and phase of the loop with increasing frequency. The twist behavior, however, is distinctly

different: even at lower frequencies the wing twist is very large, reaching the peak value of 40 deg seen over the entire test matrix (BP is also constrained by this limit, as seen in Figure 5-2). Higher frequencies do not substantially alter the twisting amplitude, though the location in the flapping stroke where this maximum occurs is shifted. Such behavior would indicate an extremely nonlinear wing structure (presumably due to the lack of batten reinforcement) wherein fairly small forces cause exaggerated deformations, though increased actuation provides little additional deformation (hardening). LEO's inability to alter its twist profile during the frequency sweep probably causes the aforementioned linear relationship between thrust and frequency, which is discussed in the next chapter. This shows that the passive deformation pattern of Figure 5-3 doesn't significantly contribute to obtain extra thrust, unlike with BP, where wing deformation patterns correspond to a parabolic increase in thrust production. This result would indicate that wings with excessive flexibility may not be ideal to achieve high thrust, albeit they can be very efficient.

The formation of the wrinkle band in Figure 5-1 can be traced in Figure 5-3 at 20 Hz and 22.5 Hz, in which right after the wing reversal the leading edge forms a small curvature radius near the root. Another cause for the wrinkle is the aerodynamic pressure acting on the membrane at high frequencies. This means the parallel battens in BP do provide structural support and would lead to better aerodynamic performance as compared in Chapter 6. Higher frequency data of LEO is desired, however, the system would require more cameras to measure further excessive deformation.

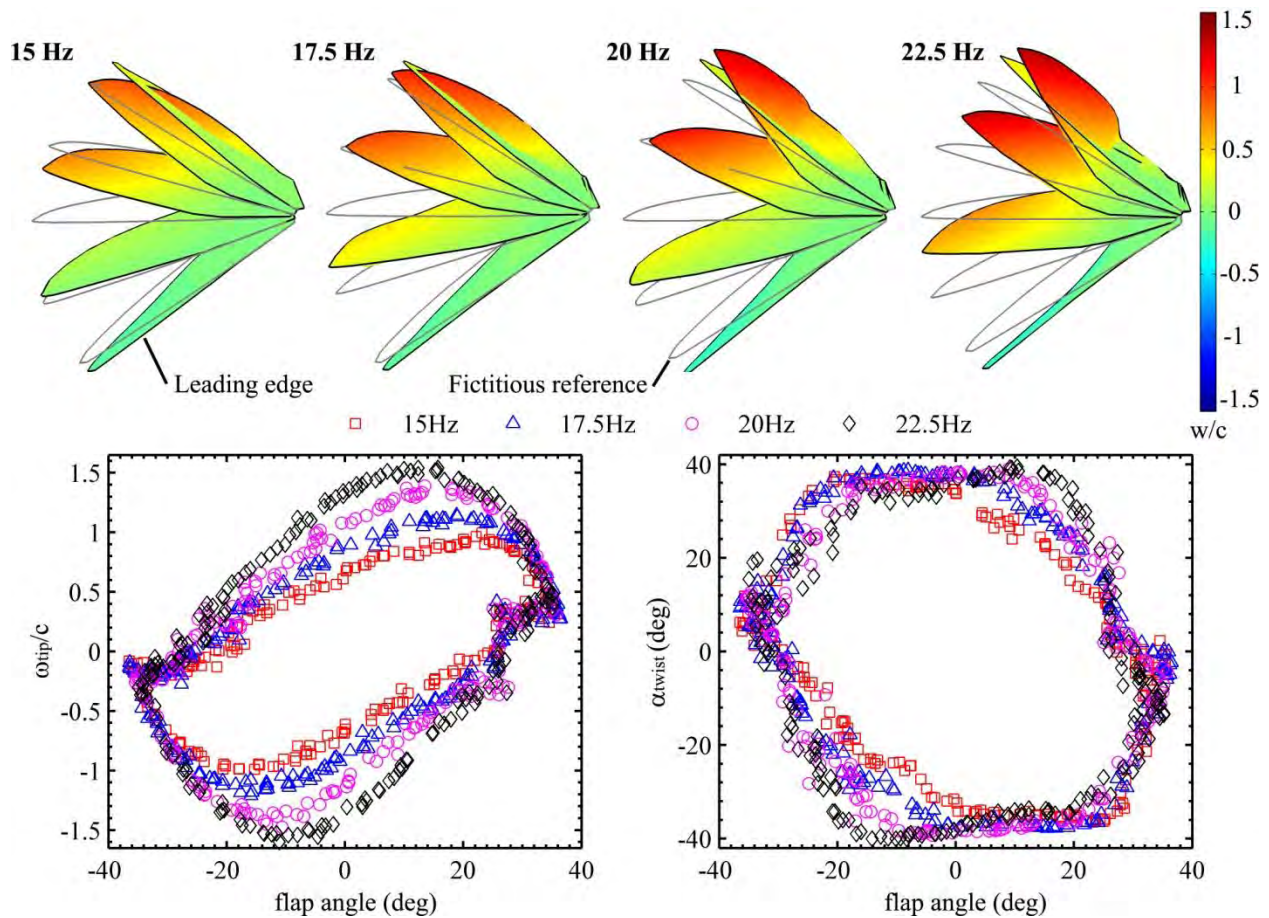


Figure 5-3. LEO structural deformation at different frequencies: contour plots through the downstroke (upper plot), cyclic tip displacement (lower left), and cyclic wing twist (lower right).

5.2.2 Effect of Stroke Amplitude

The wing BP is further studied to seek the effect of stroke amplitude, which is set at 40°, 60°, 70° and 90° here. The trend of the thrust and its coefficient varying with different flapping amplitudes and frequencies is shown in Figure 5-4. It can be seen that although the net thrust keeps increasing with larger amplitude and faster stroke to 9 grams (~0.09 N) at 35 Hz 90 deg, the thrust coefficient actually reaches a plateau due to the trade-off between power input and net force output. This result indicates that an optimal flapping wing must be defined at a certain frequency and amplitude (kinematic

parameters) and optimized for values such as thrust coefficient, efficiency, lift coefficient (for forward flight), etc.

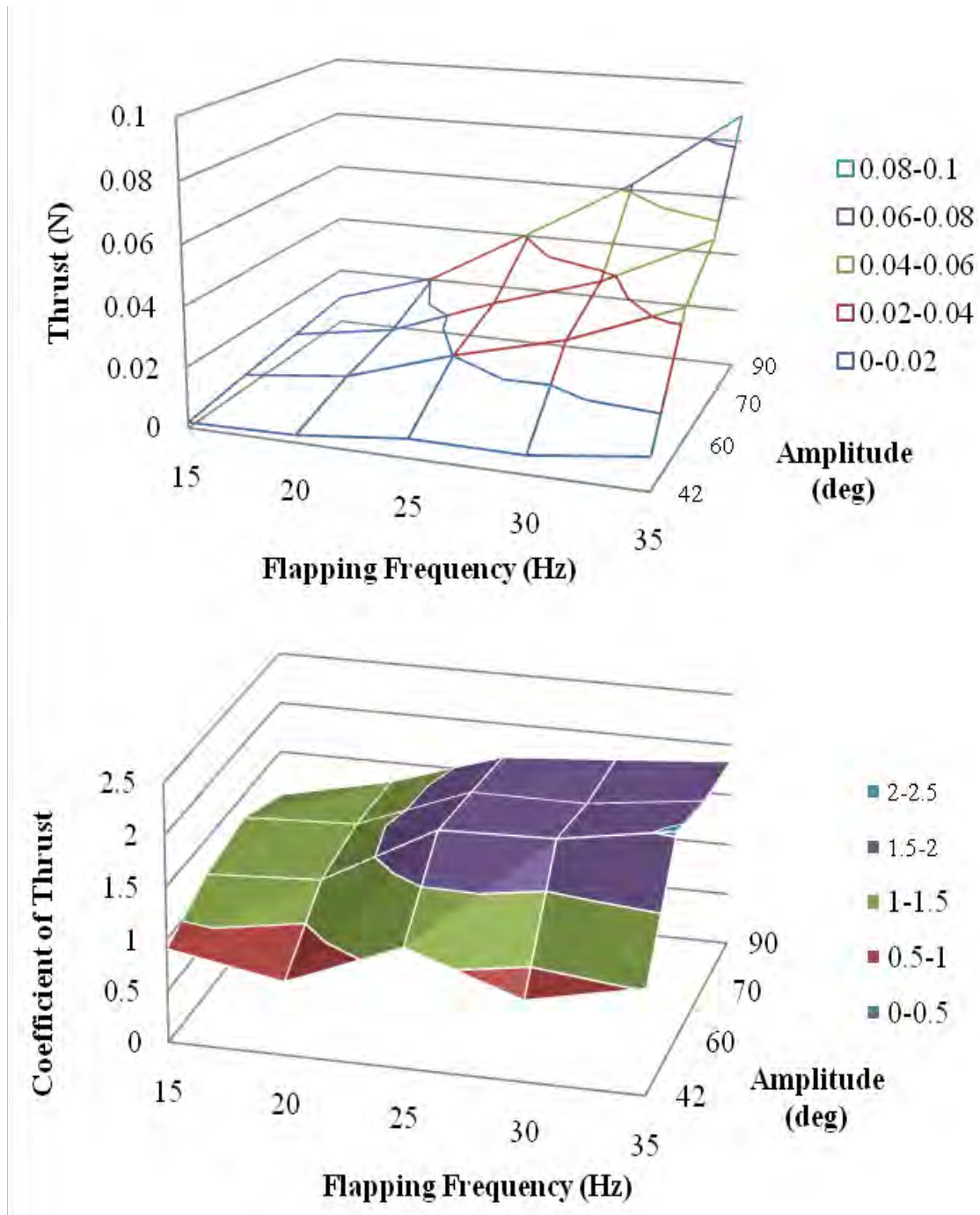


Figure 5-4. Thrust and its coefficient at different flapping amplitudes and frequencies.

An interesting aspect of varying flapping amplitude is to see if there is a tradeoff between frequency and amplitude: can a wing use higher frequency to compensate for smaller amplitude to produce the same amount of thrust as larger amplitude for lower frequency? For the stroke amplitude at 40°, flapping frequency was driven to 45 Hz to see the increase in net thrust. Detail data are presented in Table 3. At 40°, net thrust slightly increases from 35 to 40 Hz but then decreases from 40 to 45 Hz. Coefficient of thrust keeps decreasing as the frequency is driven up. This shows that for a certain wing structure, frequency is not always the most effective variable in increasing thrust force. It depends on the effective frequency range that would cause the wing to deform without consuming excessive power, as will be discussed in the next chapter. However, if thrust coefficient is compared, the case of 90° amplitude at 15 Hz is almost the same as the case of 40° amplitude at 35 Hz; so is the case of 60° at 15 Hz and the case of 40° at 25 Hz. Therefore there is indeed a certain level of trade-off between frequencies and amplitudes, because the both values contribute to aerodynamic and inertial loading ($a_{end} = 2\pi^2 f^2 \Phi l$ and $v_{mid} = \pi f \Phi l$, for the acceleration at the end of each stroke and the wing speed at the mid-plane, respectively. Detailed assumptions and limitations have been presented in 3.2). A more intuitive illustration is presented in Figure 5-5, with data from the DIC deformation measurements.

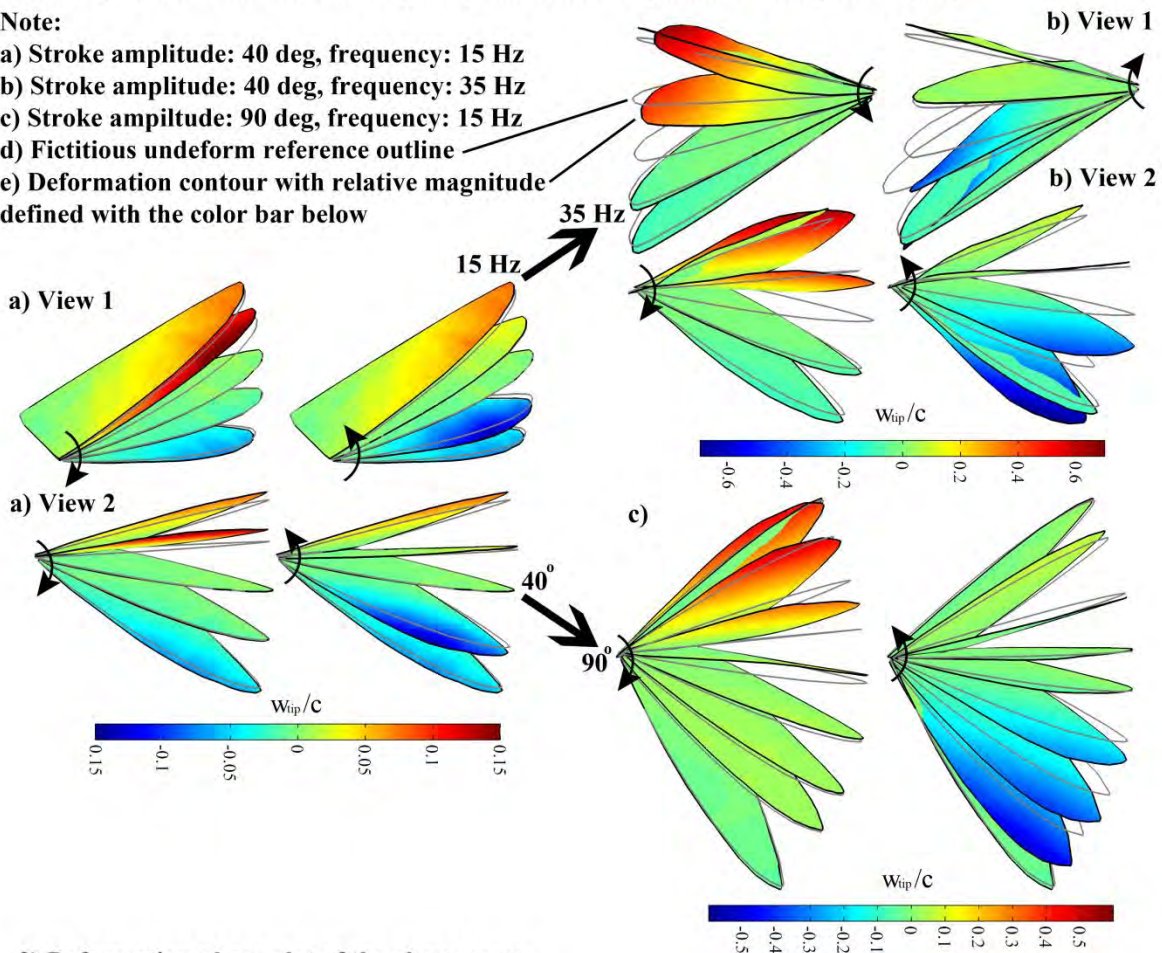
Table 5-1. Experimental data at different frequencies and stroke amplitudes

Thrust (N)					Coefficient of Thrust				
	40°	60°	70°	90°		40°	60°	70°	90°
15 Hz	1.80E-03	4.60E-03	6.90E-03	9.40E-03	15 Hz	0.91	1.16	1.27	1.05
20 Hz	2.50E-03	8.60E-03	1.26E-02	2.06E-02	20 Hz	0.71	1.22	1.32	1.30
25 Hz	6.30E-03	2.01E-02	2.62E-02	4.11E-02	25 Hz	1.16	1.82	1.74	1.66
30 Hz	6.10E-03	2.94E-02	3.76E-02	6.21E-02	30 Hz	0.78	1.85	1.74	1.74
35 Hz	1.08E-02	4.40E-02	5.53E-02	8.89E-02	35 Hz	1.02	2.04	1.88	1.83
40 Hz	1.34E-02				40 Hz	0.97			
45 Hz	1.26E-02				45 Hz	0.72			

1) Comparison of the effect of frequency and stroke amplitude on wing B1111 (BP)

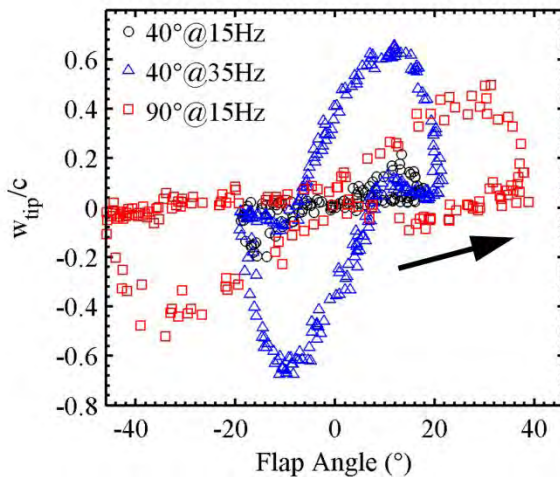
Note:

- a) Stroke amplitude: 40 deg, frequency: 15 Hz
- b) Stroke amplitude: 40 deg, frequency: 35 Hz
- c) Stroke amplitude: 90 deg, frequency: 15 Hz
- d) Fictitious undeform reference outline
- e) Deformation contour with relative magnitude defined with the color bar below



2) Deformation phase plot of the above cases

Tip deflection comparison



Wing twist comparison

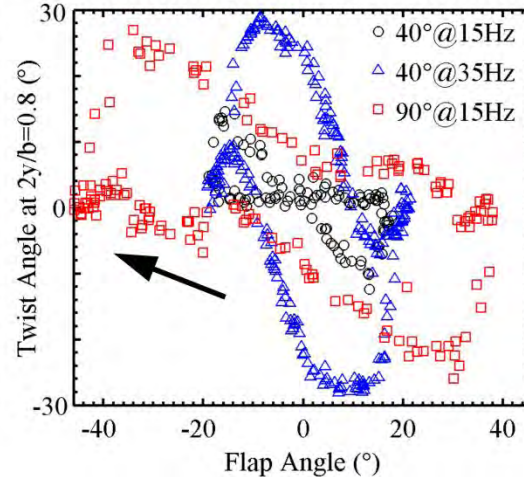


Figure 5-5. Deformation contour and phase plot of BP under the effect of frequency and stroke amplitude. Note that case 40°@35 Hz has the same thrust coefficient as case 90°@15Hz.

In Figure 5-5, the effect of the two variables frequency and amplitude is presented with both color contour for instances and phase loops for a complete cycle. The color contour has independent magnitude range for each case: 0.15 for 40°@15Hz, 0.7 for 40°@35Hz and 0.6 for 90°@15Hz. The maximum deformation is usually a result of both aerodynamic and inertial loading near the end of each stroke; its occurrence and magnitude can be observed in the phase plot. The phase loop uses two metrics to evaluate wing bending and twisting deformation – tip deflection normalized to the root chord and the twist angle in a selected cross section. It can be seen that the effect of frequency (40°@35Hz) induces the wing to deform in the same level of magnitude as the effect of stroke amplitude (90°@15Hz). This is coherent with the previous comparison between thrust coefficients.

5.3 Wing Rotation

The goal of this section is to understand the effect of active wing rotation in the aerodynamic performance of micro air vehicle flapping wings. Mimicking biological flight, flapping wing micro (or nano) air vehicles have been successfully developed by [Aerovironment](#) Inc. However, the flapping wing aerodynamic mechanisms have not been fully unveiled; especially on the topic of wing structure optimization for flapping flight. Such structure optimization is intended to enhance aerodynamic performance by passive wing deformation that results from the coupled inertial and aerodynamic loads. On the other hand, active kinematics can be used to create lift and thrust with stiff wings. Therefore, flapping wing structure can also be tailored with kinematics to achieve optimized efficiency. It has been observed that birds fly with different gaits and insects fly with different stroke patterns at different speeds. Actively controlling the wing rotation and vibration can change the interaction between the wing surface and the surrounding

air. Magnetic coil actuators are combined with a one degree-of-freedom flapping mechanism to realize the two degree of freedom kinematics up to 15 Hz. Besides synchronizing the rotational actuation with the flapping motion, the actuators are also actuated at much higher frequencies (from 30 to 1000 Hz) to examine the effect of vibration (multiple rotations during one flapping stroke). This would also allow the wing to exhibit dynamic properties during flapping. The results show that magnetic coil actuators can be used to effectively induce wing rotation during flapping and affect aerodynamics; the phase difference between the flapping and rotation motion can increase or decrease aerodynamic performance; and the high frequency structural vibration has insignificant impact on aerodynamics.

5.3.1 Overview

The flight of bumblebee has caused scientific fascination and aerodynamic mystery in the past, when people could not use steady aerodynamic theories to calculate enough lift with the given wing area and speed. Even today, the lift enhancement mechanisms involved with bumblebee's unsteady aerodynamics have not been completely identified. Although Bomphrey et al.^[168] have found that such flapping flight is not as efficient as imagined, the amount of lift generated with the flapping wings is still surprisingly high. Perhaps as intractable as the unsteady aerodynamics, the wing kinematics that causes these effects remains to be understood. While it is important to observe the insect flight with high speed cameras that are prevalent nowadays in millions frames per second, it is also necessary to study flapping flight with engineered objects under well controlled experimental environment. Significant aerodynamic forces can be produced with one degree of freedom (1-DOF) flapping motion and passive flexible wing deformation as has been shown in our previous work^[140]; however, such

wing motion may only be efficient in forward flight. The hovering efficiency of 1-DOF kinematics would be argued against with what has been observed in nature, where pronation and supination are important aspects in aerodynamics. Therefore the objective of this work is to identify the effect of wing rotation during flapping.

Dickinson et al.^[31] in 1999 pointed out that the role of wing rotation is essential in producing lift in hovering flight. The aerodynamic enhancement in insect flight results from delayed stall, rotational circulation and wake capture, of which the latter two generate aerodynamic forces during stroke reversals. The authors observed that the timing of active pronation and supination with regard to flapping motion is critical in producing rotational circulation and wake capture. Figure 5-6 shows a general scheme of insect hovering on the left, and three different stroke timings on the right (adopted from Shyy et al.^[18]) The illustrated x-y-z coordinate applies to the following experimental setup and data analysis. The advanced, symmetrical and delayed schematics of wing supination and pronation show the wing rotation at the end of each stroke. Although such a representation has simplified the actual kinematics performed by insects, it calls for a particular technique to quantitatively measure such rotational motion. Wu et al.^[169] have applied Digital image correlation and successfully measured such two degree of freedom (2-DOF) motion. Ellington^[9] has documented several insects' hovering kinematics with detailed wing path in different flight modes and airfoil cross section at discrete locations by hand drawing from high-speed film footage. His drawings show slight variations of kinematics within the same species in the same flight modes, from which he raises questions about the passive wing deformation in the observed kinematics. Such observation marks the importance of distinguishing the aerodynamic

deformation from the inertial effect. However, before effort is spent on understanding the aeroelastic aspect of the problem, the aerodynamic effect brought by the 2-DOF kinematics must first be identified.

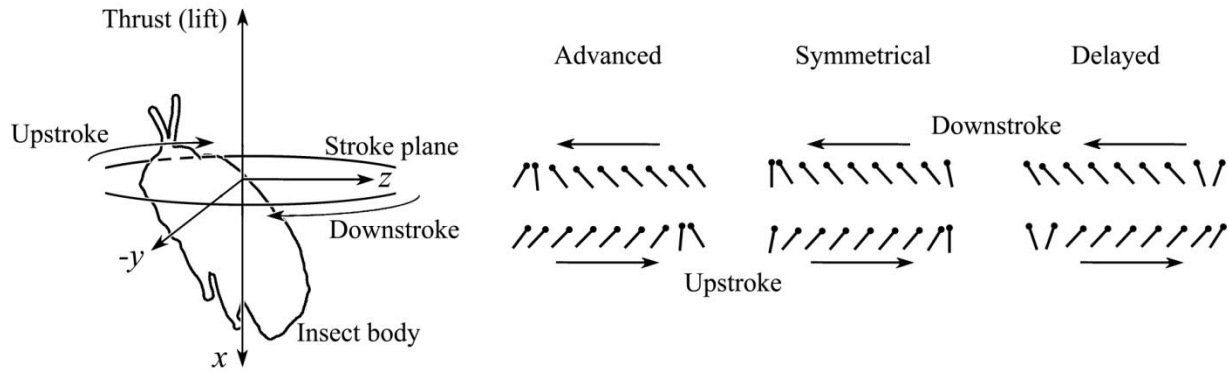


Figure 5-6. General scheme of insect hovering, coordinate system and stroke plane shown on the left, and the three different stroke timings shown on the right, adopted from Shyy et al.³

From a theory stand point, hovering fluid dynamics has been studied by Gustafson^[85] for $Re = 100$ and 400 , with experimental results presented, a new structural stability theory postulated and other theoretically related dynamic systems examined. Beran et al.^[170] uses computational frame work to synthesize and optimize flapping wing designs, considering both aeroelasticity and complex kinematics. From a biological reference stand point, Azuma^[167] has in detail documented the dragonfly flight mechanics, kinematics parameters and analysis. Altshuler and Dudley^[78] have measured hummingbird kinematics, in which the values for stroke amplitude and wing beat frequency can guide MAV designs. Several other species of great reference importance are studied: Dudley and Ellington^[70] studied bumblebees, measuring wing path and body kinematics; Willmott and Ellington^[68] studied hawkmoths, using videography to record wing kinematics. Finally, a comprehensive study by Tobalske et al.^[79] on the three dimensional kinematics of both hovering and forward flight of

hummingbird has detailed the wing tip trajectory and chord angle (wing rotation) during wing beat. All these studies serve as great references to understand flapping flight, however, the relationship between the aerodynamics and the kinematics could not be quantified due to limited experimental techniques. Therefore, this work attempts to bridge the causal link between the two. In addition to understanding how different actuation phase between the flapping and rotational motion would affect aerodynamics, this work expands the scope into investigating if active vibration of the wing structure would positively contribute to the aerodynamics.

The rest of this section is organized as follows. First, the 2-DOF actuation mechanism, which emphasized on the rotation mechanisms and includes a new control scheme, is introduced. Then the tested wing used in this study is described, followed by the explanation of the aerodynamic loads measurement procedure. Finally, the experiment results are presented and discussed.

5.3.2 Experimental Setup

The experimental setup includes a flapping mechanism, two wing rotation mechanisms, a control system, flexible membrane wings, and a force measurement system. The flapping and rotation mechanisms constitute the actuation mechanism, allowing the performance of insect-inspired kinematics. The control system is developed to actuate the wing rotation so that phase difference between the flapping and rotational motion can be achieved. The flexible membrane wings are made of composite skeletal structure and extremely thin membrane to reduce the overall inertia. The force measurement system is used to evaluate the aerodynamic performance of the wings. The mechanism FL2D3 (Figure 4-3) is used to perform the flapping motion.

Rotation mechanism

Magnetic coil actuators (MCA) have several advantages in realizing reciprocating motion such as flapping or rotation: 1) Because it does not require other mechanical parts to transform rotational motion into reciprocation, the inertia of moving components has been reduced and friction only exists at one pair of rotation bearings. Therefore it is the most direct (and therefore most efficient) way to transform electricity into flapping kinetics. 2) The actuation frequency can be very accurate and only dependent on the input signal. 3) A very wide range of frequency and amplitudes (the only limitation on actuation frequency and power is heat produced by the wires, if superconductive conditions can be achieved, any frequency and amplitude can be realized). 4) Different actuation waveform can be selected, the input signal can even be a function under any control algorithm, therefore it has great potential in sophisticated control designs. However, there are also some disadvantages: 1) The actuation can only be a torque without any mechanical magnification, therefore the kinematics cannot be controlled. 2) The current electronics and controllers are over-sized and over-weight if a wireless flyer is attempted. However, for the research objectives, MCA is ideal for creating the rotation motion.

A MiniAct magnetic coil actuator is used to realize the rotational degree of freedom, as shown in Figure 5-7. A free rotating pin assembled with two cylindrical magnets is placed in a mounting frame. A magnetic coil ring fits outside the frame. The magnetic field of the powered coil ring will be perpendicular to the magnetic field of the magnets assembly; therefore a torque will be applied to the pin assembly, causing the wing to rotate. A third magnet is placed outside the coil ring to hold the wing at a neutral position. The actuator is modified for mounting the wing to the flapping mechanism so

that the leading edge of the wing will rotate near the axis of the pin assembly and the wing's leading edge (axis y when the wing is placed horizontally) rotates in an axis parallel to the pin's axis. Therefore the wing will be flapping in the y-z plane and rotating around the magnetic pin assembly.

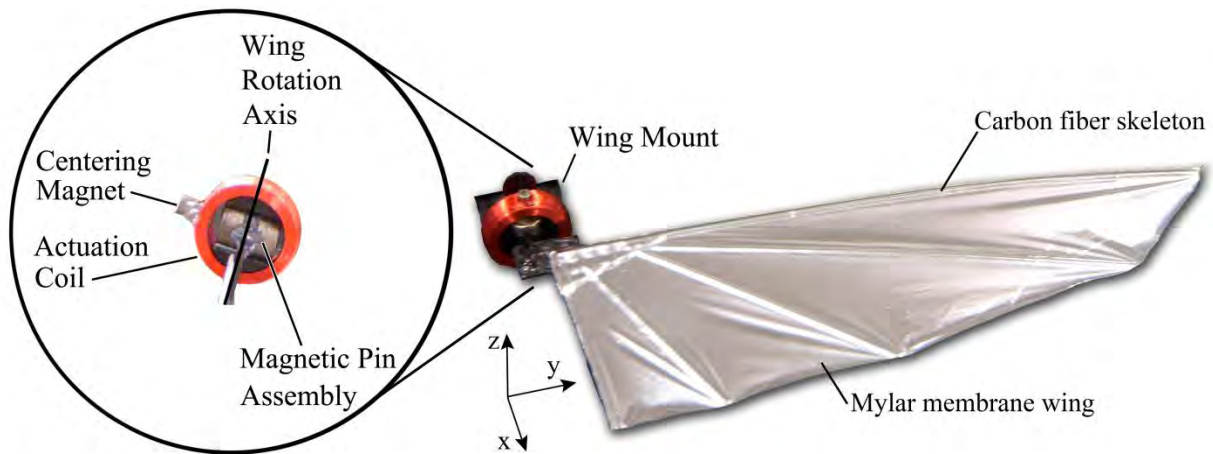


Figure 5-7. Rotation mechanism and the flexible membrane wing.

When the coil is not powered, the wing is held at the neutral position due to the equilibrium state between the permanent magnets of the pin assembly and the one outside the coil; but when the coil is powered by a direct current, a torque is applied to the magnetic pin assembly for actuation, as explained in Figure 5-8. This can be seen as the integration of each moving electrons in the coil experiencing the Lorentz force to form the macroscopic Laplace force. Via integration, the torque, which is proportional to the magnitude of the current, can be expressed as the following equation below.

$$T = \frac{4nBUrd \sin \theta_{lim}}{R}$$

where T is the torque applied to the magnetic pin assembly through the coils, proportional to the current (U/R).

n is the number of revolutions of the coils surrounding the magnets.

B is the magnetic field magnitude in Tesla, a constant value in this case.

U is the direct current voltage, controlled with a in-house program with an amplifier.

R is the coil resistance, 50 Ohm in this case.

r is the radius of the coil, an average value should be taken here because of the coil thickness.

d is the distance between the magnet poles to the rotation axis.

and θ_{im} is equal to the inverse tangent of magnet radius over d.

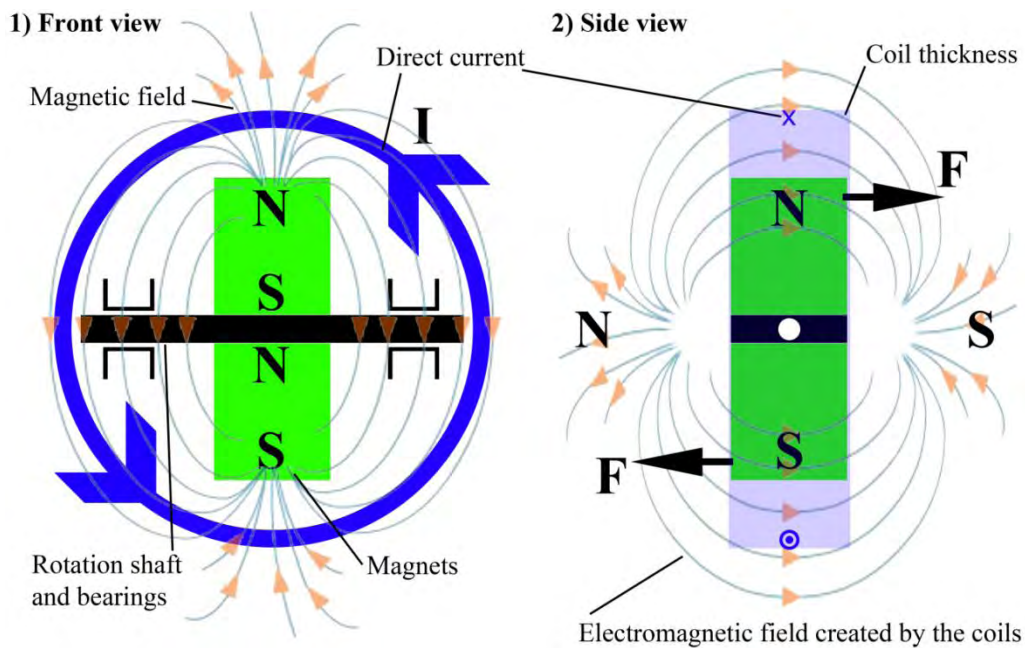


Figure 5-8. Actuation illustration for magnetic coil actuators.

In this study there are only two variables: U and R. The voltage input is controlled by the program and the resistance is not controlled. The resistance of the coil changes slightly as it heats up. Therefore the experiment does not allow long time operation. Heat will be dissipated between experiments so that its effect on the coil resistance can be neglected. The magnetic coil actuator is able to produce 26 gmm torque at 3.5 V and

it allows for a 90° ($\pm 45^\circ$) rotation amplitude. The MCA needs to be installed with carbon fiber parts for installation with the flapping mechanism and the wings. The carbon fiber structure extends the magnetic pin assembly so that the wing can be attached without interfering with the rotation. The overall mass of each of the modified MCA is 1.23 grams.

Therefore, combining both flapping and rotation mechanisms, a 2-DOF kinematics can be realized to actuate the flexible flapping wings. The overall assembly is shown in Figure 5-9. In summary, the actuation mechanism is able to perform a $\pm 35^\circ$ flapping and $\pm 45^\circ$ rotation motion. In this test, maximum frequency is set to 15 Hz because under this frequency significant time averaged thrust cannot be usually produced with 1-DOF motion. Therefore this new setup can potentially make a clear difference caused by different kinematics, if any.

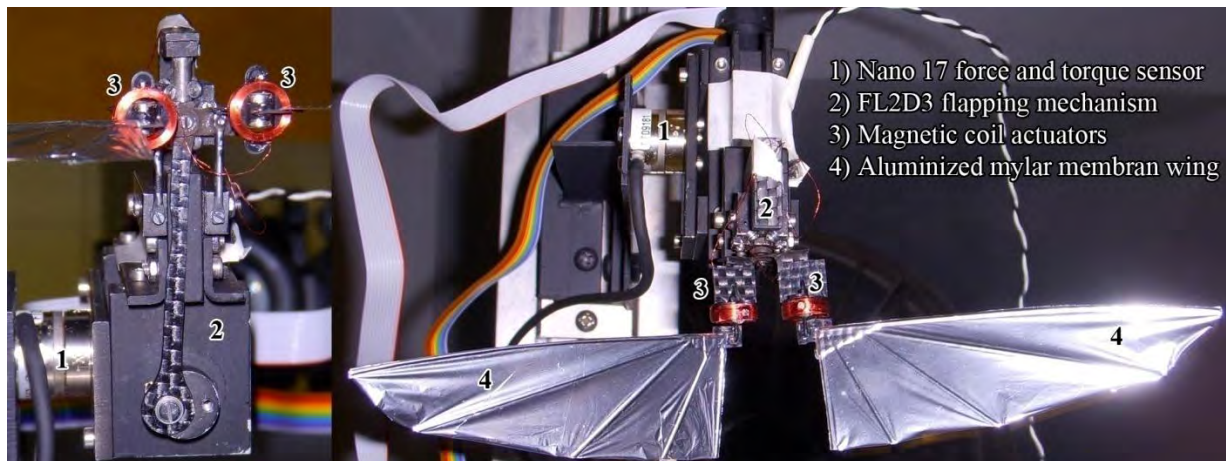


Figure 5-9. Overall experimental configuration.

Rotation kinematics verification

The rotation degree of freedom is examined first with a semi-rigid carbon fiber wing that allows for inertia induced passive rotation. The mechanism is then actuated at a frequency that allows the wing to reach maximum rotation at wing reversal. DIC is

used to measure the kinematics. Since the rotation is passive, the wing kinematics is symmetrical as described in Figure 5-6. This verifies the rotation amplitude as well as the capability of DIC for future studies. The correlation results are presented in the following figures. Full-field plots of five selected frames along the downstroke and the upstroke are shown in Figure 5-10, while a plot of the airfoil motion at two spanwise locations along the wing (at the 30% and 75% of the wing length) is given in Figure 5-11, rendered in two dimensions. Finally, the phase relationship between the flapping angle and the rotation angle is given in Figure 5-12.

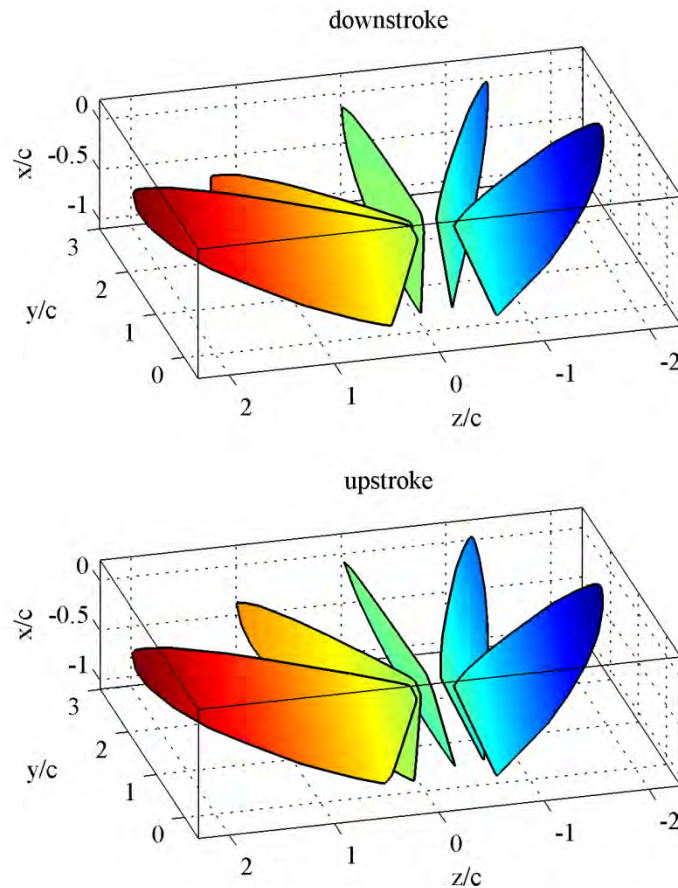


Figure 5-10. Full-field contour plot of downstroke and upstroke wing kinematics.

The color contour of Figure 5-10 is proportional to the transverse distance (z) between the static wing at mid-plane and the dynamic wing. The angle between the

contour lines and the wing root is indicative of the rotation; for pure flapping, the two lines will be parallel. The wing rotation is a passive mechanism based upon the inertial forces of the flapping motion; these forces are largest during the flapping stroke reversal, which is where the majority of the wing rotation is found, as seen in Figure 5-11. The motion is not completely symmetric along the up and the down strokes. At the beginning of the upstroke, the wing undergoes a large angular velocity (potentially providing large rotational aerodynamic forces), and some finite rotation is seen as the wing travels through the mid-stroke. During the downstroke, however, the wing is vertical as it travels through the mid-plane, clearly seen in Figure 5-10. This asymmetric rotation probably results from slight irregularities in the commanded flapping motion or the mechanism.

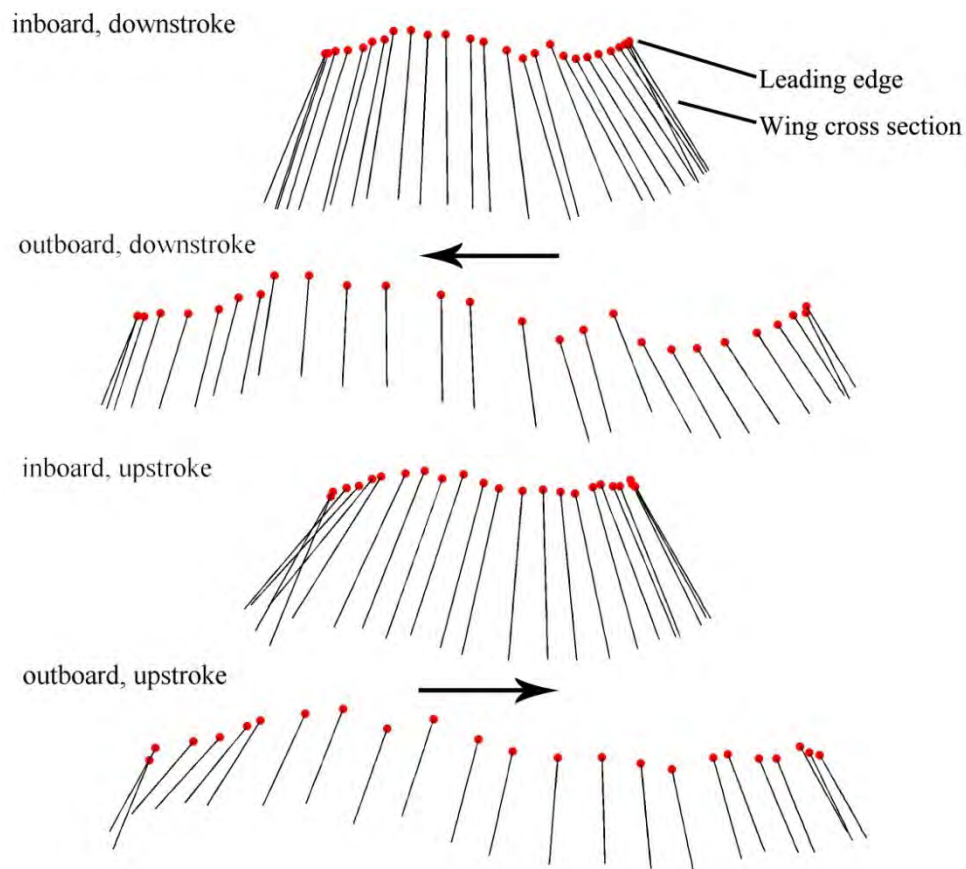


Figure5-11. Wing kinematics of two cross sections.

It can also be seen in Figure 5-11 that some minor yawing motion is encountered during the flapping stroke, as the leading edge travels up by about a quarter-chord shortly after the end of the downstroke, then travels down by the same amount prior to the end of the downstroke. The same motion is seen as the wing travels through the downstroke, forcing the leading edge to trace out a slight “s” shape. As before, these motions are probably due to slight irregularities in the flapping mechanism. This motion appears to mildly discontinuous in Figure 5-11, a result of the progressive scanning cine method described above: the flapping motion can be reconstructed for results seen below, but consecutive wing positions are actually measured from distinct flapping cycles.

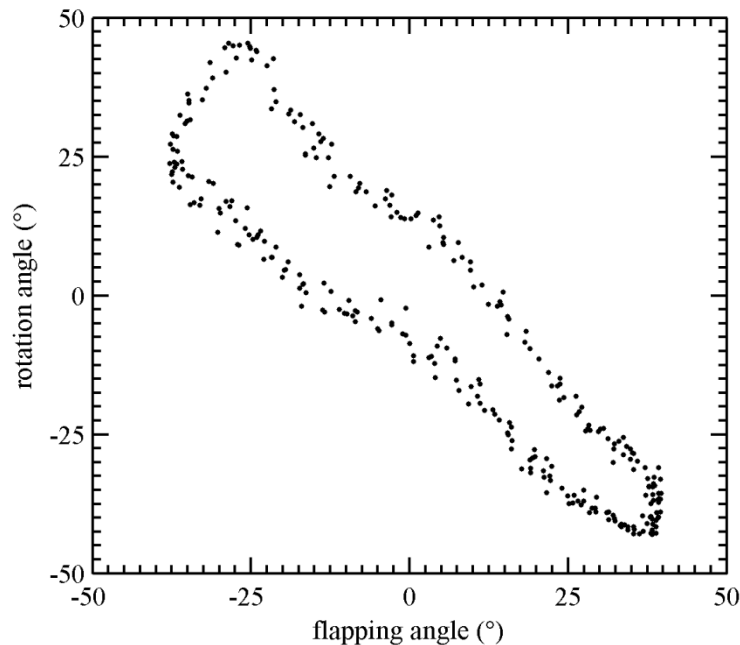


Figure 5-12. Rotation angle and flapping angle relationship.

The phase relationship given in Figure 5-12 indicates that both the flapping mechanism and the subsequent passive rotation mechanism are capable of amplitudes on the order of 45°. A slight hysteresis loop develops, which may be a result of

aerodynamic forces effecting the passive rotation. The lower leg of the phase plot is the downstroke, as the rotation angle is zero when the flapping angle is zero (i.e., at the mid-stroke). As discussed above, the upstroke as a finite rotation angle at the mid-stroke. The hysteresis loop is also wider at the end of the downstroke, potentially indicative of the large angular velocities noted above. Finally, the progressive scanning cine data of Figure 5-12 also shows some non-repeatability in the measurement of the rotation angle for a given flapping angle. This may be due to measurement error/resolution, aperiodic rotational response (due to either aerodynamic loads or nonlinearities within the wing deformation), or higher-ordered harmonics in the vibration history. Regardless, this effect is small, and the data spread about the mean hysteresis loop is very tight.

Tested wings

The wings tested in the current work are shown in both Figure 5-7 and 5-9. The planar design, with a Zimmerman planform, has an aspect ratio of 7.65. The Zimmerman shape is formed by two ellipses which intersect at the quarter-chord point. For comparison, this planform is selected to be the same as many previously tested wings, but the wing length is 80 mm and the root chord length is 26 mm. A radial batten structure is chosen because it provides reinforcement in both bending and torsional directions¹. The detailed dimensions are shown in Figure 5-13. The root chord reinforcement is offset with a small angle to avoid collision.

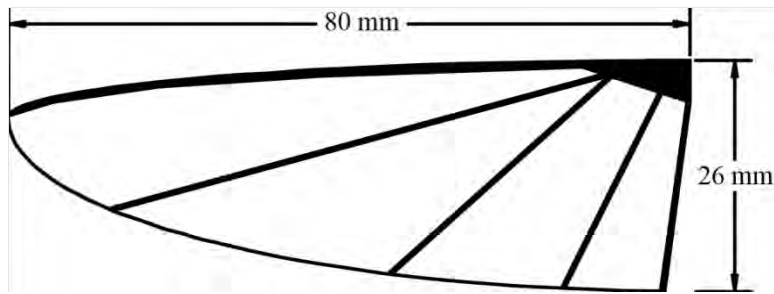


Figure 5-13. Tested wing skeleton layout.

Because a complicated kinematics is used in this study and the aerodynamic effect of active wing rotation is to be examined, the wing inertia is preferred to be low so that the related passive wing deformation effect can be ignored (This is first tested with a 1-DOF motion as a group of control data, which is insignificant compared with flexible wings that has larger passive deformation). Unidirectional Carbon fiber and a 2 micron thick Mylar membrane (density: 2.6 g/m^2) are used for wing construction. At the intersection of the leading edge and the root chord, a two-layer bidirectional carbon fiber triangular plate is placed to sandwich other structures. All unidirectional carbon fiber strips are of 0.5 mm width. The leading edge and the root are reinforced with two layers while other battens are all with one. The Mylar membrane is cured together with the carbon fiber structure, therefore slight pretension exists in the wing and the membrane stays taut even when unloaded. The weight of the resulting wings is 0.04~0.05 grams, most of which is located at the carbon fiber triangular plate.

Control system

An ideal control system to investigate the effect of the phase difference between the flapping motion and the wing rotation should be able to send out rotation control signals based on the actual flapping position. This would require sensors that measure the actual wing position and feedback to control rotation accordingly. In this work,

however, the control programs for the flapping and the rotation motion are separated, due to limited resources. But this is sufficient to achieve the objectives in understanding the effect of 2-DOF kinematics on aerodynamics. The control program for the flapping motion is a virtual instrument (VI) developed in LabVIEW. It commands the motor controller to execute a velocity profile with PID algorithm. Details pertaining this program can be found in Chapter 4.

The control system for the MCA consists of a computer with an audio output and an amplifier (such as the ones built in speakers). The computer is used to generate an audio signal that contains the wave form, frequency, phase and amplitude. This signal is then amplified with the amplifier so that enough power can be supplied with the signal to actuate the MCAs. The control program is a graphic user interface (GUI) written in MATLAB. The present version outputs a square wave signal so that the MCAs can apply a torque at the instant of command, therefore changing the timing of wing rotation as the phase difference changes. This can produce the three different stroke timings shown in Figure 5-6. The GUI has three inputs: signal duration, frequency and amplitude.

The phase difference (ϕ) between the wing rotation with respect to the flapping motion can be varied by controlling either flapping or rotation motion. If the frequency of each motion can be kept a constant, then by controlling the phase of each motion, the phase difference can be defined. However, with the present experimental equipment, it is only feasible to utilize the fluctuating mechanical flapping frequency. Because the PID motor controller cannot keep the actual frequency to be an absolute constant; a small error is always present. This amount of frequency fluctuation (similar to a random phase

shift) can be combined with the accurate electronic signal for MCA to achieve a sweep of phase difference from 0 to π , automatically and periodically. The downside is that the actual phase difference cannot be measured. The control scheme is shown in Figure 5-14. Both the amplitudes of the flapping motion and the control signal are normalized to 1 in one flapping cycle. This 2-DOF actuation method uses acceleration input (torque) instead of constraining the wing kinematics. Therefore the actual wing position would depend on the aeroelastic loading.

There are three adjustments in the power magnitude: the GUI can control the output volume to the operation system; the operation system has a master volume control and the amplifier can also adjust the amplification ratio. An 1000 W power amplifier (PylePro PTA1000) is used and the volume is set at +16 dB. During experiment, the GUI volume amplitude is normalized to 0~1 and the volume of the computer is always set at the maximum (computer model: Dell Latitude D800). Two levels of power amplitude are set in the tests, 80% and 100%.

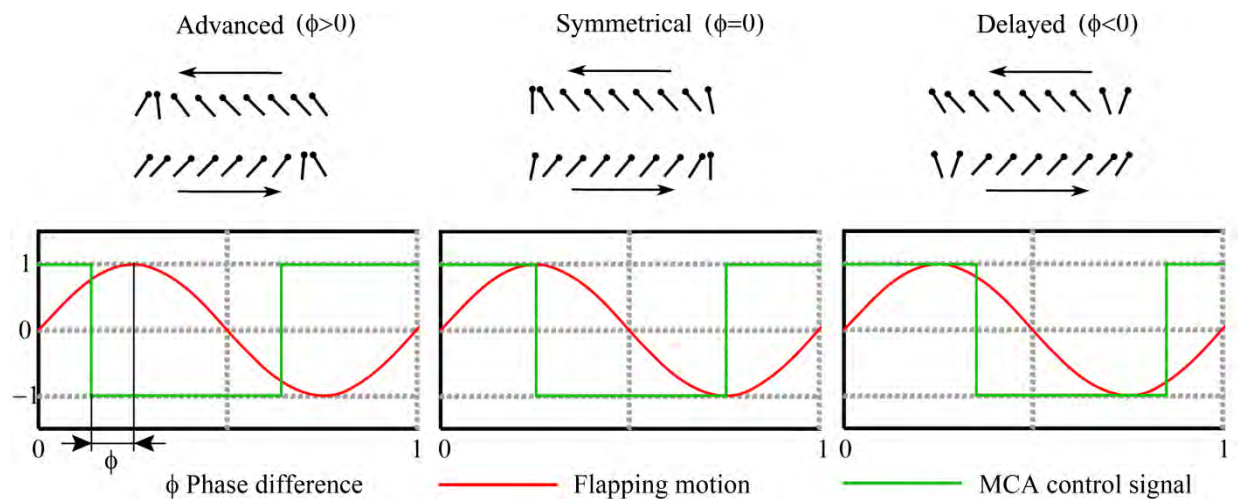


Figure 5-14. MCA control signal and flapping motion phase difference in the three different hovering modes.

Force measurement system

The force measurement system consists of a pulse generator, a force and torque sensor Nano 17, data acquisition system and the encoder on the FL2D3 flapping mechanism. The pulse generator is used to provide tagging signals to synchronize the motor position reading and the force measurements. A 100 ms interval pulse signal is combined with other measurements in the data acquisition system, which contains two NI-DAQ 6220 data acquisition cards. A simplified configuration layout is shown in Figure 5-15. It shows each piece of hardware and its function in the measurement system.

The force and torque sensor is Nano 17 from ATI Industrial Automation Inc. (<http://www.ati-ia.com/>). The sensor is mounted underneath the flapping mechanism, as shown in Figure 5-9. The sensor has 0.319 g of force resolution, which is adequate for the current application. The forces in the x and y directions correspond to the thrust and lift directions; both have the stated measurement resolution. The Maxon motor EC16 used in the flapping mechanism is assembled with an MR encoder with Hall sensors. The output from the encoder is a two channel quadrature signal as shown in Figure 5-6. The signal is repeated 256 times per revolution. The phase lag between the can tell the rotation direction and the position can be tracked with a 1/1024 turn signal resolution. After the ratio reduction due to the gearhead, the precision with which the flapping phase can be measured is 1/4490 of a turn. The output is intended to be used for PID control, but can also be combined together with the synchronization pulse signal.

Two NI-DAQ 6220 cards are used. This 6220 model can capture up to 8 differential or 16 single ended analog inputs simultaneously at an aggregate sampling rate of 250 kHz and a 16 bit resolution. The input range can be set to ± 10 V, ± 5 V, ± 1 V, or ± 0.2 V. The signal of the force measurement is sampled with one card and the signal

of the motor position another. A control program will then read in from both cards and save the data. The first DAQ card samples the 6 channels from the Nano17 necessary for determining force and torque, and an additional channel samples the synchronization signal. The sampling rate can be up to 35714 Hz (but set at 35000Hz throughout this work). The second DAQ card captures the two channels from the encoder, shown in Figure 5-15, and on a third channel the synchronization signal. On this card, the sampling rate can be up to 83333 Hz.

The start of the motor position is found by initializing the flapper to a known flapping angle (initial phase). Then, when the motor is not moving, the motor position is read from the controller. To accurately keep track of the motors position synchronously with the synchronization signal, both signals must be captured from the moment the motor starts moving from a known position. To interpret the encoder signal correctly, including direction, more than 1024 samples per revolution of the motor is necessary, which means more than 4490 samples per flapping cycle. This way, the encoder signal can only be read correctly up to approximately an 18.5 Hz flapping frequency. However, if the direction of the motor is already known, which can be read when the motor is still at low speed and starting up, only two samples per encoder count is necessary, and the encoder signal can be read correctly up to a 37 Hz flapping frequency. If yet a higher flapping frequency is needed, one of the channels from the encoder can be moved to the first DAQ card, reducing that cards maximum sampling rate to 31250 Hz. The two channels are only needed to determine the direction of the motor, and to not count any wiggling around a single position as motion in the same direction. Since the data is captured from when the motor is standing still, the direction of the motor can be

determined at low speed, and at high speed when the direction is known, only one channel is needed. This could allow for synchronization at flapping frequencies up to slightly more than 55 Hz.

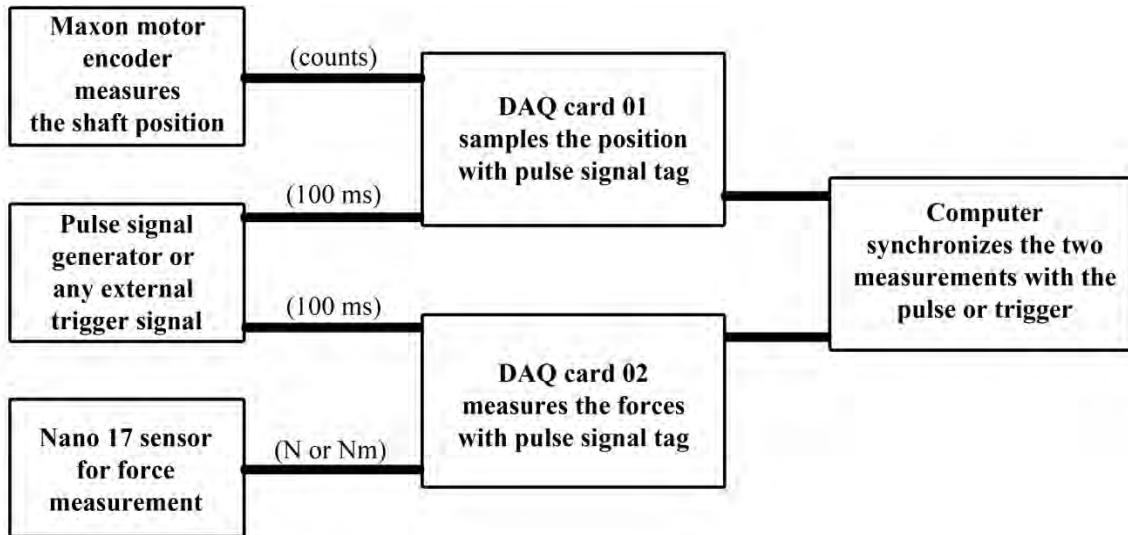


Figure 5-15. Force measurement system configuration layout.

To understand the detail of aerodynamic forces in one flapping stroke, it is necessary to synchronize the force measurements with the flapping phase. However, for wing performance evaluation, time averaged thrust is an adequate metric. This is because if both the kinematics and structural properties are symmetrical to the wing's leading edge, the average lift measurement should be zero. There are three points that needs to be made clear: 1) why the inertial forces of the wing and the mechanism would not affect the averaged measurement in both lift and thrust directions; 2) why the aerodynamic lift generated with a symmetrical 2-DOF motion should be zero; and 3) why the average thrust value can be used as a metric to evaluate the flapping wing performance.

Because of the nature of flapping, both the wings and the actuation mechanism are in reciprocal motion. Therefore inertial loading of parts during acceleration and

deceleration will be significant and measured with the sensor. Because the flapping mechanism is a complicated mechanical system that consists of many parts (gears, bearings, bars, etc.), vibration signals are also recorded. However, both the inertial loads and vibration only affect the instantaneous readings on the sensor, but not the time-averaged measurement. This is because the system on top of the sensor is conservative for momentum and the initial system momentum equals to the final one. If there is no external force applied to the wing or the mechanism, the time-averaged measurement will be zero, no matter how large the inertial or vibration force is. This is also validated with measurements in vacuum. Indeed, in the absence of air, both average lift and thrust measurements are negligible within the sensor resolution (± 0.32 g). Therefore, measuring the time-averaged forces exempts the problem from complicated dynamic loads and allows for an effective evaluation of the wing performance.

The symmetry in wing kinematics and structure makes the net lift (cycle-averaged lift) force zero (here 'lift' is not defined as the force counteracting gravity, but only the measurement in the y axis); because the same structural fluid interaction is performed in two opposite directions that cancel the forces with each other. Therefore the only significant measurement is in the thrust direction.

As the result of the previous two reasons, time-averaged thrust F_T can be used to evaluate the aerodynamic performance. Comparing to the 1-DOF case, in which the wing deformation (which is the result of the air/structure interaction) is the sole source for generating aerodynamic thrust, the effect of active wing rotation should be reflected (increase or decrease significantly) in the averaged thrust value. Although the airflow

can be directed to different directions during one cycle, the symmetry of the kinematics and deformation makes the chordwise direction the only one that allows for net force.

The output data contains the motor position, 6-axes readings and the pulse signal. The motor position data are used to calculate the actual phase difference. The 6-axes readings (although in this work only the data in the thrust axis is used, this capability can be extended to measurements in future work) and the pulse signal is used to examine the effect of wing rotation. The thrust is averaged over each interval between two pulse signals. Finally, a smoothing filter built in MATLAB is applied to the thrust data.

5.3.3 Results

Table 1 shows the experiments conducted in this work to understand how different actuation phase between the flapping and rotational motion would affect aerodynamics. This work also expands the scope to investigate if active vibration of the wing structure would positively contribute to the flapping aerodynamics.

Table 5-2. Experiments conducted in this work

Experiment #	Case Name	Degree of Freedom	Flapping Frequency (Hz)	Rotation Frequency (Hz)	Rotation Power (%)
1	1DOF	1	10, 15	N/A	N/A
2	2DOF_I	2	10, 15	10, 15	0
3	2DOF_80%	2	10, 15	10, 15	80
4	2DOF_100%	2	10, 15	10, 15	100
5	30Hz	2	10, 15	30	100
6	45Hz	2	10, 15	45	100
7	60Hz	2	10, 15	60	100
8	100Hz	2	10, 15	100	100
9	200Hz	2	10, 15	200	100
10	500Hz	2	10, 15	500	100
11	1000Hz	2	10, 15	1000	100

Each of the experiments is repeated 5 times; and in each time there are 4 cycles of phase difference variation from 0 to π . The first 4 experiments are designed to

examine the effect of the active rotation during the flapping stroke for thrust production. The experiments from 5 to 7 are designed to examine the effect of active rotation at multiple flapping frequencies. For example, when the rotation motion is actuated at 30 Hz and the flapping frequency is 10 Hz, the wing will rotate back and forth 3 times in 1 flapping cycle. The experiments from 8 to 11 are designed to examine how high frequency vibration would affect the aerodynamic performance. The overall comparison of the effects is shown in Figure 5-16.

The constructive data are selected from the average of the maximum values of the time averaged thrust (over 100 ms) when the phase difference is sweeping from 0 to π ; vice versa for the destructive data. These two descriptions may only be accurate for the cases 3 and 4. For other cases, the maximum and minimum measured values may be a result of system error, rendering the terms inaccurate. But for comparison, they are used throughout all cases.

In the 1-DOF case, the time averaged thrust is a constant (although with uncertainties); therefore its constructive and destructive values are the same. This should also be true for the 2-DOF idle case, if the kinematics of the wings is exactly periodic. However, the tolerances and errors in the mechanical parts on the mechanism will cause uncertainties in the motion, making the cycle to cycle averaged thrust value vary. From the data shown in Figure 5-16, this uncertainty does not affect the comparison made to the following cases.

The 1-DOF case produces some thrust due to the structural flexibility. The values are insignificant, similar to the results from previous studies (Figure 4-16) at this frequency range. For the MCA idle case, it can be seen that when the wings are allowed

to rotate passively at 45°, there is a noticeable increase in thrust production, especially at 15 Hz. This result shows again that the passive twist deformation is positively correlated to the thrust. However, unlike at 15 Hz, the behavior at 10 Hz is undetermined. The other 9 cases are now compared to these two.

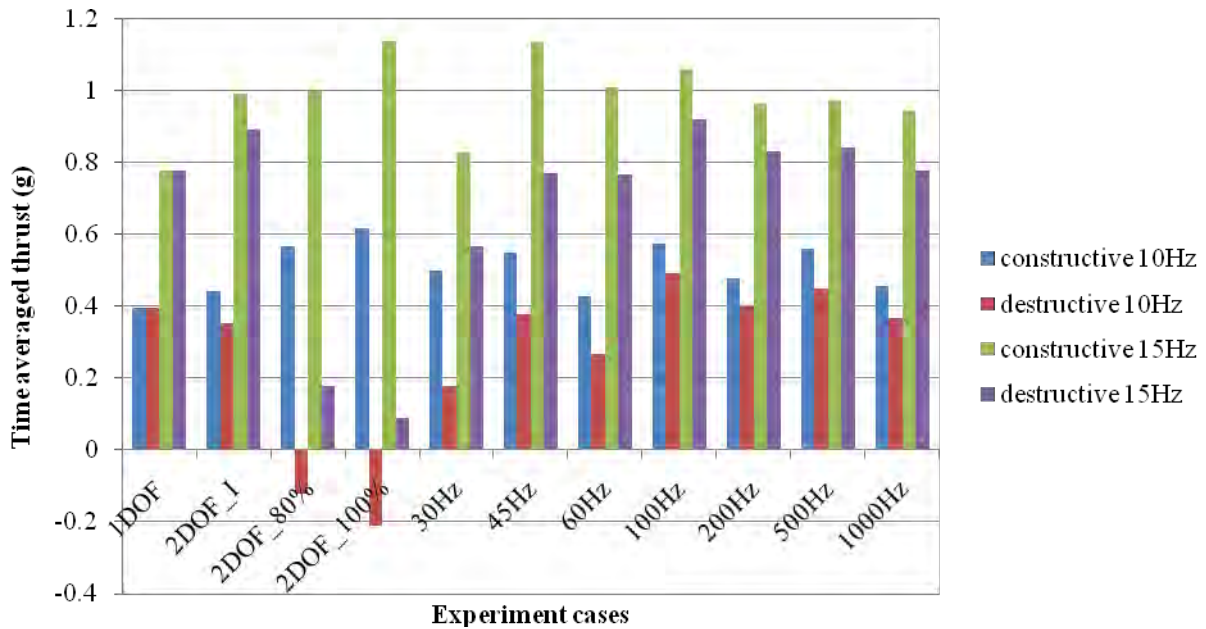


Figure 5-16. Overall performance comparison in 11 experiment cases.

Effect of active synchronized rotation

Synchronized rotation means the rotation and flapping motion have the same frequency but the phase difference between the two varies. Figure 5-17 shows the change of time averaged thrust as the phase difference changes along with time. Three cases are shown in this figure: the un-powered idle case, the 80% and 100% powered case. Both the original measurement data and the filtered one are presented for the three cases.

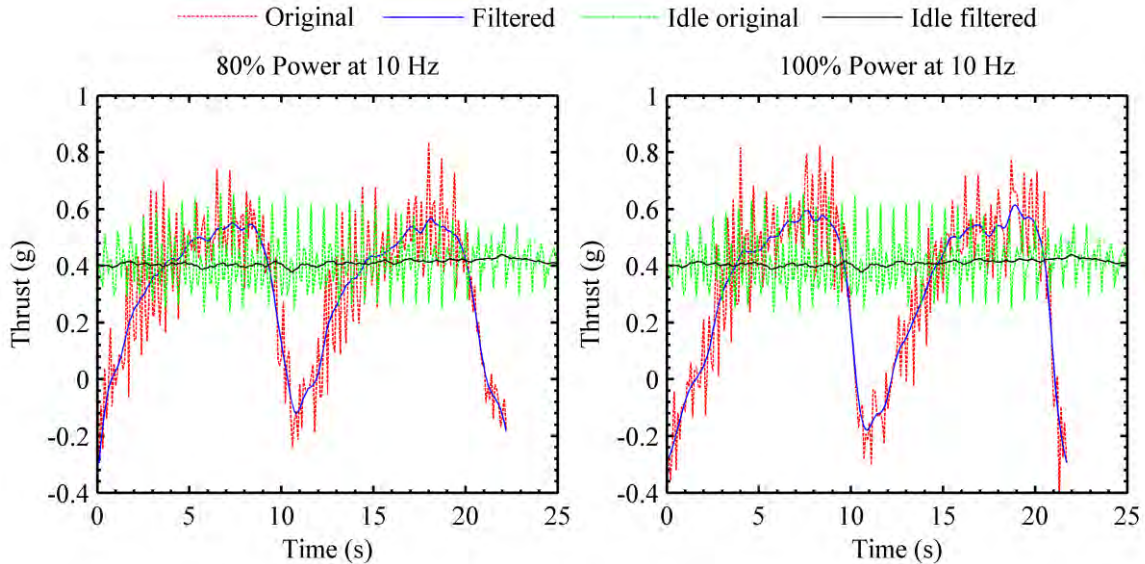


Figure 5-17. Time averaged thrust of 2-DOF kinematics, varying with motion phase difference at 10 Hz flapping frequency, flapping stroke angle $\pm 35^\circ$, rotation angle $\pm 45^\circ$.

Three points should be noted from Figure 5-17: 1) Actuation power determines the kinematics and is crucial for the thrust production; 2) The changing phase difference between the flapping and rotation motion has a substantial effect on thrust production; 3) Due to the aerodynamic loading direction, greater destructive effect can be achieved compared to a constructive one.

As the power increases from 80% to 100%, both constructive and destructive effects increase. The intersections of the idle case and the active cases indicate that the timing for applying the MCA torque coincides with the timing for wing rotation due to inertia at wing reversal. The constructive effect causes the net thrust above this idle level, and the destructive effect below. At 100% power output, the thrust magnitude has increased approximately by 50% and decreased by 150% at the extreme values.

Aerodynamic loading to the wing causes washout during downstroke and washin during upstroke. Advanced wing rotation would mean applying an MCA torque

counteracting the washout/washin in the opposite direction. The advanced timing would also increase the rotation speed at the wing reversal, because at that moment the initial speed combines with inertial effect. As observed in nature, this is considered one of the key factors in enhancing aerodynamic performance of flapping wings. Due to wing inertia, the rotation angle would be at maximum immediately after the wing reversal; the aerodynamic loading would sustain the maximum angle until equilibrium is reached between this aerodynamic loading moment and the moment produced by the neutralizing magnet outside the coil. In other words, time advanced pronation and supination with high rotation rate is beneficial in thrust production.

On the other hand, when the pronation and supination timing is delayed, which means the applied MCA torque suppresses the pronation and supination at the end of each stroke, the effect is destructive. In Figure 5-17, the minimum values due to such destructive effect can even be negative. This is because the aerodynamic loading has the same direction as applied torque so that more significant kinematic change can be achieved, and therefore, the larger negative values.

Similar results are observed for the 15 Hz, as shown in Figure 5-18. One major difference is that as the frequency increases, the inertial loading at the end of each stroke increases, so more power would be needed to achieve the same amount of thrust gain. Since in this study, the power input is fixed, the increase of thrust in constructive conditions is relatively smaller (approximately 25% versus the 50% at 10 Hz).

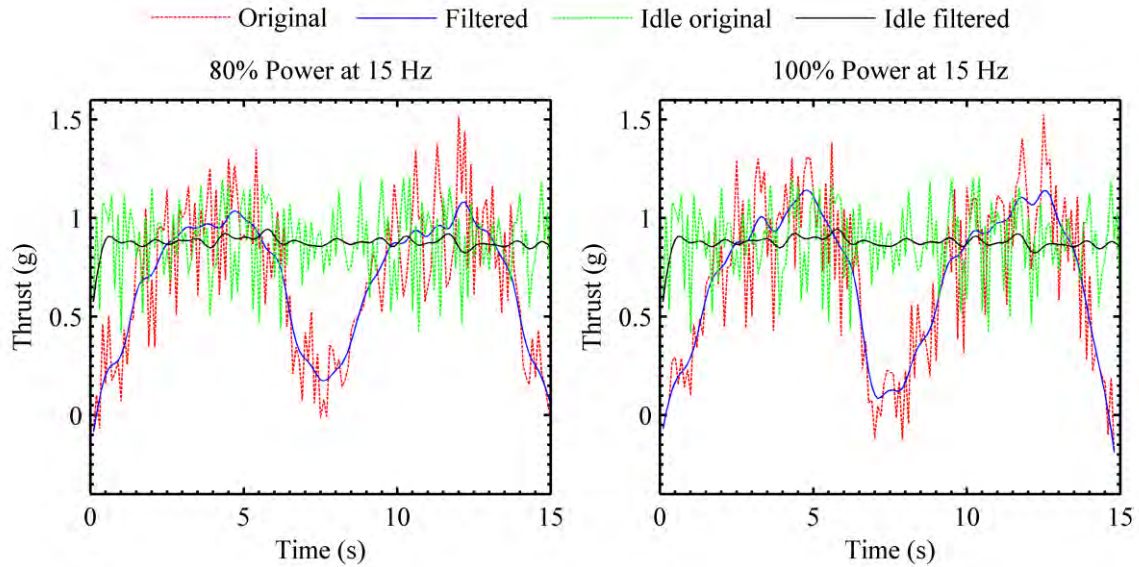


Figure 5-18. Time averaged thrust of 2-DOF kinematics, varying with motion phase difference at 15 Hz flapping frequency, flapping stroke angle $\pm 35^\circ$, rotation angle $\pm 45^\circ$.

Effect of multiple rotation in one flapping stroke

In Figure 5-19, the comparison of the 3 multiple rotation cases are shown, together with the two control cases. There are noticeable differences created with multiple rotations in each flapping stroke. However, the only improvement is at 45 Hz active rotation. At 15 Hz flapping frequency, 45 Hz rotation frequency would produce three rotations in upstroke and downstroke. This is a strange combination because it is not an integer of rotation per stroke. This would make every two flapping cycle cancel the effect of rotation in time averaged measurement. Therefore the increase in the thrust production is less likely due to the multiple rotations. One other possibility is that the flexible wing or the whole MCA mechanism has a resonant frequency near that frequency range, causing the system to have amplified motion to increase the thrust.

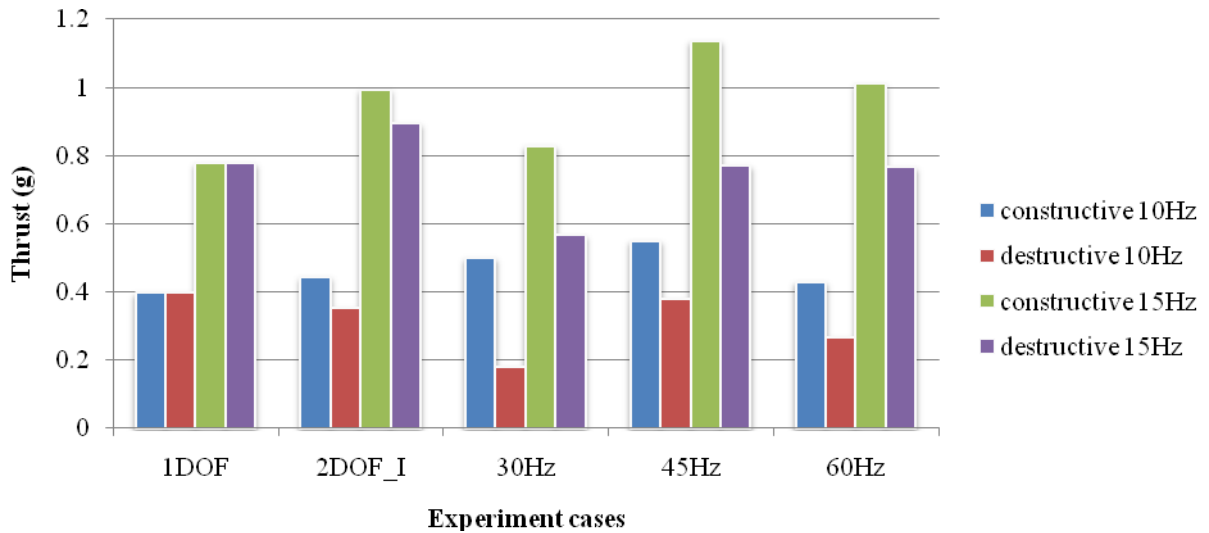


Figure 5-19. Effect of multiple rotation in one flapping stroke.

Effect of structural vibration

Figure 5-20 shows the thrust fluctuation range in the experiment. Each data point is evaluated with the difference between the maximum and the minimum cycle averaged thrust, because this can directly reflect the effect by wing rotation. For example, as analyzed previously, active 2-DOF motion does change the thrust production; therefore the fluctuation range of cases 2DOF_80% and 2DOF_100% are very large. On the other hand, the fluctuation range for the idle case is probably caused by system error; therefore the values are similar at different frequencies.

The effect of structural vibration can then be examined: when the wing is actuated over 100Hz, the dynamic behavior has no impact at all to the thrust production performance, at least at these two frequencies. This is an important conclusion because it shows that the local structural vibration is not a key factor in flapping wing aerodynamic performance, but the wing kinematics and deformation are.

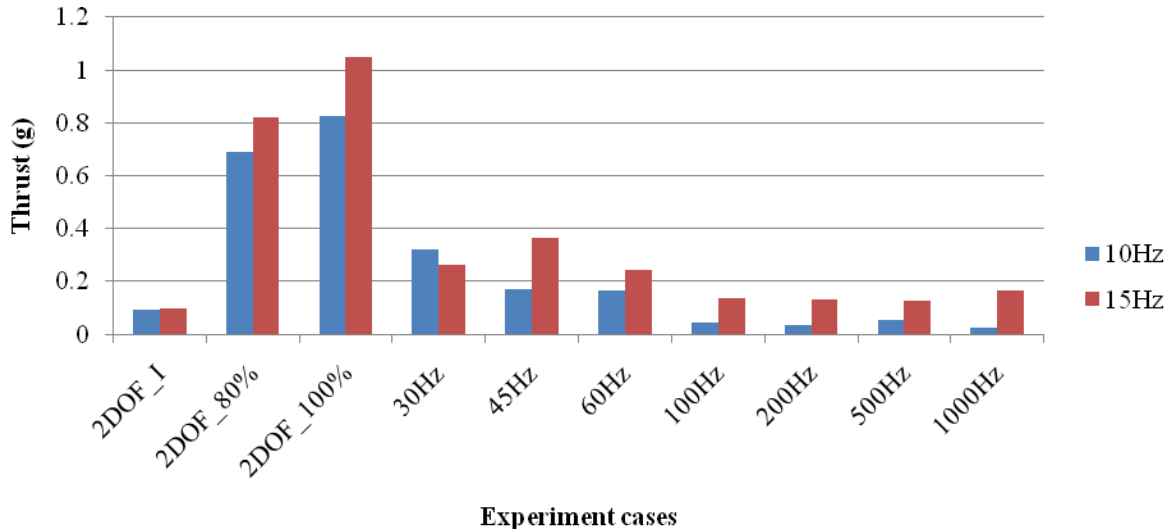


Figure 5-20. Thrust fluctuation range in different cases.

Similarly, if the maximum and minimum values of these high frequency cases are shown, as in Figure 5-21, it can be seen that as the vibration frequency increases, the effect upon thrust production decreases. At 1000 Hz, the wing performance is almost identical as the idle case. The high frequency input is corresponding to low vibration amplitude, therefore less impact. This shows at least that it is not the vibration frequency, but may be the amplitude (causing change in kinematics), that would affect time averaged thrust production.

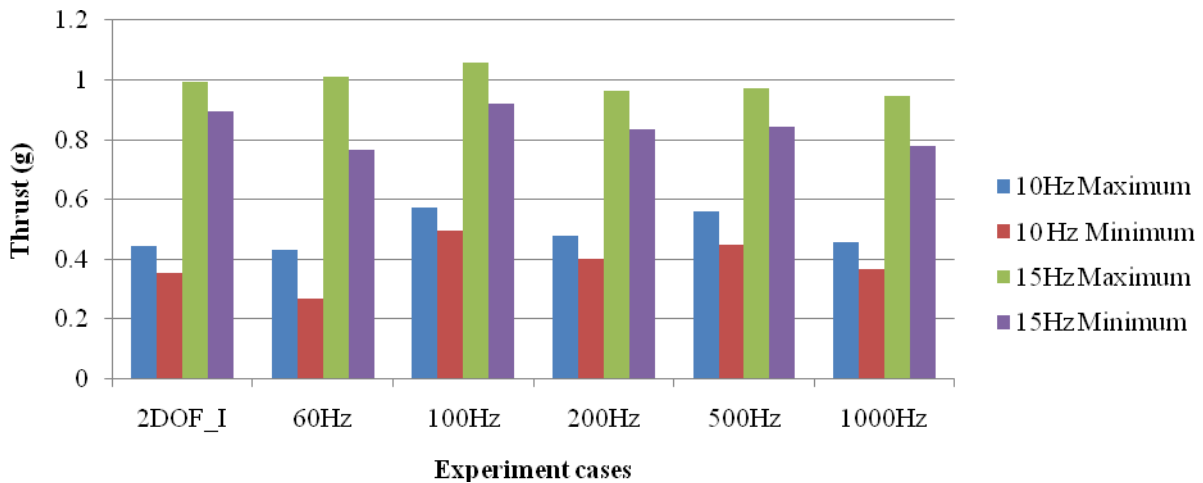


Figure 5-21. Thrust fluctuation range in different cases.

5.3.4 Conclusions

A 2-DOF flapping mechanism is created in this work to study the effect of active wing rotation and vibration during the flapping stroke of an elastic wing for thrust production. The mechanism utilizes magnetic coil actuators to apply an actuation torque for the rotation motion. A flexible membrane wing made of Mylar and carbon fiber is fabricated. A control program is written to input the rotation frequency, amplitude and duration. An experimental setup is configured to measure the aerodynamic forces. Eleven experiment cases are designed to obtain the study objectives.

It has been found that active wing rotation during flapping has a substantial effect on thrust production. The rotational degree of freedom can be either beneficial or harmful, depending on the phase difference between the two motions. Therefore this can be utilized effectively in the control aspect of flapping flight in future.

Having multiple rotation motion in one flapping cycle did not show significant improvement in performance in this work. However this result is not conclusive because higher power input may be required to effectively change the kinematics.

High frequency wing vibration during flapping has been proven irrelevant to the aerodynamic performance of these wings of the current scale. This is because the wing vibration does not change structural properties to the degree that structural deformation is affected.

Because of limited time and resources, what is concluded should only be seen as a beginning for future work: interesting preliminary results are presented, but not yet any fundamental physics principle is discovered. These conclusions are limited to the selected parameters in this experimental setup. Future work will include the measurement of the 2-DOF kinematics and structural deformation of the flapping wings

so that the aeroelastic aspect can be examined. A better actuation method based on the wing position feedback is needed to realize any desired phase difference between the two motions. Higher frequency range and amplitudes for both motions will be tested. The feasibility of controlling flapping flight with such setup will be further examined. Finally, an optimum 2-DOF kinematics will be sought to maximize thrust production for a certain wing structure.

5.4 Discussion

This chapter has examined the effect of kinematics in flapping flight in a circumspective manner: measuring the structural deformation caused by actuation kinematics, evaluating aerodynamic performance under different wing kinematics and studying the effect of active wing rotation and high frequency vibration. The results show that the two most important kinematic parameters, flapping frequency and stroke amplitude, do primarily contribute to the structural deformation. Their relationship can be supplementary to each other: a tradeoff exists so any wing would have an optimum operation condition. The study on BP with various frequencies and amplitudes has proven this tradeoff with the coefficient of thrust. However, the absolute value still favors maximizing both parameters if energy efficiency is not a concern.

An innovative approach using magnetic coil actuators to provide the second degree-of-freedom enables an effective study of the thrust production by complicated wing kinematics. The results show that, indeed, the timing and duration of the wing rotation can significantly change the aerodynamics: either constructive or destructive. However, high frequency vibration unexpectedly has no effect on time averaged thrust production. This is probably because the structural deformation pattern is not changed by the vibration to interact with air differently.

In the previous chapter, some very interesting aeroelastic behavior is observed. For a wing with enough stiffness, the amplitude of wing kinematics would increase as the flapping frequency increases, resulting in a quadratic trend of increase as observed in the previous chapter (L3B1 and L3B2 in Figure 4-16); while for a wing with too much compliance, the amplitude of wing kinematics would actually decrease at high frequencies (L1B1 and L1B2 in Figure 4-16). The next chapter will continue the investigation on wing structure, focusing on different topologies actuated in a wide spectrum of flapping frequency.

CHAPTER 6 EFFECT OF STRUCTURE

6.1 Overview

In this chapter, the experimental study investigates the relationship between flapping wing structure and the production of aerodynamic forces for micro air vehicle hovering flight by measuring full-field structural deformation and time averaged thrust generation. The available materials nowadays presents a unique opportunity for designing and constructing an artificial wing that has properties similar to natural fliers'. Flapping wing flight for MAVs is inspired by the spectacular performance observed from nature. Biological flyers have been evolving for millions of years. The current state of the structural properties of their body part is a product of the stringent natural selection. A wing too heavy, may limit flapping frequency and the level of complicated kinematics; a wing too light, may be too weak and fail at critical moments (overloading when attempting to escape from predators). Therefore it is reasonable to design the artificial flapping wings with comparable parameters to the natural model which has been proven successful. The comparison of the wing and kinematics parameters between different natural flyers (hummingbirds, hawkmoth, and cicada) and this study is summarized in Table 6-1.

The current comparison is emphasized on engineering feasibility rather than biological similarity. The parameters of natural flyers are collected from a wide range of species in the same genus so that they reflect the range for feasible low Reynolds number aircrafts. The parameters of this work are chosen to be comparable: wing size and weight are similar to a hummingbird's; wing membrane and structure properties (E :

elastic modulus) are in the same level of magnitude of a cicada's and wing motion (frequency and Reynolds number) is approximated to the hawkmoth's.

Table 6-1. The morphological, structural and kinematics parameters comparison

	Hummingbird (Various species/ages)	Hawkmoth (Various species/ages)	Cicada (<i>Homoptera</i> , <i>Cicadidae</i>)	This work (Wing and flapper)
Morphological parameters				
Wing length (<i>b</i>)	37~100 mm	35~150 mm	45~55 mm	75 mm
Chord length (<i>c</i>)	9~25 mm	9~46 mm	14~18 mm	25 mm
Aspect ratio ($2b^2/S$)	7.0~8.0	5.8~6.0	8.0~8.6	7.6
Wing weight	50~300 mg	50~4860 ⁵ mg	12~20 mg	105 mg (average)
Single wing area (<i>S</i>)	400~2500 mm ²	400~7500 mm ²	500~700 mm ²	1473 mm ²
Structural parameters				
Wing/feather <i>E</i>	2.5 GPa ⁶	47 MPa ~ 4.5 GPa	3.7 GPa	2.5~3.4 GPa
Wing/feather density	1200~1400 kg/m ³	1200 kg/m ³	2300 kg/m ³	1600 kg/m ³
Membrane thickness	N/A	45~110 micron	12.2 micron	12~14 micron
Structure/skeleton <i>E</i>	N/A	N/A	1.9 GPa	73.4 GPa
Structure density	1000~1600 kg/m ³	1200 kg/m ³	N/A	1740 kg/m ³
Kinematics parameters				
Flapping frequency	10~200 Hz	8~30 Hz	40~45 Hz	5~45 Hz
Stroke amplitude	144°~180°	115°	N/A	40°~90°
Reynolds number ⁷	7,000~15,000	5000~7000	N/A	1527~12,215

Two sets of wings are examined: the first set consists of four wings of different topologies; the second explores a design space with systematic variation of the reinforcement pattern. Intensive correlation analysis is performed on the first set while a broader range of aerodynamic performance is investigated for the second. Results from these flexible micro membrane wings with different skeletal reinforcement demonstrate that wing compliance is crucial in thrust production: only certain modes of passive aeroelastic deformation allow the wing to effectively produce thrust. The experimental

⁵ Assuming the wing density is a constant and thickness is always 1.2% of the mean chord length, therefore weight equals to the product of *S*, 1.2%*c*, and wing density.

⁶ Taken from general mechanical properties of keratin, also from Avian Flight by John ViDeler[.]

⁷ Re for hovering flapping flight is defined as: $Re = \frac{2b\Phi fc}{\nu}$, where *b* is the wing length, *f* is the flapping frequency, Φ is the flapping amplitude, ν is kinematic viscosity of fluid, and *c* is the chord length.

setup consists of the flapping mechanism FL2D3 with a single-degree-of-freedom rotary actuation up to 45 Hz at 70° stroke amplitude and with power measurement; the force and torque sensor that measures the lift and thrust; and the four-camera digital image correlation system that is capable of capturing the complete stroke kinematics and structural deformation. Several technical challenges related to the experimental testing of micro flapping wings are resolved in this study: primarily, flapping wings less than 3 inches in length produce loads and deformations that are difficult to measure in an accurate and non-intrusive manner. Furthermore, the synchronization of the loads measurement system, the vision-based wing deformation measurement system, and the flapping mechanism is demonstrated. Intensive data analyses are performed to extract useful information from the measurements in both air and vacuum.

6.2 Topology Correlation Study

6.2.1 Introduction

This section is concerned with identifying the relationship between passive flapping wing deformations due to different wing structural properties (compliance and mass distribution) and the concomitant aerodynamic force production. Unlike birds and bats that have muscles and skeletal joints to actively change their wing shape (wingspan, planform, camber, dihedral, etc.) during flight, insects fly with wings that have no active shape control. Seen in high-speed videos and documented by Ellington^[9], the key element for insect flight is the thrust produced by the sweeping motion. Wing pronation and supination also play important roles in insects' flight and control, but these aspects are outside of the scope of this article. The sweeping motion is mainly a back and forth fan movement with various wing tip traces. Here, to emphasize pure flapping motion, a test bed mechanism is designed and created to

perform a single degree-of-freedom (DOF) kinematics. This is categorized as normal mode hovering flapping flight with constant pitch angle, as illustrated by Shyy et al. ^[171]. Such kinematics are not typically considered to be biologically-inspired^[17], and the flapping of a rigid wing will probably not develop significant time-averaged lift/thrust. Wing flexibility then, becomes an important factor.

Recent interest in micro air vehicles (MAVs) research has been directed towards the design of efficient flapping wing aircraft capable of both forward flight and hover. As MAVs usually have a wingspan less 150 mm and weigh less than 50 g, many challenges exist in terms of power, control, payload, etc., along with the most fundamental of all: an effective wing with realizable kinematics to mimic nature's highly evolved flight mode. A firm understanding of the structural properties needed for an actuated wing to create effective aeroelastic forces is expected to be an enabling factor towards the widespread use of flapping MAVs for a wide range of applications within the purview of aeronautical engineering, and is the focus of this work.

Ho et al.^[17] have performed a similar work to understand flapping wing structures and aerodynamic behavior. They have tested flapping membrane wing structures with and without batten reinforcement at the trailing edge of the wing tip as a function of advance ratio (composed of forward flight speed, total flapping angle, wingspan, and flapping frequency: essentially, this metric is used to estimate flow unsteadiness). For large values, the lift capabilities of the two wings are identical, but as the unsteady features of the flow are enhanced (low advance ratio), the wing without this reinforcement is inferior. The authors state that the excessive feathering (change of chord angle related to flow direction) of the wing disrupts the leading edge vortex, and

the associated lift. Thrust, however, relies heavily upon wing flexibility for its development, and so an adequate compromise must be found. Singh and Chopra^[155] also demonstrate this concept for a membrane wing with an unconstrained trailing edge, whose feathering motion develops significantly more thrust force than one reinforced all along its perimeter. Neither of these works is able to provide quantitative experimental information concerning the passive wing deformation. In general, relatively few publications exist in the area of experimental characterization of full-scale MAV wings (under 75 mm in length, flapped at over 25 Hz).

Since hummingbirds behave in the transition region between insect flight and bird flight, it is used as an example for the current flapping MAV development. Wu et al.^[140] have studied wings whose planform and size are very similar to hummingbirds'. Experimental characterization of such wings is challenging, as scaling must preserve many parameters: Reynolds number, Strouhal number, reduced frequency, and several flexibility parameters^[171]. Due to these difficulties, it is desired to conduct tests on full-scale models, leading to resolution issues in loads measurements: time-averaged lift and thrust may only be a few grams. A wide range of measurement techniques can be found in the literature: Jones et al.^[172] measure the displacement of a flapping MAV suspended by cables to estimate the thrust, while the use of wake-deficit information via particle image velocimetry aft of the flapping wing has also been demonstrated^[173]: the accuracy of both of these techniques may suffer as the size of the wing decreases, however.

Singh et al.^[155] mount piezo-resistive strain gages to the wing joint in order to measure the aerodynamic forces. Such a method is attractive in that the (potentially

large) inertial forces of the flapping mechanism are bypassed, but assumptions must be made as to the location along the wing where the mean aerodynamic force acts, and several substantial manufacturing issues are present, as discussed in the publication. This work utilizes a commercial force/torque sensor with six degrees of freedom (similar to the model used by Khan and Agrawal^[174]) mounted beneath the flapping mechanism, as discussed below. Furthermore, several sub-systems (flapping mechanism, load sensor, strobe, cameras, etc.) must be synchronized within the flapping cycle, which requires a complex triggering system.

Due to the light-weight, fragile nature of the membrane wings, the candidate techniques for the measurement of flapping wing kinematics and structural deformation are necessarily limited to non-contact vision-based methods. Some work on this topic is found in the literature based upon point-wise techniques. For kinematics measurements, Raney and Slominski^[117] place small light-emitting diode devices at the wing tip, and capture the entire wing tip trail in a single image. For deformation measurements, Tian et al.^[158] utilize similar multiple reflective markers over a bat wing, and stereo high-speed cameras to quantify the motion. Wallace et al.^[173] and Agrawal and Agrawal^[175] utilize a similar photogrammetry technique for insect-size wings. A more full-field strategy is discussed by Zeng et al.^[159], who use a fringe shadow method to measure the flapping and torsional angle of a dragonfly wing. Similar fringe-based methods are given by Wang et al.^[160], along with sign points placed on the wing, to measure deformation of a free-flight dragonfly. Cheng et al.^[145] extend this technique with a windowed Fourier transform to process the fringe patterns and extract phase. DIC is used to measure the wing deformation in this work; the technique is generally

regarded as state-of-the-art in terms of experimental mechanics in general^[162], and is particularly well-suited to the flapping wing problem, due to its full-field, three-dimensional, high-resolution nature.

The remainder of this section is organized as follows. First the different wing topologies are introduced. Then the experiment configuration and data analysis are then presented, including measurement uncertainty discussion. Finally, results are given to reveal the intrinsic relationship between wing structure and deformation, and wing kinematics and aerodynamic performance.

6.2.2 Wings of Different Topologies

The Zimmerman planform, formed by two ellipses that intersect at the quarter-chord, is continued to be used in this chapter, as shown in Figure 6-1. The wing design is still two dimensional: without cambered airfoil profile. The wings are constructed with unidirectional carbon fiber to form the skeleton and Capran® as the membrane. The carbon fiber skeletal reinforcement differs substantially for the four wings, which is reflected in the naming convention. As mentioned in Chapter 3, the first wing is reinforced with batten oriented parallel to the root (battens parallel, BP), the second has radial diagonal battens similar to the feathering structures of a hummingbird wing (HUM), the third has no batten reinforcement other than the leading edge (leading edge only, LEO), and the final wing has carbon fiber reinforcement along the entire perimeter (perimeter-reinforced, PR).

To manufacture the wing skeleton, a three-layer bidirectional carbon fiber triangular plate is first placed at the intersection of the leading edge and wing root, which can be used as an attachment point for other structure elements. This triangle is significantly stiffer than the remainder of the wing; therefore it is used as a reference for

deformation calculations (discussed below) and as an attachment location to the flapping mechanism (as seen in Figure 4-3). Unidirectional carbon fiber strips (0.8 mm wide) are used to construct the leading edge, battens, wing root and the trailing edge (only for PR). The strips are laid up on a flat plate according to each reinforcement pattern; the number of layers used for each portion of the wing is documented in Table 1. BP has 2 complete leading edge layers and an additional layer between the root and the third batten (counting from the root), achieving a varying bending stiffness along the structure. The other three wings all have 2 layers at the leading edge. All the battens are of 1 layer and all the roots are of 2 layers.

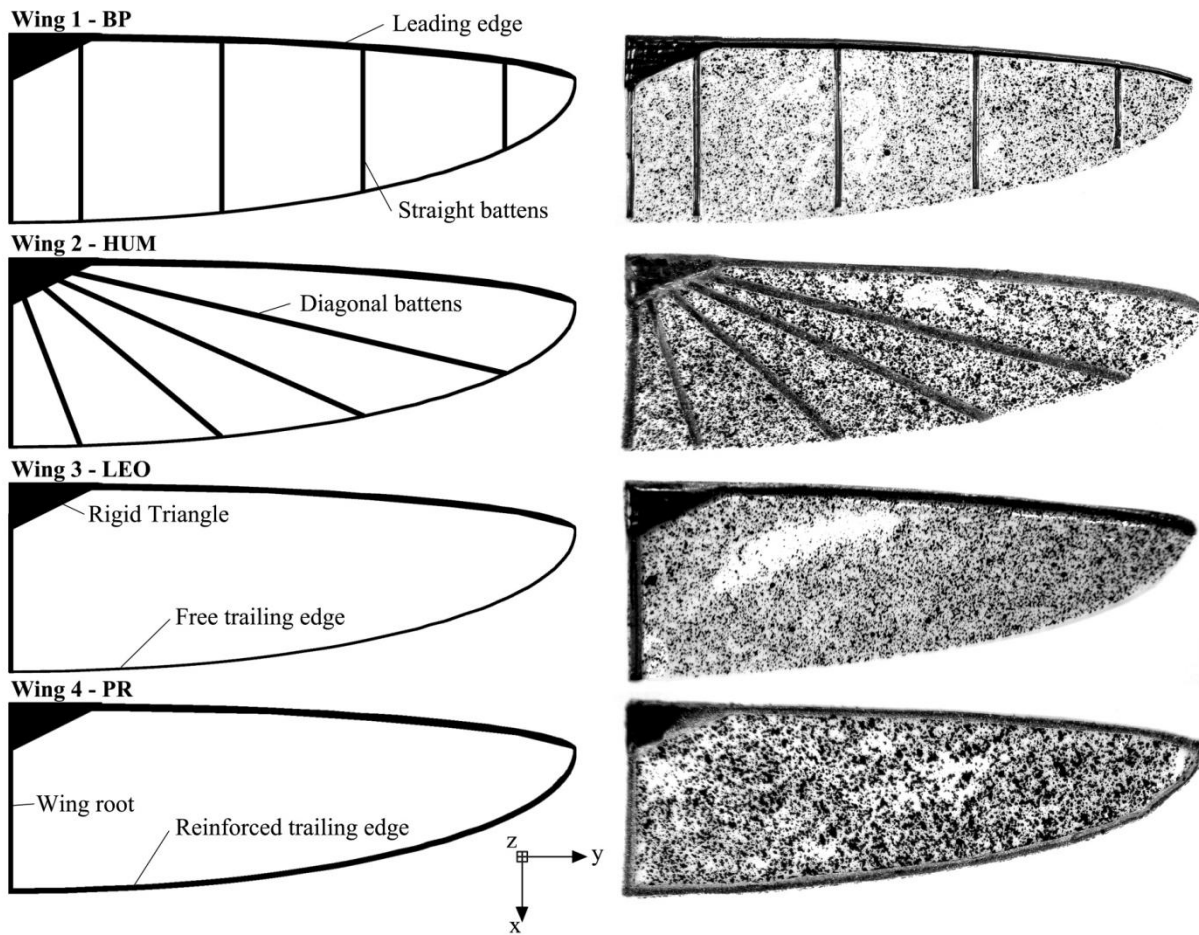


Figure 6-1. Reinforcement layout of the four tested wings.

Table 6-2. The number of carbon fiber layers used in each portion of the wings, as well as the final reinforcement weight

	BP	HUM	LEO	PR
Leading edge	2 + 1 additional	2	2	2
Batten	1	1	0	0
Root	2	2	2	2
Trailing edge	0	0	0	1
Weight	0.125 g	0.150 g	0.100 g	0.140 g

After the carbon fiber skeleton is cured, the piece is applied with spray glue and laminated to a membrane material called Capran® (Honeywell’s Capran Matt 1200), a biaxially oriented nylon film. Unlike the soft and deteriorative latex rubber, Capran® is as light as Mylar® (density: 1.16 g/cm³), as tough as Tyvek® (tensile strength at break: 193~276 MPa) and as consistent as Kapton® (thermal shrinkage coefficient: 1% ~ 2% at 160° C). This thin film is available in matt finish (diffusive), making it amenable for DIC measurements. Its low heat shrink coefficient also allows the film to be cured together with the carbon fiber without building up excessive thermal stresses. Its high elastic modulus (2.5~3.4 GPa) and tear resistant properties eliminate concerns on reinforcing the trailing edge. Finally, random patterns of flat black speckles are again sprayed onto the wings for DIC measurements.

6.2.2 Experiment Configuration and Post Analysis

The experimental setup from Chapter 4 is used here. Besides new calibrations for the DIC system, no significant modification is needed. In this work, the wings are actuated from 5 Hz to 35 Hz (the highest frequency for each of the four wings varies because of different structures). In all cases the wings start at the same initial position. The operation sequence is as follows. After the user has defined a flapping frequency,

sample number and time interval, the VI control loop starts and establishes communication with the EPOS controller and Nano17. DIC cameras are then initiated, taking pictures at the calculated frequency. The cameras control the stroboscope by a pulse signal generated with camera shutter actuation. Immediately, a trigger button is pressed in the VI to activate the flapping mechanism and loads sensor. From the initial position, the wings accelerate at 2000 rpm/s to reach the command flapping frequency. The mechanism then stays at that frequency until the measurement is completed. In the mean time, the power used by the flapping mechanism is documented. About 40~100 cycles of load measurement data are taken in each run and three separate runs of data are taken for calculating system errors. Three cycles of deformation measurements are recorded and there are about 50 frames of pictures in each cycle. This is done for each frequency and in both air and vacuum. This procedure outputs the text files for loads measurements and TIFF files for DIC measurements. Converting these raw files into data is discussed below.

Data acquisition and post processing

The loads measurement text file output from the VI contains a data array, in which each row is the measurement for one flapping cycle. Since 500 samples are taken in each flapping cycle, there are 500 columns in the array (the sampling rate is altered along with the flapping frequency, i.e. at 10 Hz, 5000 samples per second and at 30 Hz, 15000 samples per second). Usually 40 to 120 rows of data are taken for averaging. Due to random delays occurring at the hardware interface (for example, time delay at reading from computer memory buffer), each cycle recording is slightly shifted (phase delay), therefore the data are shifted back before the averaging filter is applied. An example for this procedure is shown in Figure 6-2: instantaneous data taken for one

cycle at 37.5 Hz of LEO is seen on the left of the figure, with a significant level of measurement noise.

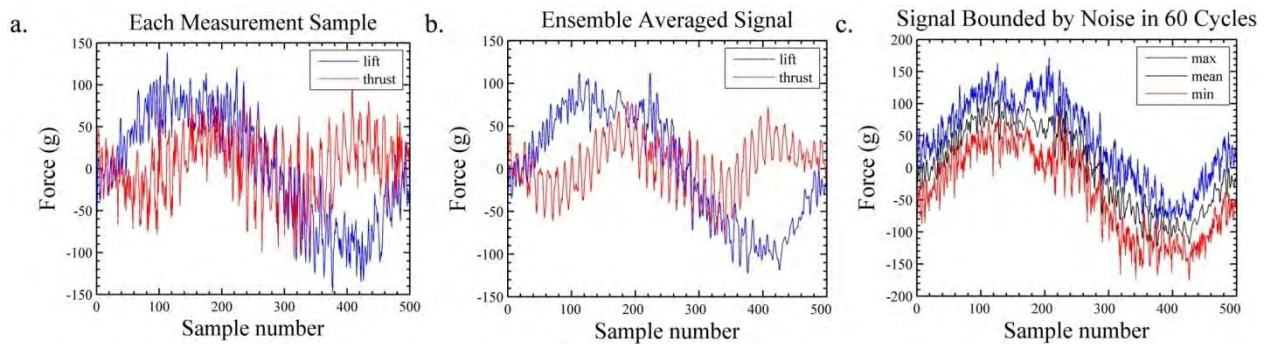


Figure 6-2. Loads measurement post processing and system noise (LEO at 37.5 Hz in air).

In the center (b), ensemble averaged data over 60 continuous cycles is shown, with a high frequency vibration content (45 peaks per cycle, flapping frequency independent) observed. This vibration is thought to be the impact force at the contact of the teeth in the gear box. The shape of the waveform of the lower frequency is as expected: two peaks and two valleys are present in one flapping cycle, corresponding to thrust peaks during both the upstroke and the downstroke (symmetric motion). The right of the figure (c) shows the maximum and minimum noise of the lift data taken from all 60 cycles, indicating the system noise level. A sinusoidal pattern is observed from the lift data, which is because the aerodynamic lift is combined with the inertial force generated by the flapping mechanism (the reciprocator, Figure 4-3). Due to the symmetrical flapping motion, the average value for the lift is always zero. Therefore in this study, because the kinematics is performed in hovering condition, only time averaged thrust is computed for each frequency and used for the following data analysis. The analysis conducted in Figure 6-2 allows the user to evaluate the measurement characteristics of the system: what the random noise level is, how the

noise can be reduced and what maximum deviated values are present. This not only gives the user more confidence in the averaged values, but also allow for future application in logging data for cyclic loading history.

The power consumed by the flapping mechanism is calculated from the electrical current required for the actuation. The data of the current is logged together with the wing position as well as the thrust data. Because the motor system allows using the electromagnetic properties to have the power output proportional to the quadratic function of the current ($7.2I^2$), the total power can be calculated. A tare case for power consumption by the mechanism is measured in vacuum (with wings attached). Therefore the net energy consumed by aerodynamics can be separated. The DIC data post processing has been discussed in 4.2.6 and the same method is used here.

Data analysis

As stated earlier, the experiment is designed to obtain a relationship between the thrust production and the related structural deformation of flapping wings, as the wing compliance is the sole source for generating aerodynamic thrust. Three raw data types have been collected: average thrust, power consumption, and the full-field deformation. For the first data type, it alone can indicate the aerodynamic performance of the wings; though thrust coefficient can also be derived. The power consumption is converted into efficiency using the metric gram-per-Watt (g/W), evaluating the thrust generated for each unit of power input. The full-field deformation has been represented with tip deflection and wing twist angle: the tip deflection tells the amount of wing bending (span-wise stiffness) and the twist angle describes the torsional compliance (or chord-wise stiffness) of the wing. These two values are functions of flap angle, as illustrated in Figure 6-3. This is because the full-field data cannot be directly used for further analysis;

therefore these two parameters are selected as abstraction: indicating respectively wing bending and twisting. Three example wings are selected from Chapter 4; their stiffness varies from weak (example 1, L1B1) to strong (example 3, L3B1), and all are actuated at 25 Hz. On the left, the phase loops go in counterclockwise direction; on the right, clockwise.

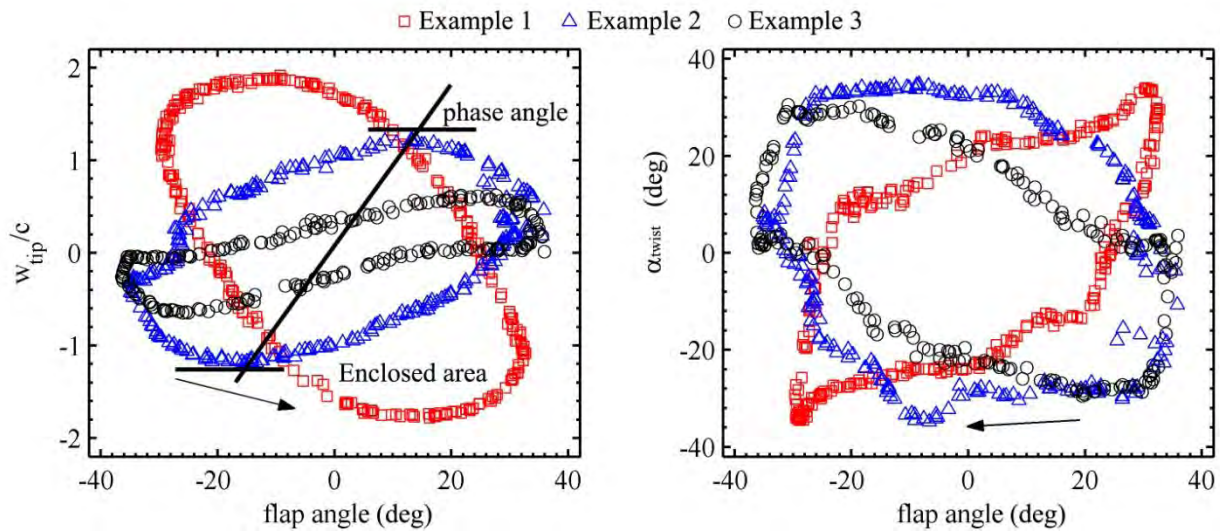


Figure 6-3. Structural deformation data analysis, defining enclosed area and phase.

The phase loops formed by the three wings enclose different areas and are oriented at different phase angles due to differences in their structural composition. The phase angle is defined as the angle between the line formed by the maximum and minimum y values (tip deflection) and the x axis, as shown on the left of the figure. Example 2 produces the most thrust and it encloses the largest area in both tip deflection and wing twist, with an orientation that largely follows the commanded kinematics. The other two examples are inferior in thrust production: example 1 is too compliant to follow the kinematics, resulting in a phase angle larger than 90 deg; and example 3 is too stiff, enclosing very small loop areas. Therefore two scalars can be used to represent the wing compliance: the loop enclosed area and phase angle. The

processed data sheet contains the following information: flapping frequency, average thrust, net energy efficiency, total energy efficiency, tip deflection loop area in air and its phase, angle of twist area in air and its phase, tip deflection loop area in vacuum and its phase, and angle of twist area in vacuum and its phase. Correlation analyses can then be used to find statistical relationships among these values.

Measurement uncertainties

The measurement uncertainties of each experiment are listed in Table 2. It should be noted that the absolute uncertainty values changes as the experiment parameter varies, therefore the uncertainty value is presented by a rounded percentage. The errors of DIC are induced during the calibration phase and the uncertainty will remain the same after calibration. If a camera pair is carefully calibrated, the system uncertainty is under ± 0.1 mm in the current setup (except occasionally the speckle pattern introduces additional errors). However, the tip deflection and angle of twist data involves more than just DIC measurements: flapping mechanism precision, wing response and density of data points in a loop would also change the extracted area and angle values. Also, because it is a low speed system, the number of samples for calculating the uncertainty is limited to using discrete data.

Table 6-3. Measurement uncertainties

Experimental result values	Unit	Uncertainties of 95% confidence	Number of samples used
Average thrust	g	$\pm 1\%$	60
Efficiency	g/W	$\pm 8\%$	20
Loop area	deg·mm or deg ²	$\pm 6\%$	3 cycles of data
Phase angle	deg	$\pm 12\%$	3 cycles of data

6.2.3 Results

Effectiveness and efficiency

In hovering conditions, flapping wing performance is evaluated with the effectiveness and efficiency in producing thrust. The average thrust produced by the four wings is shown in Figure 6-4. The results clearly show that different wing structures lead to different performance. At a low frequency range (below 25 Hz), PR and LEO have superior performance because of larger passive deformation: PR has a significant amount of mass distributed along the trailing edge and LEO has no reinforcement. At a higher frequency range (above 25 Hz), the stronger reinforcement of BP and HUM yield higher thrust values; similar trends have also been reported in Chapter 4. It should also be noted that in all four cases, a portion of the frequency range provides a nearly-linear increase in the thrust. An additional case of BP flapping in vacuum is also shown for comparison and confirmation that the wing inertia and mechanism actuation has no effect on average loads measurement.

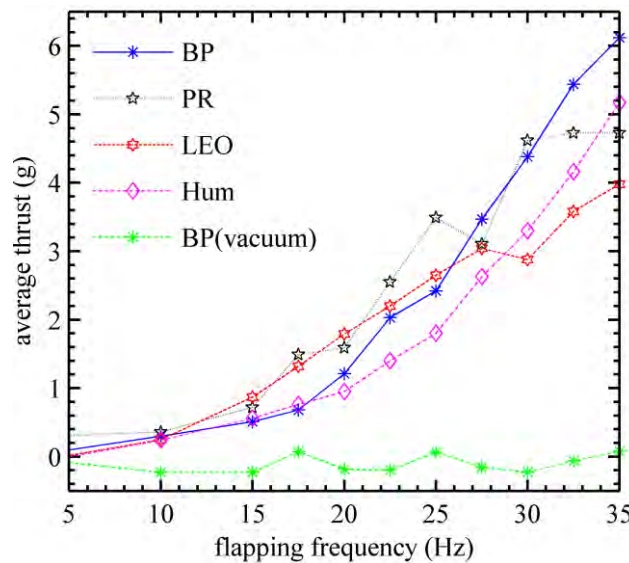


Figure 6-4. Average thrust (g) of the four differently reinforced membrane wings.

The average thrust measured in the absence of air is always near zero with errors below the sensor resolution 0.32 grams. This is totally expected because the dynamic instantaneous inertial loads should integrate to zero as the system above the Nano 17 sensor is momentum conservative.

However, wing effectiveness cannot represent overall performance, because a wing that requires higher frequency to achieve high thrusting forces may be inefficient^[171]. Therefore their net efficiency and overall efficiency are compared in

Figure 6-5.

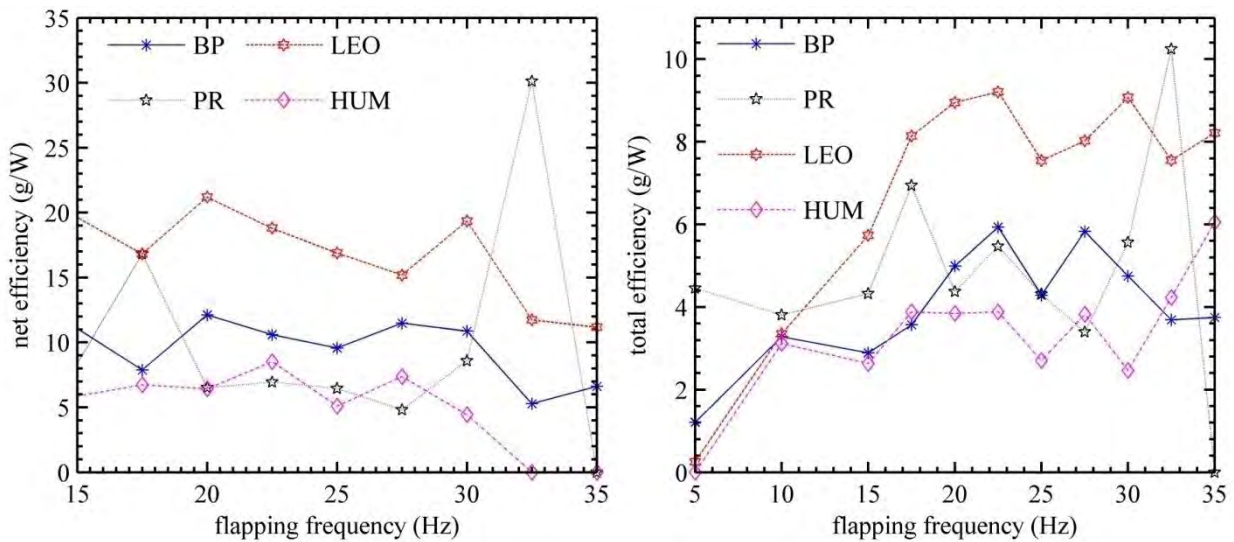


Figure 6-5. Net (left) and total (right) efficiency (g/W) of the four wings.

The total efficiency is calculated from the ratio of thrust and total power; the net efficiency uses the ratio of thrust to the difference between the total power and the power needed to flap the wing in vacuum (therefore the power consumed by the system's rotary inertia is removed in the net efficiency calculation). It can be seen that LEO is the most efficient of the four for the majority of the presented frequency range. Because LEO is not reinforced with extra carbon fiber battens, it has the lightest weight (Table 6-2) and therefore the least power consumed for wing actuation. This also allows

the wing to deform in an excessive manner (discussed below), which can be beneficial at a certain frequency range. Under the same reasoning, PR has significant mass distributed along the trailing edge (also the heaviest), requiring more energy for actuation and decreasing the efficiency. Combined with Figure 6-4, PR's deformation patterns due to this inertial load produces the most thrust between 17.5 and 30 Hz. BP and HUM have more batten reinforcement, which constrains the wing deformation and reduces the thrusting efficiency. The net efficiency data is not plotted for 5 and 10 Hz because the measurement resolution is not high enough to differentiate the input power differences, causing overestimation.

Deformation of different wing structure

At the same flapping frequency, different wing structure would generate different thrust with unique deformation patterns. The deformation contour and cyclic history comparison between BP and LEO has been briefly discussed in Chapter 5 (Figure 5-2 and 5-3). To include all four topologies, Figure 6-6 shows the four wings' deformation patterns at 20 Hz. As above, the upper portion of the figure shows the full-field deformation through the downstroke: tip-snap magnitude is indicative of the wing bending stiffness as well as the mass distribution. BP has the stiffest leading edge therefore deforms the least at the tip, though the large mass distribution along the trailing edge (and the concomitant inertial forces) must be thought of as the reason why PR has the largest bending deformation. The radial battens of HUM provide some reinforcement in the span direction, resulting in the least deformation of all the 2-layer-leading-edge wings. LEO, as noted above, has the largest wing twist because of the absence of batten reinforcement.

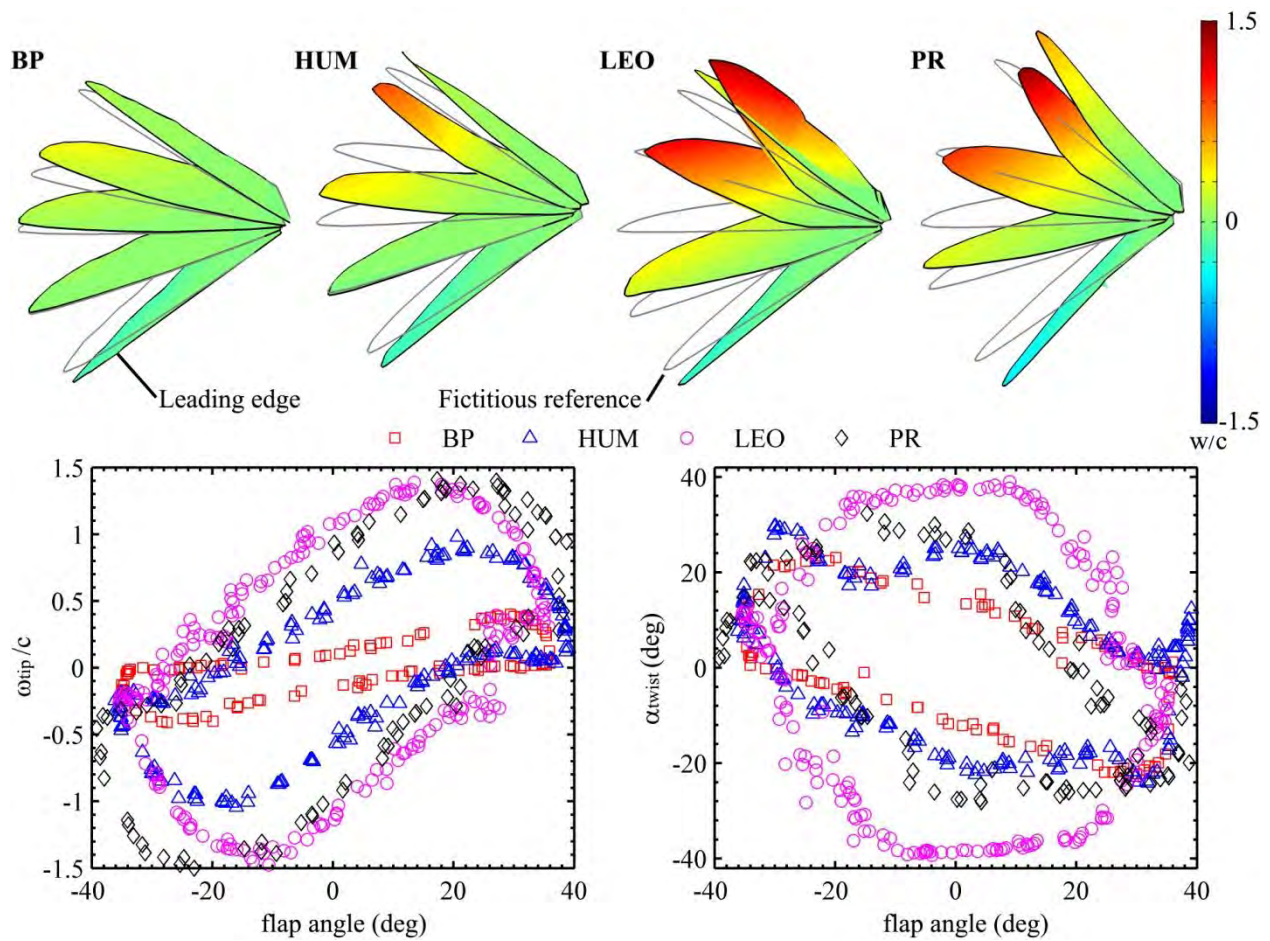


Figure 6-6. Structural deformation for all four wings at 20 Hz: contour plots through the downstroke (upper plot), cyclic tip displacement (lower left), and cyclic wing twist (lower right).

Referring to Figure 6-4, LEO produces the most thrust, PR the second, BP the third and HUM the least at a frequency of 20 Hz. The deformation history shown in the lower portion of Figure 6-6 matches with this thrust result very well: LEO encloses the largest loop area in both plots and has the largest amount of wing twist, therefore the most thrust. BP, however, encloses smaller areas than HUM while producing more thrust, which indicates that the phase angle may play a more important role: HUM is more flexible, producing tip deflection peaks much later after wing reversal. Between -15 deg and 15 deg flap angle, the area difference in the angle of twist loops does not

benefit additional flow in the thrust direction, even if passive wing twist is a good indicator of fluid/structure interaction. There may be extra airflow generated but scattered to other (non-thrusting) directions (Chapter 4). These correlation trends will be further discussed below.

Effect of aeroelastic coupling

When the experiment is conducted in vacuum, wing deformation is purely caused by inertial loadings, as shown in Figure 6-7. A direct comparison with the results given in Figure 5-2 should provide insight into the separate roles of inertial and aerodynamic loading, as well as aeroelastic coupling effects. The amplitude of the tip snap seen at stroke reversal is similar between Figure 6-7 and 5-2, which would indicate that aerodynamic loading plays a minimal role in this behavior, as expected. The most immediate result from Figure 6-7 is that, for all of the frequencies tested, the wing twist through the mid-stroke (0 deg flap angle) is nearly zero. This is to be expected, as the angular acceleration (and hence the inertial forces) should be zero through the mid-stroke for the sinusoidal flapping considered here. This is in direct contrast to the large twisting seen in Figure 5-2, which is almost solely due to aerodynamic loading (which will be maximum through the mid-stroke, where the angular velocity is peak). This behavior causes the twist and tip deflection phase loops to collapse at the origin of the plots, and the area enclosed by the loops is much smaller than seen in the air data of Figure 5-2.

The wing stiffness, therefore, dictates how large the phase loop will form in vacuum. As flapping frequency increases, inertial loads increase quadratically and the response time for the wing tip to recover after the snap becomes longer, forming the loop seen in the 25 Hz case. At the highest frequency of 35 Hz, each tip-snap becomes

a mechanism to store kinetic energy into elastic potential energy: the wing is elastically bent like a loaded spring. In the absence of air damping, the tip trajectory overshoots its kinematic route near the mid-stroke-plane and forms a third loop. It can also be seen that the vacuum environment exaggerates the asymmetrical properties of the wing (i.e., the membrane skin is bonded to the upper portion of the carbon fiber skeleton): bending stiffness is smaller through the upstroke, providing a larger loop.

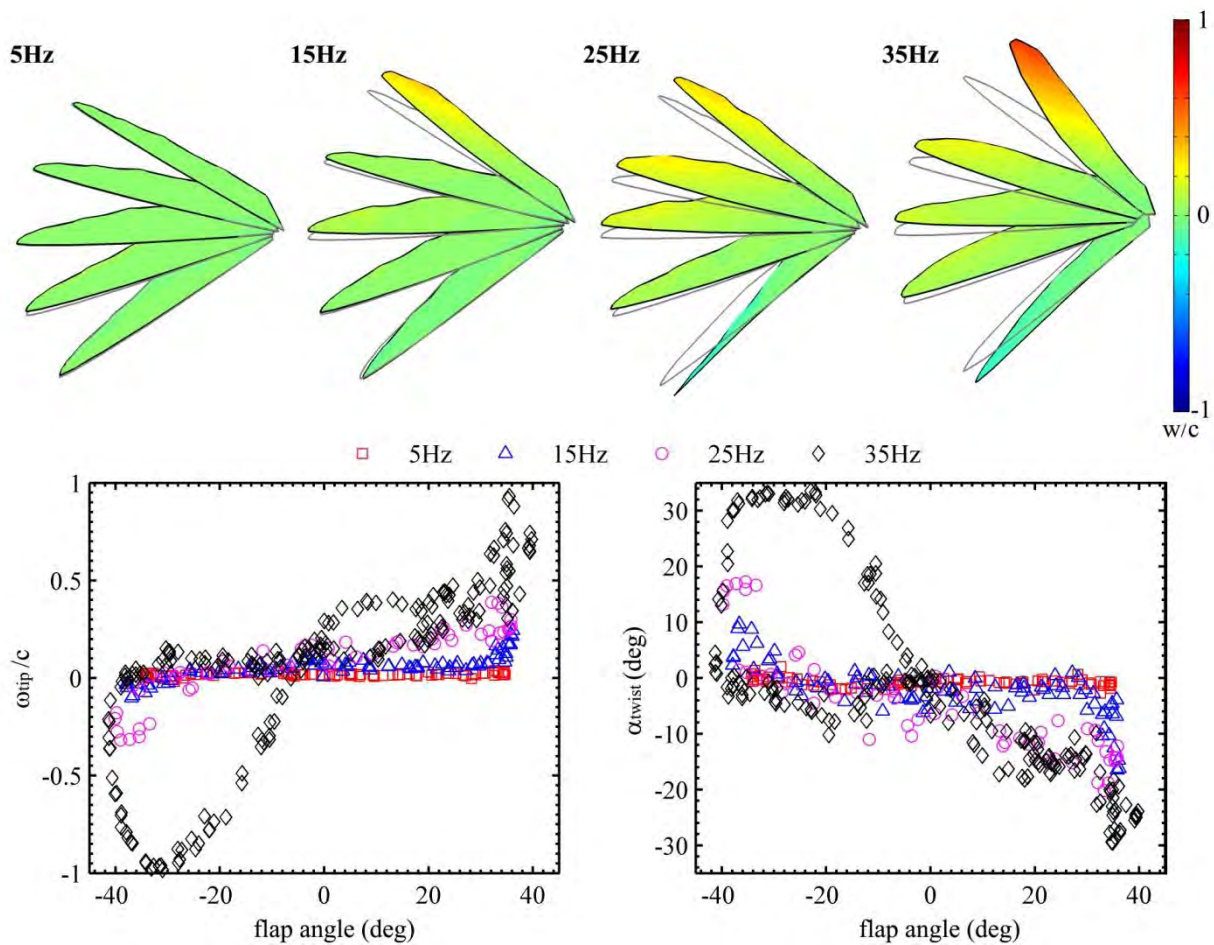


Figure 6-7. BP at different frequencies in vacuum: contour plots through the downstroke (upper plot), cyclic tip displacement (lower left), and cyclic wing twist (lower right).

Thrust and deformation correlation

Given that all the four pairs of wings are actuated under exactly the same conditions (kinematics, frequency, Reynolds number and environment), the cause for the disparate thrust (Figure 6-4) and efficiency (Figure 6-5) measurements is completely due to the differences in wing structure. Such differences are captured with the full-field DIC measurements and expressed in two key parameters: tip deflection for bending and twist angle for feathering, as shown in Figure 4-9. The statistical correlation between such parameters and the average thrust value may reveal certain trends, which in turn can provide a general set of design strategies for the aeroelastic tailoring of flexible flapping wings. Figure 6-8 shows the correlation results between thrust and tip deflection, the latter of which is converted into the area enclosed by the phase loops (deg·mm) and the loop phase angle which describes how much the actual motion (of the wing tip, for example) is lagging behind the commanded actuation. Subplot A shows the relationships of all four wings between the three variables: area, phase angle and thrust, viewed at 0° azimuth angle and 45° elevation angle. Data from BP forms a linear trend line, fitting onto a plane out of page; so are the other three wings'. This means the trend lines are bending stiffness specific: the three HUM, LEO and PR wings have the same leading edge structure (Table 6-2) and therefore similar bending stiffness, collapsing into the same trend line. It is important to realize that in this figure the trend lines are independent of flapping frequency (which is the only kinematic variable in this study), which indicates that the plot relates wing structure directly to aerodynamic performance. Similarly, subplots B and C show the two trend lines that reflects how the bending stiffness affects wing deformation during flapping and the thrust generated by such deformation. In subplot C, however, it is interesting to notice that at the last two

data points, BP reaches a maximum phase angle while the enclosed area linearly increases with thrust.

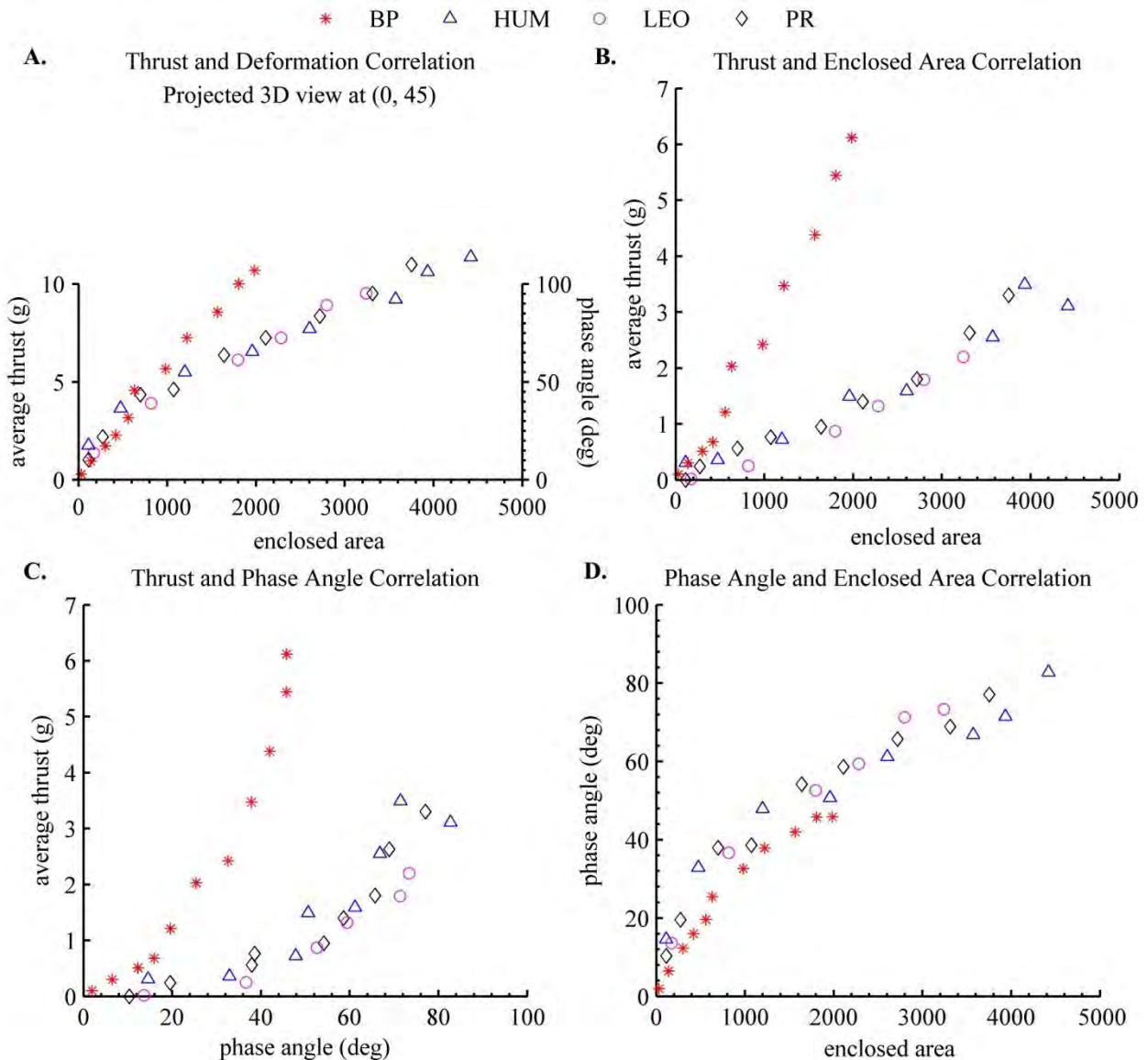


Figure 6-8. Correlation between average thrust and wing tip deformation.

Finally, subplot D of Figure 6-8 provides a result that ignores the aerodynamic thrust production: the relationship between the enclosed area and phase angle. In previous portions, two trend lines are formed distinctly because of the different leading edge stiffness. Here, the data from all four wings nearly collapse to a single curve, showing a more general trend. This result suggests that a stiffer wing would enclose a

smaller area while the phase angle increases at a very similar rate to the more compliant wings. Presumably, such characteristics of BP allow the wing to produce the most thrust at high frequencies, comparable to the results presented in Chapter 4 for three-layer-leading-edge wings. Similar correlation studies are performed for the passive twist deformation, shown in Figure 6-9.

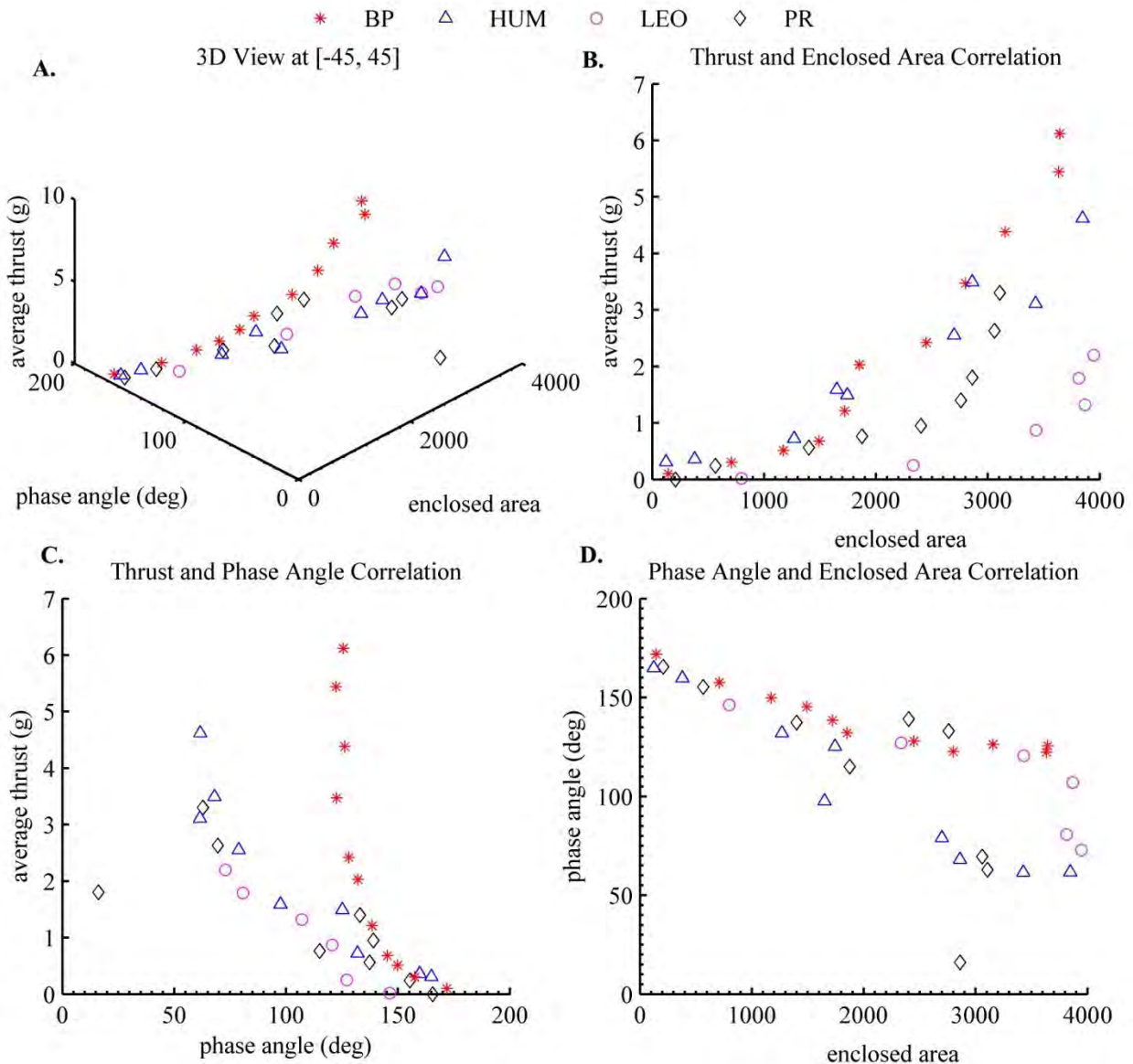


Figure 6-9. Correlation between average thrust and passive wing twist.

The trends of wing twist enclosed area, as shown in part B in Figure 6-9, are very different from each other as the wing structure varies: stiffer wings requires less twist deformation to achieve higher thrust. This is because the presentation of the data neglects the frequency required for the deformation. Both the BP and PR show a parabolic trend; while the HUM presents a near linear increase; LEO reaches maximum enclosed area at near 3500 to 4000, which is probably constrained by the in elastic Capran membrane. More distinct trends can be observed in C, where phase angle of the deformation loops are plotted against the time averaged thrust. The behavior is similar to Figure 6-8 C, the three wings of the same leading edge reinforcement have data of the same trend. BP's deformation is limited at a 135 deg phase angle while all other three wings have a decreasing phase angle as the thrust increases. This is because as the frequency and thrust increases, the peaks of the phase loop shifts towards the y axis.

Finally, the correlation between the enclosed area and phase angle of wing twist is shown in part D: showing that general trend (linear) exists when deformation is not excessive (enclosed area under 1000) and the divergence can be unexpected if under high level of aeroelastic loading. PR has significant trailing edge inertia that leads to a drastic phase change at high frequencies (indicated by the larger deformation). HUM and BP have fairly linear trend, though at different rate. This means the enclosed area increases at a constant rate as the phase angle decreases. LEO's absence of any reinforcement results in a deformation pattern that reflects the membrane's response: linear trend at the beginning but limited by a theoretical maximum enclosed area.

Figure 6-10 shows the correlations results of the total and net efficiency and tip deflection deformation. The data are scattered in a random manner except for LEO (top left), of which the phase angle and total efficiency has a clear linear relationship. It is also interesting to observe that the net efficiency of BP, HUM and PR forms a slightly decreasing plateau with both phase angle (bottom left) and enclosed area (bottom right). In all, the efficiency of different structures show tangible but complicated trends.

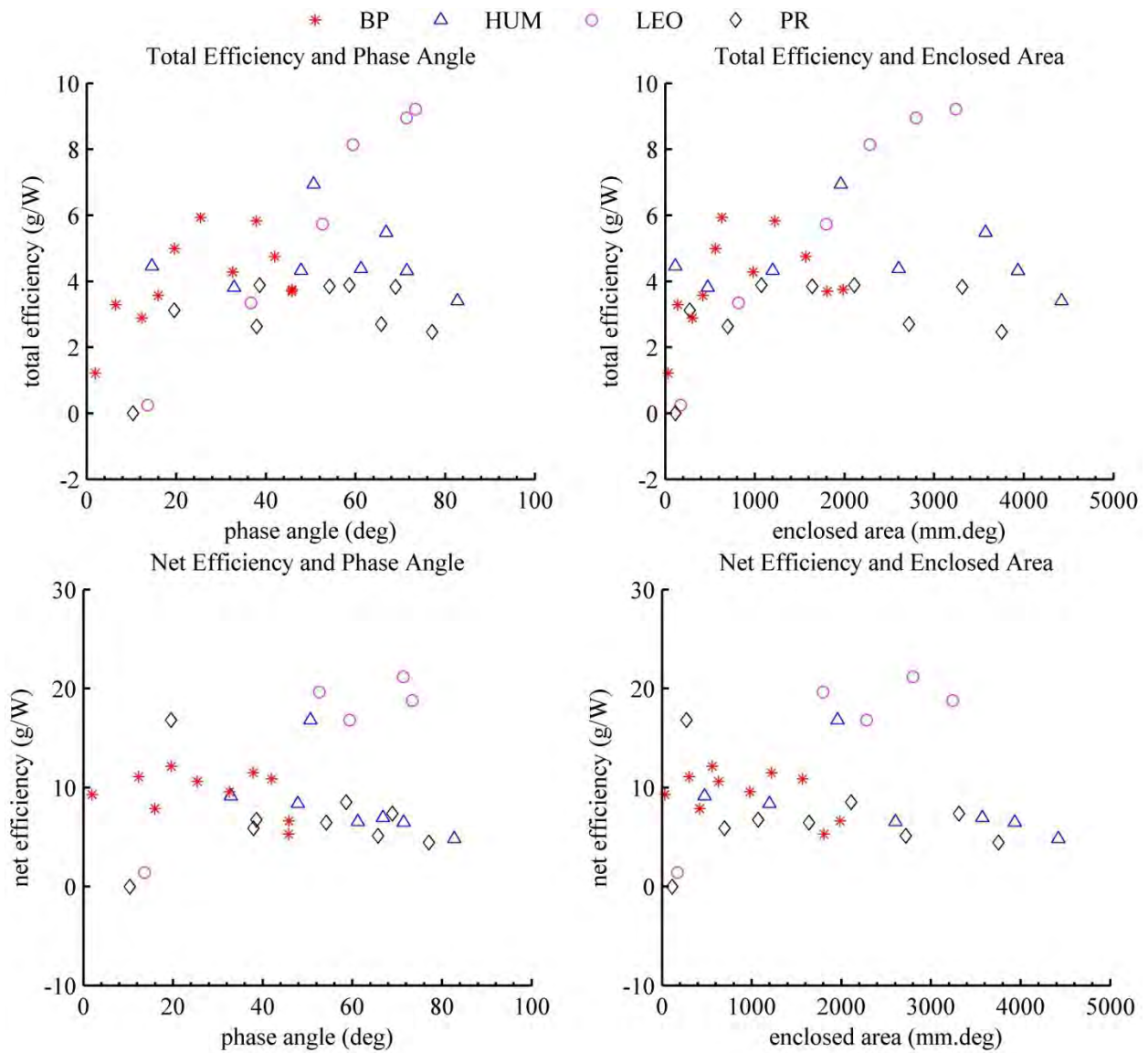


Figure 6-10. Correlation between efficiency and tip deflection.

6.2.4 Conclusions

This section has detailed the continuing work with the experimental setup aimed at providing a relationship between wing structure and thrust generated by passive deformation of different micro flexible flapping wing structures. Each of the four tested wings is constructed from a carbon fiber skeleton affixed with a thin membrane skin. The orientation and thickness of the discrete carbon fiber members has a substantial impact on the nature of the passive wing deformation (which is due to a complex combination of unsteady inertial and aerodynamic loading) and the concomitant thrust production. For this study, wings are actuated with a single degree-of-freedom rotary flapping motion: a rigid wing would generate little useful aerodynamic forces under such a motion, but the passive feathering, twisting, and bending of the membrane wings can provide meaningful thrust forces. The wing motion (which can be separated into rigid body motions and structural deformations) is measured with a high-resolution whole-field digital image correlation system, while a force-torque system is used to measure the average thrust and power-efficiency over a flapping cycle.

The results presented here has advanced the state of the art of flapping wing MAV research in many aspects and has added value to a less-noticed field of the study of flapping wing structure and its related performance. The experiments are conducted under strictly controlled parameters comparable to hummingbird's flight: flapping frequency range, wing size, wing weight and aerodynamic thrust. The application of DIC in this study, capturing the full-field structural deformation of the rapid moving wings in both air and vacuum, is pioneering. The post processing method developed based on these techniques, allows further analysis and interpretation of the data. Correlation study shows clear trends that indicate the relationship between structural stiffness and

aerodynamic performance: with 1 DOF kinematics, 1) chordwise stiffness needs to be orders of magnitude lower than the spanwise stiffness to achieve thrust effectiveness and efficiency; 2) spanwise stiffness needs to be optimized based on a particular frequency range and wing inertia to be efficient; 3) the deformation pattern created due to structural/aerodynamics coupling is what needs to be tailored to optimize performance. Different tests have been exhaustively performed to characterize the wing's structural properties and performance. Regarding the results of the tests, the following conclusions can be drawn:

i) Membrane wings with stronger skeletal reinforcement provide superior thrust at high frequencies (above 25 Hz); the opposite is true at lower frequencies. Thrust generally grows quadratic with flapping frequency, though extreme twisting deformations (seen by LEO, e.g.) can limit this growth to a linear trend.

ii) Passive wing deformation strongly governs the efficiency (ratio of thrust generation to power consumption). Non-batten reinforcement as in LEO is found to be the most efficient over the majority of the tested frequency range. Wing mass and its distribution is another important factor affecting efficiency.

iii) The effect of frequency, structure and aeroelastic coupling are examined for wing deformation, using color contour as well as phase loop representations of the wing bending and twisting.

iv) When flapping in air, the plot of wing tip deflection versus flapping angle forms a counter-clockwise loop, while wing twist versus flapping angle forms a clockwise loop. This is because as the wing travels through downstroke, aerodynamic forces press the wing upwards and cause wash-out (negative twist). This twisting motion is thought to

be a major contributor to the thrust development. At stroke reversal the wing experiences a tip snap, which is solely due to the inertial forces.

v) When flapping in vacuum, wing deformation through the middle of each stroke is minimal (as the aerodynamic forces are zero), and so the phase loops collapse at the origin of the plots. Behavior at stroke reversal is largely unaffected.

vi) Wings with adequate batten reinforcement (i.e., BP) show a monotonic growth in wing deformation with flapping frequency. Contrastingly, largely unreinforced wings (LEO) have very large twisting motions at relatively low frequencies. The amplitude of this deformation remains relatively unchanged with increased actuation, which is indicated of strong hardening geometric nonlinearities within the structure.

vii) The PR wing, which has a large amount of mass located along the out-board portions of the structure, generates the largest tip displacement at stroke reversal, while LEO, with no chordwise reinforcement, has the largest amount of wing twist.

viii) There is a strong correlation between the thrust generation, the enclosed area and the phase angle of the tip deformation phase loops. The intrinsic relationship between wing structure and its ability to produce thrust is represented in these trend lines, regardless of flapping frequency. The relationship between the two deformation parameters is also found to be irrelevant to the aerodynamic consequences.

6.3 Experimental Optimization Methodology

It has been observed from previous chapters that flapping wing flexibility can significantly enhance aerodynamic performance. By tailoring the structural properties, passive deformation can be utilized to generate higher lift and thrust. This section presents a systematic methodology to experimentally optimize the flapping wing structure for maximizing thrust production under a simple one-degree-of-freedom

motion. Different flapping frequencies and amplitudes are also examined along with different wing structure to study the relationship between kinematics and thrust; because these variables are closely related to the passive inertial deformation. The aerodynamic performance is measured with a force sensor recording both the lift and thrust; the net time-averaged thrust is used as a benchmark to evaluate wing performance. The wing structural property is obtained by measuring wing deformation using a digital image correlation system capable of capturing the full-field out-of-plane deformation of the whole flapping stroke up to 90° in both air and vacuum. The data are presented as contours to reveal details of structural deformation and later extracted as phase plots that show a loop of the deformation versus flap angle. A certain design scheme is formulated to generate a number of designs, all of which are tested for thrust production. The force and deformation data are then correlated to understand the structure that benefits thrust and used to predict parameters for potential optimal flapping flight. It is concluded that for flapping wing structure optimization in hovering flight on this scale, each structure must be tailored according to a certain kinematics (with a desired flapping frequency and amplitude) and optimized for performance values such as thrust/lift coefficient/efficiency.

6.3.1 Introduction

The anisotropic properties of insect wing have raised many questions for scientists. The venation patterns and the roles of these patterns varies greatly among species: dragonflies have a pleated leading edge for spanwise stiffening, flies have curved veins for chordwise bending, locust wing's display a fan-like distribution of veins that promote bending/extension coupling, etc. Understanding the roles of the structure characteristics demonstrated by these highly evolved lives can help with the design of artificial flapping

wings for micro air vehicles. However, at present an efficient exploration of this phenomenon is not yet possible through numerical methods: the aeroelastic flapping system is prone to numerous nonlinearities, and the computational cost involving both fluid and structure dynamics is very high^[176]. Therefore before numerical methods are reliably developed and intensely validated, the search for an optimum wing structure for manmade flapping flight needs to be conducted experimentally. This section develops the previous experimental setup and summarize it into a methodology that can be used to systematically optimize flapping wing structure.

One of the main issues in designing a flapping wing MAV is defining the wing's aeroelastic properties, which in combination with the prescribed actuated kinematics determine the lift and thrust production that eventually dictate flight performance. Aeroelasticity is an interdisciplinary study of aerodynamics, dynamics and elasticity. Therefore the term includes a wing's structural properties (elasticity and dynamic responses), dynamics (kinematics and flight mechanics) and aerodynamics around the wing. In most fixed wing aircraft, investigations of wing aeroelasticity tend to avoid or reduce unstable vibration/flutter, or improve flight performance via structural tailoring. Experimental characterization and computational optimization have been done by Stanford^[2] for flexible membrane wings for fixed wing MAVs; the study has provided a design direction for MAV wings with more stability and controllable mission-based lift and drag coefficients. Similarly, in flapping wing aircraft, the ideal situation is to tailor a wing's aeroelastic properties to enhance lift and thrust production.

The flapping membranes with and without batten reinforcement at the trailing edge of the wing tip has been studied by Ho et al.^[17] as a function of advance ratio. For large

values of this metric, the lift capabilities of the two wings are identical, but as the unsteady features of the flow are enhanced (low advance ratio), the wing without this reinforcement is inferior. The authors stated that the excessive feathering of the wing disrupts the leading edge vortex, and the concomitant lift. Thrust, however, relies heavily upon wing flexibility for its development, and so an adequate compromise must be found. This concept for a membrane wing with an unconstrained trailing edge, whose feathering motion develops significantly more thrust force than one reinforced all along its perimeter, has also been experimentally demonstrated by Singh et al.^[111]

As described in Chapter 4, the current experimental techniques allow to measure high resolution full-field deformation of the wing surface at high flapping frequencies. The structural deformation is separated from the rigid body motion to understand the relationship between passive deformation and thrust production. The deformation data is extracted as certain representative values: tip deflection that indicates wing bending and twist angle that indicates passive rotation. These values are plotted with flap angle (wing position), forming a phase loop, of which the shape and magnitudes are solely dependent on the structure flexibility and inertia (however, the measured deformation involves with complicated coupling between the structure and air). Two aspects are related to the thrust production: the area enclosed by the loop and the phase angle of the loop diagonal. The previous section has studied the relationship between these two variables and thrust production and found an apparent correlation trend for the stroke amplitude of 70°.

In this study, 37 pairs of carbon fiber battened wings laminated with thin membrane (Capran[®]) are used, including some of the wings studied in the previous

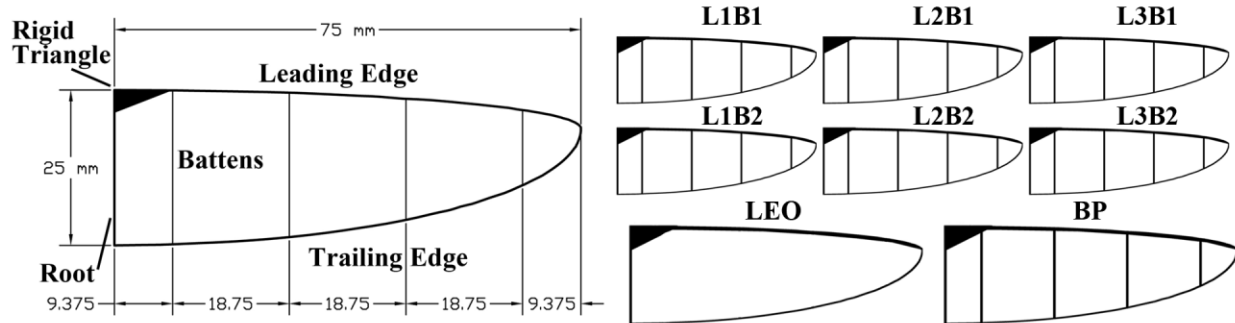
chapters. These wings are originated from the same topological pattern, but reinforced differently. Therefore a wide-range of wing flexibility can be achieved. The wings are actuated by a 1 degree-of-freedom (DOF) flapping mechanism that has different stroke amplitudes (40° , 60° , 70° and 90°) at various flapping frequencies (15~35 Hz). The thrust production and structural deformation are measured in these cases to produce a data array: each measurement contains thrust and deformation as functions of frequencies and amplitudes. The data is used to explain the relationship between passive deformation and aerodynamic performance of the wing structure. The optimum design(s) in the defined space is then selected.

The organization of the remainder of this section is as follows. First, the wings designed and used in this experiment are explained in detail. Then the flapping mechanism for wing actuation is described briefly. The experimental setup is then illustrated, followed by the detail of the measurement procedure: thrust measurement, deformation measurement, and data post processing. Finally, the results are presented and discussed.

6.3.2 Flapping Wing Design Space

The wing planform, parameters and fabrication methods are the same as the ones in the previous chapters. As shown in Figure 6-11, all 37 tested wings are made of exactly the same structural layout: reinforced leading edge, wing root and battens (parallel to the root). There is no reinforcement of the trailing edge. At the intersection between the leading edge and wing root, there is a triangle made of three layers of bidirectional carbon fiber that serves as a stiff reference for wing mounting and deformation calculation.

1) Design scheme and 8 wings in the control group



2) Variations in chordwise reinforcement (group A and B, from 0000 to 1111, 16 wings in each set)

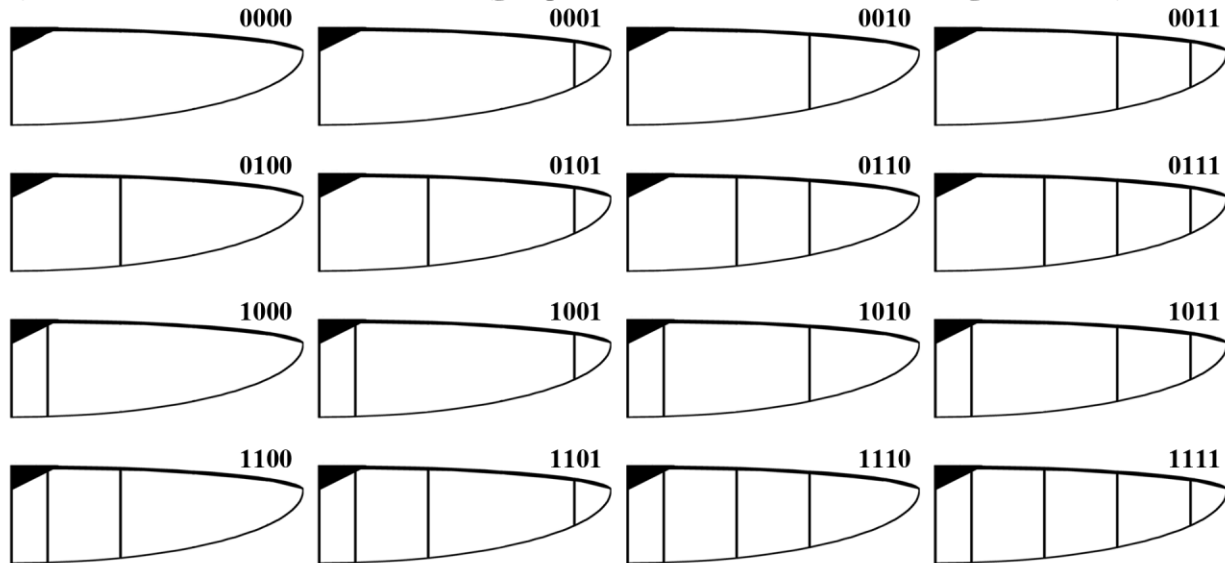


Figure 6-11. Planform and layup structure of tested wings.

The reason for selecting such design scheme is threefold: 1) By attaching straight battens to the leading edge, the wing bending stiffness depends only on the leading edge; while torsional stiffness is also mainly determined by the leading edge, battens control the torsional deformation by maintaining the cross section shape and mass distribution, which affects inertial loading. 2) This topology provides a design space for identifying the role of bending stiffness and passive deformation varied with mass distribution, by taking the four battens as variables. 3) The battens can be used to define an airfoil for forward flight in future designs.

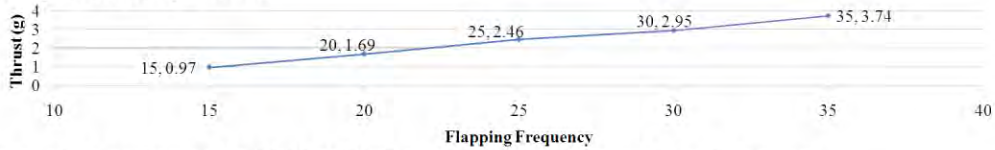
There are two groups of wings analyzed in this work: the control group that consists of previously tested wings and the variation group. The control group wings have been reported in previous chapters (4 and 5), in which the results are a good reference for this study. From top down in Figure 6-11, the first six wings are named for their leading edge (L) and batten (B) variations. The number following these letters indicates the number of reinforcements. The next two types of wings are LEO (leading edge only) and BP (battens parallel) from previous work⁷. These two wings are the same as the A0000 and B1111 in this work (explained in the following). The variation group is divided to two sets: A that consists of wings made with 2 layers of leading edge reinforcement and B with an additional layer from the root chord to the second batten counted from the tip. For the batten variation, a binary number from 0000 to 1111 are used to represent the location of the battens, as shown in the lower portion of Figure 6-11. Each A and B set contains 16 pairs of wings. There are three cases overlapped from previous work and this work: L2B1 is the same as A1111, LEO as A0000 and BP as B1111. Therefore a total of 37 pairs of wings are studied in this work.

6.3.3 Aerodynamic Performance

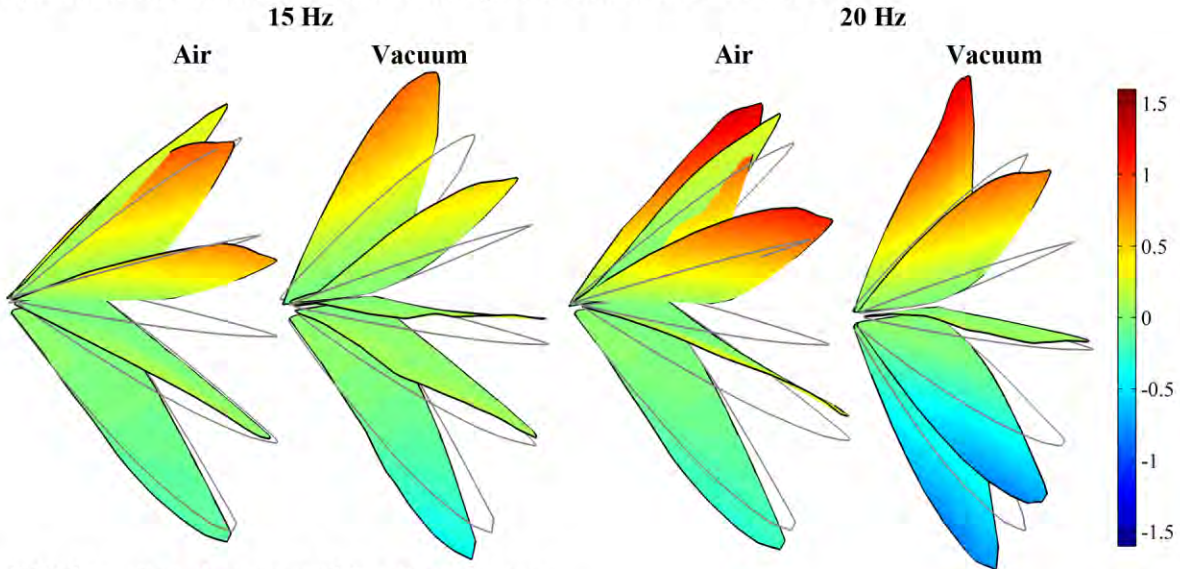
The variation group of the wings provides a design space to examine the effect of each reinforcing structure. In order to facilitate comparison, a baseline case must be first established. Wing A0000 is selected to be the reference case. Figure 6-12 summarizes A0000's performance and behavior. The thrust presented in 1) uses traditional unit: gram force; because it is easier to compare with previous work's results, which can be better normalized to a hummingbird's weight (3.5 grams). Since both thrust force (in Newton) and thrust coefficient (no unit) are directly proportional to thrust (in grams) for cases of the same flapping frequency, the normalization is applicable for

comparison at different flapping frequencies, as shown in Figure 6-13, where all 5 cases (15~35 Hz) of A0000 start at 1.

1) Thrust produced by A0000



2) Deformation contour of A0000 at 70 deg, at 15 and 20 Hz in air and vacuum



3) Deformation phase loop of the above 4 cases

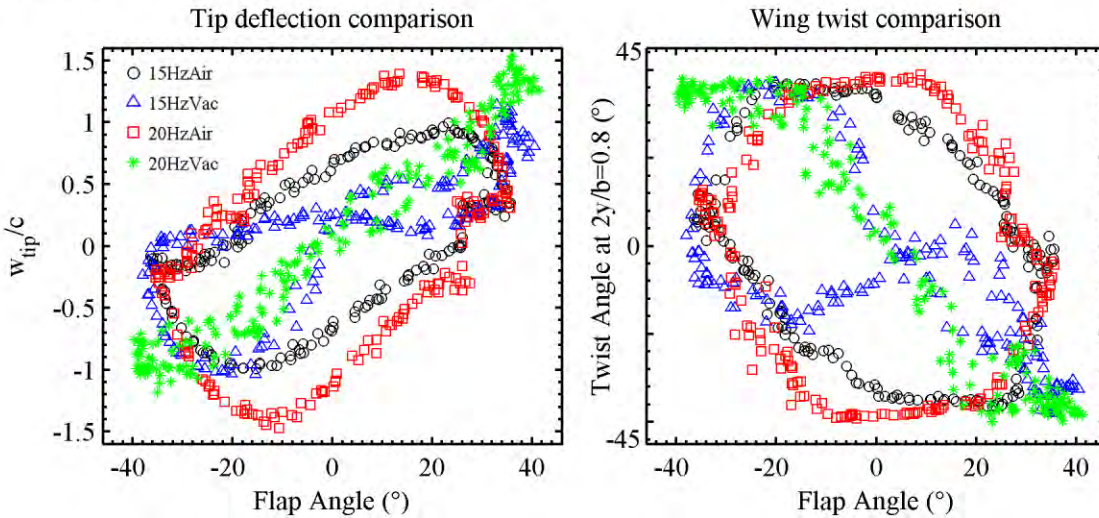


Figure 6-12. Performance and behavior summary for wing A0000.

In Figure 6-12, it can be seen that the baseline case A0000 has near-linear trend between thrust and frequency. Only downstroke is shown for the four cases in the color contour plots. The measurement of wing deformation also shows how the aerodynamic forces have significant effect on wing deformation: tip-snaps (deformation due to inertia at the end of each stroke) are significantly smaller at both frequencies due to the aerodynamic damping; wash-out and wash-in (membrane billowing during a stroke) are drastically larger in the air cases near the mid-plane. A detailed deformation history in one flapping cycle is shown in the phase loops 3). Two conclusions can be drawn: 1) the leading edge bending stiffness dictates the magnitude of tip deflection; 2) the membrane constraint limits the maximum wing twist at near 40° . The timing and magnitude of both bending and twisting deformation are the result of both inertial and aerodynamic loading.

Once the performance and deformation pattern of A0000 is understood, then the rest of 31 wing types in the variation group can be seen as using different ways to reinforce A0000. The straight parallel battens added to form A0001~A1111 would have three effects: increasing the mass of the wing, changing the mass distribution (center of gravity), and stiffening a particular cross section. These effects would impact on passive wing deformation for a case of the same amplitude and frequency. For the other 5 wings L1B1, L1B2, L2B2, L3B1 and L3B2, leading edge stiffness is also varied with different reinforcements and for the B2 wings an additional layer is added to the battens, increasing the inertia. The performance comparison of these 37 wing types is presented in Figure 6-13.

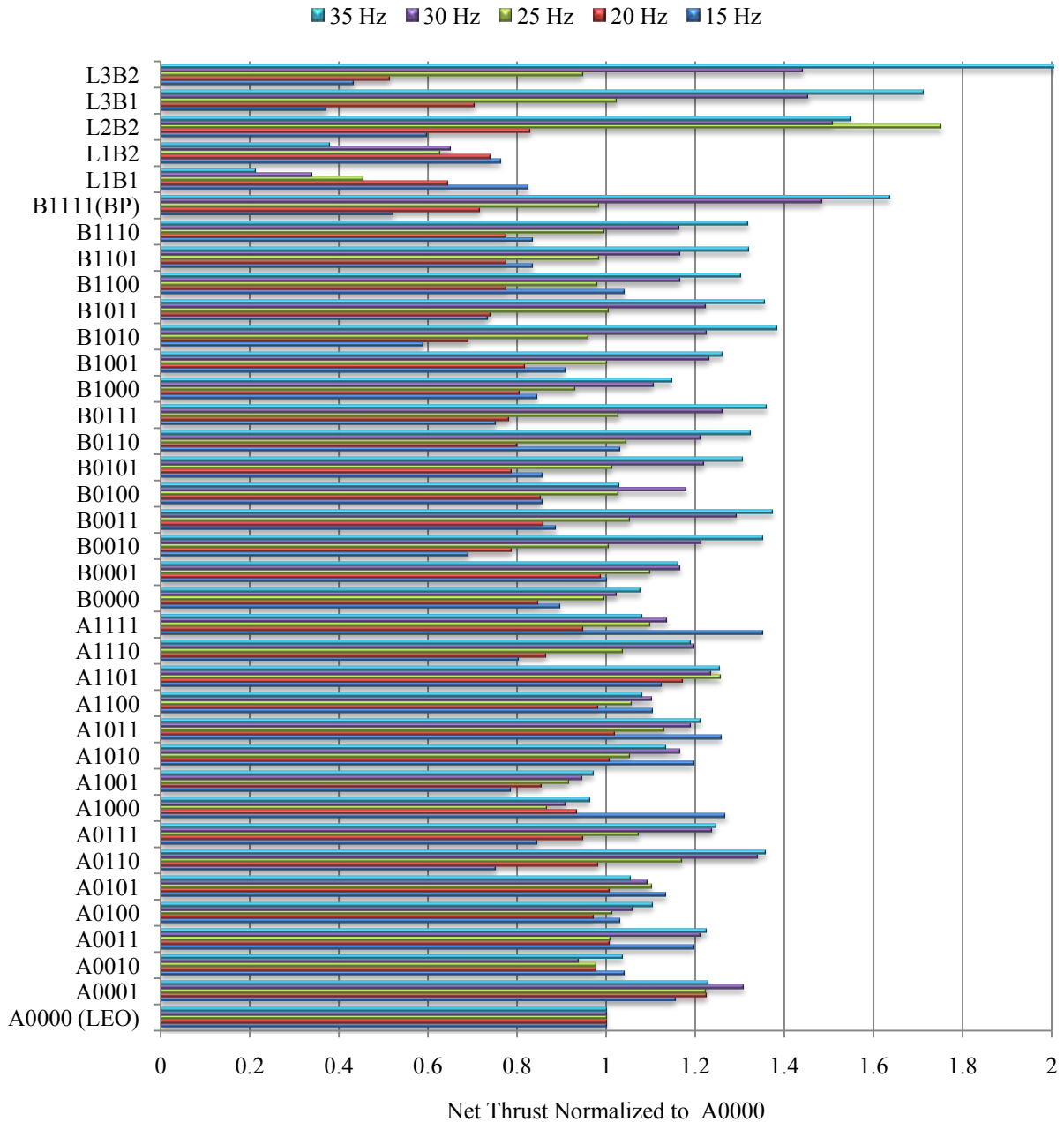


Figure 6-13. Thrust performance comparison of the 37 wing types normalized to A0000, at amplitude of 70°, and at five different frequencies.

Figure 6-13 confirms one of the previous conclusions: wings with stiffer spanwise reinforcement require high frequency actuation to increase inertial loads to achieve beneficial passive deformation to produce thrust. Group B are in general all performing better at higher frequencies (30 and 35 Hz) than group A and vice versa.

The wings outside of group A and B present very interesting results: the under-reinforced wings L1B1 and L1B2 both perform poorly comparing to A0000 and the performance keeps degrading as the frequency increases. This is due to the weak leading edge failing to transfer aerodynamic momentum to the thrust direction so the wings bend over instead. L2B2 is equivalent of A1111 with extra straight battens, which doubles the structural weight on the wing surface. This seems to be particularly beneficial at the frequency range of 25 Hz to 35 Hz, improving the wing performance by 60%. This indicates that larger inertial loading can induce deformation to improve aerodynamic performance significantly. The wings L3B1 and L3B2 perform poorly at low frequencies (15 and 20 Hz) but have significant improvement at high frequencies (L3B2 doubles A0000's thrust at 35 Hz).

Figure 6-13 explains another important aspect of structural optimization in flexible flapping wings: the structure can only be tailored to a particular frequency range so that inertia force can be used to calculate the corresponding deformation. In this study, for group A and B there are 5 optimal wings for each of the 5 frequencies. A structure designed to perform well at high frequencies is inevitably required to be stiffer and therefore is inferior at low frequencies. Therefore the optimal wings in group A and B are A1111 at 15 Hz, A0001 at 20 Hz, A1101 at 25 Hz, and B1111 at both 30 and 35 Hz. If the other five wings are considered, the only change in ranking is for high frequencies: L2B2 at 25 Hz and 30 Hz, and L3B2 at 35 Hz are now the best wings.

Figure 6-14 shows the overall comparison for the sum of the five normalized values of thrust. This method would neglect the wing performance at specific frequency but allow the stiffer wings make up for their low score at low frequencies. It can be seen

that the best wing overall is L2B2 and the worst one is L1B1. The success of L2B2 may be explained with the fact that it has the even structure density that allows for the right pattern of passive deformation, which can be achieved at 25 Hz for its stiffness and mass distribution.

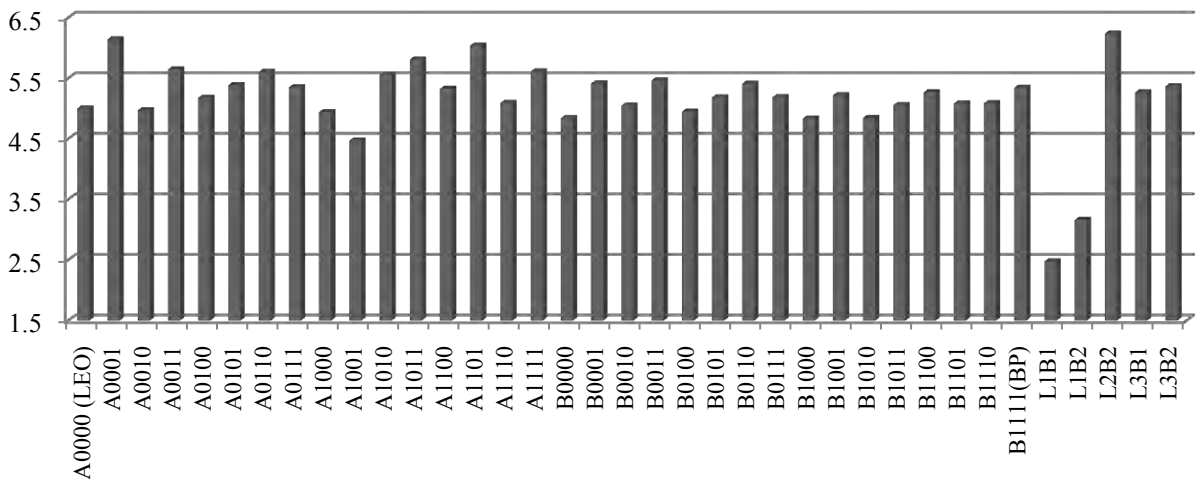


Figure 6-14. Overall thrust comparison in the range of 15 to 35 Hz, L2B2 as the overall optimal wing.

6.3.4 Conclusions

An experimental methodology is developed for flapping wing structure optimization in hovering flight of micro air vehicles, including designing and manufacturing a 1 DOF flapping mechanism as a test bed for the study, exploring a well defined structure design space with 37 pairs of wings, setting up an experimental facility for measuring the aerodynamic performance and structural deformation, and developing post processing and analysis methods. Several challenges are overcome: 1) designing the experiment so that both the kinematics and wing structure are comparable to the natural fliers that inspired this study, including flapping frequency, amplitude, Reynolds number and structural properties; 2) measuring the small magnitude of aerodynamic forces produced by the wings; 3) measuring the complicated wing deformation during rapid

flapping motion at large stroke amplitudes, with full-field techniques so that different deformation parameters can be extracted; and 4) post processing the data to characterize wing structure and reveal the relationship between deformation and aerodynamic loads.

Experimental optimization steps

The experimental methodology can be summarized as these steps:

- I) create a design space to control structural deformation;
- II) realize the desired kinematics and wing structure;
- III) select standards for performance evaluation (which would terminate the number of iterations);
- IV) measure aerodynamic forces and structural behaviors;
- V) analyze for the aeroelastic effect;
- VI) correlate the data to improve design parameters for the next iteration.

Itemized topology study summary

The results of this study can be concluded as following:

- i) With 1 DOF kinematics, flapping wing can generate significant thrust with passive deformation, which is triggered at wing reversal at the end of each stroke due to inertial loading. This deformed shape, creating a significant twist angle, is to be sustained with aerodynamic loads through the flapping stroke.
- ii) The aerodynamic force generated at certain frequency and amplitude depends on the magnitude of deformation, which is determined by the structure stiffness and mass distribution.
- iv) There is an optimal amount of deformation that needs to be found, either too small or too large deformation would be ineffective.

v) Structural optimization should be conducted towards a fixed kinematics with defined frequency and amplitude, so that inertial loading can be determined and used to design a structure with desired inertial deformation.

vi) Performance and deformation measurements must be conducted simultaneously to examine the aeroelastic effect. The correlation of the two can be used to iterate improved designs.

vii) There is a trade-off between amplitude and frequency; however, large amplitude is always preferred in hovering flight. Low amplitude may be more efficient in forward flight. Therefore the flapping amplitude is an important control parameter.

viii) In hovering, a flexible wing would have one corresponding most efficient frequency for thrust or thrust coefficient.

6.4 Discussion

This chapter echoes with Chapter 3 about how to utilize passive wing deformation to enhance flapping wing aerodynamic performance by designing wing structure. Different topologies are designed so that various stiffness and mass distribution can be examined. In 6.2, the four topologies show complete different performance in both net thrust production as well as energy efficiency: the high stiffness wing BP has promising performance at high frequency while the batten-free LEO has very high efficiency due to adaptive deformation and light weight; HUM illustrates how an over-constrained wing would have less beneficial passive structural deformation and therefore inferior aerodynamic performance; and finally PR shows how mass distribution dictates resonance and the magnitude of deformation. The correlation study shows the intrinsic trends between the pattern of deformation and thrust, making it possible to predict aerodynamic performance directly from structural properties.

In 6.3, a design space is selected to allow the structure topology to vary systematically. The idea is to investigate the effect of cross-section constraint, mass distribution and bending stiffness. The study has successfully shown that the definition of an optimum structure has to be defined under specific kinematic parameters for maximizing selected aerodynamic metric such as thrust or its coefficient. Bending stiffness and its corresponding passive wing tip deflection has shown clear effect on time averaged thrust production, as shown in Figure 6-15. This supports that the aerodynamic effect due to passive wing deformation is mainly caused by inertial loads (actuation kinematics). When wings are undergoing the same kinematics (therefore the same inertial loading), structural stiffness (or compliance) results in different amount of deformation, which interacts with air to realize the final wing kinematics. This means the aerodynamic effect on structure deformation is less relevant: at low frequencies, more compliant wings result in larger deformation that propels more air. The major presumption for this to work is that the structural deformation should be in phase with the actuation kinematics so that the final wing kinematics is enlarged. Chapter 4 shows the opposite example of L1B1 when larger structural deformation in an off-setting phase resulting in smaller stroke amplitude and therefore weaker thrust at high frequencies. But it also shows the supporting case at low frequencies when other stiffer wings undergo much smaller deformation and therefore much less thrust at low frequencies.

In Figure 6-15, general trends of the normalized thrust produced by the wings are presented. The data are arranged in the same way as in Figure 6-13: A group on the bottom and the B group on top, with LmBn wings from Chapter 4. The trend variation from 15 to 35 Hz shows that as the frequency increases, the wings with higher bending

stiffness on the leading edge produce higher thrust. Therefore, there is no ideal unchanging structure can satisfy a wide spectrum of frequencies, as shown in Figure 6-14 the tradeoff between low frequency performance and the high frequency one would make wings overall performance similar.

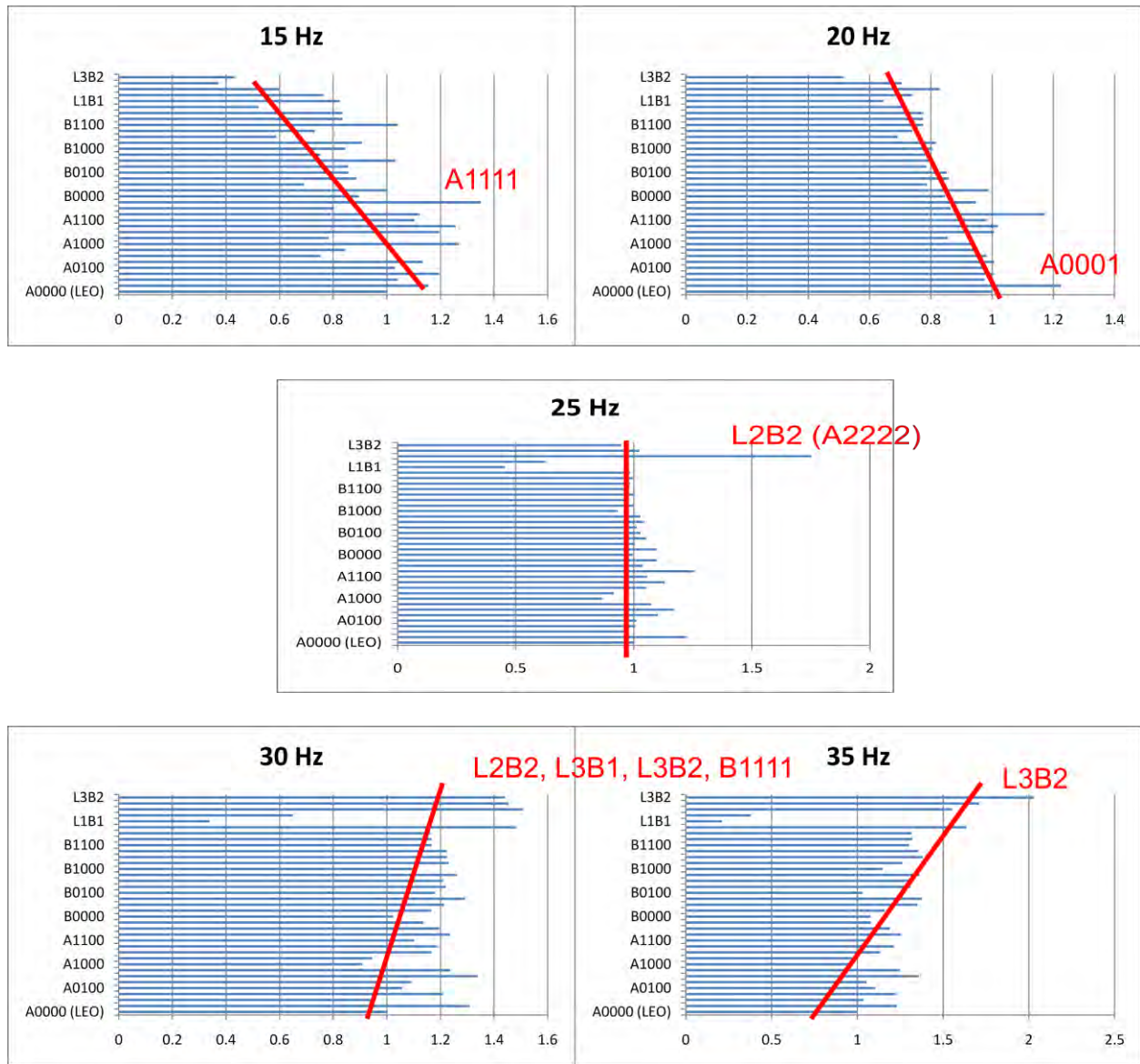


Figure 6-15. Effect of bending stiffness and local optimum wings.

The local optimum wings are also highlighted in Figure 6-15. The result cannot be comprehended intuitively. For example, if mass distribution is so crucial to passive

deformation, then at 15 Hz, the local optimum A1111 can be explained: all battens result in the largest mass distributed behind the leading edge, causing the most wing twist. This would also explain the 25 Hz case and the 35 Hz case. However, at 20 Hz, wing A0001 performs the best, rendering the previous hypothesis questionable. This points out that, similar to the effect of kinematics examined in Chapter 5 (more specifically 5.3), the key is not only the amount of structural deformation, but more importantly the timing of the passive deformation (and the resulting wing kinematics).

The effect of cross-section constraint is only partially revealed with the study of the BP and LEO cases. Detailed deformation measurements of both the A and B group are required for further correlation comparison. However, the BP and LEO comparison has shown that chord-wise structural reinforcement is essential at high frequencies; the value of stiffness and the topology are to be optimized.

In all, the aeroelastic interaction of flapping wings is complicated but can be quantified and measured. The experimental setup, techniques and data processing and analysis methods developed in this dissertation enables experimental optimization of desirable wing structure to achieve effective and efficient aerodynamic performance. The two studies presented in this chapter serve as a pioneering step towards the ultimate goal: designing an artificial wing that enables agility, stability, and maneuverability for FWMAVs.

CHAPTER 7 NUMERICAL MODEL VALIDATION

An important aspect of this research is to provide computational studies with experimental data for validation purposes. The overall team effort of the MURI program has been demonstrated in Chapter 4: using a wide variety of experimental tools to investigate the complicated problem. In this chapter, the collaboration extends to using both experimental and computational methods. Data comparison of a simple isotropic wing is made as the first step towards the validation objective: an isotropic flat plate aluminum wing is manufactured and actuated to perform a single degree-of-freedom flapping motion. The wing deformation and airflow around the wing are measured with digital image correlation and particle image velocimetry, respectively. These techniques have been used in Chapter 4 and further developed in this work. Computational analyses are performed on this wing configuration using a combined nonlinear structural dynamics and Navier-Stokes solution. Reasonable agreement obtained between experimental and computational data in this preliminary effort shows a potential to analyze more complicated flexible flapping wings in future.

7.1 Review

There has been a growing interest in the development of flapping wing micro air vehicles (FWMAVs) in the recent years. The physics behind flapping wing flight, in particular, the coupled interaction between aerodynamics and wing deformations, needs to be better understood for FWMAV development, which has been stimulated by the long history of natural flight studies. Photography and videography studies indicate that most biological flyers undergo orderly deformation in flight^[178]. Insects, bats, and birds exploit the coupling between flexible wings and aerodynamic forces, using passive wing

deformation to gain aerodynamic advantage^[179]. The interaction between unsteady aerodynamics and structural flexibility is, therefore, of considerable importance for FWMAV development^[171].

There are numerous publications discussing and analyzing flapping wings^[181] using both experimental and computational approaches. Some of those efforts that primarily focus on fluid structure interactions are discussed here. Ho et al.^[17] used the two-way coupling feature of a commercially available flow solver (CFD-ACE+) and the structural dynamics solver FEMSTRESS to create an aeroelastic solution to analyze membrane flapping wings. They showed that stiffness distribution is a key parameter in determining vortex interaction and thrust production. Heathcote and Gursul^[182] have experimentally investigated the effect of chord-wise flexibility on thrust generation of airfoils undergoing a plunging motion under various free stream velocities. Direct force measurements showed that the thrust/input-power ratio was found to be greater for flexible airfoils than for the rigid one. Katz and Weihs^[183] also showed that chord wise flexibility could increase the propulsive efficiency of a combined pitching/plunging wing. To study the effect of the spanwise flexibility on the thrust and propulsive efficiency of a plunging wing, a water tunnel study was conducted by Heathcote et al^[166] on a NACA 0012 uniform wing of aspect ratio 3. They observed that for Strouhal numbers greater than 0.2, a degree of spanwise flexibility was beneficial. In a subsequent effort, Chimakurthi et al^[184] and Aono et al.^[185, 186] conducted computations to explain the impact of spanwise and chordwise flexibility on aerodynamics with the help of a rigorous analysis of flow structures, pressure distributions, aeroelastic deformation, and phase lag. In the case of spanwise flexible plunging wing structures, it was shown that the

effective angle of attack due to prescribed motion and the phase lag of the response are the two key factors that affect the aerodynamic force generation. However, in the case of the chordwise flexible wings, it was shown that wing deformation in the chordwise direction could result in an effective projected area normal to the flight trajectory that supports thrust force generation and a subsequent re-distribution of the aerodynamic loading in the lift and thrust directions. Liu and Bose ^[187] suggested that propulsive efficiency of oscillating flexible wings can be increased, over the value of an equivalent rigid wing, by careful control of the phase of the spanwise flexibility relative to other motion parameters.

It has been observed in both nature and experiments that flapping wing elasticity/flexibility is crucial to flapping flight. Wu et al. ^[139] investigated structural deformation and airflow around three Zimmerman wings with varying flexibility flapping under hovering conditions. The wings were made from a carbon fiber skeleton and covered with a flexible membrane. Flexibility was varied by changing the number of layers of carbon fiber reinforcing the leading edge and hence it mainly affected the spanwise bending stiffness. The study showed that flapping wing stiffness and mass distribution has significant impact to the aerodynamic performance: certain structural compliance enables flapping wings to produce more thrust. Dynamic response is another important aspect: it is a direct benchmark for both the wing inertia (mass) and stiffness (inverted flexibility). This aspect has been studied by measuring the wing deformation caused by inertial loading and aerodynamic loading ^[121]; the results show that a hawkmoth's wing deformation at 26 Hz is mainly caused by inertial loads, as the experiments conducted in air and in helium (approx. 15% air density) produce similar

deformation pattern, suggesting aerodynamic forces have minimal effect. This may indicate that the passive deformation caused by inertia is utilized to affect aerodynamics. However, as pointed out by the authors, the result may be species specific and many contradictory conclusions have been reported ^[122].

To further our understanding of flexible flapping wing under hovering conditions, this chapter presents an ongoing effort to develop an integrated experimental and computational approach to investigate coupled flow-structure interactions. As the first step, an isotropic aluminum wing is manufactured and actuated to perform a single degree-of-freedom flapping motion ($\pm 21^\circ$ stroke amplitude and 10 Hz flapping frequency). The wing deformation and airflow around the wing are measured using DIC and PIV respectively. Computational analyses are performed on the same wing configuration using a combined nonlinear structural dynamics and Navier-Stokes solution. The main objectives of this paper are to: a) discuss the development of an integrated experimental and computational approach to analyze flapping wing configurations, and b) to show some preliminary comparisons of flow structures and wing deformation between experimental data and computational response.

7.2 Tested Wings and Experiment Configuration

7.2.1 Isotropic Tested Wings

The isotropic wings tested in this study are made from 0.4 mm thick aluminum sheets, as shown in Figure 7-1. The wing planform is of a 7.65 aspect ratio and has a Zimmerman shape, i.e. is formed by two ellipses which intersect at the quarter-chord point. The wing length is 75 mm and the root chord length is 25 mm. The wings are manufactured with CNC machine to achieve the exact contour and avoid stresses that may cause warping. After machining, the wing surface is primed with flat white coating

for the background and speckled with black dots for DIC measurements. Another coating (Rhodamine) is applied for reducing blooming of the laser sheet hitting the wing during PIV measurements. The final weight of a single wing is 1.685 ± 0.005 grams. The flatness is examined with DIC and bounded within $-0.05 \sim 0.05$ mm. The wing is mounted to the mechanism at a 5×5 mm² square region at the crossing of the leading edge and root. This region of the wing is assumed not to deform during the flapping motion (therefore serving as the reference for calculating the wing deformation and also the boundary condition). The test parameters are selected to be a $\pm 21^\circ$ amplitude and a 10 Hz flapping frequency.

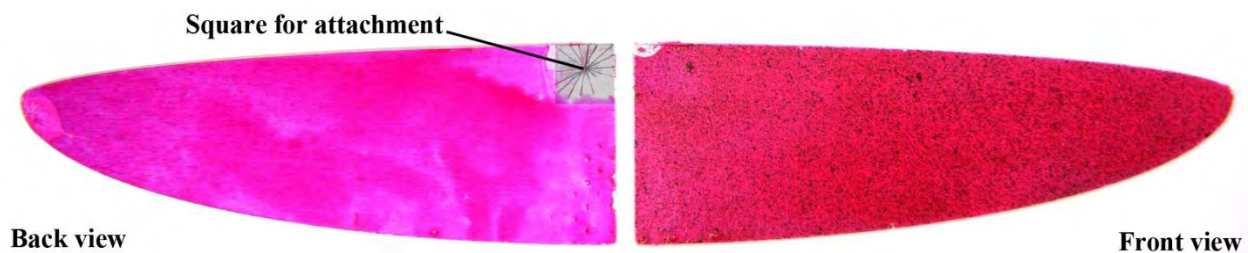


Figure 7-1. Isotropic wing with DIC speckles and Rhodamine coating.

7.2.2 High-Speed DIC System

The kinematics and deformation of the flapping wings are measured with a high speed digital image correlation system, unlike the one used in the previous chapters. A random speckle pattern is applied to the flapping wing, which is then digitized into wing surface coordinates with stereo triangulation. The full-field displacements of the wing during the flapping motion are computed with temporal matching, by minimizing a cross correlation function between discrete regions of speckle patterns on a deformed wing surface and an undeformed one. The DIC system (Correlated Solutions Inc., South Carolina, USA) used in this study consists of two Phantom high speed cameras that can store 2800 pictures of 800 pixels by 600 pixels resolution in its flash memory at a

maximum rate of 4800 frames per second. The exposure time was 150 μs and the frame rate was set to obtain 100 frames per cycle. In the 10 Hz case therefore, the frame rate is 1000 fps.

Only the left wing is measured with DIC for the kinematics and deformation. The two DIC cameras are symmetrically placed facing the wings at mid-plane. Field of view on both cameras is adjusted to fit and fill the frame. Then the cameras are calibrated and used to measure the full-field deformation and kinematics of the flapping wing. A reference image at the mid-plane of stroke is taken beforehand. All data are taken in raw format (.tif) until correlated with VIC3D (software by Correlated Solutions Inc.) and output as text files (.txt) for post processing. The data structure contains coordinates of all points on the measurement surface.

During post processing, the structural deformation is separated from rigid body kinematics by comparing the undeformed reference data to the deformed wing at the same flap angle. The errors of DIC are induced during the calibration phase and the uncertainty will remain the same after calibration. If a camera pair is carefully calibrated, the system uncertainty is under ± 0.1 mm in the current setup (except occasionally the speckle pattern introduces other error).

7.2.3 PIV Configuration

Particle image velocimetry, a mature technique used to measure the velocity of particles (assumed to follow the airflow) in the flow of interest ^[15, 31, 39, and 45], is applied to examine the airflow around a flapping wing. The flow field measurement area is defined by the confluence of the position and dimension of a laser sheet, along with the camera's field of view. Images are captured at each laser flash so that the particle spatial displacement can be extracted by correlating two images taken within a small

time interval. One LaVision Imager pro X 4M camera capable of capturing up to 7 image pairs per second with a pixel resolution of 2048x2048 is used. The camera is mounted perpendicular to the wing root, measuring a plane in the wing span direction at 7 Hz frame rate. A laser sheet is generated from a Litron Nano L PIV Pulsed Nd:YAG Laser System (max energy 135 mJ/pulse, 532nm) and is directed at the target from below. The air is seeded by a LaVision Aerosol Generator, with olive oil, an modal radius of approximately 0.25 microns. Davis 7 (software from LaVision) is used to control the PIV system and process the data. The measurements are made in the test section of a sealed open jet wind tunnel. Snapshots of the velocity field are acquired at 3 different chord locations (0.25, 0.5 and 0.75 of the chord length at the root). The measurement area is 121x121 mm², enclosing the wing at the upper right corner.

The PIV images are captured at up to 7 Hz, with the snapshots skipped that the system does not have time to process. 2500 images are captured at each location and flapping frequency. The images are processed using a multi-pass algorithm with shrinking interrogation size to produce velocity vectors. The region next to the wing and the area where the laser is shaded by the wing are masked out. The raw images are then processed to find the wing angle. The wing angle is then fit to a sine wave to extract the phase of the wing in each snapshot. The snapshots are then divided into 50 bins, with the bins equally spaced in time within the flapping cycle. Phase averages are then produced by averaging each bin. The wing angle variation within a bin varies between approximately $\pm 0.5^\circ$ to $\pm 2.5^\circ$, and each bin contains on the average 50 snapshots.

7.3 Computational Model

The work in this section is done by Satish, Aono and their research groups at the University of Michigan, as part of our collaborative effort in the MURI program. A summary of the geometric and mechanical properties of this baseline configuration are included in Table 7-1. Table 7-2 provides information about the flow properties (dimensional). In Table 3, the key dimensionless parameters related to either the structure, the flow, or to both for the aluminum wing configuration are furnished. The dimensionless parameters ρ^* and Π_1 are defined in Table 7-3. A structured multi-block grid around the Zimmerman wing of aspect ratio 7.65 is used for the CFD simulations. Based on a grid sensitivity study (discussed later), the grid configuration has 0.7 million points. The CFD grid configuration is shown in Figure 7-2.

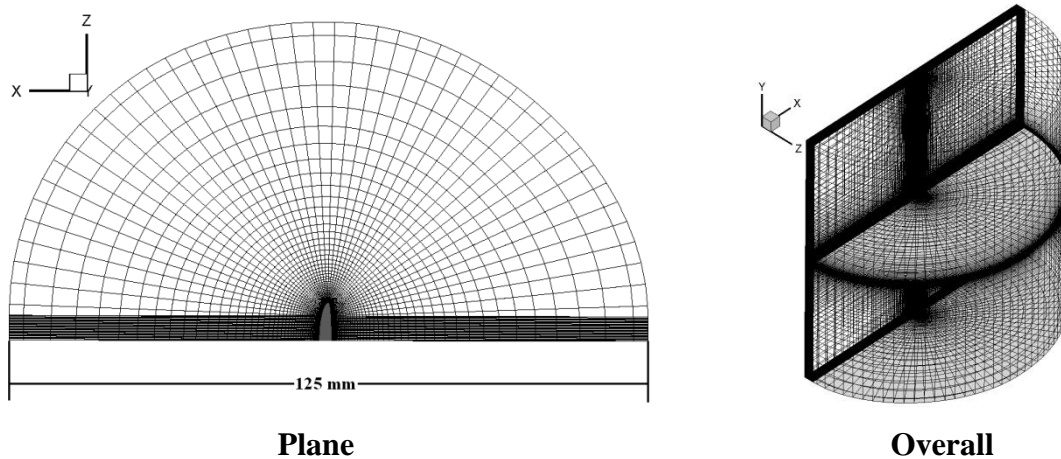


Figure 7-2. Images of computational mesh for fluid dynamics.

It has an “O-type” topology around the wing. The fluid solution is based on laminar flow assumption. The computational aeroelastic analysis of this wing configuration is done using the coupled code involving UM/NLAMS. The finite element mesh configuration developed for UM/NLAMS is shown in Figure 7-3. A 5 mm x 5 mm square region near the root at the leading edge is constrained in all degrees of freedom (with

respect to the global frame) in the structural solver, since the flapping mechanism in the experiment is used to actuate that region on the wing. A total of 480 elements (275 nodes) are used in the finite element discretization.

To assess the independence of the numerical solution to CFD grid refinement, a grid convergence study was performed and a suitable grid was subsequently chosen. Figure 7-4 shows the time history of lift coefficient on the wing for three different CFD grid configurations: coarse (0.6 million points, first grid spacing: 2.5×10^{-3}), medium (0.7 million points, first grid spacing: 1.0×10^{-3}), and fine (1.2 million points, first grid spacing: 5.0×10^{-4}). It is interesting to see that there is little sensitivity of the response to the grid refinements. This practically means that even the coarse grid configuration considered here is converged enough for the case studied. Notwithstanding this, the “medium” CFD grid configuration is chosen for all computations in this section specially keeping in view the relatively smaller first grid spacing in its case than in the “coarse” one which may become important for certain cases. Further, approximately 650 time-steps per period of computation are used in all the cases considered in this section, which are found to be sufficient for asymptotic convergence of the dynamic response. The convergence criterion for the aeroelastic convergence is chosen as a check on the Euclidean norm of the entire solution vector computed in two consecutive fluid-structure subiterations.

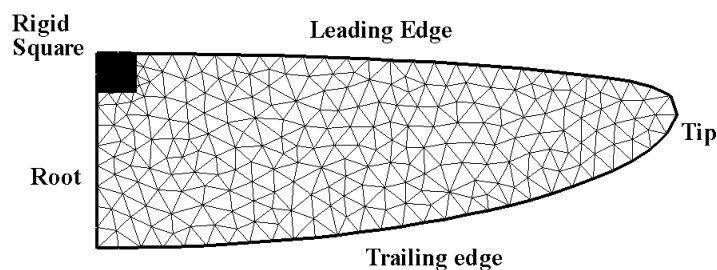


Figure 7-3. Structural mesh.

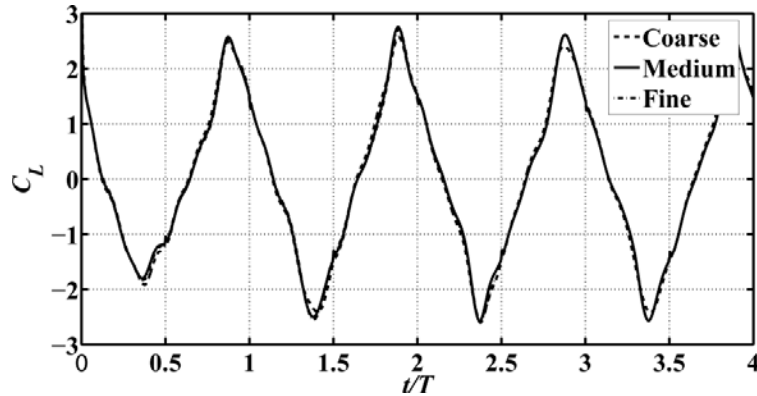


Figure 7-4: CFD grid sensitivity results for the Zimmerman aluminum flapping wing (lift coefficient)

Table 7-1. Geometric and mechanical properties of the Zimmerman aluminum flapping wing configuration.

Name	Nomenclature	Number & Unit
Semi-span at quarter chord	b	0.075 m
Chord length at wing root	c_{root}	0.025 m
Poisson's ratio	ν	0.3
Structural thickness	t	0.4×10^{-3} m
Material density	ρ_{alum}	2700 kg/m ³
Young's modulus of material	E_{alum}	70.0 GPa

Table 7-2. Flow properties associated with the Zimmerman aluminum flapping wing configuration.

Name	Nomenclature	Number & Unit
Reference flow velocity	U_{ref}	hover (1.0995 m/s)
Air density	ρ_{air}	1.209 kg m ⁻³

Table 7-3. Dimensionless parameters associated with the Zimmerman aluminum flapping wing configuration.

Name	Nomenclature	Number
	e	
Root chord-based Reynolds number	Re	2605
Reduced frequency	k	0.56
Aspect ratio	A_R	7.65
Density ratio	ρ^*	2233
Scaling parameter – I	Π_1	3.8×10^4

7.4 Validation Results

The results of the comparison between the experimental data and simulation output are presented in this section. The comparison is first made between fluid studies and then between structure studies. Figures 7-5 and 7-6 show a comparison of the velocity magnitude and vorticity between computation and the experiment for two different points in the flapping cycle ($t/T = 0.3$ and 0.48 , where T is the period of prescribed flap rotation). The flow field in these plots is shown on a slice that is cut at the quarter chord station going through the span. The experimental data could not be obtained in the region near the wing that is outside the laser sheet (appears as a white cone-like region above the wing in the experimental velocity magnitude and vorticity contours).

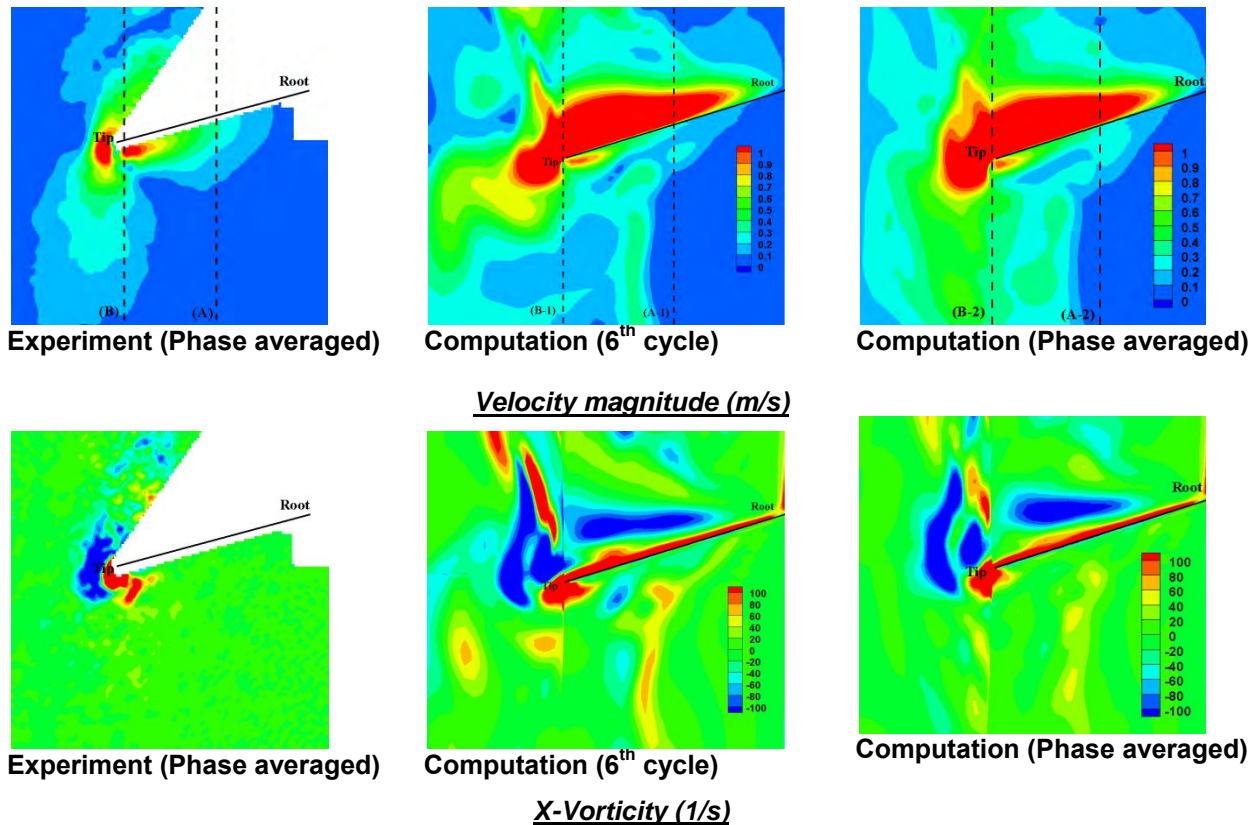


Figure 7-5. Comparison of velocity magnitude and vorticity for a slice of the wing at the quarter chord going through the span for time instant $t/T = 0.3$.

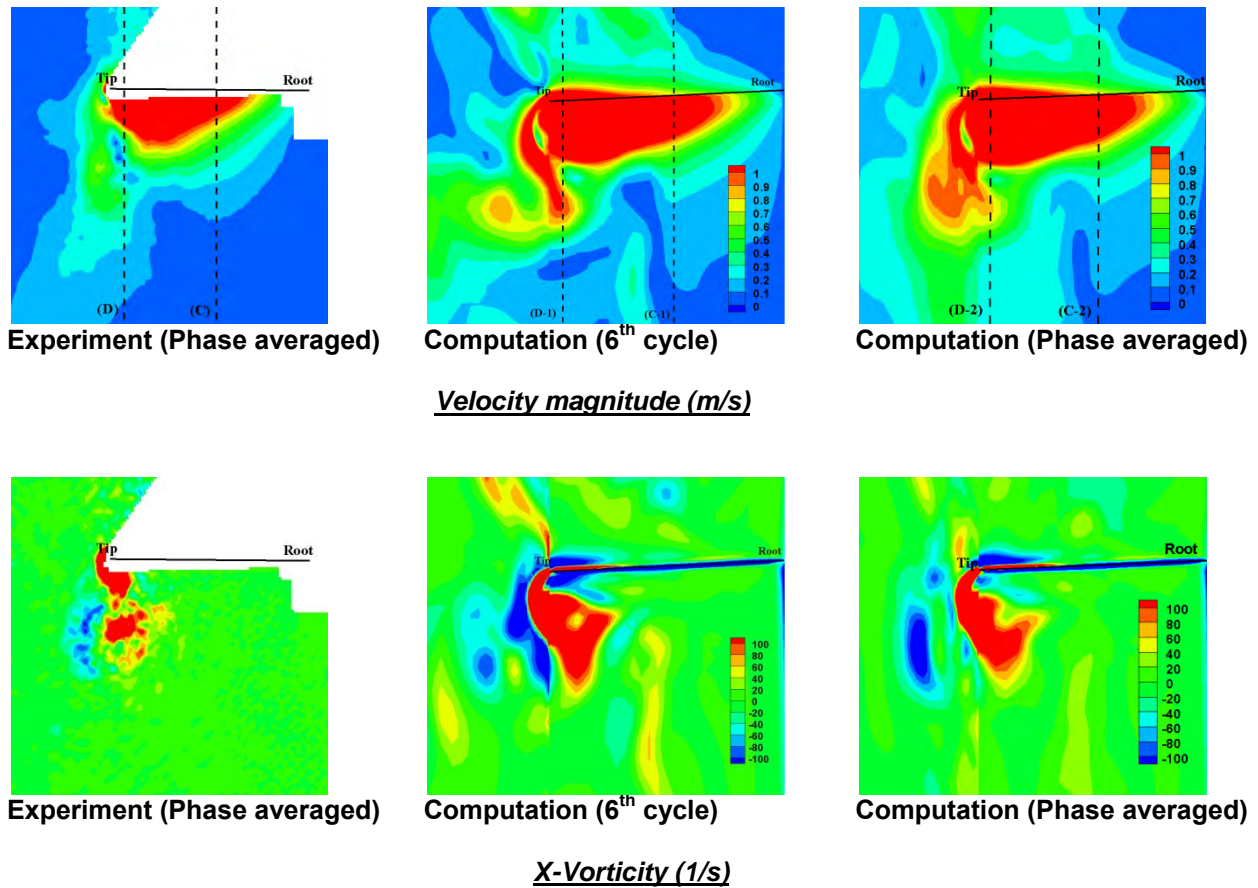
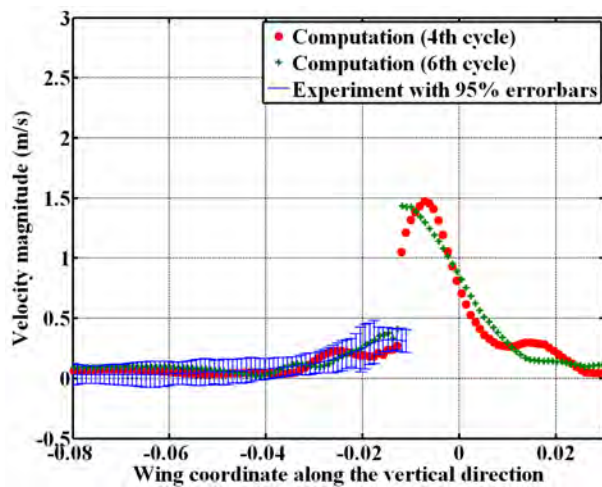


Figure 7-6. Comparison of velocity magnitude and vorticity for a slice of the wing at the quarter chord going through the span for time instant $t/T = 0.48$.

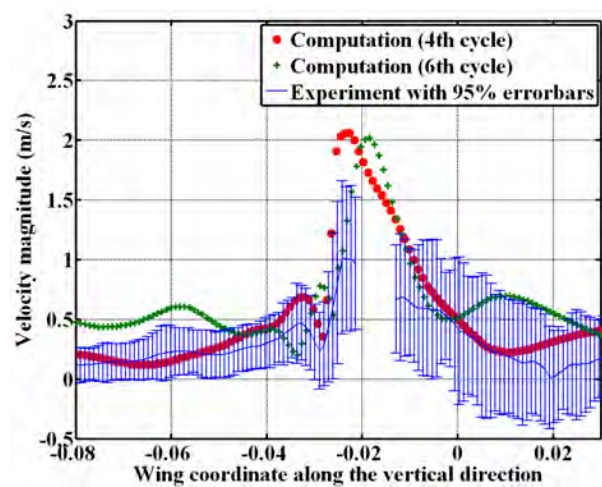
In Figure 7-5, the sub-plots in the first column correspond to the phase averaged velocity magnitude and X-vorticity contours of the experimental data. The sub-plots in the second column correspond to the velocity magnitude and X-vorticity contours corresponding to the 6th cycle of computation. The sub-plots in the third column correspond to the phase averaged (using the data corresponding to the 3rd, 4th, 5th, and 6th cycles) velocity magnitude and X-vorticity contours of the computational data. ($Re = 2605$, $k = 0.56$, $\Gamma_1 = 3.8 \times 10^4$, $\rho^* = 2233$). In Figure 7-6, the sub-plots in the first column correspond to the phase averaged velocity magnitude and X-vorticity contours of the experimental data. The sub-plots in the second column correspond to the velocity magnitude and X-vorticity contours corresponding to the 6th cycle of computation. The

sub-plots in the third column correspond to the phase averaged (using the data corresponding to the 3rd, 4th, 5th, and 6th cycles) velocity magnitude and X-vorticity contours of the computational data. ($Re = 2605$, $k = 0.56$, $\Pi_1 = 3.8 \times 10^4$, $\rho^* = 2233$).

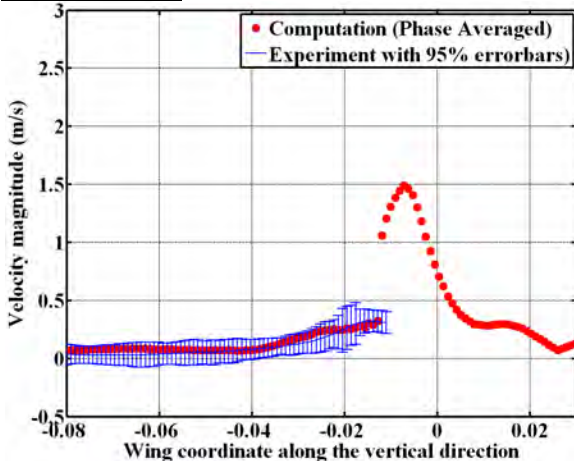
As seen from the plots, there is a good overall agreement in the flow structure between the computation and the experiment at both points in the flapping cycle. However, the vorticity is weaker and more fragmented in the experiment than in the computation. Also, in general, there is more discrepancy near the wing tip than in the rest of the wing. This is confirmed from the comparison of the velocity distributions between the computation and the experiment shown in Figure 7-7.



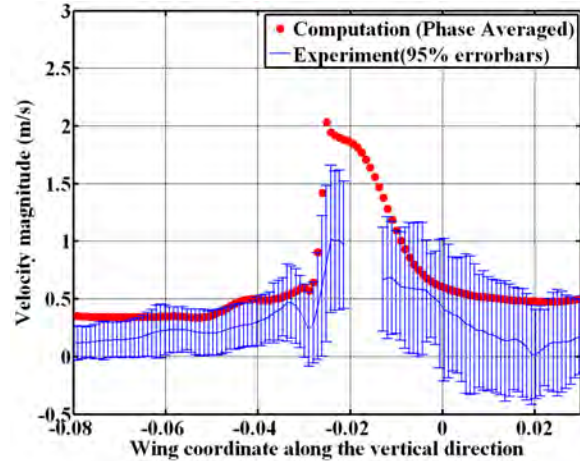
(A-1) – slice at the mid-span
Instantaneous



(B-1) – slice at the tip

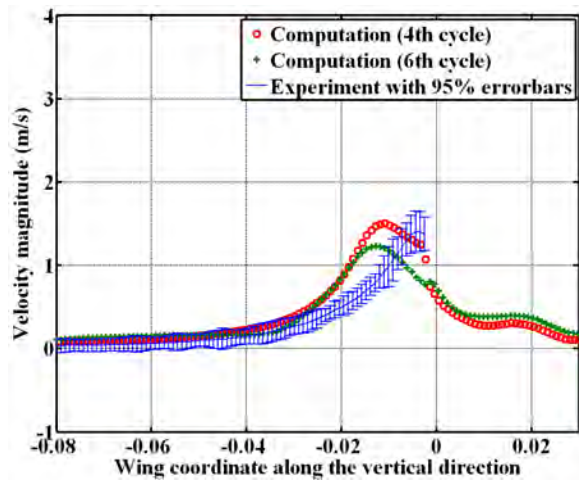


(A-2) – slice at the mid-span

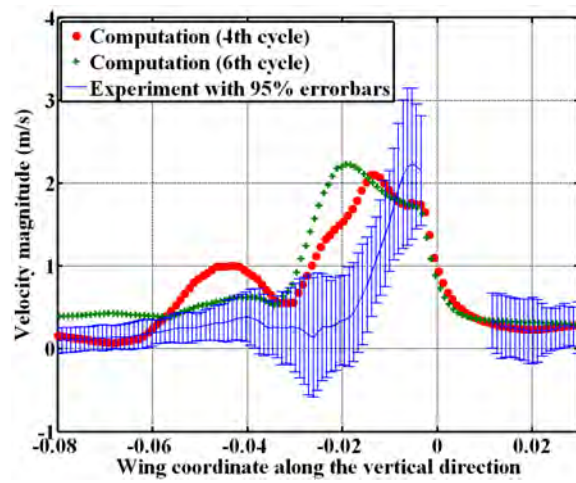


(B-2) – slice at the tip

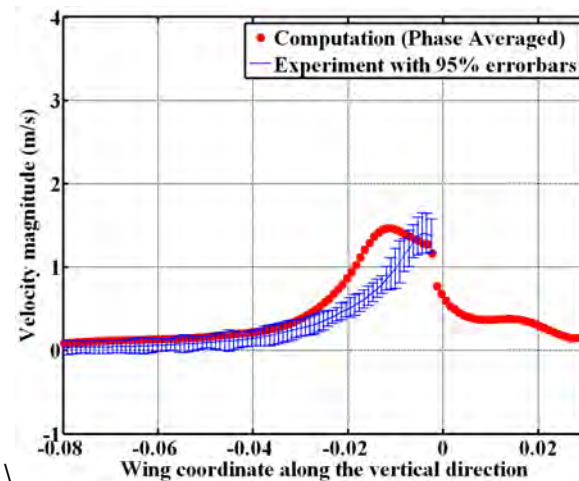
Phase Averaged



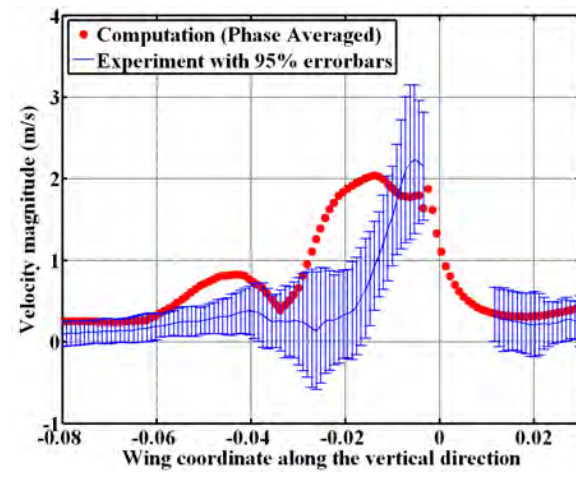
(C-1) – slice at the mid-span
Instantaneous



(D-1) – slice at the tip



(C-2) – slice at the mid-span
Phase Averaged



(D-2) – slice at the tip

Figure 7-7. Comparison of velocity magnitude between computation and experiment

In Figure 7-7, the comparison takes place at two different time instants and for two different slices along the wing span: sub-plots A-1, B-1, C-1, and D-1 correspond to instantaneous velocity magnitude profiles and sub-plots A-2, B-2, C-2, and D-2 correspond to phase averaged velocity magnitude profiles. Sub-plots on the left column correspond to those at the mid-span slice of the wing and those on the right column correspond to a slice near the tip. The error bars around the phase averaged flow

indicate the interval within which 95 % of the instantaneous values are expected to fall, assuming the distribution is Gaussian.

Each of those sub-plots is obtained by considering a line of points vertically above and below the wing obtained by intersecting a slice going through the quarter chord all along the span and another slice at either a section near the mid-span or the tip that goes through the entire chord. For example, the sub-plots (A-1) and (B-1) of Figure 7-7 show such velocity magnitude distributions corresponding to a line of points obtained by intersecting the chordwise slice at mid-span and tip respectively one after the other with the slice going through the span at the quarter chord, both for the time instant $t/T = 0.3$. Then, the sub-plots (C-1) and (D-1) of Figure 7-8 correspond to the same line of points but now for time instant $t/T = 0.48$.

Also included in Figure 7-8 are phase averaged velocity profiles for both points in the cycle, $t/T = 0.3$ and $t/T = 0.48$, (sub-plots A-2, B-2 correspond to the former time instant and C-2, D-2 correspond to the latter time instant) including the error bars for the experimental data. While there was good qualitative agreement from the contour plots in Figures 7-5 and 7-6 here one can see a more quantitative comparison. In general, there are cycle-to-cycle variations in the velocity magnitudes in both computation and experiment. Notwithstanding that, specifically, it appears that the spatial locations associated with the rise in velocities due to the wing motions do not match too well between the experiments and computations however the maximum amplitudes of the velocity magnitudes do agree quite well. In the experimental data, the magnitudes of variance near the tip region are generally larger than those near the mid-span. Figure 7-8 shows the lift coefficient computed from numerical data on the wing as a function of

non-dimensional time. Figure 7-9 shows the iso-surfaces of the vorticity magnitude (the color corresponds to the spanwise vorticity) corresponding to two different time instants labeled as (a) and (b) in Figure 7-8.

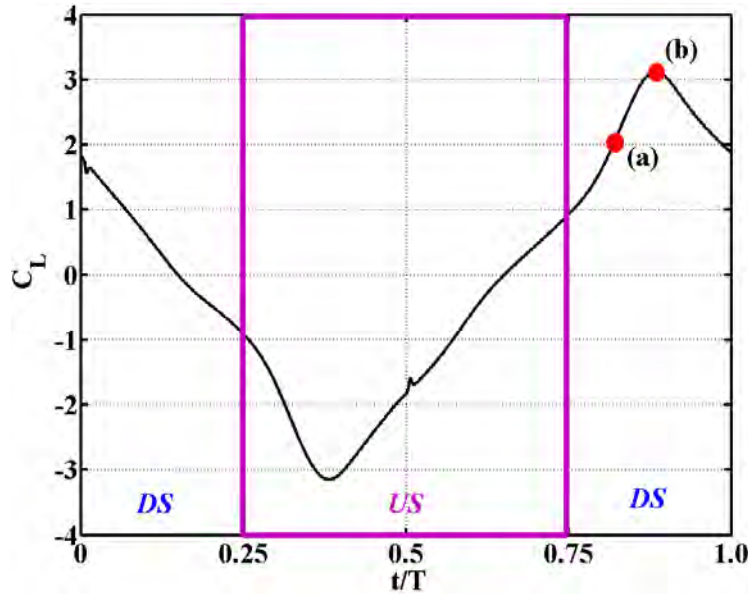


Figure 7-8. Lift coefficient on the wing as a function of normalized time (time is normalized with respect to a period of flap rotation), DS- downstroke, US – upstroke.

Three-dimensional vortex generation is seen in Figure 7-9 at both time instants wherein the counter-rotating vortices at the leading and the trailing edge interact with the tip vortex during the wing motion. In particular, the vortices generated during a previous stroke (indicated as “PV” in the figure) are captured by the wing and interact with the vortices generated during a current stroke indicated as “CV”. The results in Figure 7-9 are calculated at two stations along the wing length at two different time instants: sub-plots (i) and (ii) correspond to the iso-contours of the vorticity magnitude (color indicates the magnitude of the Z-vorticity) for time instants (a) and (b) of Figure 7-8 respectively. Sub-plots (iii) and (iv) correspond to the Z-vorticity contours at two stations along the wing length (as indicated) for time instants (a) and (b) of Figure 7-8 respectively. (CV – Vortex generated in the current stroke, PV – vortex generated in the

previous stroke, blue color indicates clockwise vorticity from the viewpoint of an observer looking into the plane of the plot).

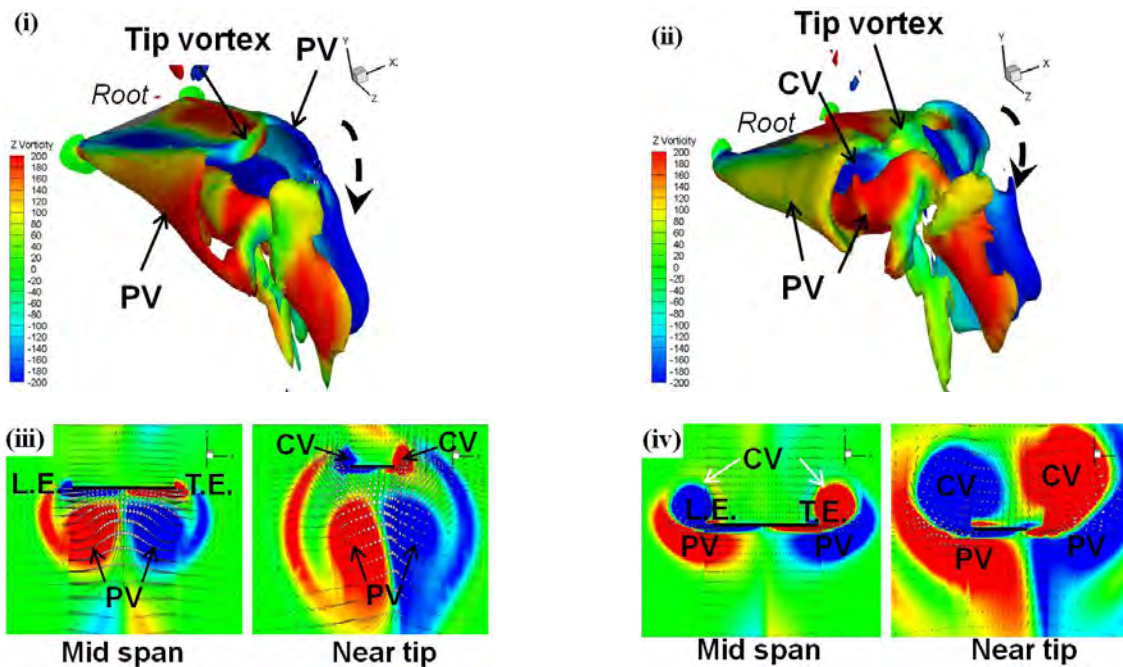


Figure 7-9. Iso-contours of vorticity magnitude on the aluminum wing and Z-vorticity contours.

Figure 7-10 shows the comparison of the normalized vertical displacement (with respect to the chord length at the wing root) at a point on the wing tip between the experiment and the computation. As shown in the figure, there is a decent overall agreement in both amplitude and phase between the computational response and the experimental data. The tip deformation obtained is only around 3 % of wing chord which means that the selected wing configuration is not compliant enough to deform significantly. Future studies will be focused on more flexible cases.

7.4 Discussion

This chapter has presented an integrated approach involving both experimental and computational methods having a potential to examine flexible flapping wing configurations. An aluminum wing is prescribed with single degree-of-freedom flap

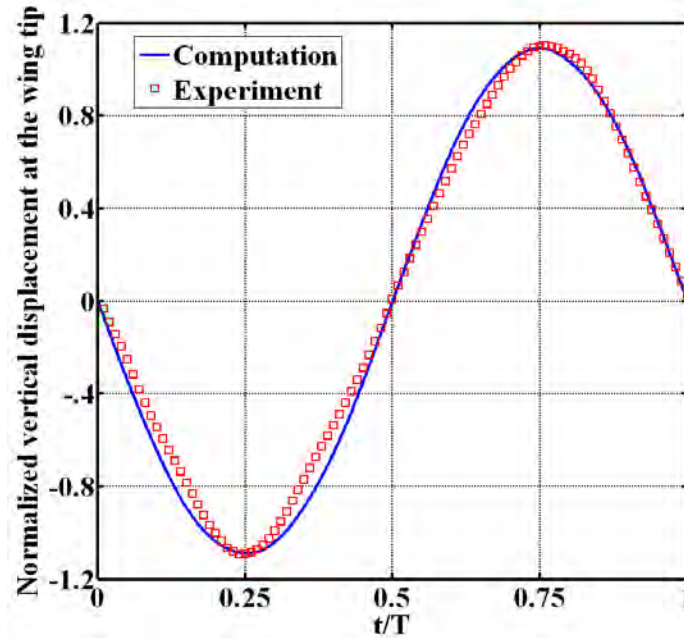


Figure 7-10. Aluminum wing response due to flapping excitation (normalized with respect to chord length at the root).

rotation at 10 Hz frequency and $\pm 21^\circ$ amplitude and both flow velocities and deformations are measured in the experiment using digital image correlation and digital particle image velocimetry techniques respectively. Preliminary comparison of flow velocities and wing deformation between the computational and the experimental data has shown a decent agreement.

On the experiment side, there are still much room for improvement. The current flapping mechanism FL2D3 inevitably has clearance at its linkage pin joints that lead to an actuation kinematics slightly different from the prescribed one: at wing reversal the wing may be free of actuation for a short period of time. This makes the orientation of the experimental setup very important because the effect of gravity cannot be neglected. The high speed wing tip deformation data are currently taken independently from the PIV data. An ideal case would have the two operating simultaneously. However, this is self-contradictory to the different lighting requirements for the two

systems. Thirdly, the isotropic elastic wing for the simple case (low amplitude, low frequency) should have been made with lighter materials and allowed for more significant elastic deformation.

On the computation side, the main experiment/computation comparison in this chapter is focused on air flow; the structural deformation is yet to be compared. In Figure 7-10, the wing tip kinematics for the computation model is approximated and achieved a reasonable comparison. The structural deformation, however, is hidden in the kinematic information and needs to be separated for comparison, such as shown in deformation phase plots.

Recent effort is directed to further research on combining structural and fluid dynamic models to simulate flapping airfoils by Shyy et al.^[188,189] and insect flapping wing aerodynamics by Liu et al.^[190] In these studies the complicated models have well captured the expected flow pattern and are very agreeable to experimental data. On the other hand, ingenious simplified models for computing the essence of flapping flight are studied by Cesnik et al.^[191], Friedman et al.^[192], and Stanford et al.^[193]. These work has made reasonable assumptions that enables more affordable calculations while maintaining good approximations. More fundamental studies related to flapping wings are pursued by Dong et al.^[194, 195] and Mittal et al.^[196], insightfully aiding the understanding of flapping flight. Other related efforts can be found in the advancing of computational method itself: Tafti et al.^[197] presented a parallel boundary fitted dynamic mesh solver for applications to flapping flight; Willis et al.^[198] used unsteady panel method with vortex particle wakes; and Tu and Aliabadi^[199] developed a hybrid finite volume/element solver for incompressible flows. The promising combination of both

approaches allows us to thoroughly unveil the sciences of flapping flight in the future, making the pioneering experimental work the most fundamental and important step in the endeavor.

Interesting progress has been made by Gogulapati et al.^[192]: by using an aeroelastic model obtained by coupling a nonlinear structural dynamic model based on MARC with an approximate aerodynamic model that incorporates leading edge vortices and a wake model, results comparable to the study performed in Chapter 4 can be generated. Figure 7-11 shows the comparison between mode shapes measured with the two flexible wings L1B1 and L1B2 and the mode shapes simulated with a finite element model. The results are very agreeable, although, the difference between L1B1 and L1B2 is more distinguishable in the experimental data.

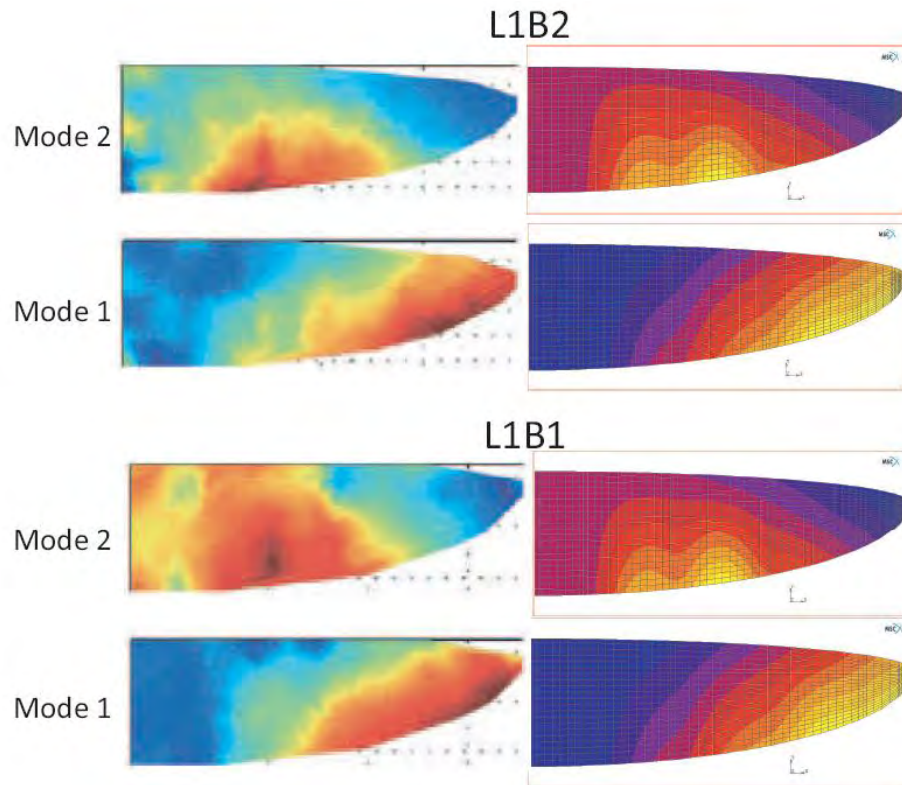


Figure 7-11. Mode shape comparison between experimental results and finite element model by Gogulapati et al.^[192].

Figure 7-12 shows the comparison of the time averaged thrust between the experiment and the computation. Although the computation under-predicts, the details of the data pattern and the trends are very similar. If the maximum value of the computation results is linearly interpolated to match the experiment data, then the agreement of the general trend would be more obvious. However, the relationship between the two batten wings "B2"s and the one batten wings "B1"s has been inverted in the computation: wings with only one layer of carbon fiber batten generate more thrust than the two layers batten ones in the computation. This may be due to errors related to material properties as well as the composite definitions between the membrane and the carbon fiber.

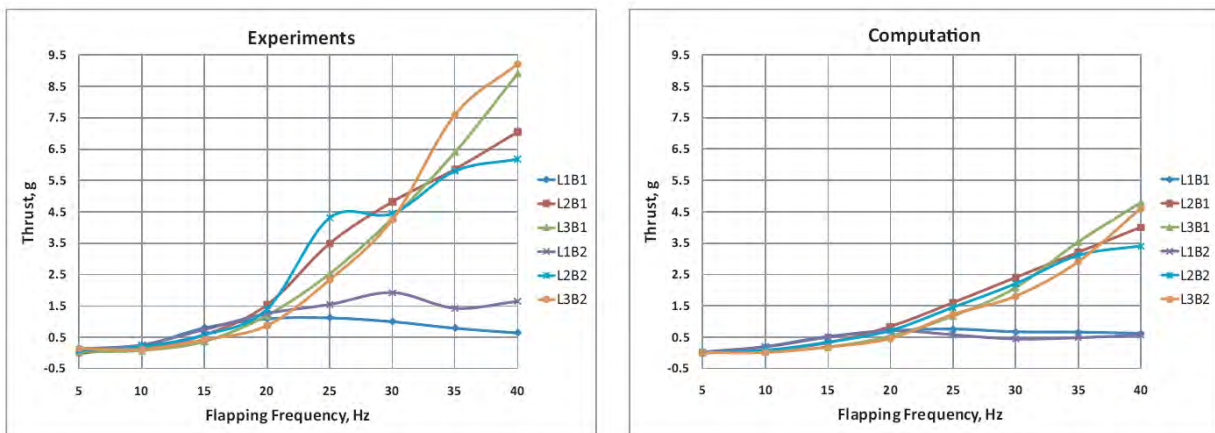


Figure 7-12. Time averaged thrust comparison by Gogulapati et al.^[192].

Such computation work shows its potential in simplifying the physics while maintaining a good approximation. The details of the aerodynamics may not be required to be computed if the aeroelastic interaction and its effect can be faithfully represented. Nevertheless, the work presented in this chapter has initiated a very good first step for using computation techniques to solve the fundamental physics of flapping flight, and potentially design the theoretical optimal wing.

CHAPTER 8 CONCLUSIONS AND FUTURE WORK

8.1 Conclusions

This work has exploited the state-of-the-art experimental techniques to investigate an extremely complicated low-Reynolds-number, unsteady aerodynamics dominated and aeroelastic coupled problem: flapping wing flight for micro air vehicles inspired by hummingbirds and insects. Numerical techniques developed for the same topic at the time when this research started were not able to correctly compute the interactive physics. Over the years, numerical methods have made significant progress, producing results agreeable to experimental work; however, experimental study on such topic still leads for several reasons:

1) Confidence in the physical phenomenon. Experiments do not suffer from trusting if the data produced would be caused by any inaccurate representation of the physics. However, experimental data are subject to more stringent requirement for controlled parameters and measurement accuracy.

2) Productivity of the data measurement technique. Due to the complexity of flapping wing flight, a high fidelity aeroelastic model at the current stage would require days or even months for computation. Experiments can be conducted at a much higher pace and the short trial-and-error cycle enables very productive collection of data. However, this will definitely change in the near future as the computation power increases according to the Moore's Law.

3) Tested feasibility. Experiments are conducted in controlled environment with actual available technologies and materials. The development path from experiments to product is much shorter than that from numerical models to product.

4) A natural discovery process. All human technologies have started from experiments⁸; flapping wing flight for micro air vehicles is of no exception. This is because all theoretical models must subject to experimental validation. Only when a validated model becomes mature, further development would be cheaper and more efficient by computation.

The fundamental difference between the two approaches can be summarized in Figure 8-1. Both approaches circle in the counterclockwise direction, separated by the Gap of Truth: the experiment approach (dedication of this work) is on the right half of the figure; the numerical approach is on the left half. If one day, the numerical model is perfected to eliminate the Gap of Truth, then the discovery process would be complete.

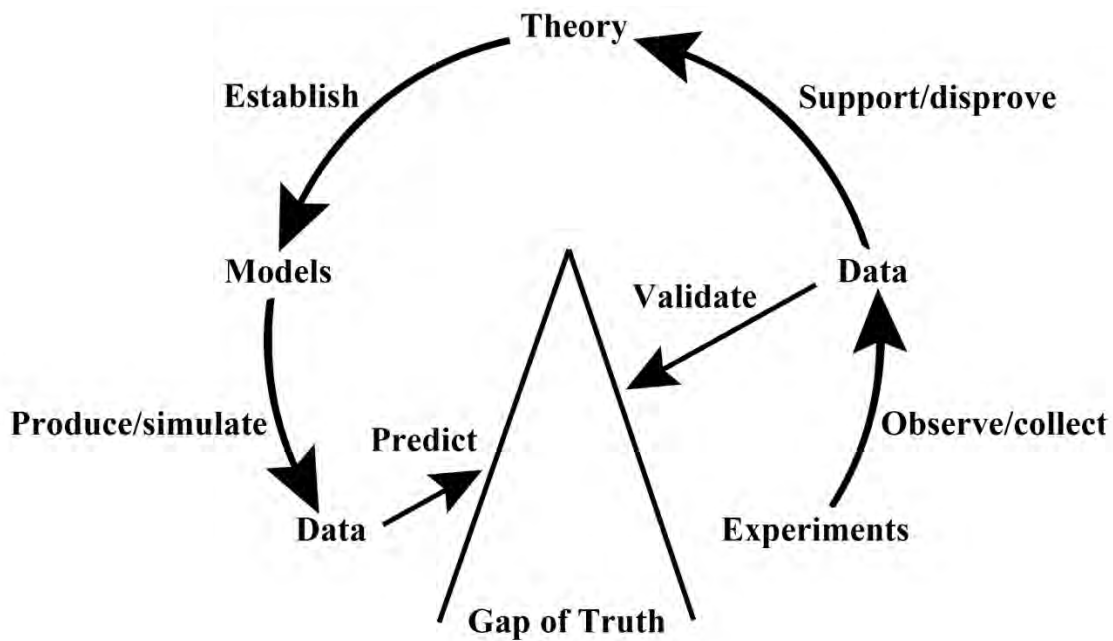


Figure 8-1. Circle of Scientific Discovery.

⁸ One may argue, future technologies may not. For example, the future invention of fusion nuclear reactor is now being computed at the Oak Ridge National Lab before any experiment is conducted. However, if one traces back to the origin of the knowledge, observation still comes first, even though not in an intended and controlled environment (astrophysics); and if one traces back to the beginning of the nuclear technology, atomic explosion experiments were, of no doubt, necessary.

Or simply put, experimentalists are like detectives, deducing for the truth by observing and collecting the minutest evidence; while theorists are like conspirators, using strategy and tactics to plan for optimal victory.

Therefore in this flapping wing flight study, the work flow has been: first to design the experiments and to complete the instrument setup; then to collect data (quantitative observation) and analyze; thirdly to support and disapprove theories related to flapping wings; and finally to validate computation results. For example, different flapping mechanisms and flexible composite wings are designed for the same aerodynamic conditions (Re number, reduced frequency, etc.) and similar structural properties (stiffness, density, etc.) as the natural counterpart. Then, the experiment facility that allows for measurements of structural deformation (DIC system), aerodynamic performance (load sensor) and other aeroelastic behaviors (vacuum chamber, PIV, LDV, etc.) is developed. The collected data are analyzed with several techniques: separation of structural deformation from rigid body kinematics, presentation of full-field deformation with color contour, identification of cyclic deformation pattern with descriptor (such as tip deflection for describing wing bending and angle of twist for passive wing twist) phase plots, deformation abstraction into enclosed area and phase, and finally correlation studies that enables prediction of thrust production. Finally, both structural deformation and airflow (collaboration) data are taken for validation with computation results. In summary, this dissertation has contributed the following abridged conclusions to the scientific community:

- 1) An experimental technique has been developed to measure large out-of-plane deformation at high velocities. This includes the optical setup of the commercially

available digital image correlation system, hardware setup of the vacuum chamber , control and synchronization of the instrument, and data acquisition and processing programs. The experimental facility allows for hummingbird/insect inspired flexible wings to produce comparable aerodynamic loads at high frequencies, as well as the measurement of such behavior. No scaling of the physical problem means the structural properties are not affected (i.e. if an experiment in water tunnel is designed for the same Re number, then the wing property would also need to scale properly, which would be difficult and therefore neglected by assuming rigidity.)

2) The study has proven that passive wing deformation can be practically used to alter wing kinematics to achieve beneficial aerodynamic effects; however, a theoretical model is yet to be developed. Wing stiffness and mass distribution are both important structural properties to be designed; while actuation kinematics should be considered as a loading condition for predicting inertial loads, which initiate and dominate the passive deformation. The results presented in Chapter 3 have disproved some of the previous theories: passive wing deformation can be solely dominated by inertia if the wing material is much denser than the air's and compliant; however, if materials similar to insect's are used, significant contribution from air and the synergistic effect of both aerodynamic and inertial loading determine the large wing deformation.

3) Wings under the same aerodynamic and kinematic conditions are studied in Chapter 4, with structure as the only variable. The results show that the passive wing deformation is the sole source for generation of thrust and appropriate (phase wise) amount of passive deformation is always helpful. Therefore the most compliant wings have better performance at lower flapping frequencies; and as the frequency increases

to a certain level when structural deformation starts to reduce the overall wing kinematics, the time averaged thrust starts decreasing. This critical frequency is the first bending mode resonant frequency for compliant wings. At the critical frequency, the wing kinematic amplitude would be maximum and therefore reaching a peak for aerodynamic loads; at higher frequencies, the structural deformation reduces the final stroke amplitude as well as the thrust. This may be an apparent, intuitive insight, however, no assertion could have been made without support from experimental data. This is also an important design guideline: wing's passive deformation should be tailored to specific inertial loads to maximize aerodynamic benefits, either using resonant frequency to cruise or setting power reserve based on that limitation.

4) Chapter 5 systematically explores the effect of kinematics on flapping wing performance. Two categories are specifically defined: actuation kinematics which is the cause for inertial loads as well as the concomitant coupled aerodynamic loads; and wing kinematics which is the combinative result of aeroelastic structural deformation and the actuation kinematics. Both effects are complicated and dependent on specific wing structure. Two most important parameters of actuation kinematics are flapping frequency and stroke amplitude, which exhibit tradeoff behavior when efficiency (indicated with coefficients) is evaluated. Deformation patterns and thrust production are evaluated over different wing structures and the results show that aeroelastic coupling of different wing structure leads to significantly different behavior.

5) Subsequently, a two degree-of-freedom case is studied to understand the effect of wing rotation and active vibration. A rotation mechanism, utilizing magnetic coil actuators, is realized to actuate the wings in different phase relations to the flapping

motion. The results show that, similar to the insect stroke patterns in nature, the timing and energy of active rotation has significant impact on thrust/lift production: either constructive or destructive. Therefore the phase difference between the flapping and rotation can be used to control the flapping wing performance, effectively. Low amplitude, high frequency wing vibration using the rotation degree of freedom is also examined. It is found that for flapping wing flight, local structural vibration has no significant effect on the overall aerodynamic performance. The vibration also has not been able to change the passive deformation enough to change aerodynamics measurably.

6) Chapter 6 has presented valuable insights into the effect of wing structure reinforcement topology with four wings (BP, HUM, LEO, PR) intensively studied for their deformation, thrust production and efficiency. The results have shown the importance of torsional compliance, chord profile constraints, membrane constraints and mass distribution. Hum has over constrained both wing bending and twisting, therefore the least efficient; LEO has no batten reinforcement, allowing for minimal inertia, therefore the most efficient. BP has straight battens that reinforces the wing structure for interaction, therefore producing more thrust. PR has low resonant frequency due to large mass distributed on the trailing edge, which is beneficial at low frequencies because of large inertial deformation, and at resonant frequencies when power consumption is reduced. The correlation study between structural deformation (abstract parameters: enclosed area and phase of deformation descriptor phase loops) shows clear trends for each structural characteristics: the three wing of the same leading edge stiffness behaves coherently in bending deformation. This proves the possibility to

predict aerodynamic performance from wing structure as well as optimizing aerodynamics through changing the structural response.

7) An experimental optimization methodology is then summarized based on the developed techniques and results. The methodology has been applied to a study of a design space based on the topology of BP, with the leading edge and each batten as variables to generate 32 different designs. The aerodynamic performance of all these wing is examined and along with previous wings, local optima are identified. The results explains that structural optimization should be performed for certain kinematics towards objectives such as maximizing thrust, thrust coefficient, efficiency, etc. The methodology consists of mainly the experimental techniques and data analysis methods presented in the previous chapters.

8) Finally, a validation for computation model is performed with a simple isotropic aluminum wing actuated at low amplitude and low frequency. As the first step to examine the computation model, the results of this simple case show reasonably agreeable data, although the comparison emphasizes more on airflow than aeroelastic interaction. The wing tip kinematics are briefly compared. More complicated anisotropic flexible wing structures will be compared in the near future (and has been using approximated aeroelastic models).

In all, a thorough experimental study has been conducted to characterize flapping wing structures, analyze their aerodynamic effects, and develop an optimization procedure. The results have comprehensively explained the effect of kinematics and structure on aerodynamics, serving as important reference for future optimization work as well as the data base for numerical validation.

8.2 Future Work

8.2.1 More Complicated Kinematics

As discussed in detail in Chapter 3, the passive wing deformation is predominantly initiated by inertial loading, which results from acceleration of the actuation kinematics. Because of practicality in efficiency and reliability, as well as limitations in time and resources, only the simplest one degree-of-freedom case is examined in this work. Future studies with more complicated actuation kinematics, similar to that is presented in Chapter 5 but more sophisticated, are expected to be conducted. Active wing rotation has been proven to have significant effect on hovering thrust production, leading to the next step of systematic study of the phase relationship between the rotation and flapping motion.

A new flapping mechanism, FL2D4, has been designed and is being manufactured at present. The new mechanism can perform a fixed phase difference flapping and rotation motion, with variable flapping and rotation amplitudes and adjustable phase difference. With add-ons, the design also allows for onboard control of the three variables during operation. The new mechanism requires about a half year build time and the add-ons another half a year. Once completed, the mechanism can actuate wings up to 40 Hz, 120° stroke amplitude, 90° rotation amplitude and 0 to 2π phase difference. This enables research on wing structure tailoring to more complicated kinematics, which may enhance both aerodynamic efficiency and efficacy under the same conditions. If the results are positive, miniaturization of the flapping mechanism for actual aircraft use can then be pursued.

The third degree of freedom, yawing, is also important for flapping flight but may not be cost-effective. However, it would be the final stage for flapping wing research.

8.2.2 New Composite Wings

New manufacturing techniques are currently being explored for building more desirable flexible flapping wings. Ideally, the right technique could allow for arbitrary definition of both structural stiffness and mass distribution, therefore the inertial deformation under specific actuation kinematics can be expected. Using molds to define structure cross-section and material use is one possibility. Using deposit of micro fiber may be another. The key is to achieve the right pattern of passive deformation.

The wing planform as well as cross-section profile should be considered in the future wing design. In this work, due to its nature of being part of a collaboration project, these two aspects are fixed so that results are comparable across different disciplines. There are many possibilities that have not been examined: wings of a larger cord length towards the wing tip such as seen in bumblebees; wings of less root chord constrains such as seen in mosquitoes; and different camber values applied across the wing. These factors will induce both aerodynamic and inertial effect on structural deformation: larger chord length near wing tip implies that there is larger mass distribution for wing bending and twisting; such planform would also have larger area at the high velocity range, substantially increasing aerodynamic loading; reducing wing root constraint would result in more wing twist flexibility, which may be beneficial in hovering flight, but not forward flight (however, in insects' forward flight, the flight mechanism is the same as hovering except that the stroke plane is tilted); finally, adding camber to the structure would change the bending stiffness as well as the symmetry of deformation, as well as pressure distribution on the wing in forward flight.

In summary, the new composite wings in future work will be fabricated with more advanced methods and have more geometric parameters.

8.2.3 Forward Flight

One of the unique features of flapping flight for micro air vehicles is the transition between hovering and forward flight. Inspired by hummingbirds, the flapping wing flight can achieve higher overall efficiency because in forward flight, the thrust produced by flapping wing only needs to balance the drag while the lift is produced as a consequence of forward velocity. This is the essential difference between rotary wing and flapping wing aircrafts; although for flapping wings there are other mechanisms (such as clap and fling, wake effect, etc.) for additional thrust production during hovering. Therefore the flapping wing study has to be taken into wind tunnels for forward flight investigation as well. This would allow for comparison fixing other parameters such as Strouhal number, reduced frequency, etc.

Replacement parts for FL2D3 have been designed for wind tunnel use. The parts would extend the wing joint further from the flapping mechanism so that it would be less intrusive to the free stream airflow. Validation for numerical models in forward flight should subsequently be performed. The wing flexibility under different flight loads should also be appropriately tuned as the operation condition has changed. The ideal wing structure may be required to balance between the hovering and forward flight conditions.

LIST OF REFERENCES

1. Abdulrahim, M. "Maneuvering Control and Configuration Adaptation of a Biologically Inspired Morphing Aircraft," Ph. D. Dissertation, Department of Mechanical and Aerospace Engineering, University of Florida, Gainesville, FL, 2007.
2. Stanford, B. "Aeroelastic Analysis and Optimization of Membrane Micro Air Vehicle Wings," Ph. D. Dissertation, Department of Mechanical and Aerospace Engineering, University of Florida, Gainesville, FL, 2008.
3. Jones, K.D., Bradshaw, C.J., Papadopoulos J., and Platzer, M.F., "Development and Flight Testing of Flapping-wing Propelled Micro Air Vehicles," 2nd AIAA Unmanned Unlimited Systems, Technologies, and Operations, 2003.
4. Chung, A.J., and Erickson, D., "Engineering Insect Flight Metabolics Using Immature Stage Implanted Microfluidics," Lab on a Chip, Vol. 9, pp. 669-676, 2009.
5. Mueller, T.J., "On the Birth of Micro Air Vehicles," International Journal of Micro Air Vehicles, Vol. 1, No. 1, 2009, pp 1-12.
6. Pornsin-Sirirak, T.N., Tai, Y.C., Ho, C.M., and Keennon, M., "Microbat: a Palm-sized Electrically Powered Ornithopter".
7. Shahinpoor, M., Bar-Cohen, Y., Simpson, J.O., and Smith, J., "Ionic Polymer-metal Composites as Biomimetic Sensors, Actuators and Artificial Muscles – a Review," Smart Materials and Structures, Vol. 7, 1998.
8. Wood, R.J., "The First Takeoff of a Biologically Inspired At-Scale Robotic Insect," IEEE Transactions on Robotics, Vol. 24, No. 2, April, 2008.
9. Ellington, C. P., "The Aerodynamics of Hovering Insect Flight III. Kinematics," Philosophical Transactions of the Royal Society of London, Series B, Biological Sciences, Vol. 305, No. 1122, 1984, pp. 41-78.
10. Ellington, C. P., "The Aerodynamics of Hovering Insect Flight I. The Quasi-steady Analysis," Philosophical Transactions of the Royal Society of London, Series B, Biological Sciences, Vol. 305, No. 1122, 1984, pp. 1-15.
11. Ellington, C. P., "The Aerodynamics of Hovering Insect Flight II. Morphological Parameters," Philosophical Transactions of the Royal Society of London, Series B, Biological Sciences, Vol. 305, No. 1122, 1984, pp. 17-40.
12. Ellington, C. P., "The Aerodynamics of Hovering Insect Flight IV. Aerodynamic Mechanisms," Philosophical Transactions of the Royal Society of London, Series B, Biological Sciences, Vol. 305, No. 1122, 1984, pp. 79-113.

13. Ellington, C. P., "The Aerodynamics of Hovering Insect Flight V. A Vortex Theory," *Philosophical Transactions of the Royal Society of London, Series B, Biological Sciences*, Vol. 305, No. 1122, 1984, pp. 115-144.
14. Ellington, C. P., "The Aerodynamics of Hovering Insect Flight VI. Lift and Power Requirement," *Philosophical Transactions of the Royal Society of London, Series B, Biological Sciences*, Vol. 305, No. 1122, 1984, pp. 145-181.
15. Wang, Z.J., "Dissecting Insect Flight," *Annual Review Fluid Mechanics*, Vol. 37, 2005, pp. 183-210.
16. Lehmann, F., "Review-The Mechanisms of Lift Enhancement in Insect Flight," *Naturwissenschaften*, Vol. 91, 2004, pp.101-122.
17. Ho, S., Nassef, H., Pornsinsirak, N., Tai, Y., Ho, C., "Unsteady Aerodynamics and Flow Control for Flapping Wing Flyers," *Progress in Aerospace Sciences*, Vol. 39, 2003, pp. 635-681.
18. Shyy, W. Berg, M. and Ljungqvist, D., "Flapping and Flexible Wings for Biological and Micro Air Vehicles," *Progress in Aerospace Sciences*, Vol. 35, 1999, pp. 455-505.
19. Sane, S.P., "Review-The Aerodynamics of Insect Flight," *The Journal of Experimental Biology*, Vol. 206, 2003, pp. 4191-4208.
20. Templin, R.J., "The Spectrum of Animal Flight: Insects to Pterosaurs," *Progress in Aerospace Sciences*, Vol. 36, 2000, pp. 393-436.
21. Willmott, A.P., Ellington, C.P., and Thomas, A.L.R., "Flow Visualization and Unsteady Aerodynamics in the Flight of the Hawkmoth, *Manduca Sexta*," *Biological Sciences*, Vol. 352, No. 1351, 1997, pp. 303-316.
22. Van den Berg, C., and Ellington, C.P., "The Vortex Wake of a "Hovering" Model Hawkmoth," *Biological Sciences*, Vol. 352, No. 1351, 1997, pp. 317-328.
23. Van den Berg, C., and Ellington, C.P., "The Three-dimensional Leading-edge Vortex of a "Hovering" Model Hawkmoth," *Philosophical Transactions: Biological Sciences*, Vol. 352, No. 1351, 1997, pp. 329-340.
24. Wakeling, J.M., and Ellington, C.P., "Dragonfly Flight I. Gliding Flight and Steady-State Aerodynamic Forces," *The Journal of Experimental Biology*, 200, 1997, pp. 543-556.
25. Ellington, C.P., "The Novel Aerodynamics of Insect Flight: Applications to Micro Air Vehicles," *The Journal of Experimental Biology*, Vol. 202, 1999, pp. 3439-3448.

26. Sunada, S., and Ellington, C.P., "Approximate Added-Mass Method for Estimating Induced Power for Flapping Flight," *AIAA Journal*, Vol. 38, No. 8, 2000, pp.1313-1321.
27. Sunada, S., and Ellington, C. P., "A New Method for Explaining the Generation of Aerodynamic Forces in Flapping Flight," *Mathematical Methods in the Applied Sciences*, Vol. 24, 2001, pp.1377-1386.
28. Wang, Z.J., "Two Dimensional Mechanism for Insect Hovering," *Physical Review Letters*, Vol. 85, No. 10, 2000, pp.2216-2219.
29. Wang, Z.J., "The Role of Drag in Insect Hovering," *The Journal of Experimental Biology*, Vol. 207, 2004, pp. 4147-4155.
30. Wang, Z. J., Birch J. M., and Dickinson, M. H., "Unsteady Forces and Flows in Low Reynolds Number Hovering Flight: Two-dimensional Computations vs. Robotic Wing Experiments," *The Journal of Experimental Biology*, Vol. 207, 2004, pp. 449-460.
31. Dickinson, M.H., Lehmann, F.O., and Sane, S.P., "Wing Rotation and Aerodynamic Basis of Insect Flight," *Science*, Vol. 284, 1999
32. Birch, J.M., and Dickinson, M.H., "Spanwise Flow and the Attachment of the Leading-Edge Vortex on Insect Wings," *Nature*, Vol. 412, 2001, pp. 729-733.
33. Birch, J.M., and Dickinson, M.H., "The Influence of Wing-Wake Interactions on the Production of Aerodynamic Forces in Flapping Flight," *The Journal of Experimental Biology*, Vol. 206, 2003, pp. 2257-2272.
34. Dickson W.B., and Dickinson, M.H., "The Effect of Advance Ratio on the Aerodynamics of Revolving Wings," *The Journal of Experimental Biology*, Vol. 207, 2004, pp. 4269-4281.
35. Fry, S.N., Sayaman, R., and Dickinson, M.H., "The Aerodynamics of Hovering Flight in *Drosophila*," *The Journal of Experimental Biology*, Vol. 208, 2005, pp. 2303-2318.
36. Lehmann, F., Sane, S.P., and Dickinson, M., "The Aerodynamic Effects of Wing-Wing Interaction in Flapping Insect Wings," *The Journal of Experimental Biology*, Vol. 208, 2005, pp. 3075-3092.
37. Poelma, C., Dickson, W.B., and Dickinson, M.H., "Time-Resolved Reconstruction of the Full Velocity Field around a Dynamically-Scaled Flapping Wing," *Experiments in Fluids*, Vol. 41, 2006, pp. 213-225.

38. Thomas, A.L.R., Taylor, G.K., Srygley, R.B., Nudds, R.L., and Bomphrey, R.J., "Dragonfly Flight: Free-Flight and Tethered Flow Visualizations Reveal a Diverse array of Unsteady Lift-Generating Mechanisms, Controlled Primarily via Angle of Attack," *The Journal of Experimental Biology*, Vol. 207, 2004, pp. 4299-4323.
39. Bomphrey, R.J., Lawson, N.J., Harding, N.J., Taylor, G.K., and Thomas, A.L.R., "The Aerodynamics of *Manduca sexta*: Digital Particle Velocimetry Analysis of the Leading-Edge Vortex," *The Journal of Experimental Biology*, Vol. 208, 2005, pp. 1079-1094.
40. Bomphrey, R.J., Lawson, N.J., Taylor, G.K., and Thomas, A.L.R., "Application of Digital Particle Image Velocimetry to Insect Aerodynamics: Measurement of the Leading-edge Vortex and Near Wake of a Hawkmoth," *Experiments in Fluids*, Vol. 40, 2006, pp. 546-554.
41. Bomphrey, R.J., Taylor, G.K., and Thomas, A.L.R., "Smoke Visualization of Free-Flying Bumblebees Indicates Independent Leading-Edge Vortices on Each Wing Pair," *Experimental Fluids*, DOI 10.1007/s00348-009-0631-8, April 2009.
42. Sane, S.P., "Induced Airflow in Flying Insects I. A Theoretical Model of the Induced Flow," *The Journal of Experimental Biology*, Vol. 209, 2006, pp. 32-42.
43. Sane, S.P., and Jacobson, N.P., "Induced Airflow in Flying Insects II. Measurement of Induced Flow," *The Journal of Experimental Biology*, Vol. 209, 2006, pp. 43-56.
44. Altshuler, D.L., Dudley, R., and Ellington, C.P., "Aerodynamic Forces of Revolving Hummingbird Wings and Wing Models," *Journal of Zoology*, Vol. 264, 2004, pp. 327-332.
45. Warrick, D.R., Tobalske, B.W., and Powers, D.R., "Aerodynamics of the Hovering Hummingbird," *Nature*, Vol. 435 No. 23, June, 2005, pp. 1094-1097. DOI: 10.1038
46. Mueller, T.J., and DeLaurier, J.D., "Aerodynamics of Small Vehicles," *Annual Review of Fluid Mechanics*, Vol. 25, 2003, pp.89-111.
47. Rozhdestvensky, K.V., and Ryzhov, V.A., "Aerohydrodynamics of Flapping-wing Propulsors," *Progress in Aerospace Sciences*, Vol. 39, 2003, pp. 585-633.
48. Heathcote, S., Martin, D., and Gursul, I., "Flexible Flapping Airfoil Propulsion at Zero Freestream Velocity," *AIAA Journal*, Vol. 42, No. 11, 2004
49. Maybury, W.J., Lehmann, F., "The Fluid Dynamics of Flight Control by Kinematic Phase Lag Variation between Two Robotic Insect Wings," *The Journal of Experimental Biology*, Vol. 207, 2004, pp. 4707-4726.

50. Tarascio, M.J., Ramasamy, M., Chopra, I., and Leishman, J.G., "Flow Visualization of Micro Air Vehicle Scaled Insect-Based Flapping Wings," *Journal of Aircraft*, Vol.42, No.2, 2005
51. Lu, Y., Shen, G.X., and Lai, G.J., "Dual Leading-Edge Vortices on Flapping Wings," *The Journal of Experimental Biology*, Vol. 209, 2006, pp. 5005-5016.
52. Vest, M. S. and Katz, J., "Unsteady Aerodynamic Model of Flapping Wings," *AIAA Journal*, Vol. 34, No. 7, July, 1996.
53. Smith, M.J.C., Wilkin, P.J., and Williams, M.H., "The Advantages of an Unsteady Panel Method in Modelling the Aerodynamic Forces on Rigid Flapping Wings," *The Journal of Experimental Biology*, Vol. 199, 1996, pp. 1073-1083.
54. Liu, H., and Kawachi, K., "A Numerical Study of Insect Flight," *Journal of Computational Physics*, Vol. 146, 1998, pp. 124-156.
55. Liu, H., "Computational Biological Fluid Dynamics: Digitizing and Visualizing Animal Swimming and Flying," *Integrative and Comparative Biology*, Vol. 42, 2002, pp. 1050-1059.
56. Jones , K.D., Castro, B.M., Mahmoud O., and Platzer, M.F., "A Numerical and Experimental Investigation of Flapping-Wing Propulsion in Ground Effect," *AIAA 40th Aerospace Sciences Meeting and Exhibit*, 2002.
57. Ramamurti, R., and Sandberg, W.C., "A Three-dimensional Computational Study of the Aerodynamic Mechanisms of Insect Flight," *The Journal of Experimental Biology*, Vol. 205, 2002, pp. 1507-1518.
58. Wu, J.H., and Sun, M., "Unsteady Aerodynamic Forces of a Flapping Wing," *The Journal of Experimental Biology*, Vol. 207, 2004, pp. 1137-1150.
59. Fritz, T.E., and Long, L.N., "Object-Oriented Unsteady Vortex Lattice Method for Flapping Flight," *Journal of Aircraft*, Vol. 41 No. 6, 2004.
60. Ansari, S.A., Zbikowski, R., and Knowles, K., "Aerodynamic Modeling of Insect-like Flapping Flight for Micro Air Vehicles," *Progress in Aerospace Sciences*, Vol. 42, 2006, pp. 129~172.
61. Azuma, A., Azuma, S., Watanabe, I., and Furuta, T., "Flight Mechanics of A Dragonfly," *Journal of Experimental Biology*, Vol. 116, 1985, pp. 79-107.
62. Wakeling, J.M., and Ellington, C.P., "Dragonfly Flight II. Gliding Velocities, Accelerations and Kinematics of Flapping Flight," *The Journal of Experimental Biology*, 200, 1997, pp. 557-582.
63. Wakeling, J.M., and Ellington, C.P., "Dragonfly Flight III. Lift and Power Requirements," *The Journal of Experimental Biology*, 200, 1997, pp. 583-600.

64. Wang, H., Zeng, L., Liu, H., and Yin, C., "Measuring Wing Kinematics, Flight Trajectory and Body Attitude during Forward Flight and Turning Maneuvers in Dragonflies," *The Journal of Experimental Biology*, Vol. 206, 2003, pp. 745-757.
65. Robertson, R.M., and Reye, D.N., "Wing Movements Associated with Collision-Avoidance Manoeuvres during Flight in the Locust *Locusta Migratoria*," *Journal of Experimental Biology*, 163, 1992, pp. 231-258.
66. Wortmann, M., and Zarnack, W., "Wing Movements and Lift Regulation in the Flight of Desert Locusts," *Journal of Experimental Biology*, Vol. 182, 1993, pp. 57-69.
67. Taylor, G.K., and Thomas, A.L.R., "Dynamic Flight Stability in the Desert Locust *Schistocerca Gregaria*," *The Journal of Experimental Biology*, 206, 2003, pp. 2803, 2829.
68. Willmott, A.P., and Ellington, C.P., *The Mechanics of Flight in the Hawkmoth *Manduca Sexta* I. Kinematics of Hovering and Forward Flight*, *The Journal of Experimental Biology* 200, 2705-2722, 1997
69. Willmott, A.P., and Ellington, C.P., *The Mechanics of Flight in the Hawkmoth *Manduca Sexta* II. Aerodynamic Consequences of Kinematic and Morphological Variation*, *The Journal of Experimental Biology* 200, 2723-2745, 1997
70. Dudley, R., and Ellington, C.P., "Mechanics of Forward Flight in Bumblebees I. Kinematics and Morphology," *Journal of Experimental Biology*, Vol. 148, 1990, pp. 19-52.
71. Sun, M., and Xiong, Y., "Dynamic Flight Stability of a Hovering Bumblebee," *The Journal of Experimental Biology*, 208, 2005, pp. 4447-459.
72. Altshuler, D.L., Dickson, W.B., Vance, J.T., Roberts, S.P., and Dickinson, M.H., "Short-Amplitude High-Frequency Wing Strokes Determine the Aerodynamics of Honeybee Flight," *Proceedings of the National Academy of Sciences of the United States of America*, Vol. 102, 2005, pp. 18213-18218.
73. Gill, F.B., "Hummingbird Flight Speeds," *The Auk* 102, 1985, pp.97-101.
74. Wells, D.J., "Muscle Performance in Hovering Hummingbirds," *Journal of Experimental Biology*, Vol. 178, 1993, pp. 39-57.
75. Chai, P., Harrykisson, R. and Dudley, R., "Hummingbird Hovering Performance in Hyperoxic Heliox: Effects of Body Mass and Sex," *The Journal of Experimental Biology* 199, 1996, 2745-2755.
76. Chai, P., Chen, J.S.C., and Dudley, R., "Transient Hovering Performance of Hummingbirds under Conditions of Maximal Loading," *The Journal of Experimental Biology*, Vol. 200, 1997, pp. 921-929.

77. Chai, P. "Hummingbird Hovering Energetics during Moulting of Primary Flight Feathers," *The Journal of Experimental Biology*, Vol. 200, 1997, pp. 1527-1536.
78. Altshuler, D.L., and Dudley, R., "Kinematics of Hovering Hummingbird Flight along Simulated and Natural Elevational Gradients," *The Journal of Experimental Biology*, Vol. 206, 2003, pp. 3139-3147.
79. Tobalske, B.W., Warrick, D.R., Clark, C.J., Powers, D.R., Hedrick, T.L., Hyder, G.A., and Biewener, A., "Three-dimensional Kinematics of Hummingbird Flight," *The Journal of Experimental Biology*, Vol. 210, 2007, pp. 2368-2382.
80. Pennycuik, C.J., "Predicting Wingbeat Frequency and Wavelength of Birds," *Journal of Experimental Biology*, Vol. 150, 1990, pp. 171-185.
81. Pennycuik, C.J., "Wingbeat Frequency of Birds in Steady Cruising Flight: New Data and Improved Predictions," *The Journal of Experimental Biology*, Vol. 199, 1996, pp. 1613-1618.
82. Tobalske, B.W., and Dial, K.P., "Flight Kinematics of Black-Billed Magpies and Pigeons over a Wide Range of Speeds," *The Journal of Experimental Biology* 199, 1996, pp. 263-280.
83. Rosen, M., Spedding, G.R., and Hedenstrom, A., "The Relationship between, Wingbeat Kinematics and Vortex Wake of a Thrush Nightingale," *The Journal of Experimental Biology*. Vol. 207, 2004, pp. 4255,4268.
84. Bullen, R.D., and McKenzie, N.L., "Scaling Bat Wingbeat Frequency and Amplitude," *The Journal of Experimental Biology*, Vol. 205, 2002, pp. 2615-2626.
85. Gustafson, K., "Biological Dynamical Subsystems of Hovering Flight," *Mathematics and Computers in Simulation*, 40, 1996, pp. 397-410.
86. Ellington, C.P., "Power and Efficiency of Insect Flight Muscle," *Journal of Experimental Biology*, Vol. 115, 1985, pp. 293-304.
87. Madangopal, R., Khan, Z.A., and Agrawal, S.K., "Biologically Inspired Design of Small Flapping Wing Air Vehicles Using Four-bar Mechanisms and Quasi-steady Aerodynamics," *Journal of Mechanical Design*, Vol. 127, 2005
88. Issac, K.K., and Agrawal, S.K., "An Investigation into the Use of Springs and Wing Motions to Minimize the Power Expended by a Pigeon-sized Mechanical Bird for Steady Flight," *Journal of Mechanical Design*, Vol 129, 2007
89. Khatait, J.P., Mukherjee, S., and Seth, B., "Compliant Design for Flapping Mechanism: A Minimum Torque Approach," *Mechanism and Machine Theory*, Vol. 41 3-16, 2005

90. Madangopal, R., Khan, Z.A., and Agrawal, S.K., "Energetics-Based Design of Small Flapping Wing Micro Air Vehicles," IEEE/ASME Transactions on Mechatronics, Vol. 11, No.4, 2006
91. Khan, Z.A., and Agrawal, S.K., "Force and Moment Characterization of Flapping Wings for Micro Air Vehicle Application"
92. Khan, Z.A., and Agrawal, S.K., "Modeling and Simulation of Flapping Wing Micro Air Vehicles," ASME International Design Engineering Technical Conferences, DETC2005-85237, Sept. 2005.
93. Banala, S.K., and Agrawal, S.K., "Design and Optimization of a Mechanism for Out-of-Plane Insect Wing Like Motion with Twist," Journal of Mechanical Design, Vol. 127, 2005
94. McIntosh, S.H., Agrawal, S.K., and Khan, Z., "Design of a Mechanism for Biaxial Rotation of A Wing for A Hovering Vehicle," IEEE/ASME Transactions on Mechatronics, Vol. 11, No.2, 2006
95. Zbikowski, R., Knowles, K., Pedersen, C.B., and Galinski, C., "Some Aeromechanical Aspects of Insect-like Flapping Wings in Hover," Proc. Instn Mech. Engrs Vol. 218, 2004
96. Zbikowski, R., Galinski, C., and Pedersen, C.B., "Four-bar Linkage Mechanism for Insect-like Flapping Wings in Hover: Concept and an Outline of Its Realization," Journal of Mechanical Design, Vol. 127, 2005
97. Galinski, C. and Zbikowski, R., "Insect-like Flapping Wing Mechanism Based on a Double Spherical Scotch Yoke," Journal of Royal Society Interface, 2005
98. Galinski, C., and Zbikowski, R., "Materials Challenges in the Design of an Insect-like Flapping Wing Mechanism Based on a Four-bar Linkage," Materials and Design, Vol. 28, 2007, pp. 783-796.
99. Wood, R.J., and Fearing, R.S., "Flight Force Measurements for a Micromechanical Flying Insect"
100. Yan, J., and Fearing, R.S., "Wing Force Map Characterization and Simulation for the Micromechanical Flying Insect"
101. Avadhanula, S., Wood, R.J., Steltz, E., Yan, J., and Fearing, R.S., "Lift Force Improvements for the Micromechanical Flying Insect"
102. Steltz, E., Wood, R.J., Avadhanula, S., and Fearing R.S., "Characterization of the Micromechanical Flying Insect by Optical Position Sensing"
103. Wu, W.C., Wood, R.J., and Fearing, R.S., "Halteres for the Micromechanical Flying Insect"

104. Yan, J., Wood, R.J., Avadhanula, S., Sitti, M., and Fearing, R.S., "Towards Flapping Wing Control for a Micromechanical Flying Insect," 2000
105. Avadhanula, S., and Fearing, R.S. "Flexure Design Rules for Carbon Fiber Microrobotic Mechanisms"
106. Fearing, R.S., Chiang, K.H., Dickinson, M.H., Pick, D.L., Sitti, M., and Yan, J., "Wing Transmission for a Micromechanical Flying Insect," IEEE International Conference on Robotics and Automation, 2000
107. Sitti, M., Campolo, D., Yan, J., and Fearing, R.S., "Development of PZT and PZN-PT Based Unimorph Actuators for Micromechanical Flapping Mechanisms"
108. Campolo, D., Sahai, R., and Fearing, R.S., "Development of Piezoelectric Bending Actuators with Embedded Piezoelectric Sensors for Micromechanical Flapping Mechanisms"
109. Valentine, P.L., "A Variable Stroke Mechanism for Ornithopters," 1996
110. Khan, Z.A., "Design of Flapping Mechanisms Based on Transverse Bending Phenomena in Insects," IEEE International Conference on Robotics and Automation, 2006
111. Singh, B., Ramasamy, M., Chopra, I., and Leishman, J.G., "Experimental Studies on Insect-based Flapping Wings for Micro Hovering Air Vehicles"
112. Singh, B., "Dynamics and Aeroelasticity of Hover Capable Flapping Wings Experiments and Analysis," Ph. D. Dissertation, Department of Aerospace Engineering, University of Maryland, College Park, MD, 2006.
113. Deng, X., Schenato, L, Wu, W.C., and Sastry, S., "Flapping Flight for Biomimetic Robotic Insects: Part I – System Modeling"
114. Cox, A., Monopoli, D., Cveticanin, D., Goldfarb, M., and Garcia, E., "The Development of Elastodynamic Components for Piezoelectrically Actuated Flapping Micro Air Vehicles," Journal of Intelligent Material Systems and Structures, Vol. 13, 2002
115. Taylor, G.K., and Thomas, A.L.R., "Animal Flight Dynamics II. Longitudinal Stability in Flapping Flight," Journal of Theoretical Biology, Vol. 214, 2002, pp. 351-370.
116. Lehmann, F., "Aerial Locomotion in Flies and Robots: Kinematic Control and Aerodynamics of Oscillating Wings," Arthropod Structure & Development, Vol. 33, 2004, pp. 331-345.
117. Raney, D.L., and Slominski, E.C., "Mechanization and Control Concepts for Biologically Inspired Micro Air Vehicles," Journal of Aircraft, Vol. 41, No. 6, 2004

118. Dickinson, M.H., "The Initiation and Control of Rapid Flight Maneuvers in Fruit Flies," *Integrative and Comparative Biology*, Vol. 45, 2005, pp. 274-281.
119. Combes, S.A., and Daniel, T.L., "Flexural Stiffness in Insect Wings I. Scaling and the Influence of Wing Venation," *The Journal of Experimental Biology* 206, 2003, pp. 2979-2987.
120. Combes, S.A., and Daniel, T.L., "Flexural Stiffness in Insect Wings II. Spatial Distribution and Dynamic Wing Bending," *The Journal of Experimental Biology* 206, 2003, pp. 2989-2997.
121. Combes, S.A., and Daniel, T.L., "Into Thin Air: Contributions of Aerodynamic and Inertial-Elastic Forces to Wing Bending in the Hawkmoth *Manduca sexta*," *The Journal of Experimental Biology* 206, 2003, pp. 2999-3006.
122. Sun, M. and Tang, J. "Unsteady aerodynamic force generation by a model fruit fly wing in flapping motion," *J. Exp. Biol.* 205, 55-70. 2002.
123. Wu, P., Stanford, B., and Ifju, P., "Passive Bending and Twisting Motion during the Flapping Stroke of a Micro Elastic Wing for Thrust Production," AIAA Aerospace Sciences Meeting and Exhibit, Orlando, FL, January 5-8, 2009.
124. Ennos, A.R., "The Importance of Torsion in the Design of Inset Wings," *Journal of Experimental Biology*, 140, 1988, pp.137-160.
125. Sunada, S., Zeng, L., and Kwachi, K., "The Relationship between Dragonfly Wing Structure and Torsional Deformation," *Journal of Theoretical Biology*, Vol. 193, 1998, pp.39-45.
126. Zeng, L., Hao, Q., and Kawachi, K., "A Scanning Projected Line Method for Measuring a Beating Bumblebee Wing," *Optics Communications* 183, 2000, pp. 37-43.
127. Sudo, S., Tsuyuki, K., and Kanno, K., "Wing Characteristics and Flapping Behavior of Flying Insects," *Journal of International Society of Experimental Mechanics*, Vol. 2, No. 4, 2002, pp. 257-263.
128. Tsuyuki, K., Sudo, S., and Tani, J., "Morphology of Insect Wings and Airflow Produced by Flapping Insects," *Journal of Intelligent Material Systems and Structures*, Vol. 17, 2006.
129. Stiles, F.G., Altshuler, D.L., and Dudley, R., "Wing Morphology and Flight Behavior of Some North American Hummingbird Species," *The Auk*, Vol. 122, 2005, pp. 872-886.
130. Van den Berg, C., and Rayner, J.M.V., "The Moment of Inertia of Bird Wings and the Inertial Power Requirement for Flapping Flight," *The Journal of Experimental Biology*, Vol. 198, 1995, pp.1655-1664.

131. Pornsin-Siriak, T.N., Tai, Y.C., Nassef, H., and Ho, C.M., "Titanium-Alloy MEMS Wing Technology for A Micro Aerial Vehicle Application," 1998
132. Lin, C., Hwu, C., and Young, W., "The Thrust and Lift of an Ornithopter's Membrane Wings with Simple Flapping Motion," *Aerospace Science and Technology*, Vol. 10, 2006, pp. 111-119.
133. Lee, J.S., Kim, C., and Kim, K.H., "Design of Flapping Airfoil for Optimal Aerodynamic Performance in Low-Reynolds Number Flows," *AIAA Journal*, Vol. 44, No.9, 2006.
134. Liani, E., Guo, S., and Allegri, G., "Aerodynamics and Aeroelasticity of Flexible Flapping Wings," 2007.
135. Tsuzuki, N., "Design Guidelines of Rotary Wings in Hover for Insect-Scale Micro Air Vehicle Applications," *Journal of Aircraft*, Vol. 44, No. 1, Feb. 2007. DOI: 10.2514/1.23165
136. Wu, P., Stanford, B., Bowman, S., Schwartz, A., Ifju, P., "Structural Deformation Measurements of Anisotropic Flapping Micro Air Vehicle Wings," *AIAA Structures, Structural Dynamics, and Materials Conference*, Schaumburg, IL, April 7-10, 2008.
137. Wu, P., Stanford, B., Bowman, W., Schwartz, A., and Ifju, P., "Digital Image Correlation Techniques for Full-Field Displacement Measurements of Micro Air Vehicle Flapping Wings," *Experimental Techniques* Vol. 33-6, 2009.
138. Wu, P., Stanford, B., Ifju, P., "Passive Bending and Twisting Motion during the Flapping Stroke of a Micro Elastic Wing for Thrust Production," *AIAA Aerospace Sciences Meeting and Exhibit*, Orlando, FL, January 5-8, 2009.
139. Wu, P., Ifju, P., Stanford, B., Sällström, E., Ukeiley, L., Love, R., and Lind, R., "A Multidisciplinary Experimental Study of Flapping Wing Aeroelasticity in Thrust Production," *AIAA Structures, Structural Dynamics, and Materials Conference*, Palm Springs, CA, May 4-7, 2009.
140. Wu, P., Stanford, B., and Ifju, P., "Flapping Wing Thrust and Deformation Correlation Study with Flexible Membrane Wings of Different Reinforcement," *AIAA Journal*, 2009. (Accepted)
141. Wu, P. and Ifju, P., "Experimental Methodology for Flapping Wing Structure Optimization in Hovering Flight of Micro Air Vehicles," *AIAA Structures, Structural Dynamics, and Materials Conference*, Orlando, FL, April 12-15, 2010.
142. Wu, P., Sällström, E., Bou, J., Ukeiley, L., and Ifju, P., "Active Rotation and Vibration during the Flapping Stroke of a Micro Elastic Wing for Thrust Production," *AIAA Structures, Structural Dynamics, and Materials Conference*, Orlando, FL, April 12-15, 2010.

143. Sutton, M., Wolters, W., Peters, W., Ranson, W., McNeill, S., "Determination of Displacements Using Improved Digital Image Correlation," *Image and Vision Computing*, Vol. 1, pp. 133–139, 1983.
144. Lu, H., Cary, P., "Deformation Measurements by Digital Image Correlation: Implementation of a Second-Order Displacement Gradient," *Experimental Mechanics*, Vol. 40, pp. 393-397, 2000.
145. Cheng, P., Sutton, M., Schreier, H., McNeill, S., "Full-Field Speckle Pattern Image Correlation with B-Spline Deformation Function," *Experimental Mechanics*, Vol. 42, pp. 344-352, 2002.
146. Tay, C., Quan, C., Huang Y., Fu, Y., "Digital Image Correlation for Whole Field Out-Of-Plane Displacement Measurement Using a Single Camera," *Optics Communications*, Vol. 251, Issues 1-3, pp. 23-36, 2005.
147. Schreier, H., Braasch, J., Sutton, M., "Systematic Errors in Digital Image Correlation Caused by Intensity Interpolation," *Optical Engineering*, Vol. 39, pp. 2915-2921, 2000.
148. Yoneyama, S., Kikuta, H., "Lens Distortion Correction for Digital Image Correlation by Measuring Rigid Body Displacement," *Optical Engineering*, Vol. 45, pp. 1-9, 2006.
149. Siebert, T., Becker, T., Spilthof, K., "High-Speed Digital Image Correlation: Error Estimations and Applications," *Optical Engineering*, pp. 1-7, 2007.
150. Albertani, R., Stanford, B., Hubner, J., Ifju, P., "Aerodynamic Coefficients and Deformation Measurements on Flexible Micro Air Vehicle Wings," *Experimental Mechanics*, Vol. 47, pp. 625-635, 2007.
151. Stewart, K., Albertani, R., "Experimental Elastic Deformation Characterization of a Flapping-Wing MAV Using Visual Image Correlation," *European Micro Air Vehicle Conference and Flight Competition*, Toulouse, France, September, 2007.
152. Schreier, H., Braasch, J., Sutton, M., "Systematic Errors in Digital Image Correlation Caused by Intensity Interpolation," *Optical Engineering*, Vol. 39, pp. 2915-2921, 2000.
153. Mengesha, T.E., Vallance, R.R., Barraja, M., and Mittal, R., "Parametric Structural Modeling of Insect Wings," *Bioinspiration and Biomimetics*, Vol. 4, 2009.
154. Xie, L., Wu, P., and Ifju, P., "Advanced Flapping Wing Structure Development for Biologically-Inspired Hovering Flight," *51st AIAA Structures, Structural Dynamics, and Materials Conference*, Orlando, FL, April 12-15, 2010.

155. Singh, B., Chopra, I., "Insect-Based Hover-Capable Flapping Wings for Micro Air Vehicles: Experiments and Analysis," *AIAA Journal*. 46, 2115-2124. 2008.
156. Bisplinghoff, R., Ashley, H., and Halfman, H., *Aeroelasticity*, Cambridge, MA: Dover, 1955.
157. Mountcastle, A., and Daniel T., "Aerodynamic and Functional Consequences of Wing Compliance," *Experimental Fluids*. 46, 873-882, 2009.
158. Tian, X., Iriarte-Diaz, J., Middleton, K., Galvao, R., Israeli, E., Roemer, A., Sullivan, A., Song, A., Swartz, S., and Breuer, K., "Direct Measurements of the Kinematics and Dynamics of Bat Flight", *Bioinspiration and Biomimetics*, 1, No. 4, pp. S10-S18, 2006.
159. Zeng, L., Matsumoto, H., Kawachi, K., "A Fringe Shadow Method for Measuring Flapping Angle and Torsional Angle of a Dragonfly Wing", *Measurement Science and Technology*, 7, No. 3, pp. 776-781, 1996.
160. Wang, H., Zeng, L., Yin, C., "Measuring the Body Position, Attitude and Wing Deformation of a Free-Flight Dragonfly by Combining a Comb Fringe Pattern with Sign Points on the Wing", *Measurement Sciences and Technology*, 13, No. 6, pp. 903-908. 2002.
161. Cheng, P., Hu, J., Zhang, G., Hou, L., Xu, B., and Wu, X., "Deformation Measurements of Dragonfly's Wing in Free Flight by Using Windowed Fourier Transform", *Optics and Lasers in Engineering*, 46, No. 2, pp. 157-161. 2008.
162. Orteu, J., "3-D Computer Vision in Experimental Mechanics", *Optics and Lasers in Engineering*. 47, 282-291. 2009.
163. Tarascio, M., Ramasamy, M., Chopra, I., Gordon, L., "Flow Visualization of Micro Air Vehicle Scaled Insect-Based Flapping Wings", *J of Aircraft*, 42, 385-390. 2005.
164. de Clercq, K., de Kat, R., Remes, B., van Oudheusden, B., Bijl, H., "Flow Visualization and Force Measurements on a Hovering Flapping-Wing MAV „DeIFly II’," *AIAA Fluid Dynamics Conference*, San Antonio, TX. 2009.
165. Fuchiwaki, M., "Vortex Flow Visualization of a Flapping Butterfly Wing Performing a Fixed Flight," *Comparative Biochemistry and Physiology – Part A: Molecular & Integrative Physiology*. 153, S121. 2009.
166. Heathcote, S., Wang, Z. and Gursul, I., "Effect of Spanwise Flexibility on Flapping Wing Propulsion," *Journal of Fluids and Structures*, 24, 183-199, 2008.
167. Azuma, A., *The Biokinetics of Flying and Swimming*, Second Edition, 1992.

168. Bomphrey, R.J., Taylor, G.K., and Thomas, A.L.R., "Smoke Visualization of Free-Flying Bumblebees Indicates Independent Leading-edge Vortices on Each Wing Pair," *Experiments in Fluids*, Vol. 46, pp.811-821, 2009.
169. Wu, P., Stanford, B., and Ifju, P., "Insect-Inspired Flapping Wing Kinematics Measurements with Digital Image Correlation," *SEM Annual Conference & Exposition on Experimental and Applied Mechanics*, Albuquerque, New Mexico, June 1-4, 2009.
170. Beran, P.S., Parker, G.H., Snyder, R. D., and Blair, M., "Design Analysis Strategies for Flapping Wing Micro Air Vehicles," *International Forum on Aeroelasticity and Structural Dynamics*, Stockholm, Sweden, June 18-20, 2007.
171. Shyy, W., Lian, Y., Tang, J., Viieru, D. and Liu, H. *Aerodynamics of Low Reynolds Number Flyers*, Cambridge University Press, NY, 2008.
172. Jones, K., Duggan, S., Platzer, M., "Flapping-Wing Propulsion for a Micro Air Vehicle," *AIAA Aerospace Sciences Meeting and Exhibit*, Reno, NV, January 8-11, 2001.
173. Wallace, I., Lawson, N., Harvey, A., Jones, J., Moore, A., "High-Speed Photogrammetry System for Measuring the Kinematics of Insect Wings," *Applied Optics*, Vol. 45, No. 17, pp. 4165-4173, 2006.
174. Khan, Z., Agrawal, S., "Design and Optimization of a Biologically Inspired Flapping Mechanism for Flapping Wing Micro Air Vehicles," *IEEE International Conference on Robotics and Automation*, Rome, Italy, April 10-14, 2007.
175. Agrawal, A., Agrawal, S., "Design of Bio-Inspired Flexible Wings for Flapping-Wing Micro-Sized Air Vehicle Applications," *Advanced Robotics*, Vol. 23, No. 7, pp. 979-1002, 2009.
176. Wu, P., Sällström, E., Chimakurthi, S., Aono, H., Cesnik, C.S.E., Ukeiley, L., Shyy, W., and Ifju, P., "An Integrated Experimental and Computational Approach to Analyze Flexible Flapping Wings in Hover," *IMAC-XXVIII Conference and Exposition on Structural Dynamics*, Jacksonville, Florida, February 1-4, 2010.
177. Aono, H., Chimakurthi, S.C., Wu, P., Sällström, E., Stanford, B., Cesnik, C.E.S., Ifju, P., Ukeiley, L., and Shyy, W., "Computational and Experimental Studies on Flexible Flapping Wings," *48th AIAA Aerospace Sciences Meeting*, Orlando, FL, January 4-7, 2010.
178. Wootton, J. "Support and Deformability in Insect Wings," *Journal of Zoology*, 193, 447-468, 1981.
179. Weis-Fogh, T., "Quick Estimates of Flight Fitness in Hovering Animals, Including Novel Mechanisms for Lift Production," *The Journal of Experimental Biology*, 59, 169-230, 1973.

180. Ellington, C. P., Van Den Berg, C., Willmott, A. P. and Thomas, A. L. R., "Leading-edge Vortices in Insect Flight," *Nature*, 384, 626-630, 1996
181. Liu, H. and Aono, H., "Size Effect on Insect Hovering Aerodynamics: an Integrative Computational Study," *Bioinspiration & Biomimetics*, 4, 1-13, 2009.
182. Heathcote, S. and Gursul, I., "Flexible Flapping Airfoil Propulsion at Low Reynolds Numbers," *AIAA Journal*, 45, 1066-1079, 2007.
183. Katz, J. and Weihs, D., "Hydrodynamic Propulsion by Large Amplitude Oscillation of an Airfoil with Chordwise Flexibility," *Journal of Fluid Mechanics*, 88, 485-497, 1978.
184. Chimakurthi, S. K., Tang, J., Palacios, R., Cesnik, C.E.S. and Shyy, W., "Computational Aeroelasticity Framework for Analyzing Flapping Wing Micro Air Vehicles," *AIAA Journal*, 47, 1865-1878.
185. Aono, H, Chimakurthi, S. K., Cesnik, C.E.S., Liu, H. and Shyy, W., "Computational Modeling of Spanwise Flexibility Effects on Flapping Wing Aerodynamics," AIAA-2009-1270.
186. Aono, H., Tang, J., Chimakurthi, S.K., Cesnik, C.E.S., Liu, H., and Shyy, W. "Spanwise and Chordwise Flexibility Effects in Plunging Wings", under review
187. Liu, P. and Bose, N., "Propulsive Performance from Oscillating Propulsors with Spanwise Flexibility," *Proceedings of The Royal Society A. Mathematical Physical & Engineering Sciences*, 453, 1763-1770, 1997.
188. Chimakurthi, S. K., Standford, B., Cesnik, C.E.S. and Shyy, W., "Flapping Wing CFD/CSD Aeroelastic Formulation Based on a Co-rotational Shell Finite Element," AIAA 2009-2412.
189. Shyy, W., Udaykumr, H. S., Rao, M. H. and Smith, R. W., *Computational Fluid Dynamics with Moving Boundaries*. Dover. 1996.
190. Liu, H., "Integrated Modeling of Insect Flight: From Morphology, Kinematics to Aerodynamics," *Journal of Computational Physics*, Vol. 228, 2009.
191. Su, W., and Cesnik, C.E.S., " Nonlinear Aeroelastic Simulations of a Flapping Wing Micro Air Vehicle Using Two Unsteady Aerodynamic Formulations," AIAA Structures, Structural Dynamics, and Materials Conference, Orlando, FL, April 12-15, 2010.
192. Gogulapati, A., Friedmann, P.P., Kheng, E., and Shyy, W., "Approximate Aeroelastic Modeling of Flapping Wings: Comparison with CFD and Experimental Data," *51st AIAA Structural Dynamics and Materials Conference*, Orlando, FL, April 12-15, 2010.

193. Stanford, B., Kurdi, M., Beran, P., and McClung, A., " Shape, Structure, and Kinematics Parameterization of a Power-Optimal Hovering Wing," AIAA Structures, Structural Dynamics, and Materials Conference, Orlando, FL, April 12-15, 2010.
194. Dong, H., M. Harff, and R. Mittal, "Vortex Structures and Aerodynamic Performance of Finite-Aspect-Ratio Flapping Wings in Hovering Motion", AIAA paper 2007-4210.
195. Dong, H., R. Mittal, and F. Najjar, Wake Topology and Hydrodynamic Performance of Low Aspect-Ratio Flapping Foils, *Journal of Fluid Mechanics*, 566(2006), 309-343.
196. Mittal, R., H. Dong, M. Bozkurttas, A. Vegas, and F. Najjar "A Versatile Sharp Interface Immersed Boundary Method for Incompressible Flow with Complex Boundary", *Journal of Computational Physics*, 2007, in press.
197. Tafti, D.K., and Gopalakrishnan, P., " A Parallel Boundary Fitted Dynamic Mesh Solver for Applications to Flapping Flight," *Computers & Fluids*, Vol. 38, pp 1592-1607, 2009.
198. Willis, D.J., Peraire, J., and White, J.K., "'A Combined pFFT-multipole Tree Code, Unsteady Panel Method with Vortex Particle Wakes," *Int. J. Numer. Meth. Fluids*, 53, 1399-1422, 2007.
199. Shuangzhang Tu and Shahrouz Aliabadi, "Development of a Hybrid Finite Volume/Element Solver for Incompressible Flows", accepted for publication in the international journal of Numerical Methods in Fluids.

BIOGRAPHICAL SKETCH

Pin (Frequency) was born on April 5th, 1983, in a middle class family in Zhaoqing (Cause of Prosperity), Guangdong Province, China. His parents were extremely concerned with his education and wanted him to start his academic life as early as possible, therefore changing his birthday to February 5th and kicking him to kindergarten when he was three. Twenty four years later, he has finally had enough of school. His 'official' birthday conceals his Aries personality with an Aquarius one, which does not explain his competitiveness: when he was attending the local No.7 elementary school in Zhaoqing, he fell in his mother's 'tactics' about earning snack rewards by performing well in front of teachers till the 3rd grade. In 1992, he moved with his family to Shenzhen (Deep Ditch), where the economy was booming due to special policies. He continued his study at Binhe (Near River) elementary school, where his teachers again exploited his competitive nature to set good examples for the class. For example, they would motivate him by pointing out the difficulties which may seem discouraging but in fact tantalizing to him.

In 1996, Pin participated in a city-wide entrance examination intended to select thirty out of two thousand of the top students for a pilot class in the Shenzhen Middle School (Shen Zhong). He was lucky enough to get in because he was considered 'too old for the class' at the beginning: what a backfire of the 'official' birthday! He subsequently finished the middle school courses in the pilot class in five years, during which he finally realized that his competitiveness was often manipulated by his teachers. He also realizes that his love for engineering and innovation could not be satisfied in China due to the limited resources. He started planning to study abroad. In 2001, after a year of misery (depressed by the value proposed in the Chinese examinations), he

attended Hunan University to pursue higher education in mechanical engineering (Automotive) in Changsha, Hunan Province. Famous for its long history (founded in 976 A.D.) and its affiliation with Chairman Mao Zedong, Hunan University was one of his favorite photography subjects and it allowed him to make full use its best resources. Pin finally made good use of his competitive personality with his own intention: he honed his English and mechanical design skills during the four college years: in 2004, he won the 1st places in both the China National Collegiate English Speech Contest and Debate Contest in Haerbin; in the same year, he also won the China National Collegiate Mechanical Design Innovation Contest in Wuhan. Later that year, he applied to several graduate schools in the United States, fulfilling his plan to study abroad.

In 2005, Pin completed his Bachelor of Science degree at Hunan University and subsequently arrived at the University of Florida to pursue his PhD in mechanical engineering. He found Prof. Peter Ifju's research topics on micro air vehicles extremely interesting and joined his lab. In 2006, he tagged along the UF team and participated two competitions, in which he witnessed the amazing teamwork of champions. Half year later, his advisor introduced him to his new research topic on flapping wings, which led to this dissertation: the previous 300 pages have well documented what happened between 2007 and 2010, with a few exceptions: this dissertation did not include how many bets he had lost to his best friend Bret, on topics such as whose tofu tastes better or who would graduate younger; nor that he has travelled more than ten thousand miles of road trip in his Dixography Adventure Series, visiting more than fifteen US national parks and historic sites; nor that he continued with his competitiveness and winning the 1st place in the 2009 International Student Paper Competition held by the Society for

Experimental Mechanics, in which Bret was 2nd in 2007; nor how much he had learnt as a semifinalist in the 2010 Global Venture Challenge held by the Oak Ridge National Laboratory; nor how lucky he had been finding his true love over the internet, leading to his conclusion that "One can shop for anything on the internet these days, including a future wife". In May of 2010, Pin successfully defended his dissertation, putting an end to the 24 years of his campus life, as well as starting the next chapter of his professional one. He has determined to be a lifetime learner and researcher, not limited to any narrow topics, to deliver value to society and to bring happiness to people.